

MODELING EARTHQUAKES WITH
LOCAL AND REGIONAL
BROADBAND DATA

Thesis by
Douglas S. Dreger

In Partial Fulfillment of the Requirements
for the Degree of
Doctor of Philosophy

California Institute of Technology
Pasadena, California
1993

(Submitted July 1, 1992)

© 1993

Douglas S. Dreger

ALL RIGHTS RESERVED

Acknowledgements

My stay at Caltech has been tremendously rewarding and enjoyable. I consider myself very lucky to have been at the lab during the past five years. This time has seen the installation of the TERRAscope array without which, this thesis would not have been possible. Hiroo Kanamori's efforts and enthusiasm at developing the TERRAscope array and ensuring that it remain a world-class seismic instrument are greatly appreciated. Don Helmberger, my thesis advisor, taught me how to appreciate the intricacies of seismograms; something that I truly enjoy. Working with Don has been a wonderful experience. The excitement that both Don and Hiroo radiate as the first signals from a nearby earthquake reach the lab, as well as the energetic atmosphere of the coffee hour following a recent earthquake are powerful inspirational forces that I am thankful for being able to share.

Of course this time has also seen an increase in local southern California seismicity, beginning with the 1986 north Palm Springs earthquake. In fact my first day of classes at Caltech was marked by the 1987 Whittier Narrows event. This earthquake in a way, set the stage for my interest in local seismology. The June 28, 1992 Landers earthquake ($M_w=7.4$) occurred three days before my defense of this thesis. In light of this, I am inclined to acknowledge the goddess Seismolaune (Thanks to Bob

Sharp for introducing me to her, Pahoehoe '92) for providing me with the fuel for my curiosity.

Mrinal Sen, Richard Stead, Chandan Saikia, and Shawn Larsen deserve special credit for helping me with the reflectivity, finite difference, F-K codes, and the mplot plotting package, respectively.

I also thank my family for their help and support. To Kyoko, thank you for your love and support, and especially for being understanding, patient, and encouraging me to think about the future. I am sure living with a professional student has not been easy.

I am indebted to the following for showing me that science is fun, rewarding, and for making it possible for me to attain my goals; Frank Barr (Palo Alto High School Geology Teacher), Failure Analysis Associates, Foothill Jr. College, Shawn Biehler (University of California, Riverside, Geophysics Professor), Fernando Aragon (Aragon Geotechnical Consultants).

The work in this thesis was supported by The Advanced Research Projects Agency of the Department of Defense under the contract F1962889K0028, National Science Foundation Grant EAR9014787, U.S.G.S contract 14-08-0001-G1872, and Kajima Corporation.

Abstract

Douglas S. Dreger, Ph.D.

California Institute of Technology 1993

Waveform modeling techniques are applied to several recent, moderate sized earthquakes recorded by the broadband TERRAScope array in southern California. A method for the determination of source parameters at regional distances with three-component, sparse network data is described. The sensitivity of the method to source mislocations and velocity model is investigated. The method is relatively insensitive to source mislocation. The choice of velocity model can affect the inversion results, but it appears that for a number of paths throughout southern California, a simple plane layered velocity model derived from travel-time studies explains much of the observed waveforms.

The broadband waveforms of two small earthquakes that occurred in 1988 near Upland, California are forward modeled to determine Green's functions for the path to Pasadena, California. The effects of near surface gradients, crustal interface sharpness, and two-dimensional basin-ridge structures were studied. This analysis resulted in a simple plane layered velocity model that best fit the data. The Green's functions are then used to study the source characteristics of the 1990 Upland mainshock

($M_L = 5.2$). The long-period body waves are inverted to determine the orientation and seismic moment. Comparisons of the 1990 mainshock with the 1988 events revealed that the mainshock was a relatively complicated event. Multi-point source and distributed finite slip models show that the mainshock ruptured down dip (6 km to 9km) with a non-uniform slip distribution in which 30 % of the total seismic moment was released from a relatively small area at 9 km depth. The overall area of the mainshock was found to be significantly smaller than the aftershock zone.

The source process of the June 28, 1991 Sierra Madre earthquake ($M_L = 5.8$) is investigated using the broadband data recorded at 6 TERRAScope stations. The long-period body waves are inverted to determine the orientation and seismic moment. Ratios of the peak amplitudes of simulated short-period Wood-Anderson and long-period Wood-Anderson seismograms are compared for the mainshock and the two largest aftershocks. The ratios show that stations southwest of the epicenter have elevated levels of short-period energy relative to stations to the east suggesting the presence of directivity. The displacement waveforms were forward modeled using distributed finite slip models. The best fitting model consists of an updip rupture toward the west. This model fails however to explain the amplitudes of the short-period waves. A non-uniform slip model was developed that better explains the short-period amplitudes. The results of this analysis indicate that the shorter-period energy is controlled more by the patches on the fault that experience the greatest slip, rather than the accumulative motions due to slip on the whole fault surface.

Table of Contents

1	Introduction to Broadband Seismology	1
1.1	General Introduction	1
1.2	Overview of the Following Chapters	7
2	Determination of Source Parameters at Regional Distances with Three Component Sparse Network Data	10
2.1	Introduction	10
2.2	Case for the Standard Southern California Velocity Model	12
2.3	Inversion Method	21
2.3.1	Effects of Hypocenter Mislocation	23
2.4	Applications	34
2.4.1	December 3, 1991 Baja Event	34
2.4.2	October 24, 1990 Lee Vining Event	47
2.5	Discussion and Conclusions	57
3	Upland Earthquakes	60
3.1	Broadband Modeling of the 1988 Upland Events	60
3.1.1	Introduction	60
3.1.2	Data and Processing	61
3.1.3	Methodology	66
3.1.4	Modeling Results	66
3.1.5	Sensitivity Analysis	82
3.1.6	Discussion and Conclusions	94
3.2	Broadband Modeling of the 1990 Upland Sequence	98
3.2.1	Introduction	98
3.2.2	Data Comparisons and Analysis	102
3.2.3	Point Source Models	105
3.2.4	Distributed Fault Models	117
3.2.5	Discussion and Conclusions	122

4	The 1991 Sierra Madre Earthquake	126
4.1	Inversion of Long-Period Body Waves	126
4.1.1	Introduction and Data Analysis	126
4.1.2	Inversion Results	131
4.1.3	Conclusion and Implications	136
4.2	Broadband Analysis of the Mainshock Source	138
4.2.1	Introduction	138
4.2.2	Amplitude Constraints on Directivity	143
4.2.3	Waveform Constraints on Directivity	146
4.2.4	Discussion and Conclusions	170
	Bibliography	174
A	Comparison of Several Q Models	179
B	Standard Southern California Model Synthetics	182

List of Tables

2.1	One-dimensional velocity models	17
2.2	Lee Vining source solutions using 3 different velocity models	52
3.1	One-dimensional velocity models	68
3.2	First motion polarity solutions for the 1988 and 1990 Upland earthquakes	102
4.1	Locations of TERRAscope stations	128
4.2	One-dimensional velocity models	131
4.3	Fault plane solutions for the 1991 Sierra Madre earthquake from several studies	139
4.4	Sierra Madre short-period to long-period amplitude ratios	144
A.1	Q models	179

List of Figures

1.1	Example of a locally recorded broadband record	4
1.2	Example of a regionally recorded broadband record	5
2.1	Locations of TERRAscope stations	14
2.2	Comparison of broadband displacement data and synthetics for the Sierra Madre earthquake	15
2.3	Profile of vertical strike-slip displacement synthetics computed with a standard velocity model	19
2.4	Three-component displacement data for Baja California and the Lee Vining, California earthquakes	20
2.5	Geometry used in lateral source mislocation sensitivity analysis	24
2.6	Lateral source mislocation analysis parameter space	25
2.7	Lateral source mislocation waveform comparisons	27
2.8	Geometry used in vertical source mislocation sensitivity analysis	29
2.9	Vertical source mislocation sensitivity analysis parameter space	30
2.10	Vertical source mislocation waveform comparisons	32
2.11	Pasadena displacement, simulated Press-Ewing and Wood-Anderson data for the Baja, California earthquake	35
2.12	Pinyon Flat displacement, simulated Press-Ewing and Wood-Anderson data for the Baja, California earthquake	37
2.13	Seismic moment parameter space for the Baja California earthquake	40
2.14	Parameter space for the Baja California earthquake	41
2.15	Comparison of PAS and PFO data and synthetics for the Baja California earthquake	44
2.16	PAS displacement, Press-Ewing and Wood-Anderson synthetics for the Baja California earthquake	45
2.17	Distance sensitivity of PAS synthetics	46
2.18	Pasadena displacement, simulated Press-Ewing and Wood-Anderson data for the Lee Vining, California earthquake	48
2.19	Goldstone displacement, simulated Press-Ewing and Wood-Anderson data for the Lee Vining, California earthquake	50
2.20	Parameter space for the Lee Vining, California earthquake	53

2.21	Data and synthetic body wave comparisons for the Lee Vining, California earthquake	55
2.22	Data and synthetic whole displacement waveform comparisons for the Lee Vining, California earthquake	56
3.1	Locations of the Upland earthquakes	62
3.2	Example of waveform similarity for two different sized events	63
3.3	Three-component displacement and Wood-Anderson data for the 1988 Upland earthquakes	65
3.4	Example of generalized ray summation	69
3.5	Comparison of tangential component data and synthetics for the 1988 Upland earthquakes	71
3.6	Comparison of radial component data and synthetics for the 1988 Upland earthquakes	74
3.7	Comparison of vertical component data and synthetics for the 1988 Upland earthquakes	76
3.8	Variation of synthetics with source depth (3 to 17 km)	79
3.9	Variation of synthetics with source depth (6 to 9 km) and with main-shock versus aftershock focal mechanism	80
3.10	Sensitivity of synthetics to layer boundary sharpness	84
3.11	Sensitivity of synthetics to layer thickness versus velocity and deeper crustal structure	85
3.12	Tangential component finite difference calculations of ridge-basin-ridge structures	89
3.13	Comparison of elastic finite difference synthetics for a basin-ridge structure and plane layered reflectivity synthetics	92
3.14	Seismicity distribution of the 1990 Upland sequence	100
3.15	Comparison of displacement and simulated Wood-Anderson data for the 1988 and 1990 Upland earthquakes	104
3.16	Inversion of long-period waves	107
3.17	Single and multi-point source models	110
3.18	Inversion of long-period waves with Green's functions computed with a multi-point source model	115
3.19	Distributed finite fault models	119
4.1	Location of the 1991 Sierra Madre earthquake	127
4.2	Comparison of broadband displacement data and synthetics for the Sierra Madre earthquake	129
4.3	Inversion results using long-period body wave data	133
4.4	Seismic moment parameter space	134
4.5	Orientation parameter, parameter space	135

4.6	Fault plane solutions for the mainshock	139
4.7	Seismicity distribution for the sequence	141
4.8	Short-period to long-period amplitude ratios	145
4.9	Example of ray decomposition	148
4.10	Sensitivity of the synthetics due to source depth	149
4.11	Geometries of tested rupture models	151
4.12	Directivity analysis at PAS (Uniform slip)	152
4.13	Directivity analysis at GSC, ISA and PFO (Uniform slip)	155
4.14	Comparison of SH displacement spectra for the mainshock and two of the largest aftershocks	159
4.15	Three-component displacement and Wood-Anderson data and syn- thetics for the uniform slip model	161
4.16	Geometry of the non-uniform slip model	166
4.17	Three-component displacement and Wood-Anderson data and syn- thetics for the non-uniform slip model	167
4.18	Comparison of uniform and non-uniform slip displacement synthetics with PAS data	170
4.19	Comparison of tangential velocity and displacement waveforms recorded at PAS	171
A.1	Displacement SH amplitude spectra for several Q models	181

Chapter 1

Introduction to Broadband Seismology

1.1 General Introduction

The focus of this thesis is on the application of waveform modeling techniques to modern broadband and high dynamic range data recorded at local and regional distances. Data obtained from recent, moderate sized earthquakes recorded by the Caltech TERRAScope array were used. At the writing of this manuscript, this array consists of 6 stations. Each station is comprised of a broadband Streckeisen STS-1 seismometer (STS-2 at Seven Oaks Dam site), a 24 bit Quanterra data logger, and a Kinematics FBA-23 strong motion sensor with a 16 bit digitizer. Together, the Streckeisen-Quanterra and Kinematics systems give approximately 200 db dynamic range. The Streckeisen-Quanterra system records ground velocity with a flat instrument response from 0.0027 to 7 Hz. The Kinematics system records ground acceleration to 50 Hz. Typically the data used in the following chapters has been integrated to displacement within the band where the instrument response is flat. The signal processing was performed with the Seismic Analysis Code (SAC) [Tull, 1987]. Although specifics of the signal processing differ for each of the chapters, generally the following steps were taken: mean removal, de-trend, 10 % taper, and

bandpass filter.

At local and regional distances the effects of propagation through the crustal waveguide is complex. The motions are composed of direct, reflected, refracted, diffracted, surface waves, and also P to S and S to P converted phases. The goal is to understand the wave propagation of the whole wavefield in both timing and in amplitude, as well as to understand contributions from the earthquake source. To effectively study either wave propagation or the seismic source it is necessary to separate the two competing influences. Broadband, high dynamic range data facilitate attaining this goal. First, the dynamic range provides on-scale recordings of motions spanning several orders of magnitude, allowing the propagation effects to be studied using smaller earthquakes with simpler sources. Second, the broadband recording makes it possible to identify various types of waves by their frequency content, aiding in the understanding of the propagation effects. Once the motions of smaller earthquakes are understood in terms of propagation and a catalog of Green's functions are determined, more detailed investigations into the source processes of larger earthquakes are possible. In the past, this approach was hindered by the analog, narrow band instrumentation. Digitizable records often were available for only a small range of earthquake magnitudes for a given source to receiver distance, resulting in incomplete data sets.

To illustrate this point, Figure 1.1 compares the tangential component displacement record of the 1990 Upland, California earthquake ($M_w = 5.5$), recorded at Pasadena (distance 44 km), with simulated Wood-Anderson (WASP) records. The WASP records are produced by convolving the displacements with the appropriate instrument response. The first WASP record (Figure 1.1a) has a clip level set at 12.7 cm, which is half the width of the recording paper on a heliocorder. Despite such an optimal placement, this record would still have been severely clipped at the S-wave onset and unusable. Figure 1.1b shows the full scale WASP record. Note the greater

than 2 meter peak-to-peak amplitude. In fact, even much smaller earthquakes at this distance would have clipped the traditional instrumentation (see Figure 3.15). Figure 1.1c shows the displacement data with several of the important phases identified. Note that both the Love wave and near-field (occurring between the P-wave onset and the S_0 phase) are not apparent in the WASP records.

Figure 1.2a shows an example of a WASP record for a regional distance earthquake (345 km) recorded at Pasadena. While this record is not clipped, other traditional instrumentation, such as the Press-Ewing and long-period Wood-Anderson, would have clipped on the tangential component. Figure 1.2b shows the displacement data and a synthetic seismogram computed from a standard velocity model. Note that the subtle features of the onset of S_n are well modeled by the synthetic and that they would not be identifiable on the Wood-Anderson record. These examples demonstrate the importance of utilizing the broadband characteristics of the TERRAScope data to better understand the influence of the crustal wave guide on the waveforms by improved identification of a greater number of arrivals.

The conclusions drawn in the following chapters indicate that a simple plane layered velocity structure, derived from travel-time studies can explain much of the waveform data. At regional distances the model produces P_{nl} and S_n that match observations both in timing and in amplitude for a number of travel paths. In fact, the synthetic shown in Figure 1.2 is plotted in absolute travel-time. At near regional distances (100 to 300 km) waves exhibiting the properties of mantle P_{nl} waves have been identified [Dreger and Helmberger, 1991b; and Helmberger et al., 1992c]. The characteristics of these types of waves are that they are relatively long-period, propagate along crustal interfaces primarily as P-waves, and are relatively insensitive to lateral heterogeneity. These properties make them extremely useful in source inversions. Robust estimates of earthquake source parameters such as seismic moment, strike, rake and dip can be made even where spatial coverage is poor,

Tangential Component, 1990 Upland

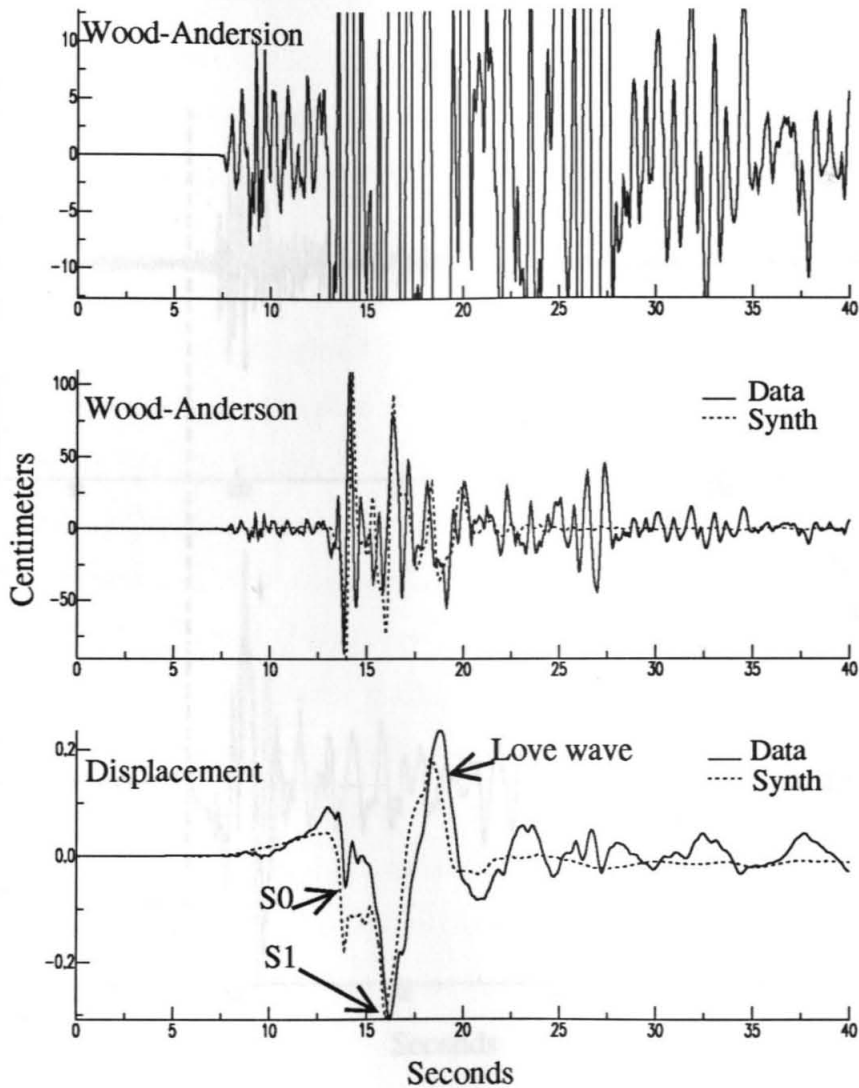


Figure 1.1: Tangential component data recorded at Pasadena for the 1990 Upland, California mainshock. (a) Simulated WAMP record with clip level set at 12.7 cm. (b) Full scale simulated WAMP record. (c) Broadband (0.02 to 7.0 Hz) displacement record. Synthetics computed with a plane layered model are dashed. Amplitudes are in centimeters.

Tangential Component, 1991 Baja California

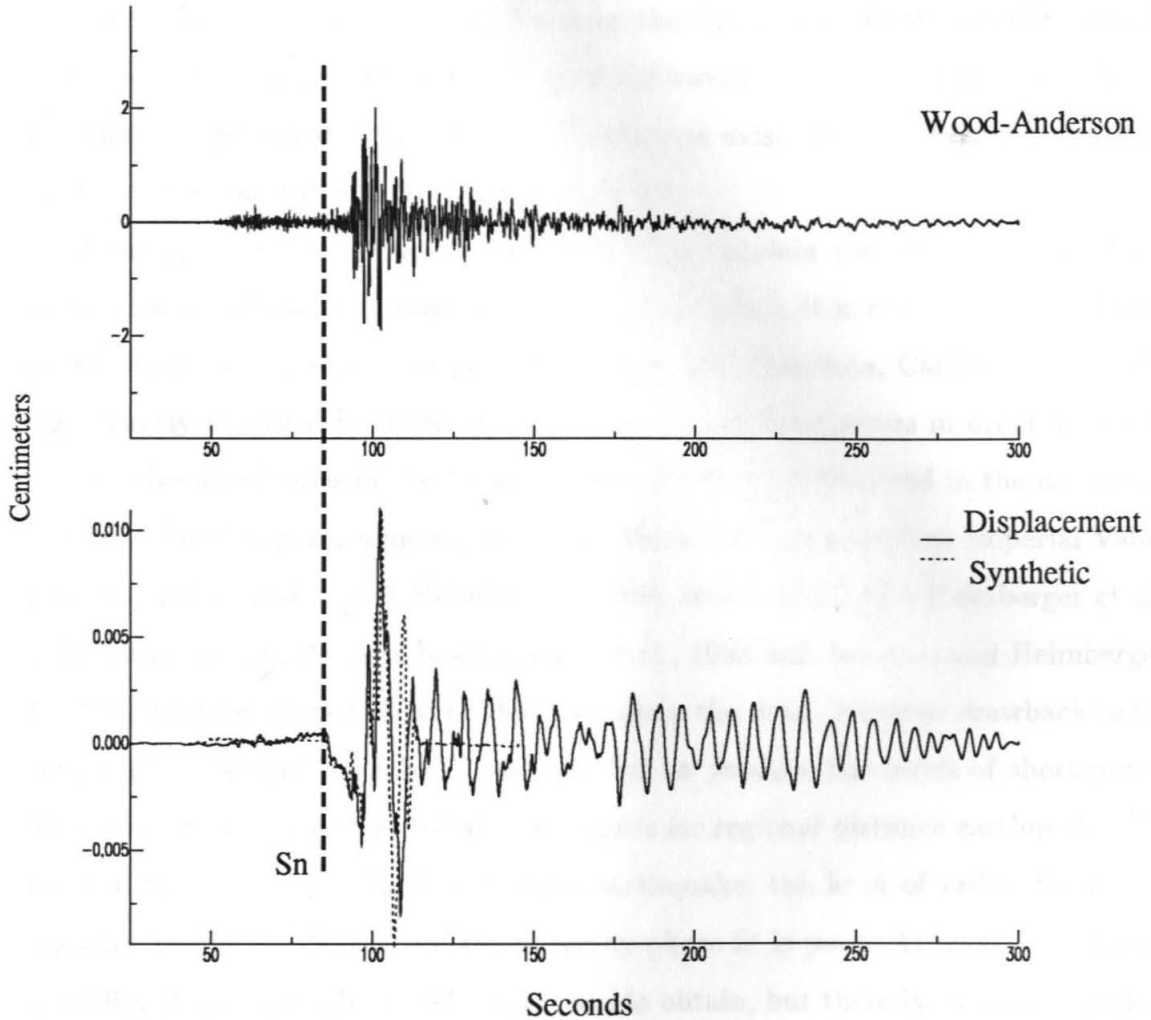


Figure 1.2: Tangential component data recorded at Pasadena for a regional distance (345 km) earthquake in Baja California. (a) Simulated WASP record shown actual size. (b) Broadband (0.02 to 7.0 Hz) displacement data and synthetic. The synthetic was computed with a standard velocity model (see Table 2.1). Amplitudes are in centimeters.

but the instrumentation provides high quality, three-component data. Estimates of source depths are obtained by modeling the relative amplitudes of depth phases such as S_1 at local distances and sS_mS and sP_mP at regional distances.

Successful inversions are dependent upon the signal to noise ratios in the data. At local distances, it appears possible to invert the waveforms for events with magnitudes less than 3.0 provided accurate Green's functions exist. At near regional distances (160 km) the lower bound is approximately 4.0.

Although it appears that a single model can explain the waveform data for a number of travel paths throughout southern California, it is not appropriate to use everywhere. For example, the path from Upland to Pasadena, California had to be significantly modified in terms of velocity and layer thicknesses in order to model the relative amplitudes of the S_1 and Love wave arrivals observed in the data (Figure 1.1). Furthermore, some regions in southern California such as Imperial Valley [Ho-Liu, 1988; Ho-Liu and Helmberger, 1989; Stead, 1989; and Helmberger et al., 1992a] and the Los Angeles basin [Saikia et al., 1992 and Scrivner and Helmberger, 1992] require two-dimensional models to explain the data. Another drawback to the simple plane layered models is that they fail to produce the levels of short-period SV energy observed on the radial components for regional distance earthquakes. At local distances, at least for the Upland earthquake, the level of radial SV is well matched by the synthetics, but the phase-by-phase fit is poor. At regional distances good fits at long-periods are relatively easy to obtain, but there is an obvious lack of radial component SV energy in the WASP bandwidth (> 1 Hz). This may in part be due to an incorrect receiver function, in which the surface velocities are too high [Helmberger et al., 1992c], but the influences of lateral heterogeneity are also very important. Understanding the generation of radial component, short-period SV energy is important for seismic hazard assessment and should be investigated further. Despite these complexities, it seems that the systematic forward modeling approach

described herein is effective in the development of crustal Green's functions that are adequate to study the source processes of earthquakes.

It is important to investigate the sources of earthquakes with a broadband perspective. Studies of the smaller foreshocks and aftershocks are needed to better understand the propagation effects so that estimates of the mainshock source process may be obtained. While seismic moment and orientation parameters can be readily determined by inverting the body waves of local and regional earthquakes with relatively simple models, higher order source complexity such as directivity, multiple sources, and distributed finite rupture require more detailed analysis. The high dynamic range of the data is critical in allowing the identification of the source complexity. Ratios of short-period and long-period peak amplitudes compared between mainshocks and aftershocks are found to be a valuable tool in the identification of directivity. Vertical directivity and non-uniform slip problems are addressed with the waveform data. In the two cases studied in this text, it was found that the short to long-period amplitude ratios differ considerably for the mainshocks compared to the aftershocks, while the waveforms were very similar. These observations suggest that the shorter period energy is being controlled by the relatively small patches of larger slip within the whole fault plane.

1.2 Overview of the Following Chapters

The organization of this manuscript is generally based on source region and event chronology, with the exception of chapter 2. Several of the chapters are comprised of previously published or submitted papers. Some effort was made at tying the sections of each of the chapters together, but the chapters themselves are for the most part meant to stand alone.

Chapter 2 discusses the determination of source parameters at regional distances

with three-component sparse network data. A three-component waveform inversion technique using a single station or sparse network data is presented and the sensitivity of the method to source mislocations is explored with synthetic test cases. The method is applied to two recent earthquakes that occurred well outside the TERRAscope array. Despite completely different travel paths these events display remarkable similarities in the body wave portions of the records that are easily understood using a simple crustal model developed from travel time studies.

Chapter 3 focuses on the 1988 and 1990 Upland, California earthquakes. At the time of these events only the Pasadena (PAS) station was operational. The first section discusses the forward modeling procedure used to investigate the influence of crustal structure on the waveforms of the two largest earthquakes of the 1988 sequence ($M_L=3.7$ and 4.6). The effects of near surface gradients, crustal interface sharpness, and two-dimensional basin-ridge structures were studied. This analysis resulted in a simple plane layered velocity model that best fit the data. The effects of differing radiation pattern and source depth were explored for this model. A set of Green's functions appropriate for the Upland to Pasadena path were developed.

The second section applies these Green's functions to study the source process of the 1990 mainshock ($M_L=5.2$). A point source solution was obtained by inverting the three-component data recorded at PAS. Comparisons of the 1990 data with the 1988 data reveal that the mainshock was relatively more complicated. Multi-point source and distributed finite slip models were tested against the data. The results of this study found that the mainshock ruptured downdip from 6 km to 9 km, and there was a non-uniform slip distribution in which 30 % of the total seismic moment was released from a relatively small patch at 9 km depth.

Chapter 4 focuses on the June 28, 1991 Sierra Madre earthquake ($M_L=5.8$). At the time of this event 6 stations of the TERRAscope array were operational. The first section discusses the inversion of the three-component data for 5 of these stations

to obtain a point source solution.

The second section discusses the source of the earthquake in more detail. Ratios of the peak amplitudes of simulated WASP and WALP records are compared for the mainshock and the two largest aftershocks. The ratios show that stations southwest of the epicenter have elevated levels of short-period energy relative to stations to the east suggesting the existence of directivity. The displacement waveforms were forward modeled using distributed finite slip models. The best fitting model consists of an updip rupture toward the west. This model fails however to explain the amplitudes of the short-period waves (> 1 Hz). A non-uniform slip model was developed that better explains the short-period amplitudes.

Chapter 2

Determination of Source Parameters at Regional Distances with Three Component Sparse Network Data

2.1 Introduction

The regional networks of broadband instrumentation currently being installed are expected to improve our understanding of wave propagation and source problems. Progress has been made in studying wave propagation at regional distances using the broadband, whole waveform data [Helmberger et al., 1992a,b; Zhao and Helmberger, 1991]. These studies are providing information on both the P-wave and S-wave velocity structures. At local distances the study of wave propagation is further complicated by the greater influence of near surface lateral heterogeneity and the small time separations between direct, reflected, converted and surface wave phases; however, it seems possible to model the data broadband with simple, regionalized upper crustal models [Dreger and Helmberger, 1990].

The broadband characteristics of the high quality data is especially useful be-

cause it allows one to extract the bandwidth which is most sensitive to the problem at hand. For source problems long-period data has been found to be particularly useful. There are numerous examples of the use of teleseismic body waves to obtain estimates of source parameters of large earthquakes ($m_b \geq 6.0$) in the literature. Smaller events however, are recorded with poor signal-to-noise ratios at distances greater than 30° . This is especially true for strike-slip earthquakes that have a P-wave radiation node for diving energy. To circumvent this problem, data recorded at regional distances ($1^\circ - 12^\circ$) are used. Although the regional waveforms are relatively more complicated, the long-period P_{nl} waves are relatively stable (i.e., change slowly with distance) [Helmberger and Engen, 1980] and have proven to be quite successful in source inversions [Wallace et al., 1981]. PL waves propagating in the upper crust (along a shallow interface at approximately 4 to 6 km depth) also appear to be stable and useful in obtaining source parameters of earthquakes in the near-regional distance range (100 km to 300 km) [Dreger and Helmberger, 1991b]. There is evidence that source depth can be resolved with the long-period data [Dreger and Helmberger, 1991a,b], but source time histories and other higher order source processes such as directivity and/or distributed rupture require shorter period information and an earth structure that adequately explains the short-period propagation characteristics. The wide dynamic range of these systems allow studies of both small and large earthquakes in a given source region enabling the isolation of source and propagation terms. This property provides a great advantage over the older systems where observations of mainshock-aftershock data occurred only rarely, when low-gain and high-gain instruments were co-located (see Helmberger et al., 1992a).

The regional broadband networks will provide excellent coverage for the larger events, however for smaller events coverage will not be as good due to reduced signal-to-noise ratios. For smaller events it is necessary to investigate the sources of earthquakes with techniques appropriate for sparse networks or single stations.

This is especially important for the studies of earthquakes not located in regions of dense instrumentation and historic earthquakes. Some progress has already been made at inverting waveform data recorded at a single station at local distances (< 100 km) [Dreger and Helmberger, 1991a; Fan and Wallace, 1991]. Adding the direct P and S amplitude data to constrain first motion mechanism analyses has also proven to be successful at local distances [Ma and Kanamori, 1991].

The purpose of this paper is to describe a procedure of obtaining source parameters such as focal mechanism, seismic moment and source depth from regional data with sparse coverage and demonstrate its usefulness with data from the TERRAscope array. In particular, we apply a method that has proven successful in modeling regional P_{nl} waves and extend it to include the whole three-component record, excluding surface waves. The effects of hypocentral mislocations are studied with synthetic test cases. The method is applied to two recent, moderate sized earthquakes whose energy traversed completely different paths. We examine the critical assumption that the velocity model is known. It does seem however, that adequate Green's functions can be calculated from models derived independently from travel-time studies as is demonstrated below.

2.2 Case for the Standard Southern California Velocity Model

Although this study is primarily concerned with source retrieval from sparse network data it is interesting to consider first, a case in which there is good azimuthal coverage. Figure 2.1 shows the locations of the TERRAscope stations, relative to the 1990 Lee Vining, 1991 Sierra Madre and the 1991 Baja California earthquakes. The June 28, 1991 Sierra Madre earthquake ($M_L = 5.8$) was the topic of an earlier study in which the three-component, long-period body waves were inverted for source parameters [Dreger and Helmberger, 1991b] and is discussed in detail in chapter 4. The

following section discusses the inversion method used in this and the following chapters. The Sierra Madre earthquake was optimally located within the TERRAScope network and was recorded by all six of the stations in operation at the time, with very good azimuthal coverage. Four of the stations were located at distances of 159 ± 1 km from the event. We inverted the long-period body wave data for that event and obtained results that were in excellent agreement with solutions obtained from first motion polarities (Hauksson, 1992), local strong motions and teleseismic P and S waves [Wald, 1992], regional surface waves (H. K. Thio, personal communication), and local P-SV and P-SH amplitude ratios (K. F. Ma, personal communication). The standard deviation of the mean of these solutions is less than 7° . Of greater interest however was the similarity of the waveforms at three of the equidistant stations indicating that a common Green's function was sufficient for use in the source inversion. Figure 2.2 compares the displacement data recorded at GSC, ISA and PFO with displacement synthetics computed with an F-K integration method. The data was integrated to ground displacement from velocity within the frequency band from 0.005 to 7.0 Hz. The synthetics were computed up to 5 Hz using a slightly modified version of the standard southern California velocity model (SC, Table 2.1) commonly used to locate earthquakes. This model is based primarily on travel-times from quarry blasts [Hadley and Kanamori, 1977] and teleseismic surface waves [Hadley and Kanamori, 1979]. The body wave portions of the records in Figure 2.2 are well modeled. Phases produced by discontinuities in the model are clearly identifiable in the data. The surface waves are also reasonably well modeled in terms of dispersion, but they have the largest variation in arrival times. The similarity in waveform, despite very different travel paths suggest that this model may be appropriate for use over a wide area in southern California. Of course it will not work everywhere due to differing degrees of two and three-dimensional influences on wave propagation (see Helmberger et al., 1992a).

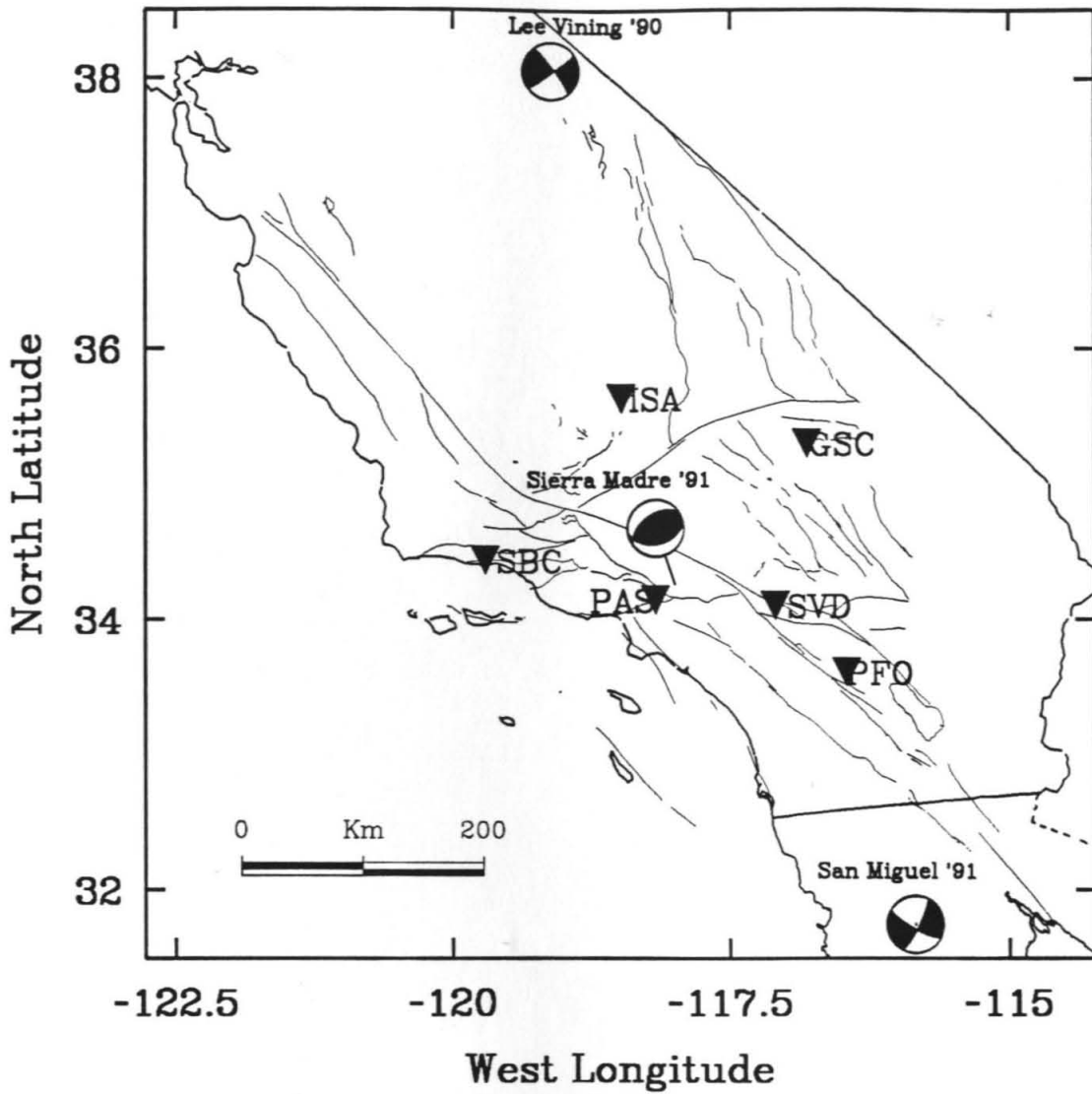


Figure 2.1: Map showing the locations of the TERRAscope stations currently operational (inverted triangles), and the locations of the two events considered in this study (Lee Vining and Baja). The location of the Sierra Madre earthquake is also shown. The mechanisms were determined by inverting three-component data recorded by TERRAscope.

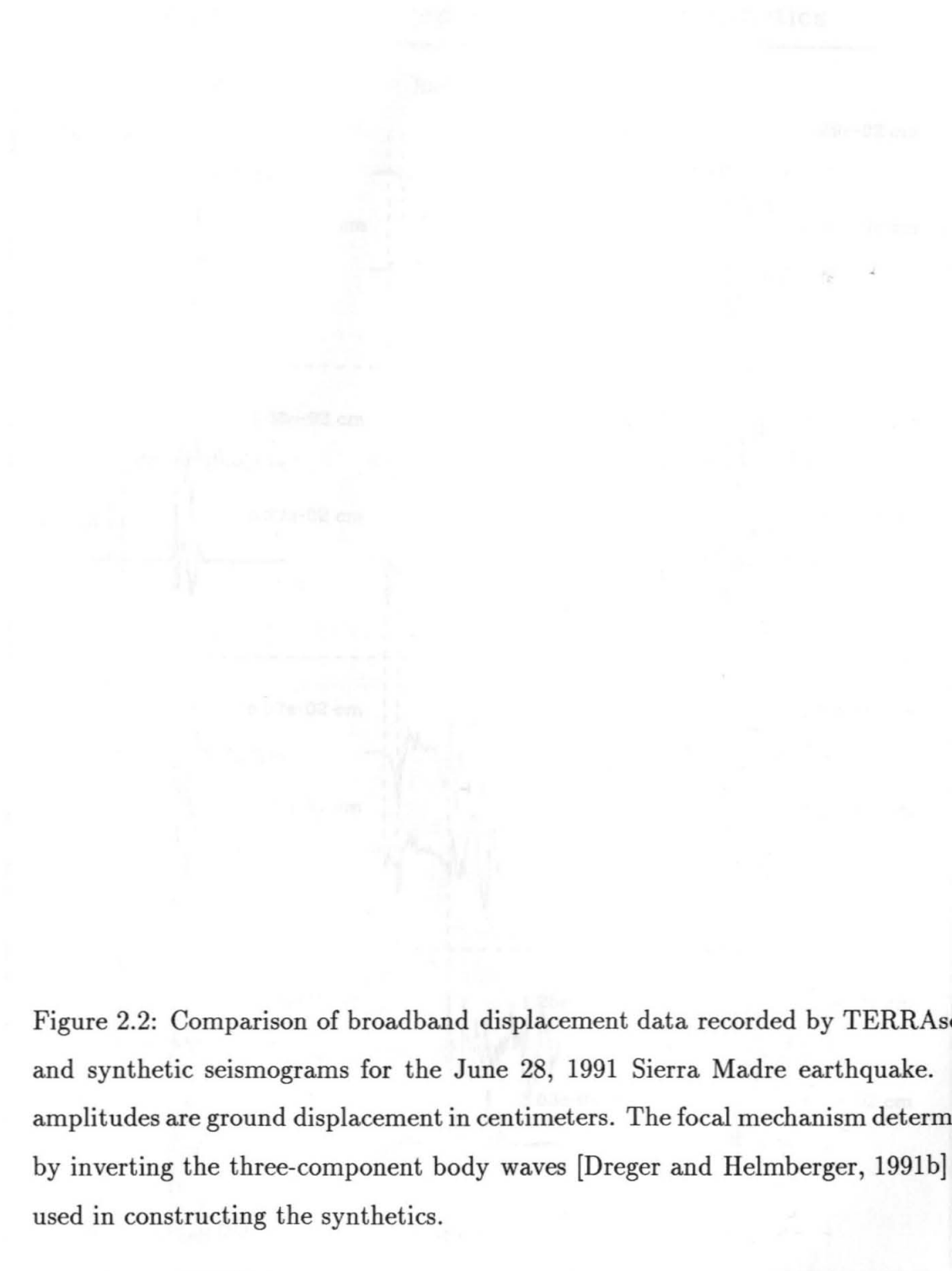
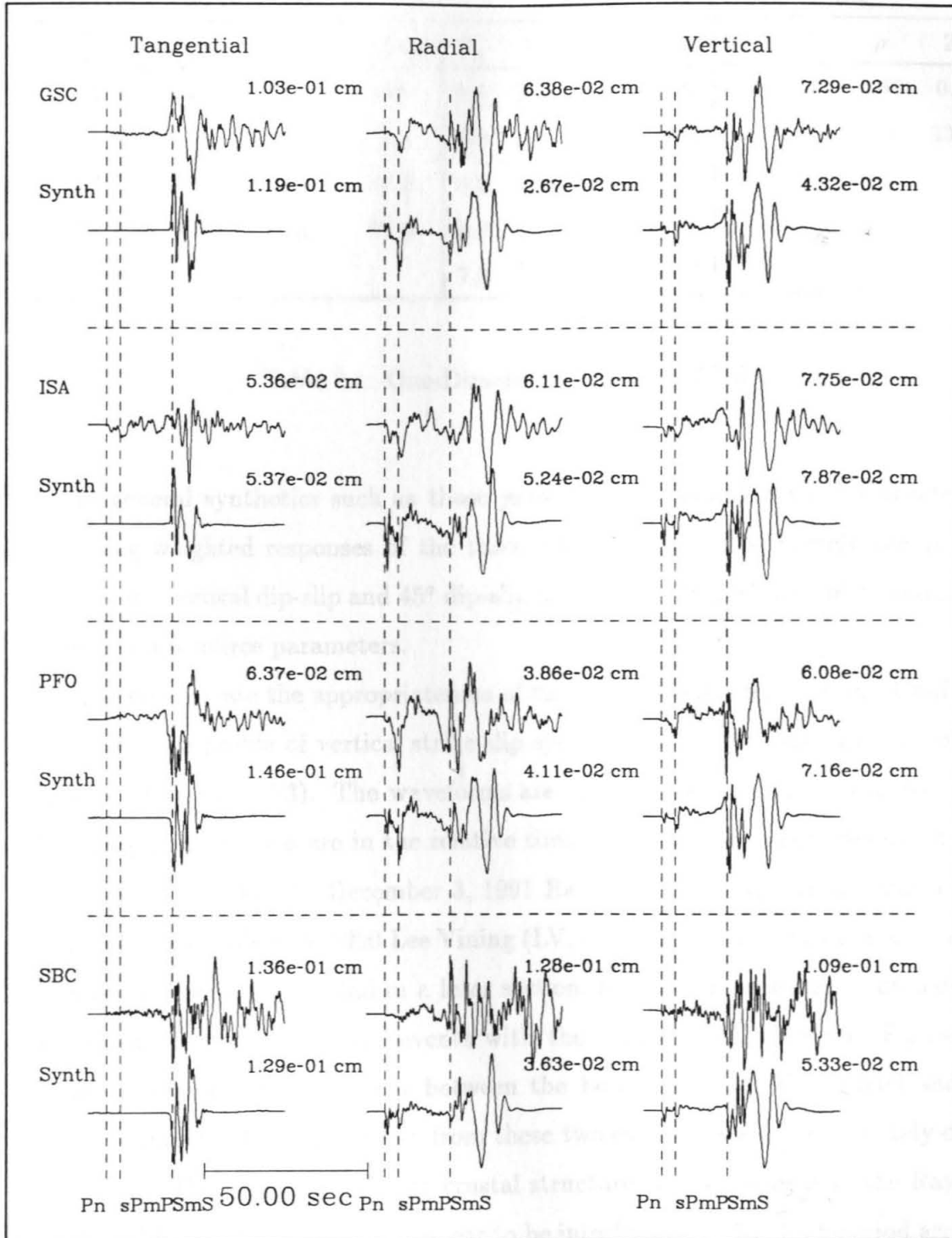


Figure 2.2: Comparison of broadband displacement data recorded by TERRAScope and synthetic seismograms for the June 28, 1991 Sierra Madre earthquake. The amplitudes are ground displacement in centimeters. The focal mechanism determined by inverting the three-component body waves [Dreger and Helmberger, 1991b] was used in constructing the synthetics.

Comparison of Broadband Data and Synthetics



SC				JD				LH			
$V_p(\frac{km}{sec})$	$V_s(\frac{km}{sec})$	$\rho(\frac{g}{cm^3})$	Z (km)	V_p	V_s	ρ	Z	V_p	V_s	ρ	Z
5.5	3.18	2.4	0.0	5.1	3.02	2.5	0.0	5.9	3.45	2.67	0.0
6.3	3.64	2.67	5.5	5.8	3.45	2.65	2.0	7.8	4.3	3.3	33.0
6.7	3.87	2.8	16.0	6.2	3.65	2.73	8.0				
7.8	4.5	3.0	35.0	6.9	3.85	2.9	22.0				
				7.9	4.4	3.21	36.0				

Table 2.1: One-Dimensional Velocity Models

In general synthetics such as those presented in Figure 2.2 are constructed by summing weighted responses of the three fundamental faults, namely the vertical strike-slip, vertical dip-slip and 45° dip-slip faults. The weights depend on the strike, rake and dip source parameters.

To demonstrate the appropriateness of the SC synthetics for southern California we consider a profile of vertical strike-slip synthetics computed for distances of 100 to 450 km (Figure 2.3). The waveforms are very similar at neighboring distances. The largest differences are in the relative timing. Figure 2.4 shows broadband data recorded at PAS for the December 3, 1991 Baja California (BAJA, distance of 345 km) and the October 24, 1990 Lee Vining (LV, distance 438 km) earthquakes. These events are discussed in detail in a later section, but it is interesting to compare the waveforms recorded for these events with the synthetics displayed in Figure 2.3. There is remarkable agreement between the body waves for this model and the data. Remember that the energy from these two events traversed completely different paths. The effects of differing crustal structure is most evident in the Rayleigh waves, which for the Baja event appear to be interfered with by short-period arrivals. In contrast, the Rayleigh wave for the Lee Vining event is well developed. Thus it

appears that the SC model has considerable applicability with respect to body waves from Baja California to central California. A catalog of SC Green's functions from 30 km to 395 km with a spacing of 5 km is provided in appendix B for reference.



Figure 2.4
 Vertical component
 of Green's functions
 for various hypocenters
 from Baja California to
 central California.

Figure 2.4
 Vertical component
 of Green's functions
 for various hypocenters
 from Baja California to
 central California.

Figure 2.4
 Vertical component
 of Green's functions
 for various hypocenters
 from Baja California to
 central California.

Vertical Strike-slip Synthetics

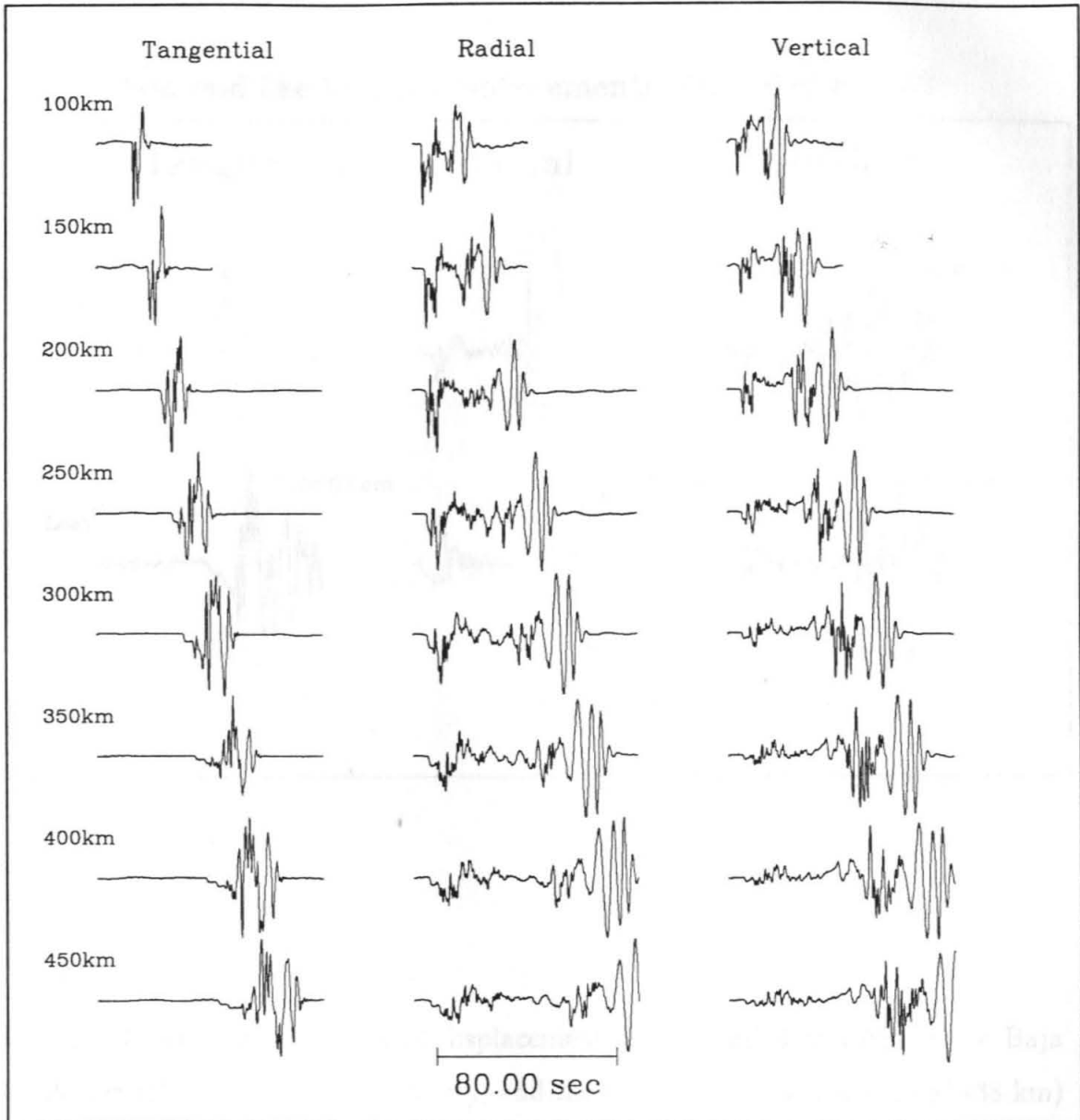


Figure 2.3: Profile of broadband synthetic displacement seismograms for a vertical strike-slip fault. The synthetics were convolved with a triangular source time function with a duration of 1 second. The polarities of the tangential and radial components were flipped to allow easier comparison with the data shown in Figure 2.4.

Baja and Lee Vining Displacements Recorded at PAS

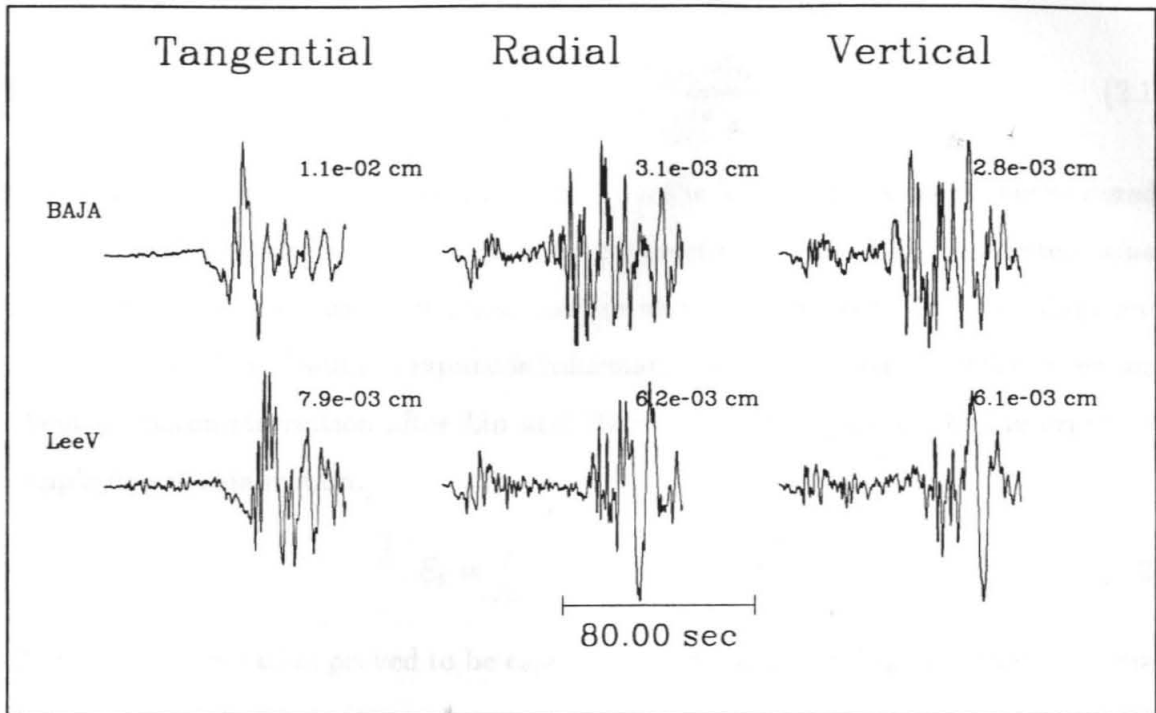


Figure 2.4: The three-component displacement data recorded at PAS for the Baja California (BAJA, distance of 345 km) and the Lee Vining (LV, distance of 438 km) events. Amplitudes are ground displacement in centimeters.

2.3 Inversion Method

To use inverse theory some measure of fitting error is needed to quantify the misfit of the model to the data. Wallace et al. [1981] used

$$E_i = 1 - \frac{\int_0^T [f_i(t)g_i(t)] dt}{\sqrt{\int_0^T f_i(t)^2 dt} \sqrt{\int_0^T g_i(t)^2 dt}} \quad (2.1)$$

where the index i refers to the component, T is the length of seismogram considered, $f_i(t)$ is the data vector and $g_i(t)$ is the Green's function vector. This parameterization is based on the zero-lag correlation coefficient and normalizes both the data and synthetics so that absolute amplitude information does not enter into the inversion. Another parameterization after Liu and Helmberger [1985] uses a fitting error not employing normalization.

$$E_i = \int_0^T [f_i(t) - g_i(t)]^2 dt \quad (2.2)$$

This parameterization proved to be especially useful when trying to extract information about complex multi-source events. Although not presented, we tested both parameterizations and found that including the amplitude information produced greater stability and more rapid convergence when using a single station because of the importance of the SH to SV amplitude levels.

The Green's functions in equation 2.2 depend nonlinearly on strike, rake and dip [Helmberger, 1983]. The problem is linearized by writing the error as a sum of the error of an initial model and the error due to a perturbation to the model.

$$E_i = e_i^0 + \delta e_i \quad (2.3)$$

where δe_i is the error due to a perturbation and is defined as

$$\delta e_i = \frac{\partial e_i}{\partial \theta_j} \delta \theta_j. \quad (2.4)$$

Where $\frac{\partial e_i}{\partial \theta_j}$ is a matrix of partial derivatives of equation 2.2 with respect to the model parameters. The $\delta\theta_j$'s are the perturbations to the initial model. By minimizing the sum of the squared error (equation 2.3) with respect to the perturbations to the model parameters, a solution is found in which,

$$\delta\theta_j = (A^T A + \delta I)^{-1} A^T e \quad (2.5)$$

where $\delta\theta_j$ are the changes to the source parameters, e is the error matrix defined in equation 2.2, δI is a unit matrix damping term to stabilize the inversion and A is a matrix of partial derivatives defined as,

$$A = a_{ij} = \frac{\partial e_i}{\partial \theta_j}. \quad (2.6)$$

It is assumed that the δe_i terms are small. To arrive at a solution, a process of iteration from a starting model is used, where each successive iteration uses the preceding solution as a starting model. The iterative process is continued until convergence is obtained. One of the problems with nonlinear inversions however, is the fact that there maybe some inherent dependence of the final solution on the starting model. *A priori* information can be used to help constrain the inversion, but for small earthquakes, earthquakes without good coverage and historical earthquakes, *a priori* information may be lacking. One way of testing to see if there is any dependence is to use graphical means to examine the parameter space. For inversions involving many parameters this approach is prohibitively complex. The number of parameters in a source inversion however are relatively few. The approach taken here is to invert solely for strike rake and dip, and to use graphical means to determine the uniqueness and resolvability of the solutions. Since we iterate to a solution, each iteration provides a measure of the misfit for that solution. By using a number of starting models the parameter space can be effectively mapped out and allow one to ascertain the uniqueness and resolvability.

In practice we low-pass filter both the data and Green's functions to minimize errors due to misalignment of the shorter period arrivals. Since surface waves are very sensitive to shallow, lateral heterogeneity [Ho-Liu, 1988; Stead, 1989], only the body waves are used. The whole body waveforms from the initial P-wave to approximately $S_m S$ are used, thereby inverting both the P-waves and the S-waves simultaneously. Although it is possible to weight each of the components, we normally weight all of the data traces equally.

2.3.1 Effects of Hypocenter Mislocation

It is useful to explore the effects of source mislocations on the inversion procedure using synthetic seismograms. We examine the cases of epicentral and vertical source mislocations. Both single and multiple station cases are considered. The synthetic data and Green's functions were processed in the same manner that has proven effective with real data. A low-pass filter was used to minimize errors due to misaligning the shorter period arrivals and only the body waves were used. The same velocity model was used to compute both the synthetic data and Green's functions with an F-K integration method. The synthetic data was given a source orientation of $\theta = 75^\circ$, $\lambda = 45^\circ$ and $\delta = 65^\circ$.

Lateral Mislocation

Figure 2.5 shows the assumed geometries. First, we examined the effect of mislocating the source 10 km in the radial direction (single station case S1). Figure 2.6a shows the graphical representation of the parameter space. Each dot represents the error of a single iteration. The conjugate solution is also plotted for each iteration. Four starting models were used and the inversion was permitted to iterate 50 times. Usually convergence was obtained within 10 iterations. Examination of the parameter space (Figure 2.6a) reveals that a mislocation in distance produced two global

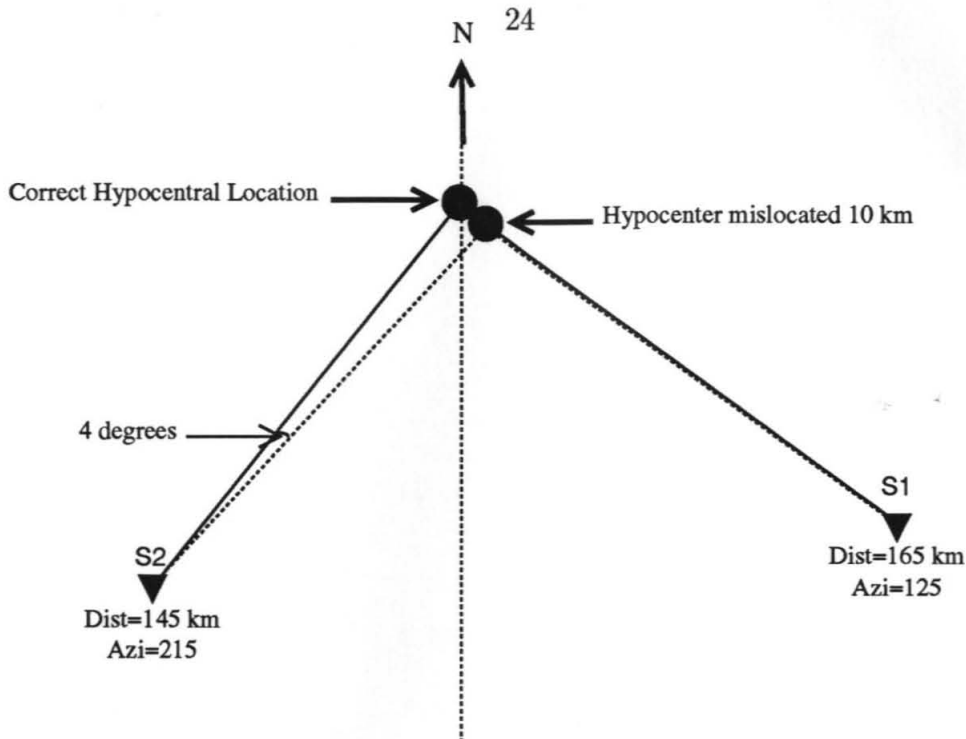


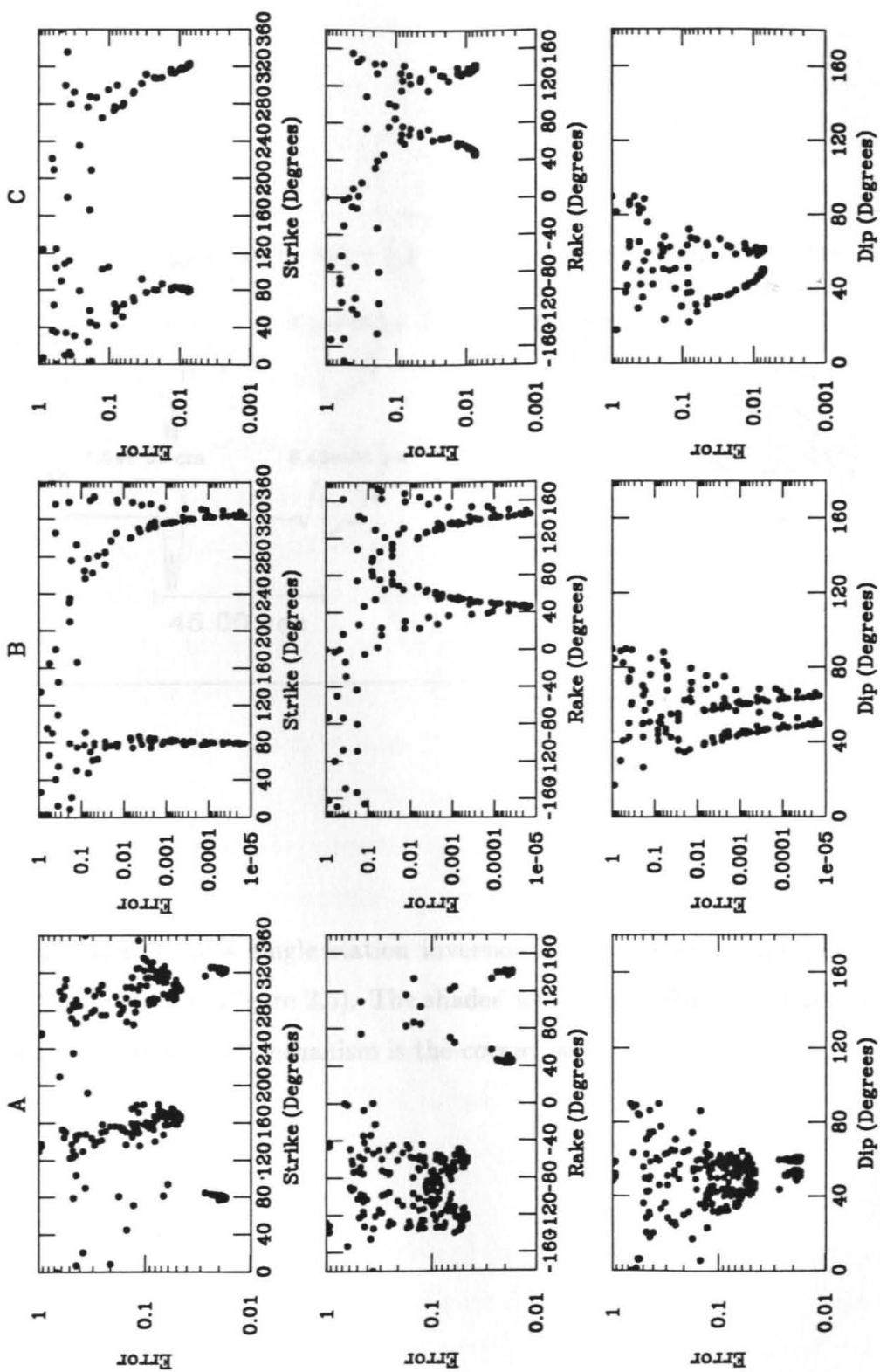
Figure 2.5: Diagram showing the station-source geometries used in the lateral mislocation sensitivity analysis.

minima in strike and rake. Rather pronounced local minima are also evident. The global minima give a solution of $\theta = 80^\circ$, $\lambda = 46^\circ$ and $\delta = 60^\circ$. A sample of the fits to the data is given in Figure 2.7.

Second, we examined the effect of mislocating the source 10 km in the tangential direction. The geometry is from station S2 to the source (Figure 2.5). Figure 2.6b shows the graphical representation of the parameter space. In this case only the global minima are observed, and the error reduction is over 5 orders of magnitude. The global minima give a solution of $\theta = 80^\circ$, $\lambda = 48^\circ$ and $\delta = 64^\circ$ which is nearly the correct answer.



Figure 2.6: Parameter space for lateral mislocation sensitivity tests. (a) shows the parameter space for the strike (θ), rake (λ) and dip (δ) model parameters using only station S1 (Figure 2.5) in the inversion. (b) shows the parameter space using only station S2. (c) shows the parameter space using both stations S1 and S2.



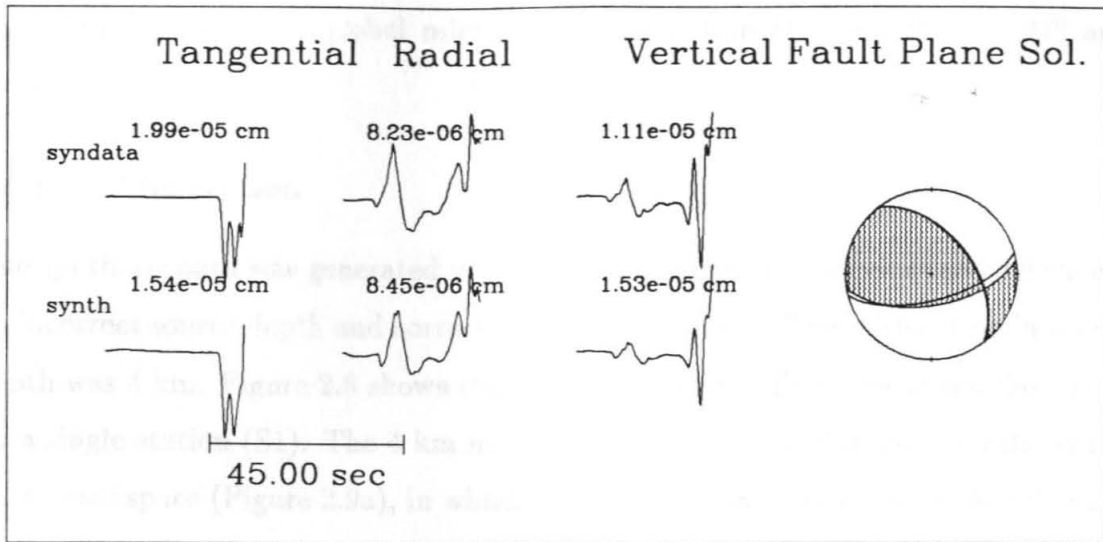


Figure 2.7: Results of a single station inversion using a Green's function with an incorrect distance (S1, Figure 2.5). The shaded focal mechanism was determined by inversion. The unshaded mechanism is the correct solution.

Third, we test the case where the source is mislocated as above, but was recorded by two stations (S1 and S2). In this case there is 90° aperture between the stations. Figure 2.6c shows the parameter space. The addition of the second station improves the parameter space significantly, in that the local minima observed in Figure 2.6a have disappeared. The global minima yield a solution of $\theta = 79^\circ$, $\lambda = 47^\circ$ and $\delta = 62^\circ$.

Vertical Mislocation

The synthetic data was generated in the same manner as the previous section except an incorrect source depth and correct distances were used. The mislocation in source depth was 4 km. Figure 2.8 shows the geometries tested. First, we tested the effects on a single station (S1). The 4 km mislocation in depth has dramatic effects on the parameter space (Figure 2.9a), in which a significant non-uniqueness is characterized by local minima in both strike and rake. The non-uniqueness occurs at a strike of 170° , 95° from the 75° and 140° from the 310° minima associated with the correct strikes. Occasionally, with steeply dipping faults as many as four minima in strike can be observed due to the uncertainty in dip. If the dip exceeds 90° then the strike rotates 180° in our convention. The redundant minima are distinguished from non-uniqueness by the 180° separation. The lowest errors give a solution close to the starting solution, where $\theta = 73^\circ$, $\lambda = 54^\circ$ and $\delta = 65^\circ$. Without additional (*a priori*) information it would not be possible to choose the correct solution based solely on the misfit error. Figure 2.10 compares the waveforms for the two possible mechanisms. Note that the mechanisms are significantly different, yet the waveforms are remarkably similar.

Second, we used two stations with an aperture of 20° (S1 and S2a), representing an event occurring outside the array. Figure 2.9b shows the parameter space. The non-uniqueness observed in Figure 2.9a is removed with the addition of the second

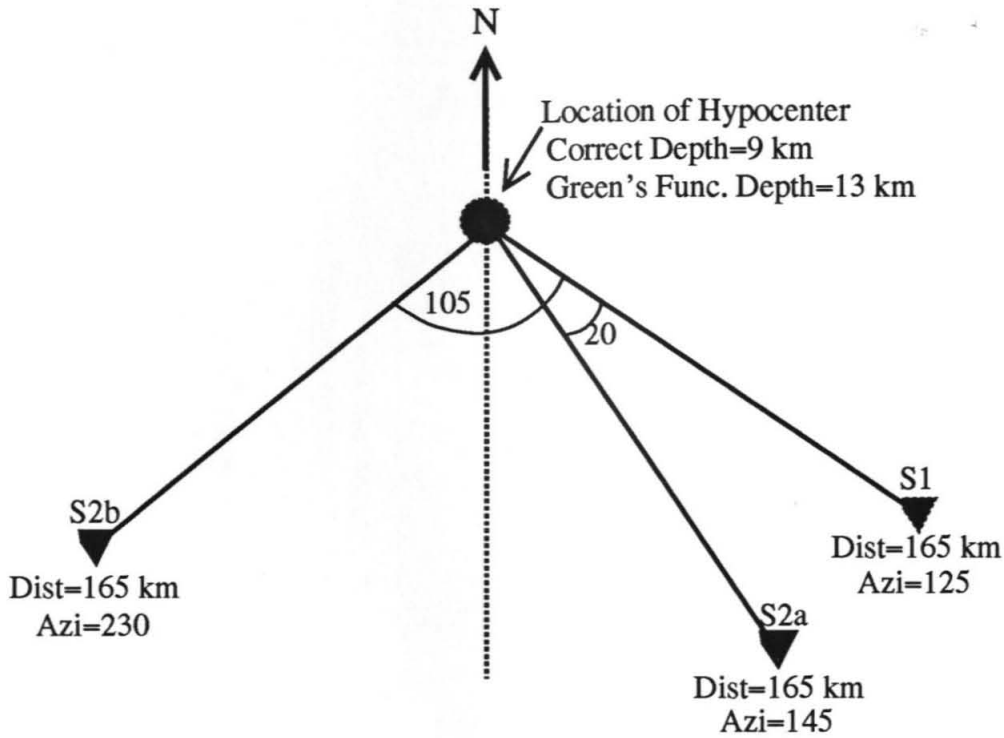
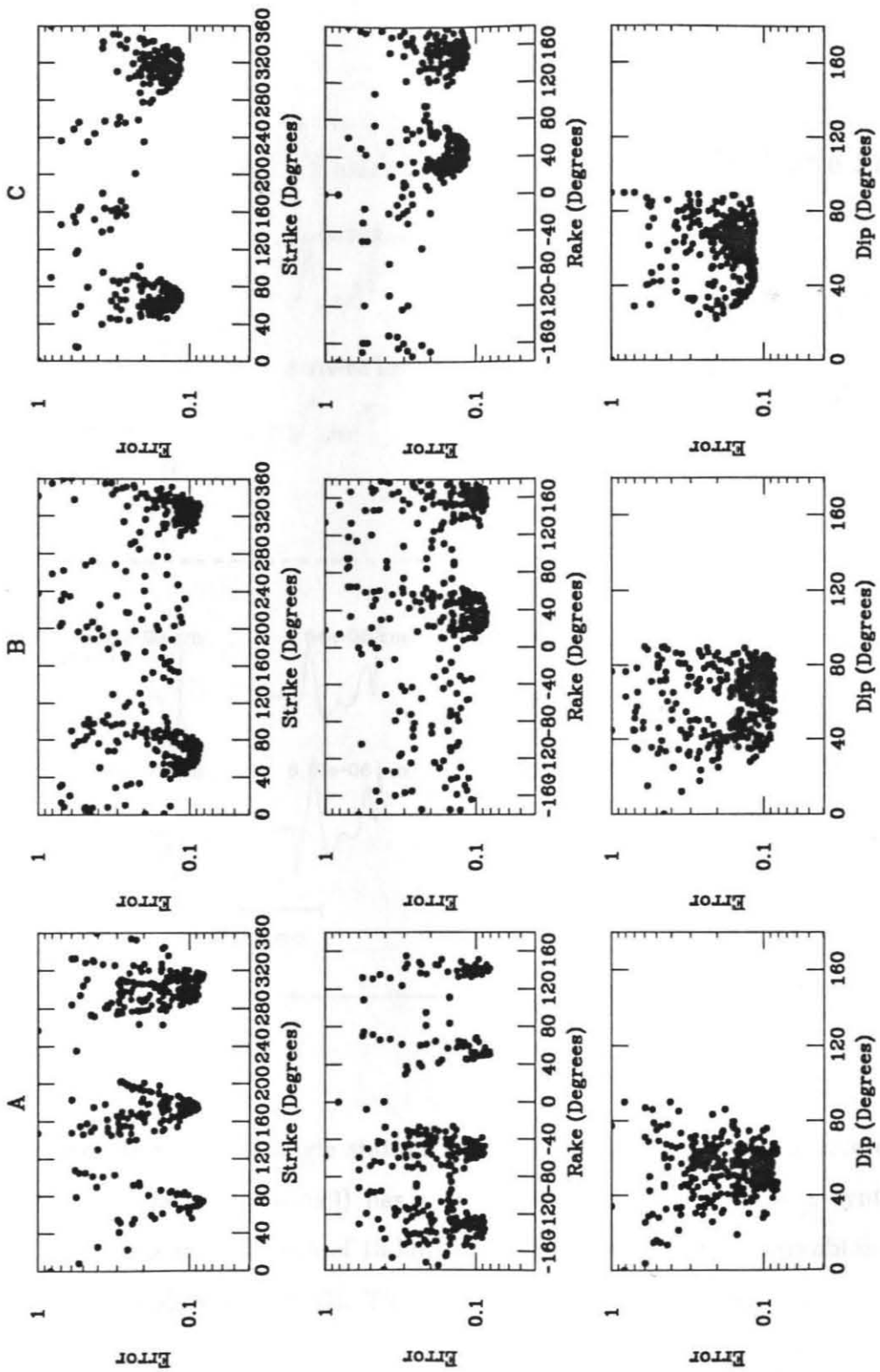


Figure 2.8: Diagram showing the station-source geometries used in the vertical mislocation sensitivity analysis.



Figure 2.9: Parameter space for vertical mislocation sensitivity tests. (a) shows the parameter space for the strike (θ), rake (λ) and dip (δ) model parameters using only station S1 (Figure 2.8) in the inversion. (b) shows the parameter space using both stations S1 and S2a. (c) shows the parameter space using both stations S1 and S2b.



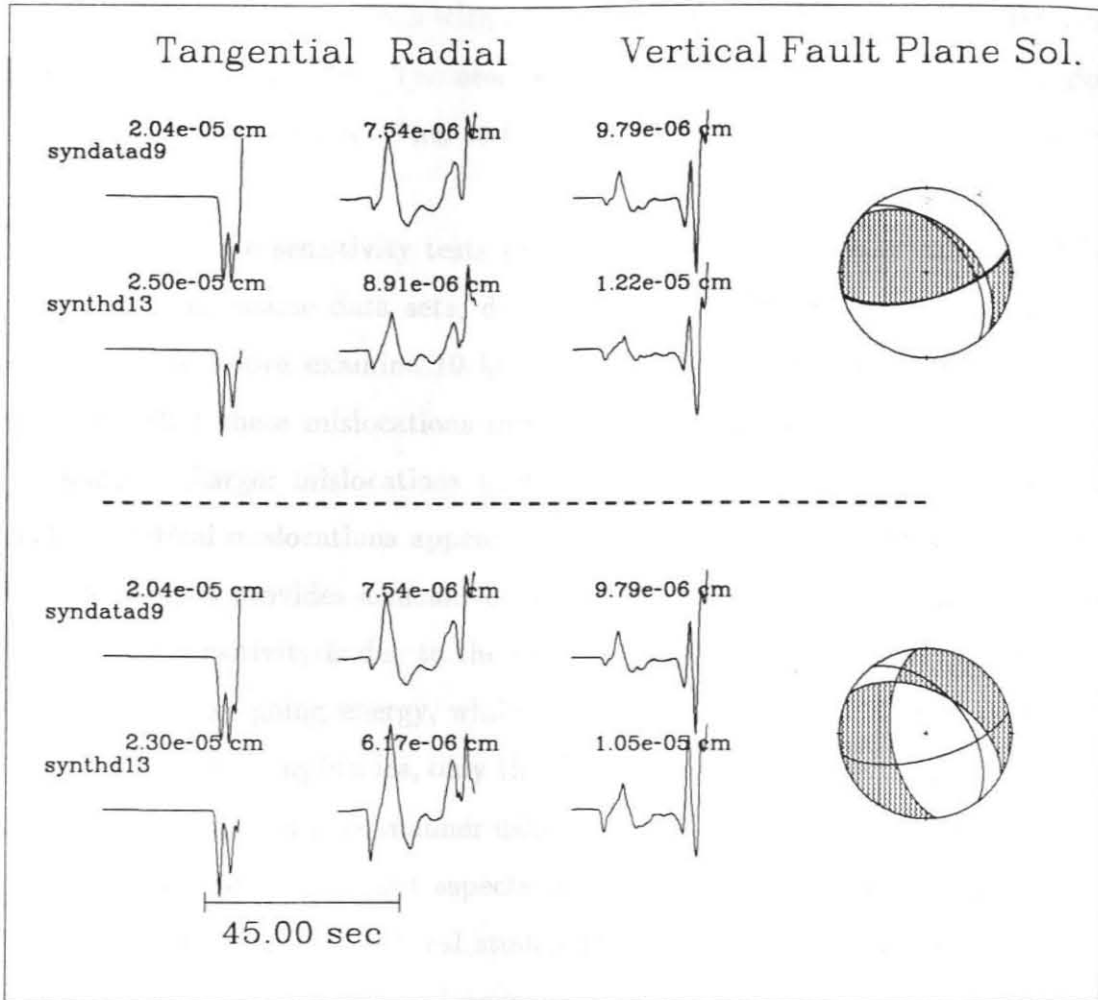


Figure 2.10: Results of a single station inversion using an incorrect source depth. The synthetic “data” (`syndatad9`) has a source depth of 9 km and the synthetics (`synthd13`) have a source depth of 13 km. Both of the focal mechanisms obtained by the inversion are shown (shaded). The correct solution is unshaded.

station, even though the aperture is small. This test yielded a solution of $\theta = 69^\circ$, $\lambda = 35^\circ$ and $\delta = 70^\circ$.

Third, we used two stations with an aperture of 105° (S1 and S2b). Figure 2.9c shows the parameter space. The non-uniqueness is further removed and the global minima are better defined. This test yielded a solution of $\theta = 69^\circ$, $\lambda = 44^\circ$ and $\delta = 71^\circ$.

Generally, these sensitivity tests show that source parameters can be obtained confidently from sparse data sets, despite possible errors in source location. The tests described above examine 10 km lateral and 4 km vertical mislocations. It was found that these mislocations introduced small errors ($< 10^\circ$) in the source mechanisms. Larger mislocations would, of course, introduce larger errors. The effect of vertical mislocations appears to be much stronger, which in fact is quite useful because it provides a means of constraining the source depths. The greater source depth sensitivity is due to the changes in relative amplitudes of initially up-going versus down-going energy, while the lateral mislocations do not significantly change the relative amplitudes, only the differential travel-times. The source depth can be found in an iterative manner using the RMS misfit error (equation 2.2).

One of the most important aspects of this method is the assumption that we know the velocity model. Several studies to date, using local and regional three-component data indicate that at longer periods simple plane layered velocity models derived from travel-time studies appear to be adequate in explaining the long-period data. Using an inappropriate velocity model can have significant effects on the final result, as discussed later with the Lee Vining section.

2.4 Applications

Although the technique has been applied to numerous events we will limit this particular study to two events which serve to demonstrate its usefulness. The first event occurred in Mexico and the second in central California, roughly in opposite directions and well outside the TERRAScope array.

2.4.1 December 3, 1991 Baja Event

On December 3, 1991 a moment magnitude 5.1 earthquake occurred at 31.75° north latitude and 115.83° west longitude (J. Garcia of CICESE, written communication), approximately 20 km north of the San Miguel fault. This event was recorded by all six of the TERRAScope stations (see Figure 2.1) at distances ranging from 215 km to approximately 515 km with an aperture of approximately 40° . Figure 2.11 shows the displacement data recorded at PAS (distance of 345 km) and the simulated WASP, WALP and Press-Ewing (3090) instrument seismograms. The displacement records were obtained by integrating the broadband velocity data within the frequency band from 0.005 to 7.0 Hz. The simulated instrument seismograms were computed by convolving the displacement records with the instrument response of the traditional instrumentation. Several features to take note of in the broadband data are the very pronounced onset of S_n on the tangential component, the long-period P_{nl} waveform and the lack of a coherent Rayleigh wave on the radial and vertical components. For the most part, the energy propagated through the Peninsula Ranges, however the last 50 km traversed the Los Angeles basin structure which probably accounts for the complexity observed in the surface waves. In addition, note the relative simplicity of the 3090 waveforms. The large instrumental amplitudes indicate that this record would have been clipped on the traditional instrumentation. Figure 2.12 shows the displacement, 3090, WALP and WASP data recorded at PFO. Compared to PAS

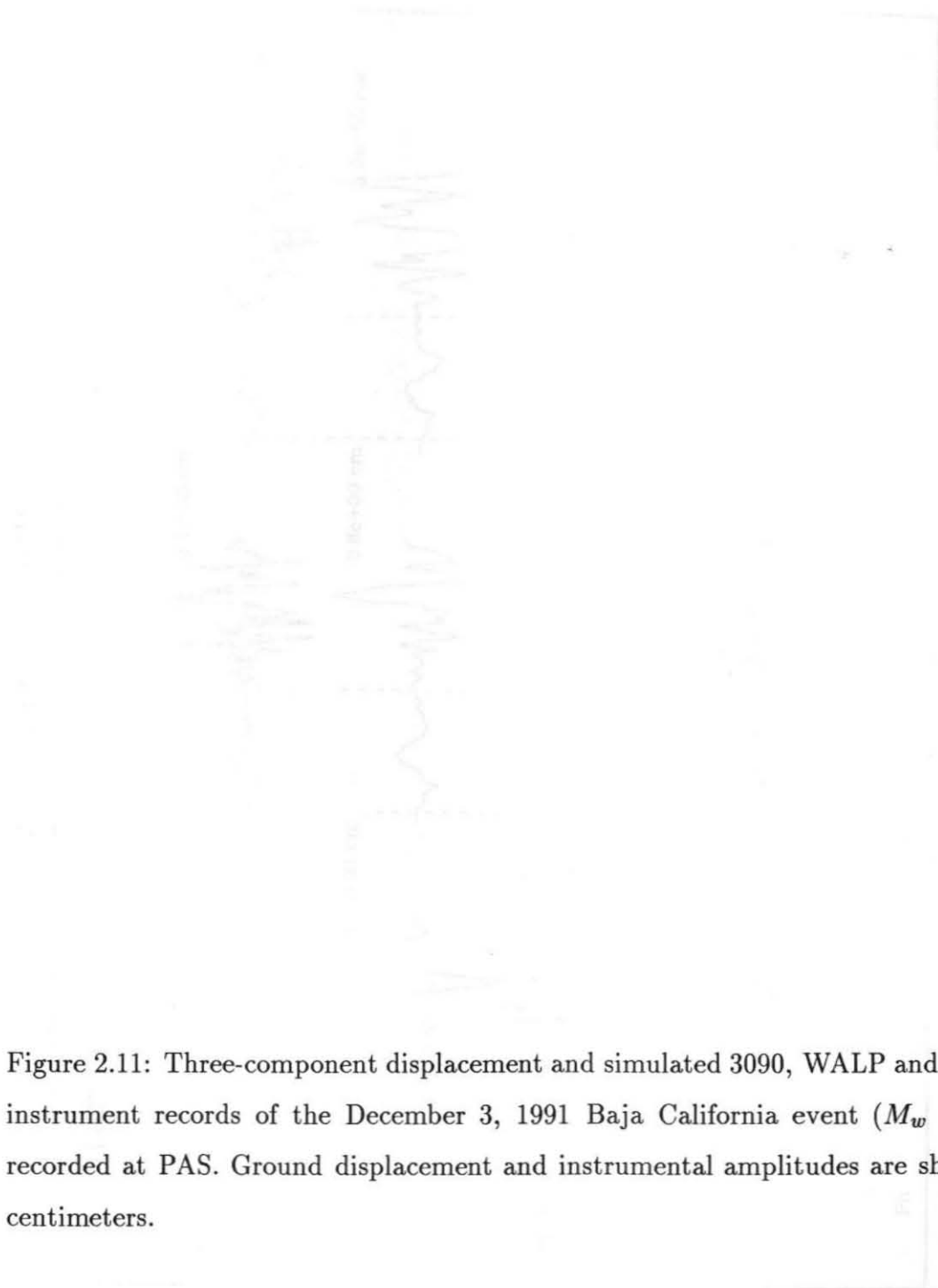
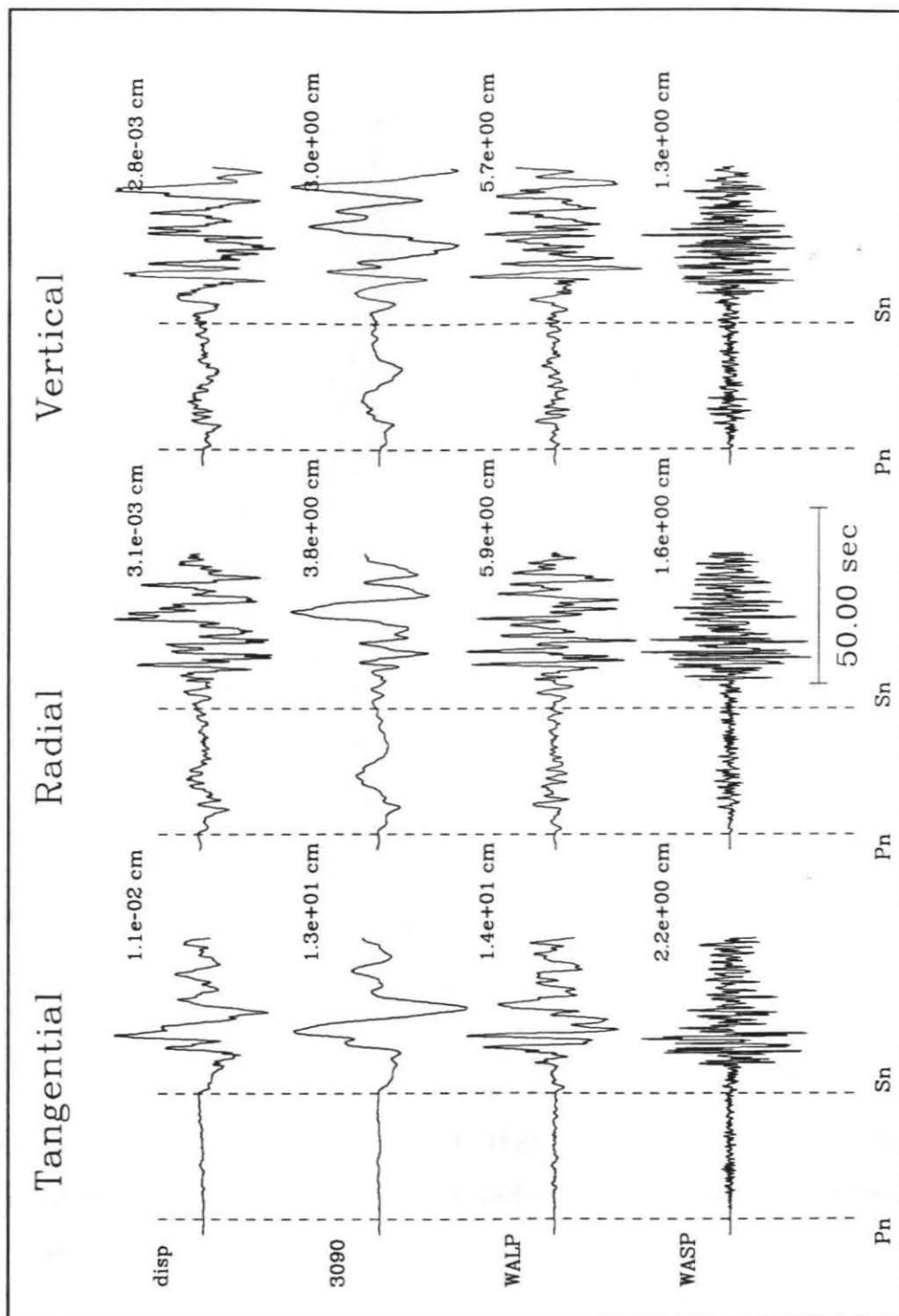


Figure 2.11: Three-component displacement and simulated 3090, WALP and WASP instrument records of the December 3, 1991 Baja California event ($M_w = 5.1$) recorded at PAS. Ground displacement and instrumental amplitudes are shown in centimeters.

Data Recorded at PAS




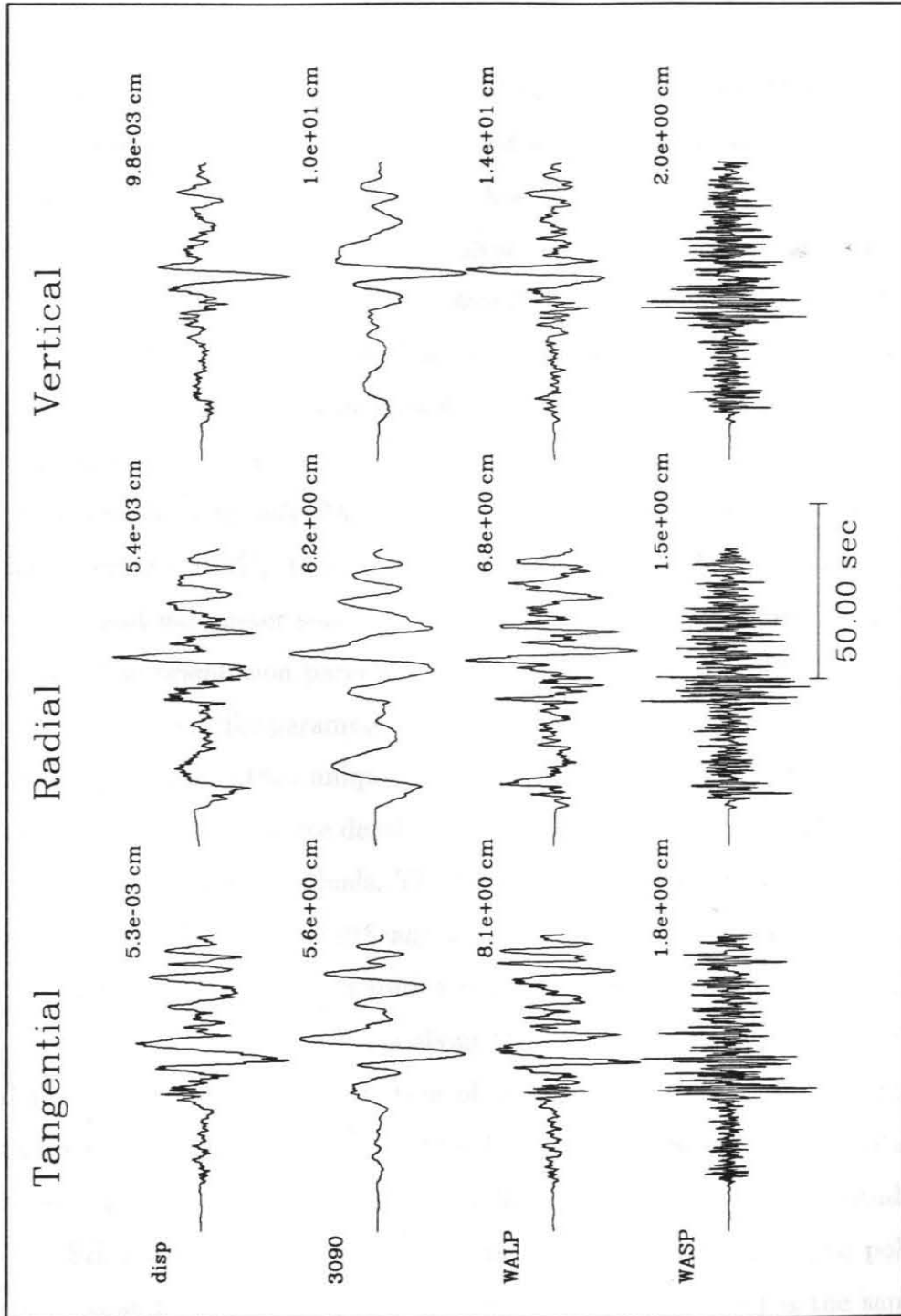


Figure 2.12: Three-component displacement and simulated 3090, WALP and WASP instrument records of the December 3, 1991 Baja California event ($M_w = 5.1$) recorded at PFO. Ground displacement and instrumental amplitudes are shown in centimeters.

Data Recorded at PFO



the Rayleigh waves are more coherent. The long-period P-waves are the result of interfering P_{nl} and upper crust PL waves.

We used the 3090 data recorded at PAS (Figure 2.11) and PFO (Figure 2.12) in the inversion. These stations were located at distances of 345 and 215 km, and azimuths of 321° and 344° , respectively. Inversions were performed using both a single station (PAS) and two stations (PAS and PFO), for several source depths. F-K synthetics previously computed for a standard crustal model (SC, Table 2.1) were used. A triangular source time function with a width of 1 second was assumed. In addition, only the body waves were used to eliminate the problems with the surface waves as discussed earlier.

The inversion using only PAS produced stable results. The inversion yielded a solution where $\theta = 305^\circ$, $\lambda = 163^\circ$, $\delta = 80^\circ$, and $M_o = 5.2 \times 10^{23}$ dyne-cm. The seismic moment parameter space is given in Figure 2.13, and shows a well defined minimum. The orientation parameter space is shown in Figure 2.14. Two of the four minima in the strike parameter space are redundant (i.e., 180° separated). The parameter space shows that unique results were obtained with a single station. As indicated above, several source depths were tried, namely 8, 11 and 14 km. A depth of 11 km gave the lowest residuals. The two station inversion produced very similar results with $\theta = 119^\circ$, $\lambda = 191^\circ$ and $\delta = 78^\circ$. As before, a seismic moment of 5.2×10^{23} dyne-cm and a 11 km source depth reduced the residuals. The largest difference between these solutions is about 22° in the dip of the northwest trending nodal plane. The fault plane solution obtained by inverting the data from both stations is plotted on Figure 2.1. Figure 2.15 shows the waveform fits obtained by the inversion. There is good agreement in both waveform and in amplitude. Note that the SH waves have opposite polarities at the two stations. The polarity of SH recorded at SVD (azimuth of 336° and distance of 286 km) is the same as at PAS indicating that the SH node is located somewhere between 336° , and 344° . It

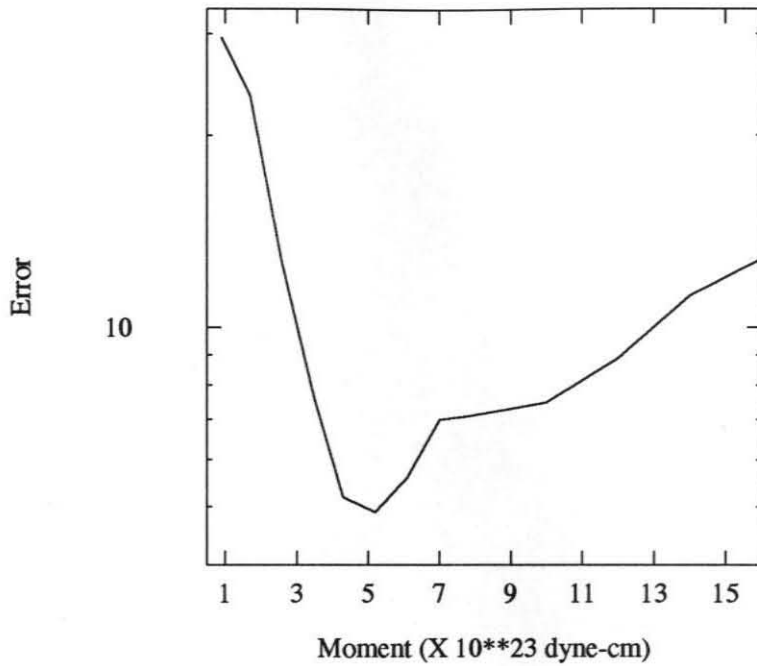
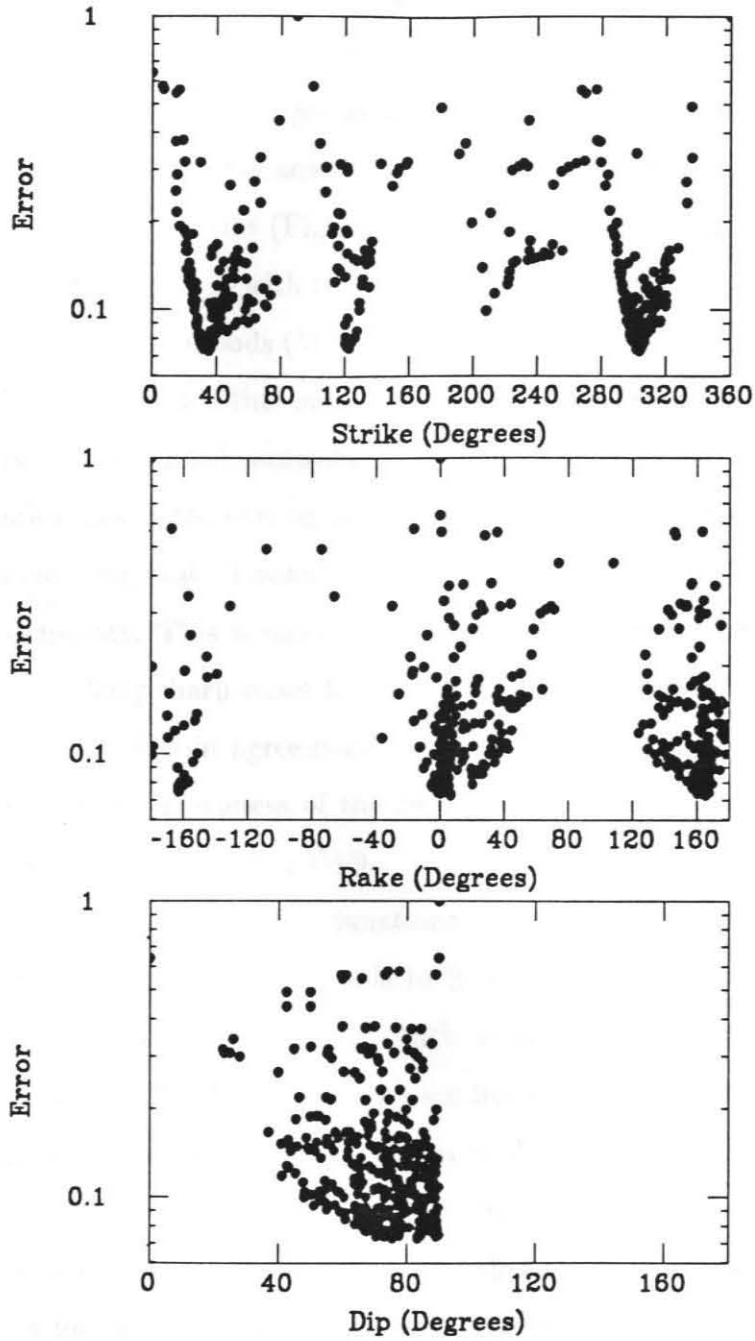


Figure 2.13: Seismic moment parameter space of a single station (PAS) inversion of the 3090 body waves. The lowest RMS error was obtained with a seismic moment of 5.2×10^{23} dyne-cm.

Figure 2.14: Strike, rake and dip parameter space of a single station (PAS) inversion. The minima give a solution of $\theta = 305^\circ$, $\lambda = 163^\circ$ and $\delta = 80^\circ$.

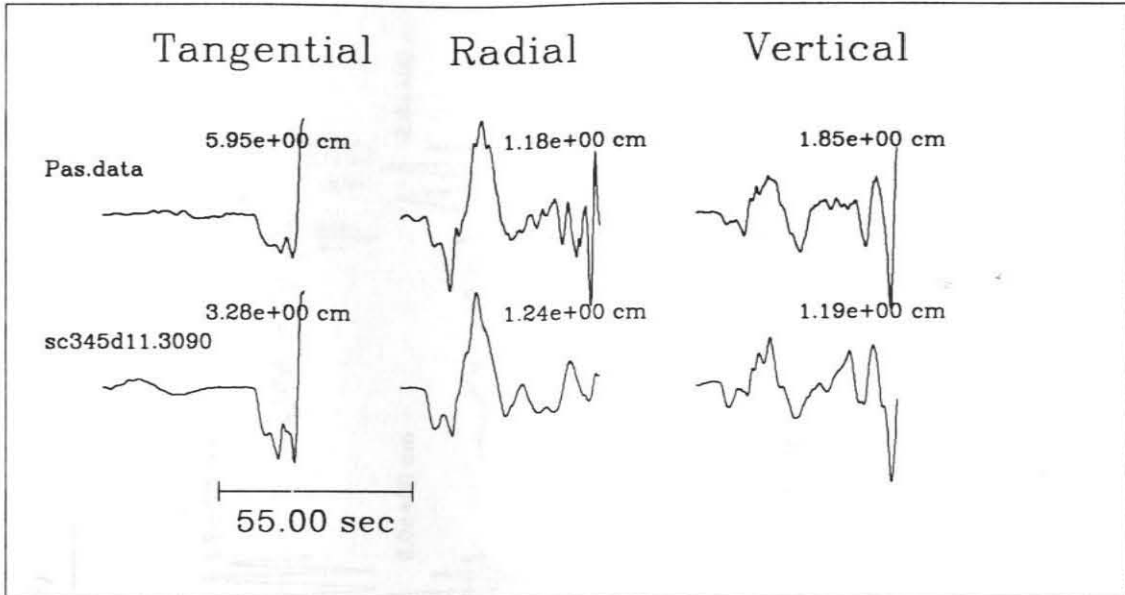


should also be noted that the data recorded by SBC at a distance of 469 km and an azimuth of 308° indicates that the P-SV waves (P_{nl}) are nodal, supporting the results obtained by inverting PAS and PFO.

Figure 2.16 shows the displacement, 3090, WALP and WASP synthetics predicted for PAS by the source parameters obtained by inverting the 3090 body waves. In comparing the synthetics (Figure 2.16) with the data in Figure 2.11 we find that there is good agreement with the body waves for the displacement, 3090 and WALP records. At shorter periods (WASP records) the fit is not as good because the simple model fails to produce the complexity observed in the data, especially the level of SV energy on the radial component. We point out however that many of the arrivals from major discontinuities in the model seem to be observed in the short-period data, indicating that although lateral heterogeneity plays a roll the major body phases dominate. This is especially true for the tangential component. Notably, S_n has a particularly sharp onset for this path, and is observed at shorter periods (e.g., WALP and WASP) in agreement with the synthetics shown on Figure 2.16. This suggests that the sharpness of the Moho discontinuity in model SC is appropriate along the path from Baja to PAS.

Using a catalog of Green's functions computed with the SC model for different depths and distances, we were able to locate the earthquake based on S - P times. A location approximately 15 km south of the location reported by CICESE was obtained (360 km from PAS and 225 km from PFO). An inversion of the data using this location yielded a mechanism similar to that obtained with the CICESE location, where $\theta = 120^\circ$, $\lambda = 183^\circ$, $\delta = 83^\circ$ and $M_o = 5.2 \times 10^{23}$. Figure 2.17 compares the three-component displacement data recorded at PAS with displacement synthetics computed for distances of 345 and 360 km and their respective source mechanisms. Note that the waveforms change slightly in terms of S - P times, but they are more or less unchanged in both shape and amplitude.

Waveform Comparison (PAS)



(PFO)

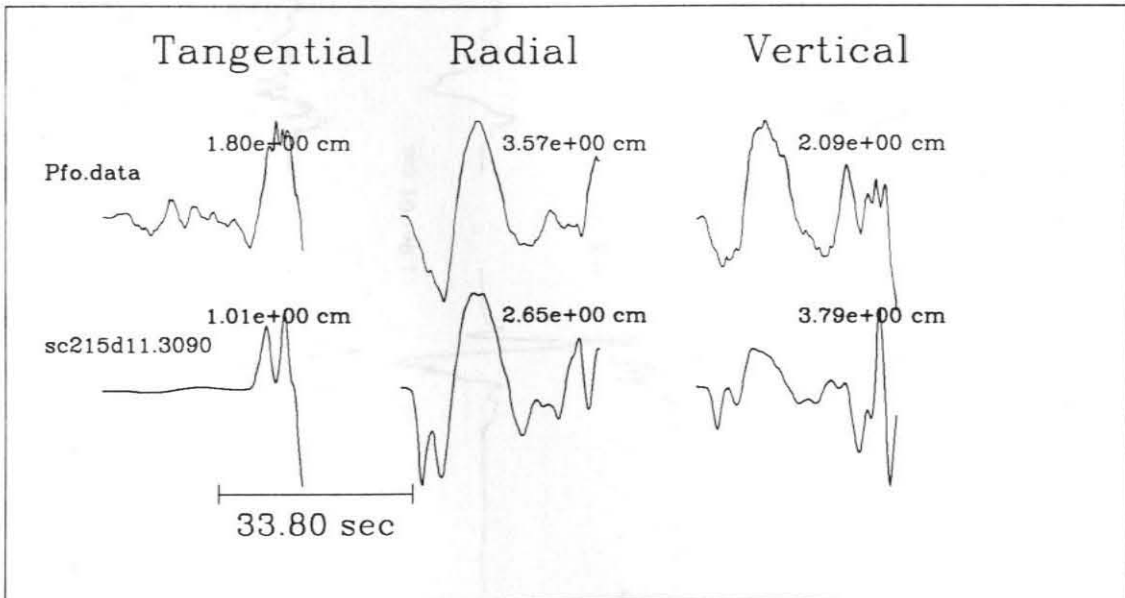


Figure 2.15: Comparison of 3090 data and synthetics for stations (a)PAS and (b)PFO. The synthetics were computed with a strike of 119° , a rake of 191° , a dip of 78° and a seismic moment of 5.2×10^{23} dyne-cm. Instrumental amplitudes in centimeters are shown.

Synthetics (PAS)

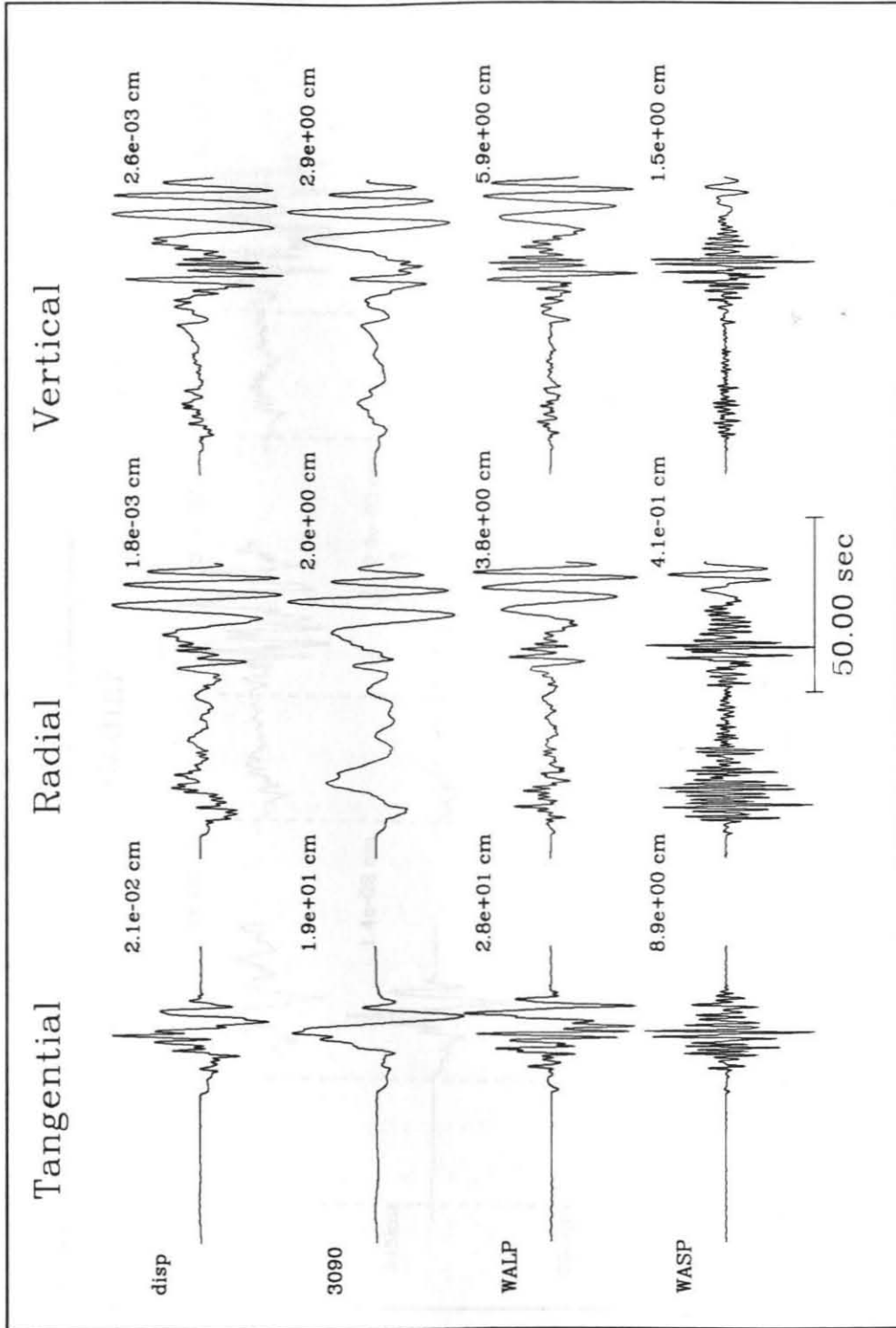


Figure 2.16: Three-component, whole waveform, displacement, 3090, WALP and WASP synthetics computed with the mechanism obtained by inverting only the PAS 3090 body waves.

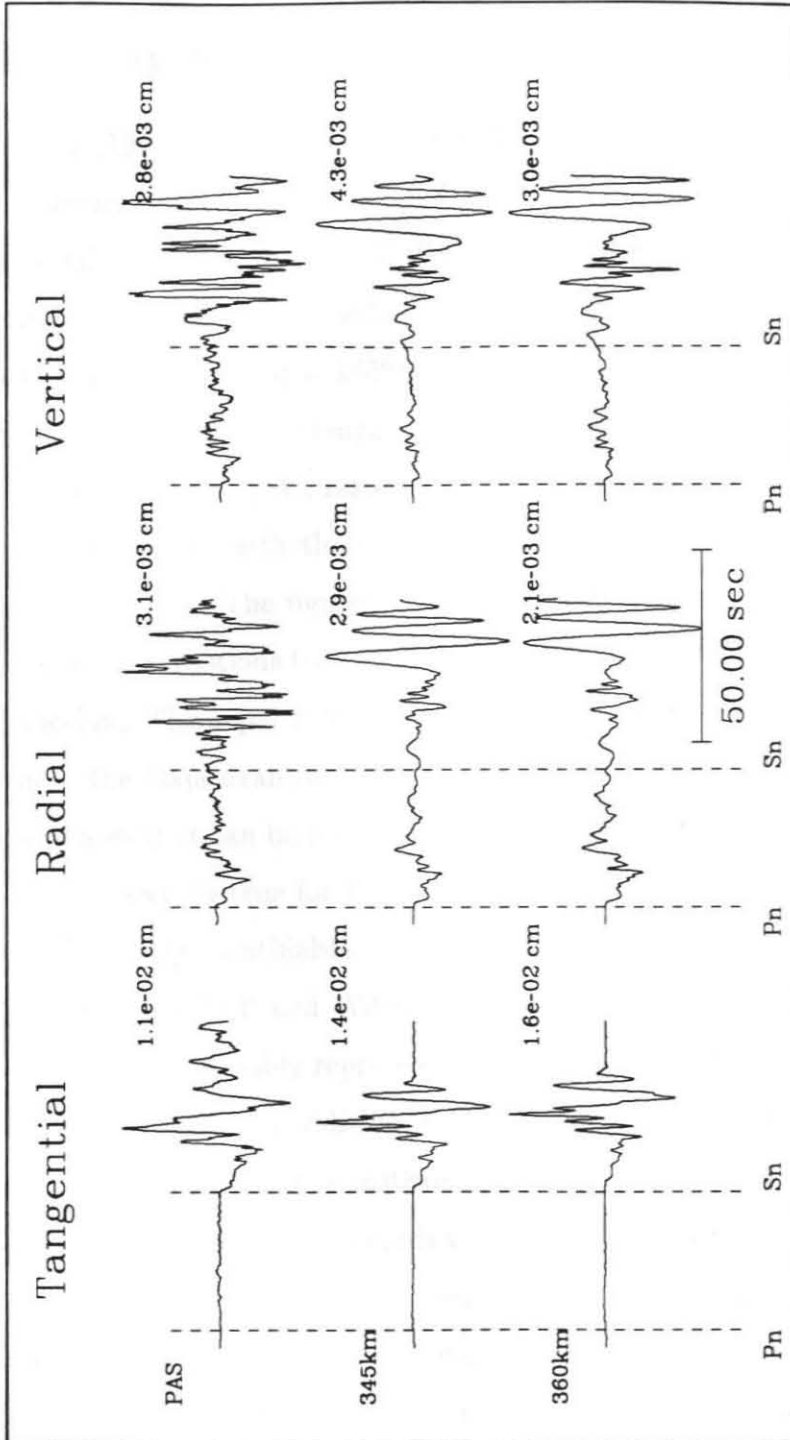


Figure 2.17: Comparison of three-component displacement data recorded at PAS and displacement synthetics computed for distances of 345 and 360 km, using the mechanisms obtained by inverting both PAS and PFO data and a 1.5 second symmetric trapezoidal source time function.

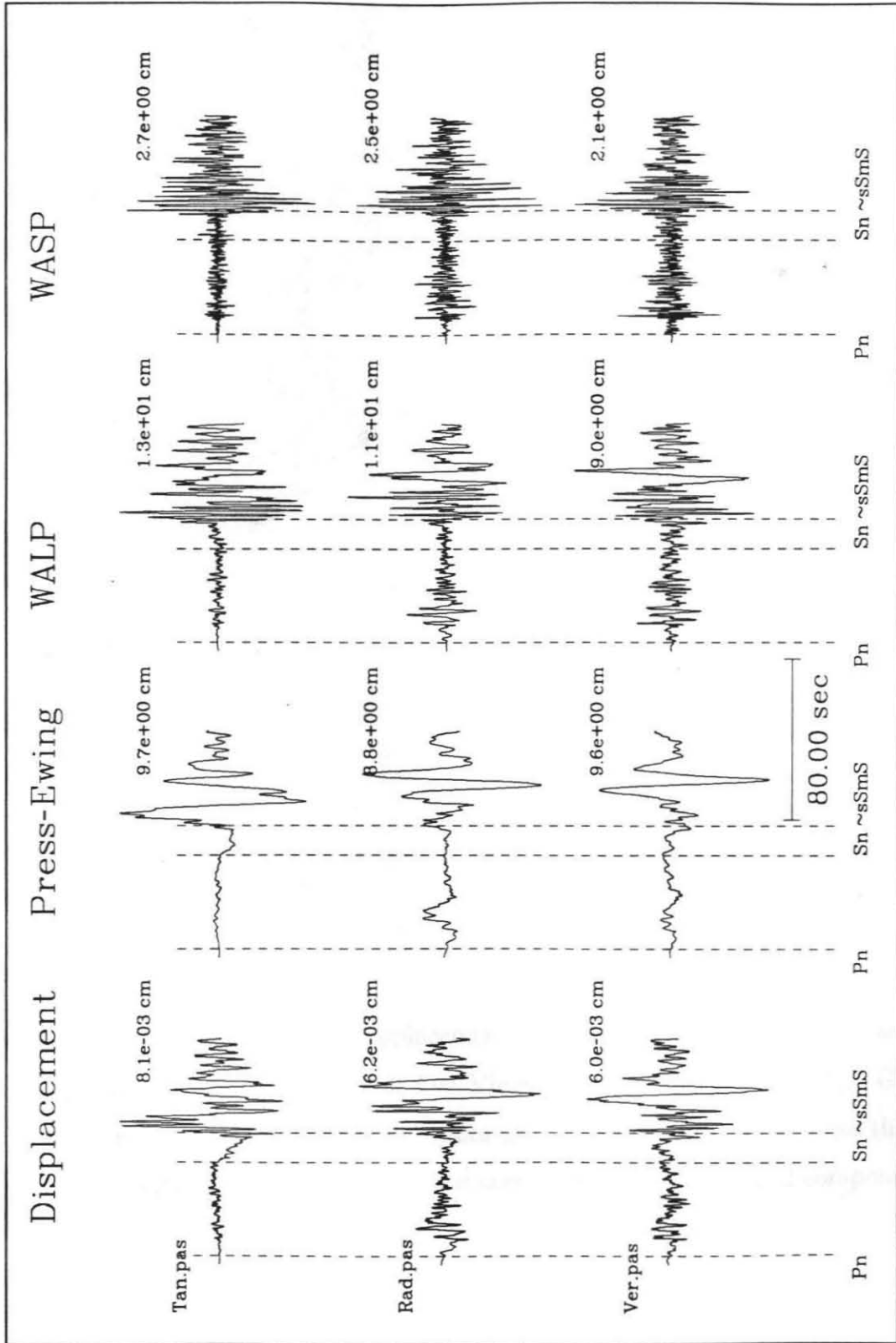
2.4.2 October 24, 1990 Lee Vining Event

The October 24, 1991 Lee Vining event was located at 38.05° north latitude and 119.12° west longitude, near Lee Vining, California at a depth of about 12 km (S. Horton, personal communication). At the time of this event only two of the six TERRAScope stations were installed. This earthquake was well recorded by the GSC (distance=365 km, azimuth= 145°) and PAS (distance=438 km, azimuth= 169°) stations. Figures 2.18 and 2.19 compare the displacement, 3090, WALP and WASP data recorded at PAS and GSC, respectively. The data was processed in the same manner as the Baja data with the exception that the bandpass corner frequencies were 0.02 and 7.0 Hz. The figures display the tangential motions directly above the radial and vertical motions to emphasize the clean separation of the (P-SV)-(SH) systems of motion. The separation tends to break down in the WASP bandwidth, however. As in the Baja example, the waveforms are well ordered in that they are composed of phases that can be modeled using simple one-dimensional plane layered models. This is especially true for the long-period phases such as P_{nl} , and S_n . Note that while S_n is clearly identifiable in the displacement and 3090 records it is not a distinct phase in the WALP and WASP data. This contrasts with what was found for the Baja event and probably represents a fundamental difference in the sharpness of the Moho for this path. In addition, the Rayleigh wave recorded at PAS for this event is much more coherent. The instrumental amplitudes are given on these plots and in most cases we find that the records would have been clipped on the traditional instrumentation. Another interesting observation is that the GSC station appears to be situated near a P-SV node, as evidenced by the lack of coherent energy on the radial and vertical components and the very large difference in the peak amplitude of the tangential component compared to the radial and vertical components.

We inverted the 3090 body waves recorded at PAS and GSC using three different velocity models. The first model was the standard southern California velocity model

Figure 2.18: Comparison of the displacement, 3090, WALP and WASP data recorded at PAS for the October 24, 1990 Lee Vining earthquake ($M_w = 5.2$). Ground displacement and instrumental amplitudes are shown in centimeters.

Lee Vining Recorded at PAS



WASP

WALP

Press-Ewing

Displacement

2.7e+00 cm

1.3e+01 cm

9.7e+00 cm

8.1e-03 cm

Tan.pas

2.5e+00 cm

1.1e+01 cm

8.8e+00 cm

6.2e-03 cm

Rad.pas

2.1e+00 cm

9.0e+00 cm

9.6e+00 cm

6.0e-03 cm

Ver.pas

80.00 sec

Sn ~sSmS

Pn

Sn ~sSmS

Pn

Sn ~sSmS

Pn

Sn ~sSmS

Pn


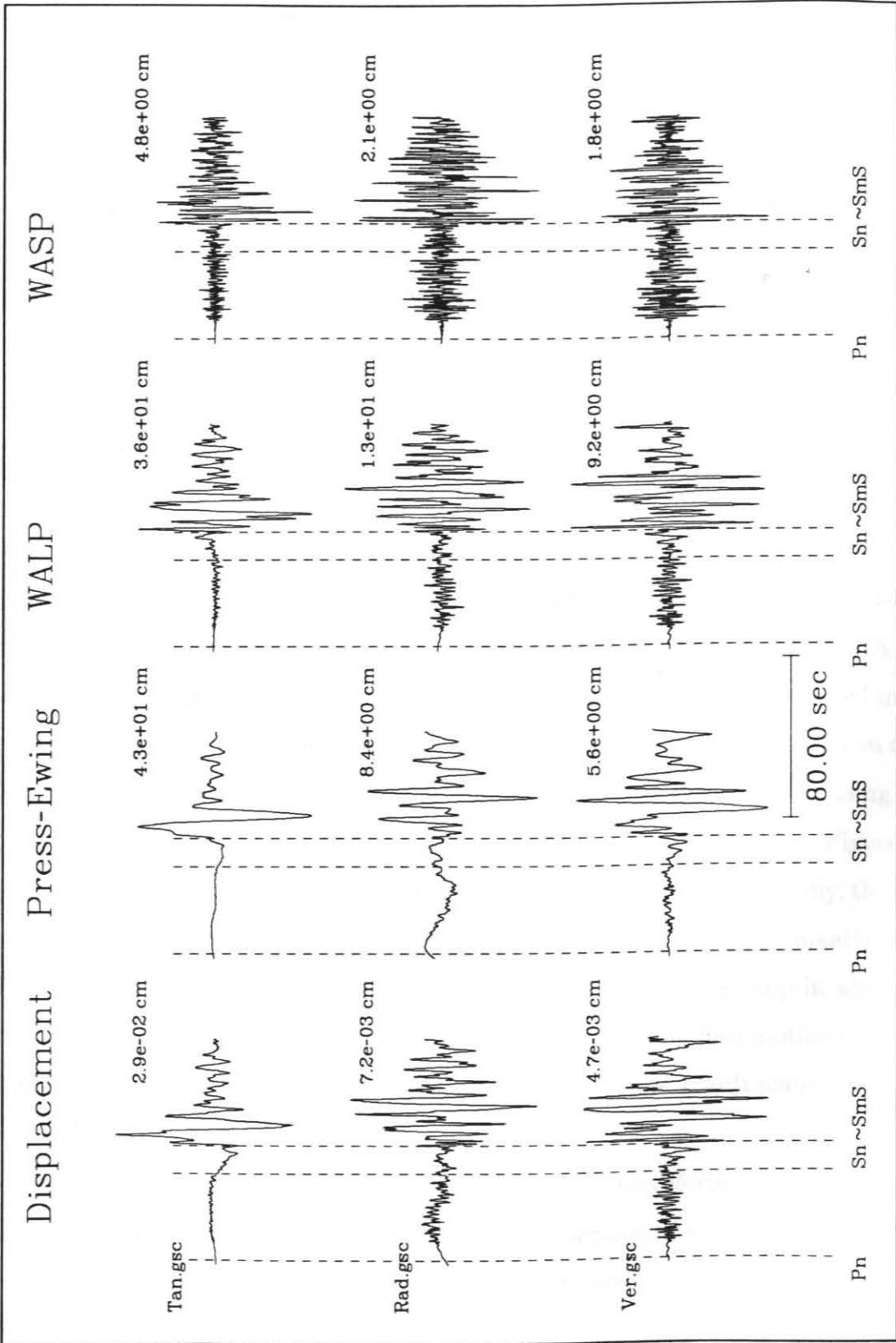


Figure 2.19: Comparison of the displacement, 3090, WALP and WASP data recorded at GSC for the October 24, 1990 Lee Vining earthquake ($M_w = 5.2$). Ground displacement and instrumental amplitudes are shown in centimeters. Note that the radial and vertical components are nodal compared to the tangential component

Lee Vining Recorded at GSC



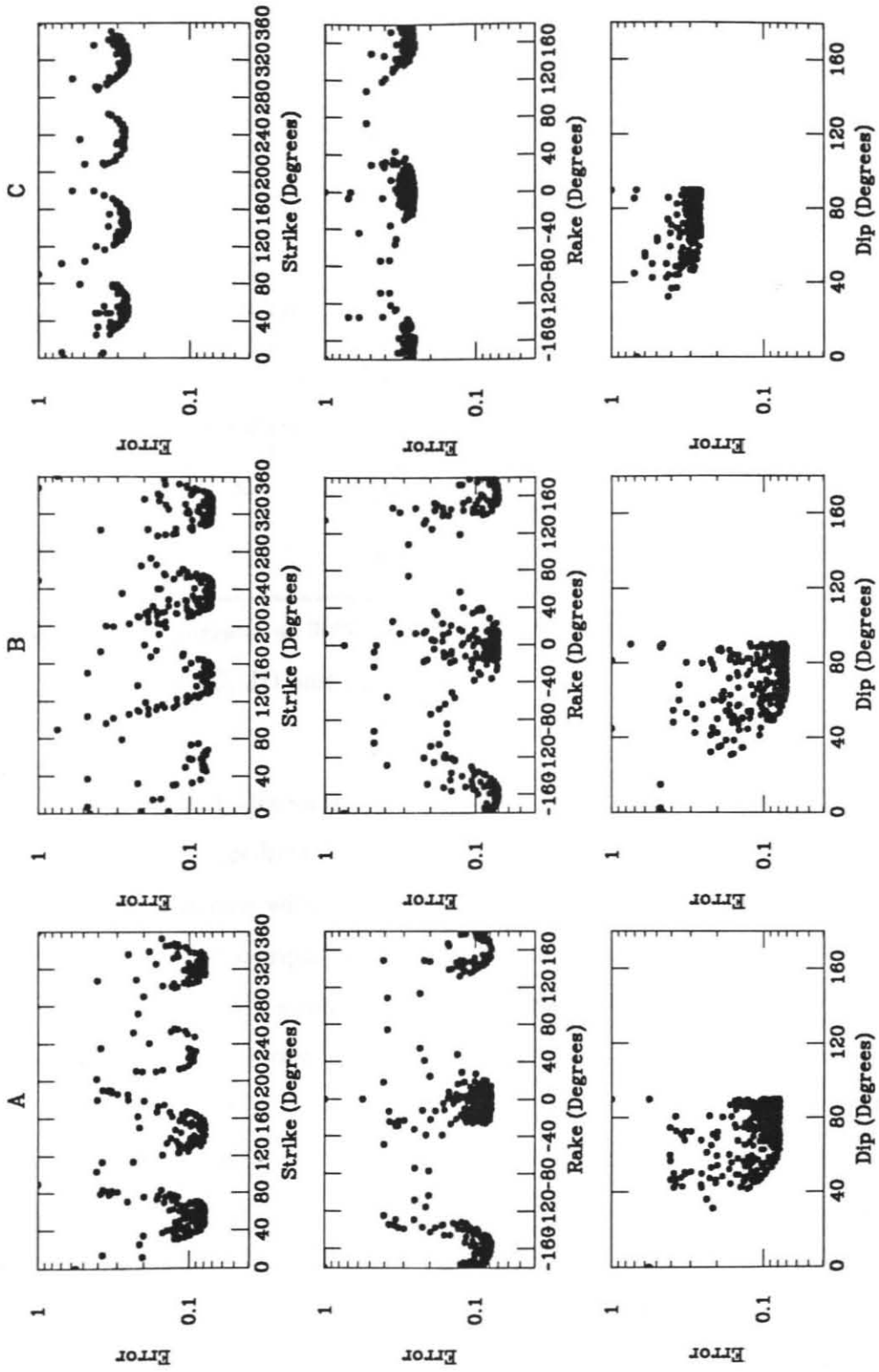
Model	θ	λ	δ	M_o
SC	322	162	83	9×10^{23}
JD	325	193	80	8×10^{23}
LH	321	167	80	6×10^{23}

Table 2.2: Lee Vining results using different velocity models

(model SC), used to invert the Baja data. The second model was used by Jones and Dollar [1986] (model JD) to explain travel-times of Sierran earthquakes recorded in southern California. The third is a layer over a half-space (model LH) approximation to the JD model. The models are listed in Table 2.1. We performed single station inversions using the PAS data and found that the JD and LH models produced non-unique results, while unique results were obtained with the SC model. A fault plane solution of $\theta = 316^\circ$, $\lambda = 171^\circ$, and $\delta = 62^\circ$ was obtained with the SC model. Better defined minima in the parameter space were obtained with the inclusion of the GSC data. Table 2.2 lists the solutions obtained with the three models using both stations. Figure 2.20 shows the parameter space for these calculations. Figure 2.21 compares the data with synthetics computed for these solutions. Generally, the three results are very similar. The source mechanism of this event is predominantly strike-slip, with the northwest trending plane experiencing right lateral slip in agreement with the solution obtained by Depolo and Horton [1991] using first motion polarities. Unfortunately the distribution of aftershocks does not define a fault plane (S. Horton, personal communication).

Figure 2.22 compares the three-component whole waveform displacement data recorded at PAS with displacement synthetics computed for each of the velocity models and their respective source mechanisms. In contrast to what was found in

Figure 2.20: Strike, rake and dip parameter space for an inversion using both the PAS and GSC stations and the (a) SC (Table 2.1) velocity model. (b) JD velocity model. (c) LH velocity model. See Table 2.2 for the solutions.



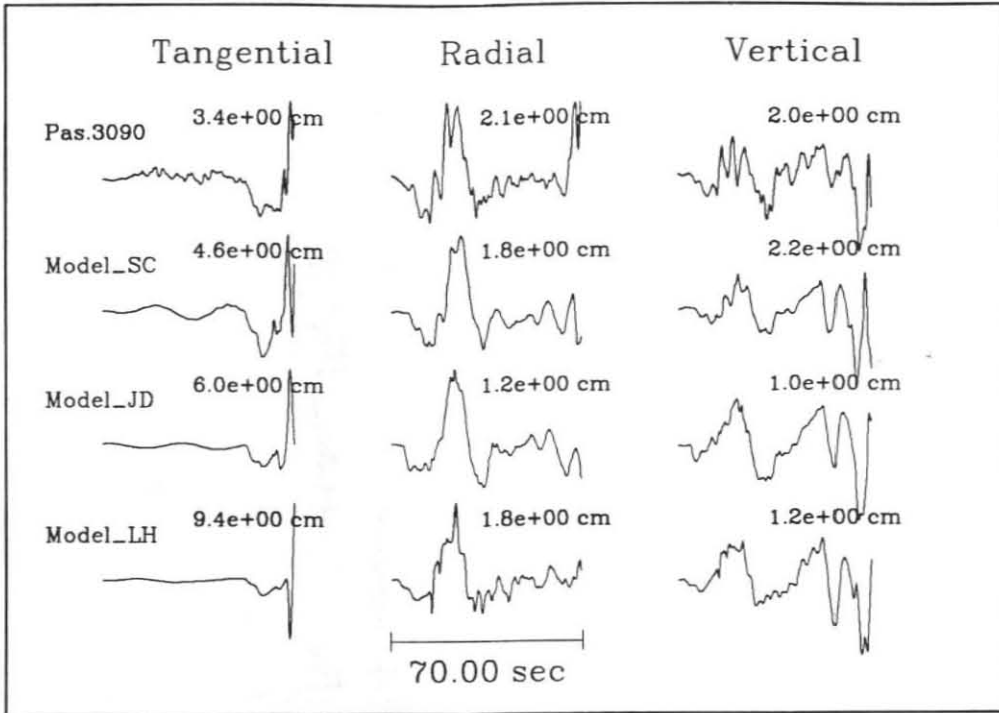


Figure 2.21: Comparison of 3090 body waves recorded at PAS and the best fit synthetics using the SC, JD and LH velocity models.

Figure 2.21 for the body waves, the three models produce significantly different surface waves. Model SC predicts the tangential component fairly well, but as discussed earlier there are problems with S_n . The body waves are also fairly well modeled on the radial and vertical components. The Rayleigh waves appear to arrive at the correct relative time, but are too dispersed. Model JD also predicts tangential waveform well. In contrast to model SC, the relative amplitudes of the body waves to the Rayleigh waves on the radial and vertical components do not match the data. The dispersion of the Rayleigh waves appears to match the data better than for model SC, but they arrive slightly late. Model LH produces the poorest fits to the three components, but as Figure 2.21 indicates, at long-periods, the model performs well enough to obtain the source parameters from the body waves.

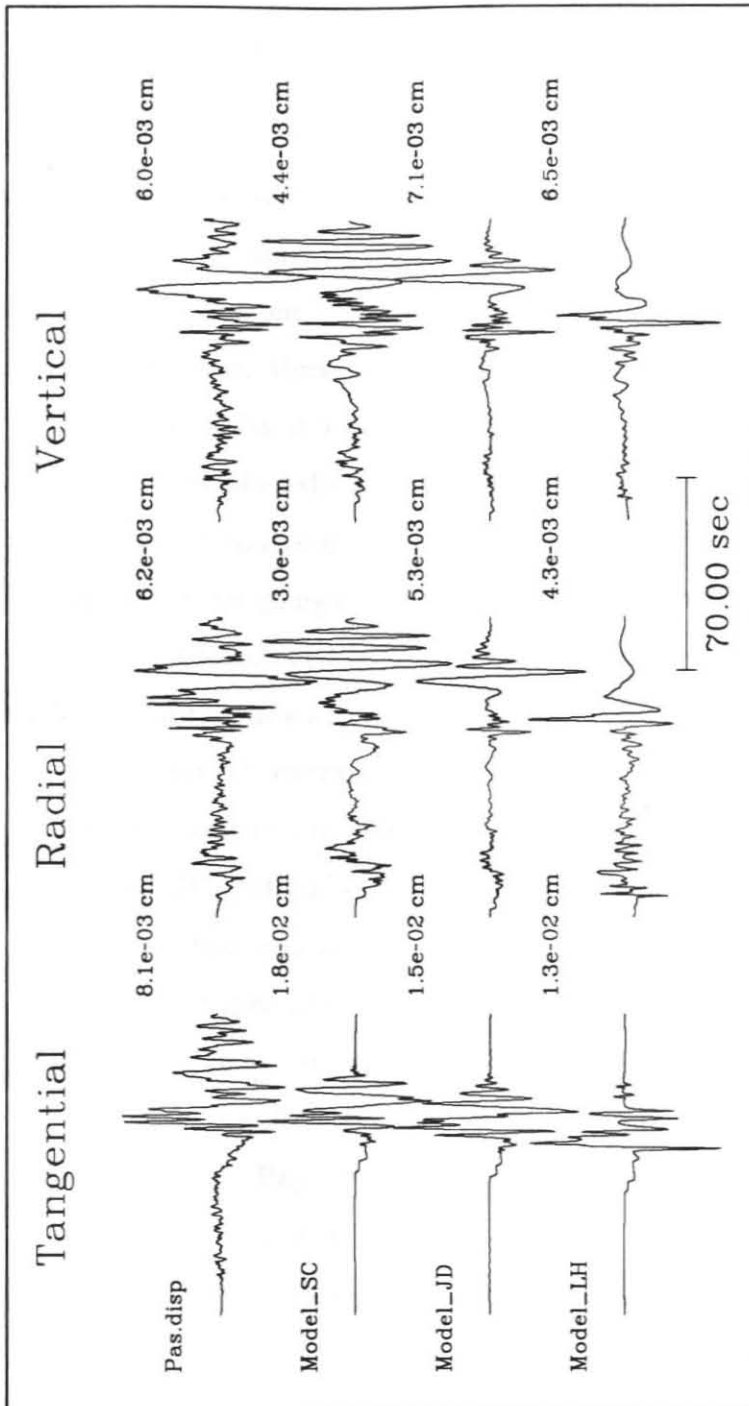


Figure 2.22: Comparison of whole waveform, displacement data recorded at PAS and synthetics for the SC, JD and LH velocity models.

2.5 Discussion and Conclusions

In this paper we addressed the issue of source retrieval from high quality, but limited data sets. We demonstrated that at long-periods regional structure is sufficiently well understood to estimate source parameters with very few stations. How few depends on the situation, but our various sensitivity tests suggest that one station will suffice in many situations. Horizontal mislocations of up to 15 km generally do not degrade the inversion results as demonstrated with the Baja event. The synthetic sensitivity analysis of vertical mislocations revealed that the long-period, regional body waves are sensitive to source depth because of changes in relative amplitudes of initially up-going and down-going energy, and are therefore useful in source depth determinations. Problems associated with the mislocations, such as non-uniqueness, disappeared with the addition of a second station. Another important result of these tests was that good azimuthal coverage is not required when three-component data is used. This result was confirmed by both applications where the aperture between stations was only about 24° , yet stable results were obtained.

The assumption that the velocity model is known is an important one. The analysis presented in this paper showed that even with radically different velocity models (SC and JD compared to LH), the long-period body waves (primarily P_{nl} and S_n) are insensitive to lateral and vertical heterogeneity, but are sensitive to source orientation. For example, the Baja and the Lee Vining events recorded at PAS at distances of 345 and 438 km have remarkably similar body waveforms. Returning to Figures 2.15 and 2.21, we see that at long-periods, despite the 93 km difference in range and completely different travel paths, the waveforms are very similar in shape. Of course there is a big difference in the relative timing of the phases. If the Sierra Madre earthquake is included we find that model SC models the data very well from 160 to 438 km for a variety of azimuths. Although regional distance P_{nl} and long-period SH and SV waves are relatively insensitive to upper crustal

structure, the lowest errors were obtained with models SC and JD which include upper crustal interfaces. In fact, at near-regional distances (100 to 300 km) the PL waves propagating along shallow interfaces are observed and are very important arrivals in the data.

For the Baja earthquake we obtain a predominantly strike-slip solution, where $\theta = 119^\circ$, $\lambda = 191^\circ$ and $\delta = 78^\circ$ using the PAS and PFO TERRAScope stations. A seismic moment of 5.2×10^{23} dyne-cm was obtained for this event. The SBC station located at an azimuth of 308° from the event is P-SV nodal supporting the solution. The location of this event determined by CICESE places it approximately 20 km north of the San Miguel fault. In 1956 a $M_L = 6.5$ earthquake occurred on the San Miguel fault and broke the surface. The mechanism we obtained for the 1991 earthquake is consistent with the surface break observed after the 1956 event [Shor and Roberts, 1958].

For the Lee Vining earthquake a predominantly strike-slip solution is also obtained. The average solution obtained from the three inversions using different velocity models is $\theta = 323 \pm 2^\circ$, $\lambda = 174 \pm 17^\circ$, $\delta = 81 \pm 2^\circ$ and $M_o = (7.7 \pm 1.5) \times 10^{23}$ dyne-cm. The errors are the standard deviation from the mean of the solutions listed on Table 2.2. A rather large uncertainty exists for the rake parameter, but it is possible to distinguish that a strike-slip fault ruptured. Our solution compares reasonably well with the results of Clark et al. [1991] with respect to strike, but poorly in terms of rake and dip. They find the northwest fault plane dipping west with a significant normal component of motion. They used P-wave first motions, but do not have good azimuthal coverage, and most of their P-wave picks are at P_n distance. Our results compare better with the P-wave first motion results of Depolo and Horton [1991]. Their study had better azimuthal coverage and some local distance stations. They report a mechanism striking 330° with a dip of 90° . Their rake is also somewhat poorly constrained and is consistent with the average value that we obtained.

In conclusion, we have demonstrated that regional, three-component, long-period body waves are stable enough to invert for source parameters. To have good signal-to-noise ratios for these phases at these distances the events need to be larger than approximately magnitude 4.5. To recover source parameters for smaller earthquakes better Green's functions that explain the shorter period propagation characteristics are needed. While the signal-to-noise ratios become small at long-periods for events smaller than magnitude 4.5, the ratios in the frequency band from 0.1 to 1 Hz (roughly the bandwidth of the WALP instrument) remain large for smaller events. Some preliminary results in modeling regional waves in this bandwidth appear promising and will be addressed in future efforts. Surface waves are clearly the largest arrivals in the regional data, but are sensitive to lateral heterogeneity and shallow crustal structure. Progress has been made by calibrating certain paths for surface wave propagation [Patton and Doser, 1988; Beck and Patton, 1991; Thio and Kanamori, 1991] to make better use of this portion of the regional seismograms.

Chapter 3

Upland Earthquakes

3.1 Broadband Modeling of the 1988 Upland Events

3.1.1 Introduction

The installation of the Pasadena, California (PAS) very broad-band, high dynamic range instrument (Wielandt-Streckeisen sensor and Quanterra data logger) of the IRIS (International Research Institution for Seismology) and TERRAScope networks has allowed the comparison of seismic waveforms from events over a wide range of magnitudes. On traditional instruments however, such as the short-period Wood-Anderson (WASP) and the long-period Wood-Anderson (WALP), there is a rather narrow range of earthquake magnitudes that provide on-scale waveforms at a given receiver distance. In many cases, local events in the range of $M_L=3.0$ to about $M_L=5.0$ from a common source region have been observed to have similar waveforms. Figure 3.1 shows the location of the PAS station and five local earthquakes. Figure 3.2 shows an example of two small local earthquakes that occurred near Chino, California (stars, Figure 3.1) in February, 1989. These tangential component records were recorded on the very broad-band channel of the PAS instrument, integrated,

and then convolved with the response of a WASP instrument. Although different in size by more than an order of magnitude, these two events have nearly identical seismograms, demonstrating the deterministic nature of the records. It is evident that the smaller event would be barely recognizable on the record, while an event slightly larger than the larger of the two would be off-scale.

Events in this region are well located since they occurred within the dense USGS-Caltech array. In addition, focal mechanisms from first motions are easily obtained and appear quite accurate for events in this magnitude range. These smaller events also have simpler sources and generally do not show the complexity associated with larger ruptures. There are also more earthquakes in this size range providing a larger data set.

In short, we can assume the events are well located point sources, and analyze these seismograms in terms of propagational effects to study the crustal structure. The purpose of this paper is to demonstrate the methodology of obtaining accurate Green's functions from broadband data. We also intend to show that information about earthquake sources and propagation effects can be extracted from the broadband waveform data recorded at a single station. This paper is a two part study. First, a crustal model is determined and the modeling approach is discussed. Second, the sensitivity of the synthetic seismograms with respect to two-dimensional model perturbations is examined. Once the crustal structure or Green's functions are known, they can be used to study the sources of sparsely recorded historic earthquakes or to scale up the source and estimate strong ground motion for larger earthquakes.

3.1.2 Data and Processing

The data was recorded at the IRIS-TERRAscope instrument, PAS. The gain of this instrument is constant in ground velocity between 0.0027 Hz and 7 Hz for the very

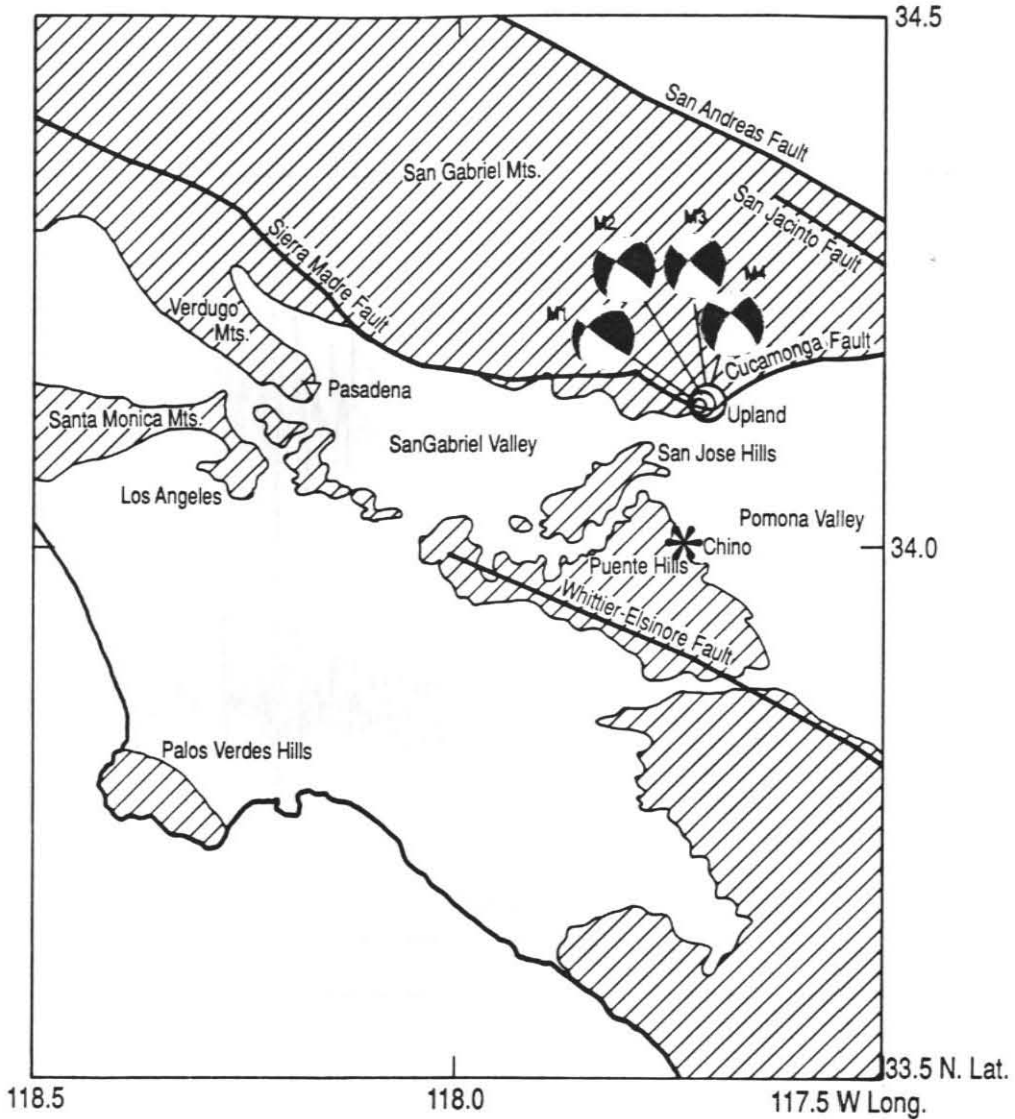


Figure 3.1: Location Map: the inverted triangle is the Pasadena station, the stars mark the Chino events, and the circles denote the Upland events. Hatched regions represent areas of shallow or surficial basement rocks after Yerkes et al. [1965]. Focal mechanisms M1 and M2 were derived from first motions on the Southern California Seismic Network for the two 1988 events. M3 and M4 were obtained for the 1990 mainshock.

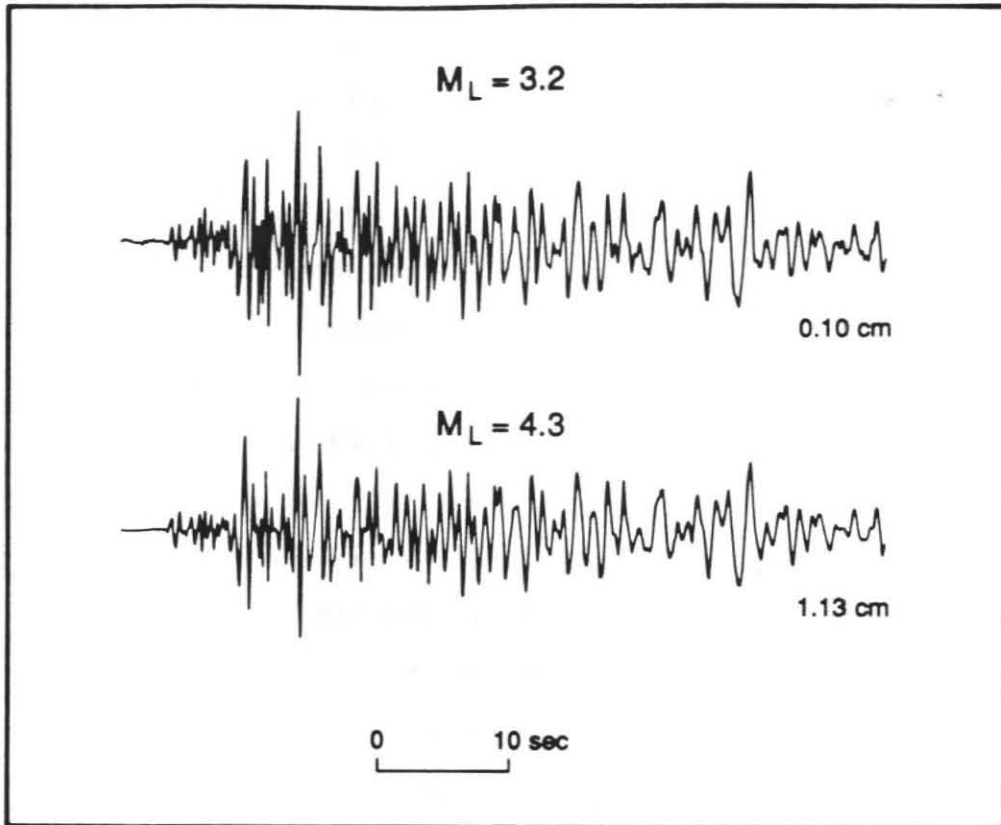


Figure 3.2: Tangential components of the 16 February 1988 ($M_L = 3.2$) and 18 February ($M_L = 4.3$) Chino earthquakes. The displacement data has been convolved with a short-period Wood-Anderson instrument response. Each seismogram is scaled to its maximum amplitude.

broadband channel. Integration within this frequency band produces displacement seismograms that can be convolved with the response of any instrument to obtain equivalent instrument seismograms. In this study, the displacement seismograms (0.02 to 7.0 Hz), as well as the WASP and WALP instrument seismograms are used in the forward modeling approach.

Two small earthquakes ($M_L = 4.6$ and 3.7) were recorded by this instrument on June 26, 1988 and July 6, 1988, respectively. Both of these earthquakes occurred in the Upland, California area (Figure 3.1), and the hypocenters located by the Southern California Network are within 1 km of each other, at a depth of about 8 to 9 km. These events occurred at a distance of about 43 km and the azimuth to the PAS station is 272° . Two focal mechanisms were obtained from first motion polarities on the Southern California array. They are $\phi = 221^\circ$, $\delta = 40^\circ$, $\lambda = 8^\circ$, for the mainshock, and $\phi = 212^\circ$, $\delta = 60^\circ$, $\lambda = -6^\circ$ for the aftershock (L. Jones, personal communication). Figure 3.1 shows that these mechanisms (M1 and M2) are very similar with a slight difference in the dip angle. Figure 3.3 displays the three-component displacement records and the WASP instrument seismograms. It is evident that these two earthquakes have very similar waveforms, however the similarity is not as great as for the earthquakes presented in Figure 3.2. Since the events occurred in nearly the same location, the differences in the waveforms are probably due to differing source history, orientation, and/or location. The most significant difference in the waveforms for the two events is in the relative amplitudes of the various S-wave phases on the tangential components. The identification of these phases and an understanding of the differences of the waveforms is a priority in modeling these events to obtain useful Green's functions.

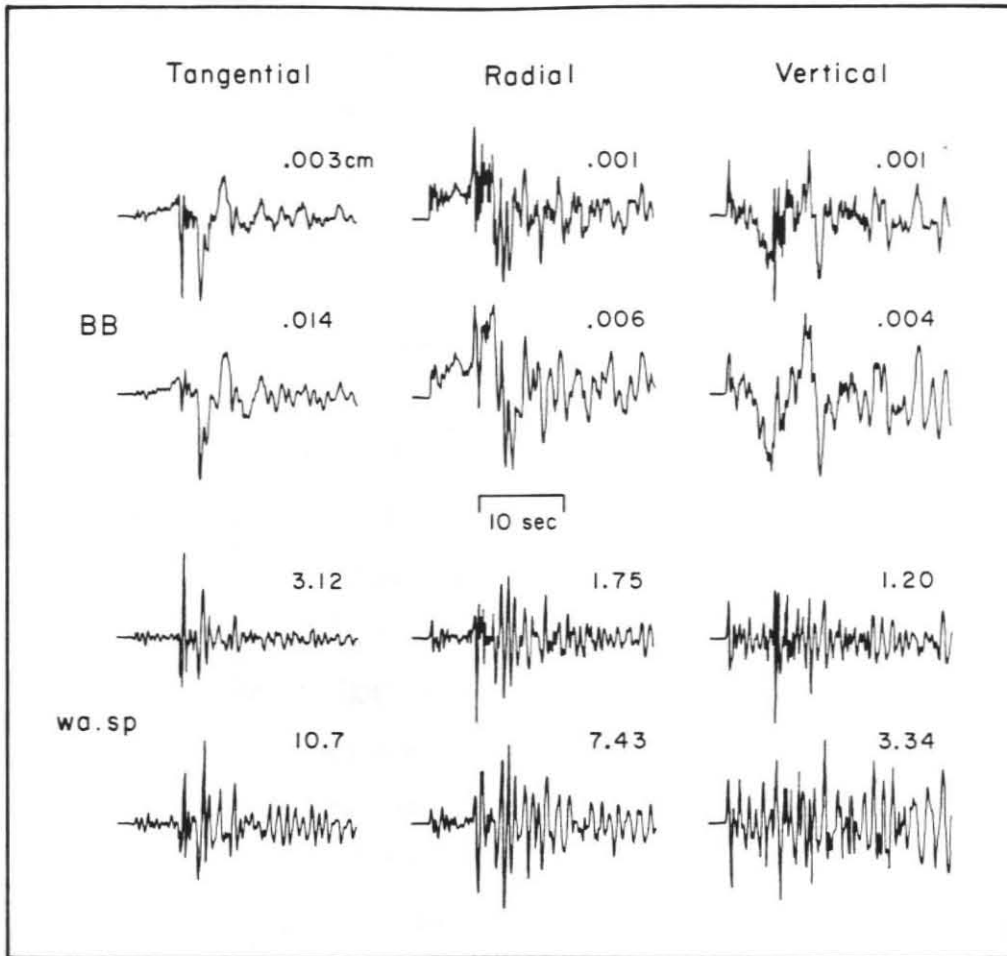


Figure 3.3: Three component displacement and short-period Wood-Anderson data for the 26 June 1988 ($M_L = 4.6$) and 6 July 1988 ($M_L = 3.7$) Upland earthquakes. Each seismogram is scaled to its maximum amplitude.

3.1.3 Methodology

The approach taken in this study was to identify the phases in the waveforms via forward modeling using Generalized Ray Theory (GRT). See Helmberger [1974, 1983] for details. GRT is especially useful for this purpose because it allows one to build the waveform with individual rays and gain insight. Since both source and propagation parameters are needed in computing synthetic seismograms, the source parameters must be constrained by other seismic measurements or assumptions in order to study crustal structure. Here we hold the source parameters (location, focal mechanism) determined from first motion studies utilizing the entire Caltech-USGS network data fixed. We assumed a point source for both events, with a trapezoidal source time function. A 0.15 sec. rise-time, 0.15 sec. duration, and 0.15 sec fall-time was determined by modeling the width of the direct S-wave. The same source time function was used for both the main shock and the aftershock. In modeling the tangential components we found that the two focal mechanisms produced very similar synthetics. With the exception of Figure 3.9, all of the synthetic seismograms presented in this paper were constructed using the focal mechanism of the mainshock. In Figure 3.9, we compare synthetics constructed for both focal mechanisms. With the source parameters constrained, the velocity model was perturbed until good agreement with the the data was obtained.

3.1.4 Modeling Results

The tangential component seismograms for both events contain a large amplitude phase which arrives after the initial direct S-wave. This phase is identified as a near receiver multiple within a near surface layer. In addition, there is a long-period phase arriving after the multiple which is interpreted as a Love wave. A simple layer over a half-space model works well in explaining the occurrence of these phases in the data. Figure 3.4 shows how the synthetics are developed with the addition of rays,

aiding the identification of the multiple phases (S_1 and S_2). The first two layers of the velocity model LOHS1 (Table 3.1) were used in computing these synthetics. This model was developed by the trial and error modeling of the various tangential component arrivals using the SoCal model as a starting model. The phases S_0 , S_1 , S_2 are all observed in the data, especially on the tangential records. The ramp like feature beginning at the P-wave travel-time and continuing to the arrival of the direct S-wave (S_0) arises with the addition of near-field terms in the calculations, and is evident on the tangential component displacement records (Figure 3.3) This model also produces the longer-period Love wave which arrives after S_1 . Five phases have been identified on the tangential component seismograms using GRT. It is rather surprising that such a simple model can give rise to such complexity.

Figure 3.5 compares the tangential component GRT synthetic seismograms for the preferred model LOHS1, to the Upland data. The amplitudes of the displacement synthetics were adjusted to the data by multiplying by a seismic moment scaling factor. The same scaling factor was used for the WASP and WALP synthetics, and there is good agreement in absolute amplitudes in the frequency bands of these instruments. The fits of the synthetics to the tangential data are exceptional. The S_0 , S_1 and Love wave are all well modeled. In these calculations the near-field problem was neglected. The addition of the near-field terms in the calculation would serve to improve the fits of the synthetics to the data by including the ramp like phase arriving between the direct P and S phases on the tangential component displacement records. The traditional WASP and WALP instruments effectively remove the near-field phase from the data. In addition, it was found that the amplitude ratio of S_0 and S_1 on the tangential component record of the mainshock is better modeled with a source depth of 6 km. The effect of differing source depth on the synthetics is discussed later.

Figure 3.6 and Figure 3.7 compare the radial and vertical component synthetics,

LOHS1				SoCal				LOHS2			
V_P	V_S	ρ	Z	V_P	V_S	ρ	Z	V_P	V_S	ρ	Z
4.5	2.6	2.4	0.0	5.5	3.18	2.4	0.0	4.7	2.4	2.4	0.0
5.9	3.5	2.67	4.0	6.3	3.64	2.67	5.5	5.5	3.5	2.67	3.3
6.6	3.8	2.8	16.0	6.7	3.87	2.8	16.0	6.0	3.6	2.7	10.3
8.0	4.1	3.1	26.0	7.8	4.5	3.0	37.0	6.6	3.81	2.8	22.3
8.2	4.2	3.3	30.0					7.4	4.27	2.95	26.3
								8.0	4.4	3.0	30.3

L1				L2			
V_P	V_S	ρ	Z	V_P	V_S	ρ	Z
4.5	2.6	2.4	0.0	4.5	2.6	2.4	0.0
5.9	3.5	2.67	4.0	5.9	3.5	2.67	4.0
6.5	3.75	2.7	10.0	6.5	3.75	2.7	10.0
5.6	3.23	2.7	15.0	6.55	3.78	2.8	15.0
6.6	3.81	2.8	21.0	6.6	3.81	2.8	21.0
7.2	4.16	2.9	23.0	7.2	4.16	2.9	23.0
7.4	4.27	2.95	25.0	7.4	4.27	2.95	25.0
8.0	4.62	3.2	32.0	8.0	4.62	3.2	32.0
8.3	4.8	3.35	38.0	8.3	4.8	3.35	38.0

Table 3.1: One Dimensional Velocity Models

Figure 3.4: The summation of rays to construct synthetic displacement waveforms for the tangential (T), radial (R) and vertical (V) components. A moment of 10^{25} dyne-cm was used. S_0 and P_0 are the direct P and S-waves, respectively. Note the ramp like near field term on the tangential component. Each seismogram is scaled to its maximum amplitude.

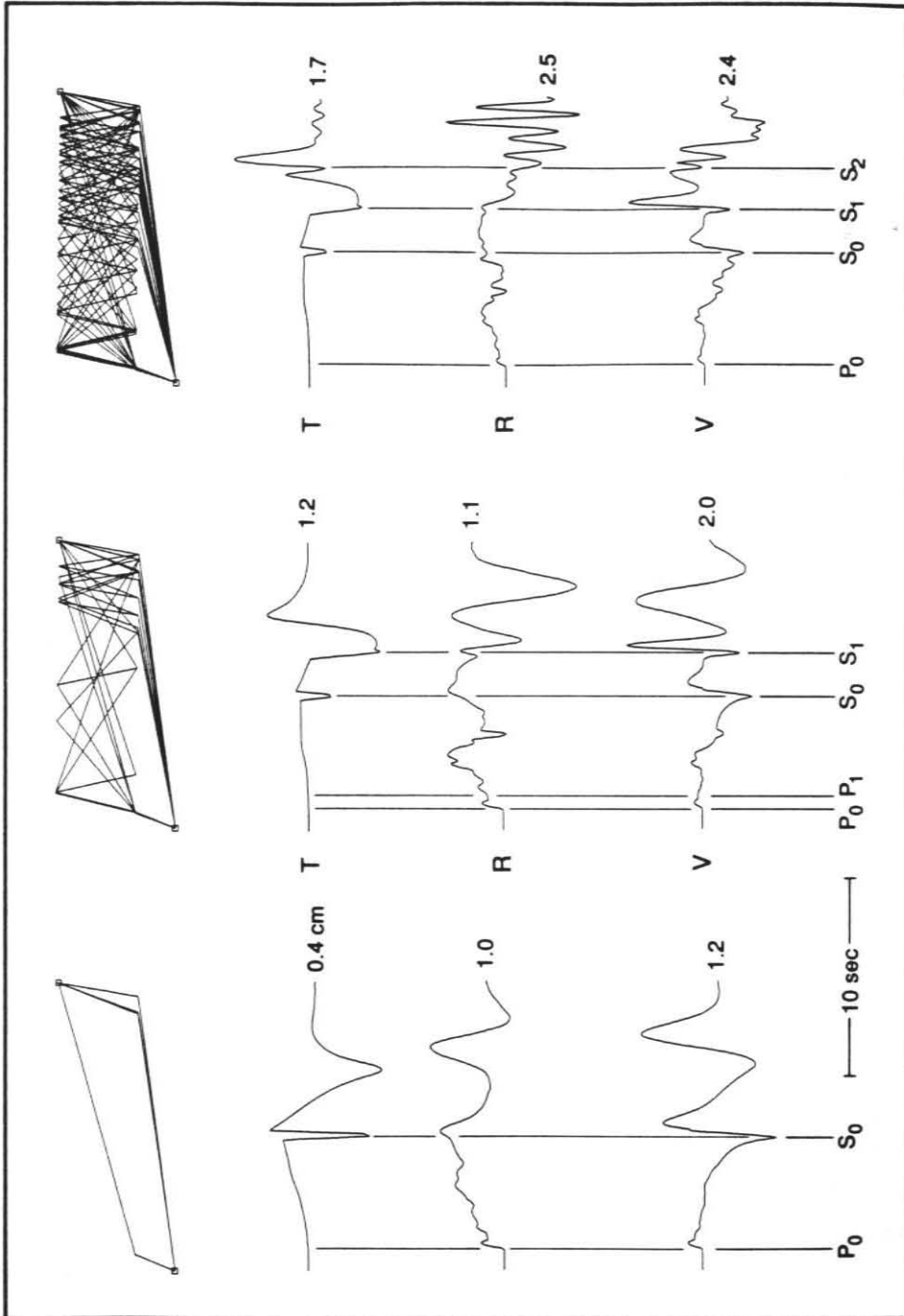
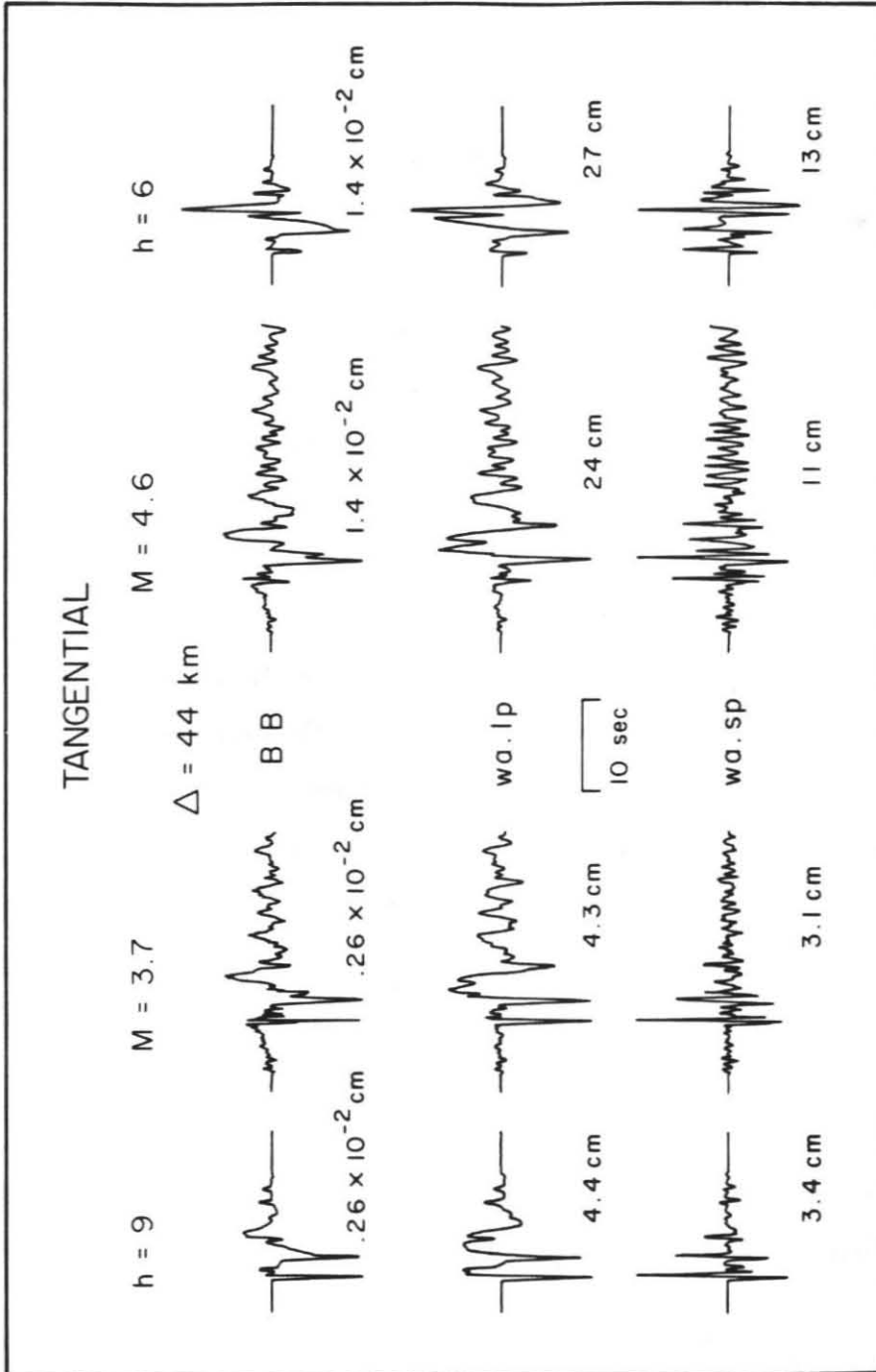


Figure 3.5: Comparison of tangential component synthetic seismograms with data (synthetics were computed with generalized rays). Moments are 1.7×10^{22} and 7.9×10^{22} dyne-cm for the aftershock and mainshock respectively. Each seismogram is scaled to its maximum amplitude. Source depths of 6 km and 9 km were used for the mainshock and aftershock synthetics, respectively.



respectively, with the data. These synthetics were computed using a reflectivity code vectorized and programmed by S. Mallick and M. Sen. This method also neglects the near-field problem. These synthetics were computed with the LOHS1 (Table 3.1) velocity model. As in Figure 3.5 the amplitude of the displacement synthetics were scaled to the data by multiplying by a seismic moment scaling factor and the same factor was used for the WASP and WALP synthetics. The fit of the radial and vertical synthetics to the data is not as good as for the tangential component, however at longer periods model LOHS1 works well. As in Figure 3.5 there is also good agreement in the maximum amplitudes of the synthetics and the data convolved with the WASP and WALP instruments. The coupled P-SV system is more sensitive to lateral heterogeneity, hence our simple model does not explain the high frequencies (WASP) very well, however the fits to the WALP instrument and the displacement data are good. One of the problems with the fit to the radial and vertical components, is that the relative amplitude of the direct P-wave is not well modeled for the 6 km source depth. This is especially true for the vertical component. The relative strength of the direct P-wave (P_0) is nearly the same for both events, yet the synthetics show large differences in relative amplitude. In addition, the vertical component waveform of the mainshock is better fit by the synthetic for a 9 km source depth. There is some indication that the disagreement with the radial and vertical component data is in part due to our choice of source mechanism, and is discussed later. The later arriving coda is difficult to model but the relative amplitudes do show a strong depth dependence. It is important to note that although the model used contains deeper structure, the tangential and the long-period radial and vertical component waveforms are really controlled by a layer over a half-space, composed of the velocities of the top two layers of the model LOHS1.

Figure 3.8 shows synthetics for different source depths (3 km to 17 km) constructed with the LOHS1 model, and the mainshock focal mechanism. These dis-

Figure 3.6: Comparison of radial component synthetic seismograms with data (synthetics were computed with reflectivity). Moments are 1.5×10^{22} and 8.2×10^{22} dyne-cm for the aftershock and mainshock respectively. Each seismogram is scaled to its maximum amplitude. Source depths of 6 km and 9 km were used for the mainshock and aftershock synthetics, respectively.

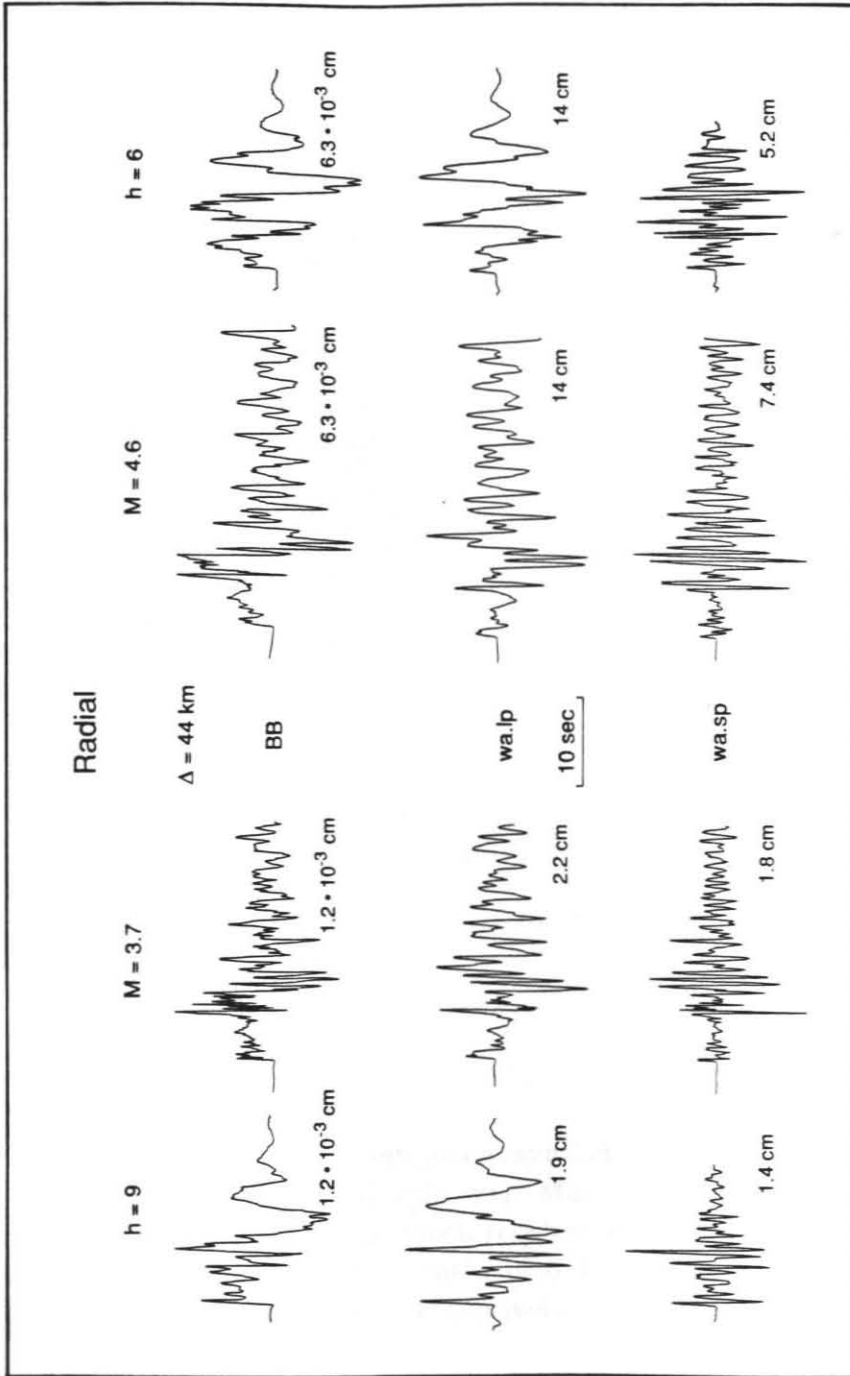
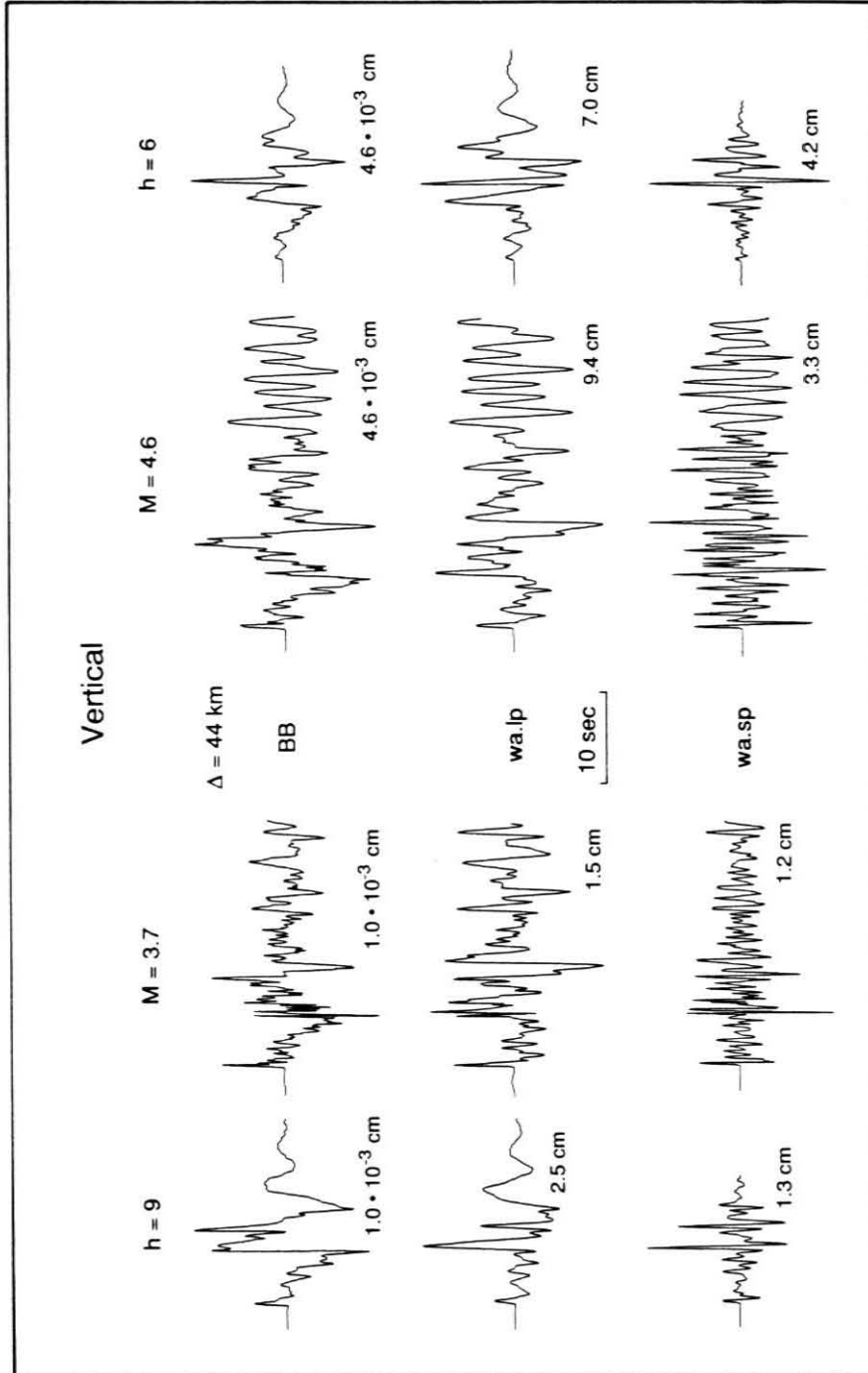




Figure 3.7: Comparison of vertical component synthetic seismograms with data (synthetics were computed with generalized rays). Moments are 7.7×10^{21} and 1.9×10^{22} dyne-cm for the aftershock and mainshock respectively. Each seismogram is scaled to its maximum amplitude. Source depths of 6 km and 9 km were used for the mainshock and aftershock synthetics, respectively.



placement synthetics were computed with the reflectivity code discussed earlier. Direct S (S_0) increases in amplitude with increasing depth, while multiple S (S_1) becomes more nodal and the strength of the Love wave and Rayleigh wave decreases. The character of the synthetic waveforms become simpler with greater depth for all three components. The synthetics at 3 km depth are considerably different in waveform and amplitude. The large amplitudes are due to short-period energy trapped within the near surface layer. The longer-period first arrival is a head-wave. Figure 3.9ab compare synthetics for source depths between 6 km and 9 km, for the mainshock and the aftershock focal mechanisms, respectively. This figure demonstrates that the two focal mechanisms produce similar waveforms on the tangential component. The relative amplitudes of S_0 and S_1 are not due to the differences in the focal mechanisms. In addition, we perturbed the focal mechanism and found that when direct S (S_0) became nodal a reflection from the layer at 16 km depth arriving just after S_0 became large compared to either S_0 or S_1 , and the overall waveform was drastically changed. Judging from Figure 3.9a, the tangential component of the mainshock is best modeled with a 6 km source depth, and the aftershock is best modeled with a 9 km source depth. Figure 3.9b shows the source depth sensitivity of the synthetics for the aftershock focal mechanism. Again, the tangential component of the mainshock is best modeled with a source depth of 6 km and the aftershock between 8 km and 9 km. Use of the aftershock mechanism improves the fit to the radial and vertical components, however. The relative amplitude of direct P is more consistent for the different depths than it was when the mainshock focal mechanism was used. Moreover, there is less variation of the vertical synthetic waveforms with increasing source depth.

Variation of Synthetics with Depth

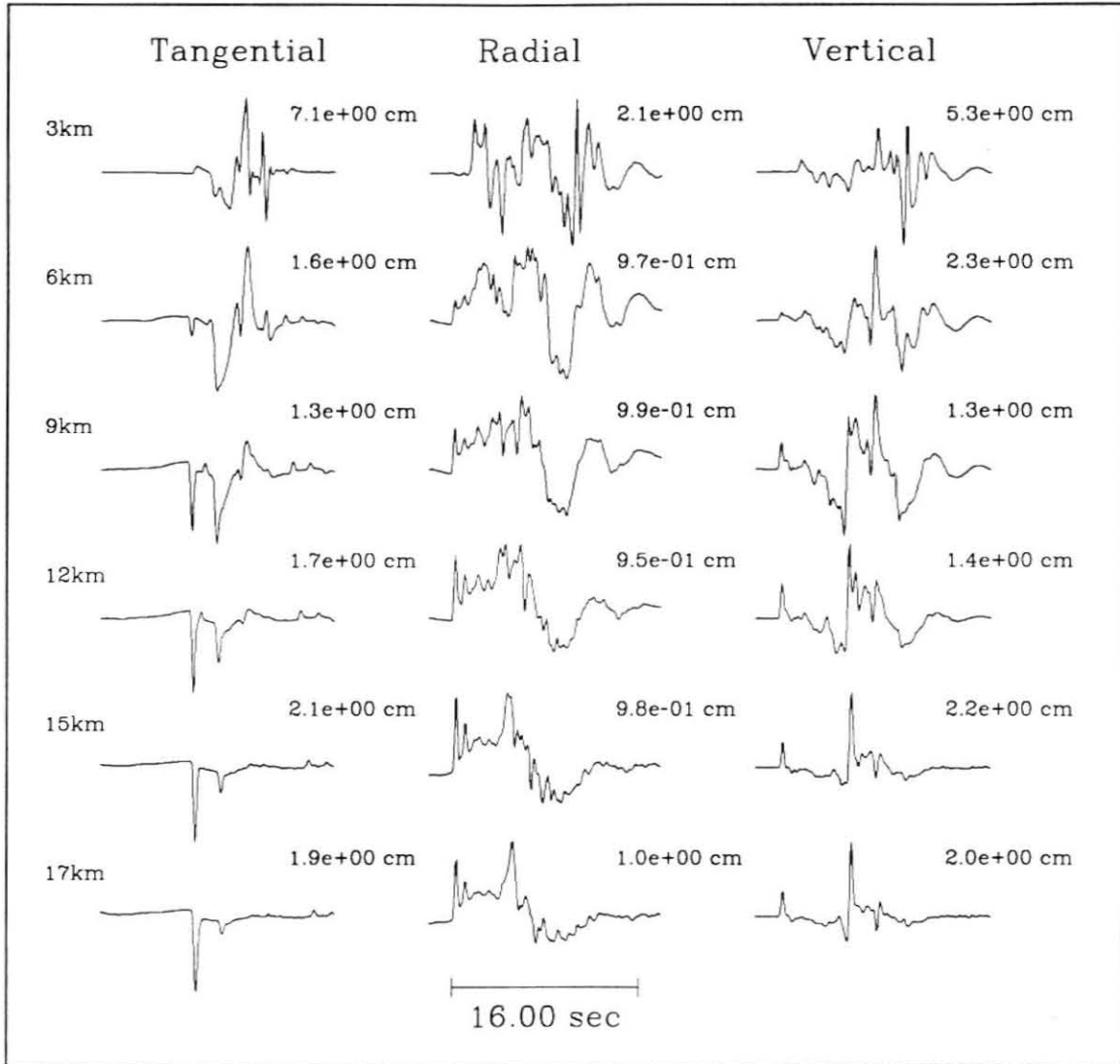
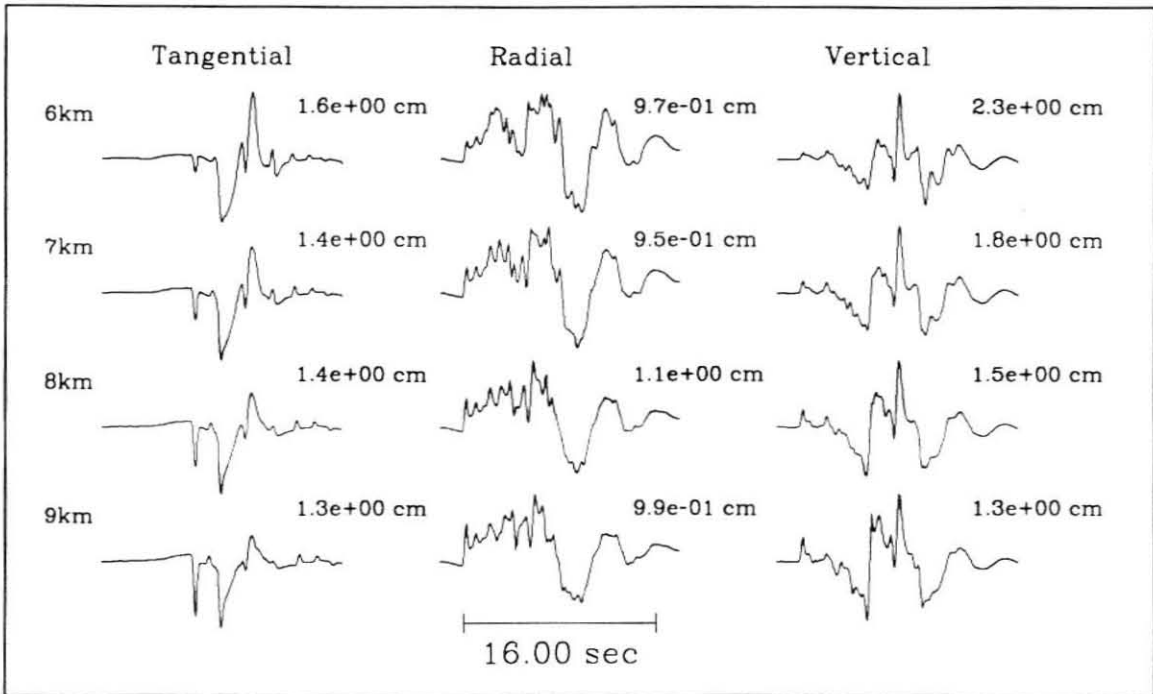


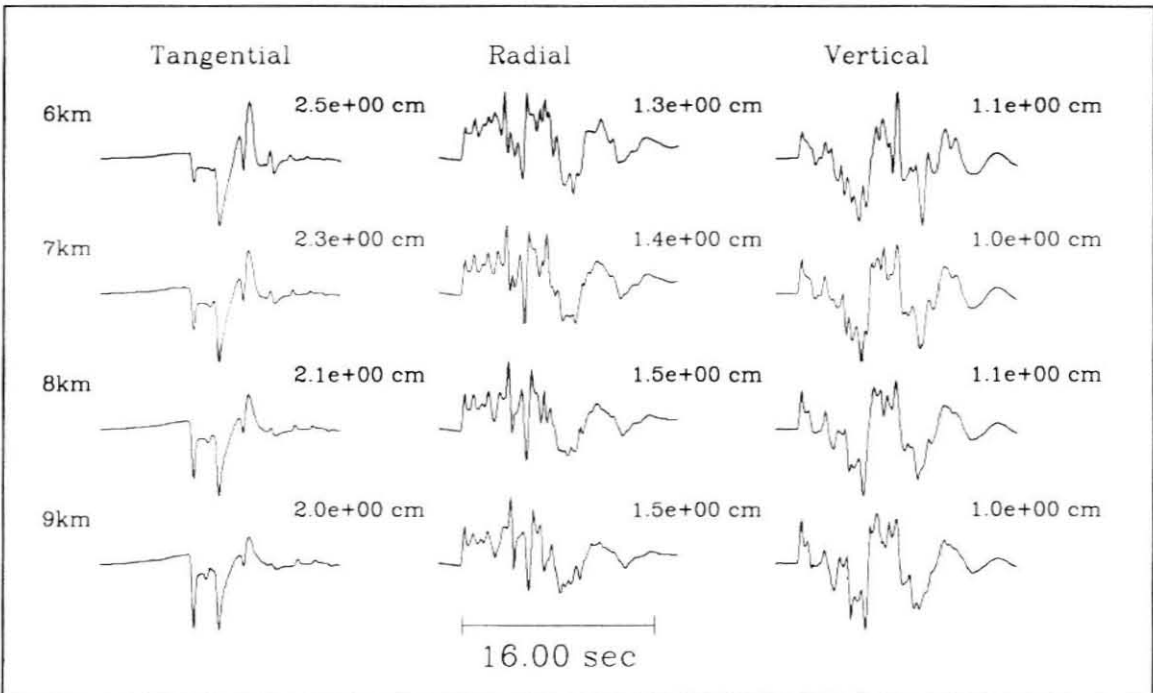
Figure 3.8: Profile of synthetic seismograms for source depths from 3 to 17 km. The synthetics were constructed with the mainshock focal mechanism and a moment of 10^{25} dyne-cm using an F-K integration code. Near-field terms are included. Each seismogram is scaled to its maximum amplitude.

Figure 3.9: (a) Profile of synthetic seismograms for source depths from 6 to 9 km constructed with the mainshock focal mechanism. (b) Profile of synthetic seismograms for source depths from 6 to 9 km constructed with the aftershock focal mechanism. A moment of 10^{25} dyne-cm was used.

(A)



(B)



3.1.5 Sensitivity Analysis

The result of a simple structure controlling the waveforms is surprising. Figure 3.1 indicates that there is considerable geologic complexity along this profile. Ignoring details of faulting and folding, the profile still retains a ridge-basin-ridge structure. Specifically, the energy released during the earthquakes propagated through the San Jose Hills, San Gabriel basin, and the eastern margin of the Verdugo mountains. The second part of this paper investigates sensitivity of the synthetic seismograms to perturbations of the layer over a half-space structure. Smoothed layer boundaries, deep crustal structure, layer thickness, and two-dimensional velocity models were tested. Three-component synthetic seismograms for flat layered models were computed by the same reflectivity method discussed earlier. The mainshock focal mechanism was used in these calculations. Synthetic seismograms for the two-dimensional studies were computed with a finite-difference approach [Helmberger and Vidale, 1988]. In these analyses the source depth was kept fixed at 9 km.

Figure 3.10 shows the results of perturbing the layer over a half-space structure by introducing velocity gradients. All of the perturbed models produce synthetics resembling the layer over a half-space result. This is especially true for Figures 3.10cd. Velocity gradients are introduced in those models to remove the sharpness of the contact between the two layers. Some of the effects to take note of are the removal of the second multiple (S_2), and the change in relative amplitudes of S_0 and S_1 . Figure 3.10b has a linear gradient from the free-surface to the half-space approximated with discrete layers. The shape of the Love wave is severely altered, as are the radial and vertical component synthetics. The second well developed peak on the vertical and radial components is caused by the phase SP, which is an S-wave converted to a P-wave at the free-surface with a subsequent path turning in the near surface velocity gradient. This phase becomes more complex when multiple conversions are introduced by more boundaries. Generally it is possible to smooth the contact between

the two layers and still obtain synthetics which are good fits to the data, however it is important that there is a well defined surface layer to develop the Love wave and the S_1 multiple. It was found that 1 to 2 km of smoothing of the layer boundary could be tolerated in the synthetics at the frequencies we are modeling.

Figure 3.11 shows the results of varying deep crustal structure, and the effect of the velocity/thickness tradeoff for the shallowest layer. LOHS1 is the preferred model, discussed earlier. Table 3.1 gives the details of all of the models used in the construction of the following synthetics. Comparison of the synthetics constructed with the LOHS1, SoCal, and LOHS2 models shows that there is some variation, in the waveforms. The SoCal model is an average model of southern California which is used to routinely invert for source location and focal mechanism from first motion data. The synthetics produced by this model do not fit the data well. The primary reason is the thickness and velocity of the surface layer. This layer is 5.5 km thick, with a velocity of 3.18 km/s. The Love wave does not develop as strongly as it does with model LOHS1. For model LOHS2, the surface layer was made thinner and slower. An additional mid-crustal layer was also included. The effects are that the Love wave and the S_2 multiple are more developed than for model LOHS1. This indicates that the thickness of the surface layer must be less than 5.5 km and greater than 3 km, and that the velocity vs. thickness ambiguity in travel-time is resolvable by studying waveforms.

Langston [1989] studied PS crustal conversions of teleseismic signals recorded at PAS, and obtained a one-dimensional receiver structure. Model L1 (Table 3.1) is a modified version of this receiver structure in which the velocity of the surface layer was changed to that of model LOHS1. Model L1 contains a low velocity zone at depth. Model L2 is the same model as L1 except the low velocity zone was removed, and replaced with a positive velocity gradient. Figure 3.11 shows that the synthetic seismograms do not change very much for these two models as compared

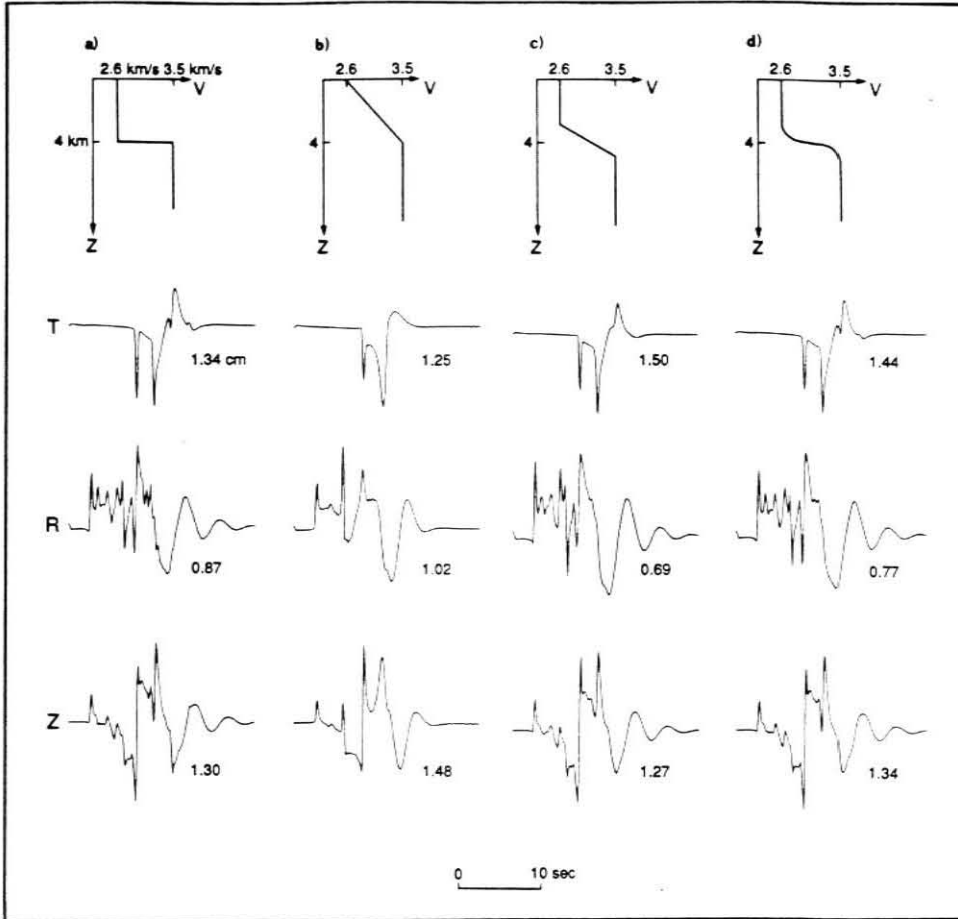
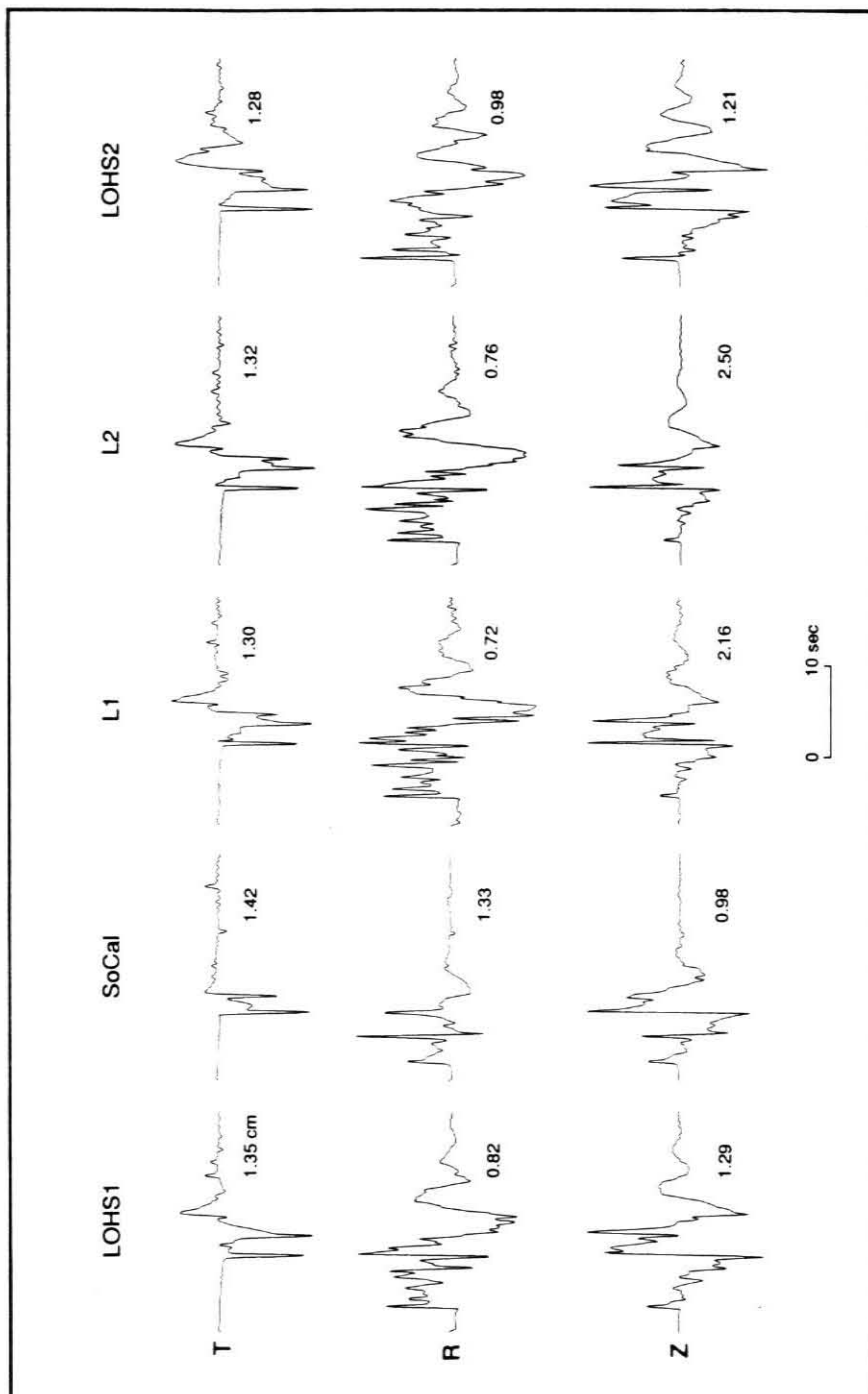


Figure 3.10: Boundary sharpness sensitivity assuming a moment of 10^{25} dyne-cm. Each seismogram is scaled to its maximum amplitude. A source depth of 9 km was used.

Figure 3.11: Flat layered model sensitivity assuming a moment of 10^{25} dyne-cm. Each seismogram is scaled to its maximum amplitude. A source depth of 9 km was used. See Table 3.1 for the details of the different models used.



to synthetics computed with model LOHS1, although they do tend to have a greater number of short-period arrivals. The details of deep crustal structure are not particularly important in the waveforms of local earthquakes (ranges less than 44 km), for frequencies less than 1 Hz.

Figure 3.12 shows the results of including lateral variations using a two-dimensional finite difference calculation. For these models the two SH fundamental faults were computed separately and convolved with a square-root singularity to map the line source response to a point source. The two fundamental faults were summed to produce displacement synthetics with the mainshock focal mechanism. Figure 3.12a shows the tangential displacement synthetic for a layer over a half-space model. Comparing the reflectivity result (Figure 3.10) with Figure 3.12a it is evident that the two methods correlate well. This comparison is useful in identifying the occurrence of artifacts in the finite-difference synthetics. Two artifacts are present. These artifacts arise from reflections from the finite grid boundaries. Since they occur later in time than the Love wave, they do not cause any substantial distortion of the synthetic waveforms.

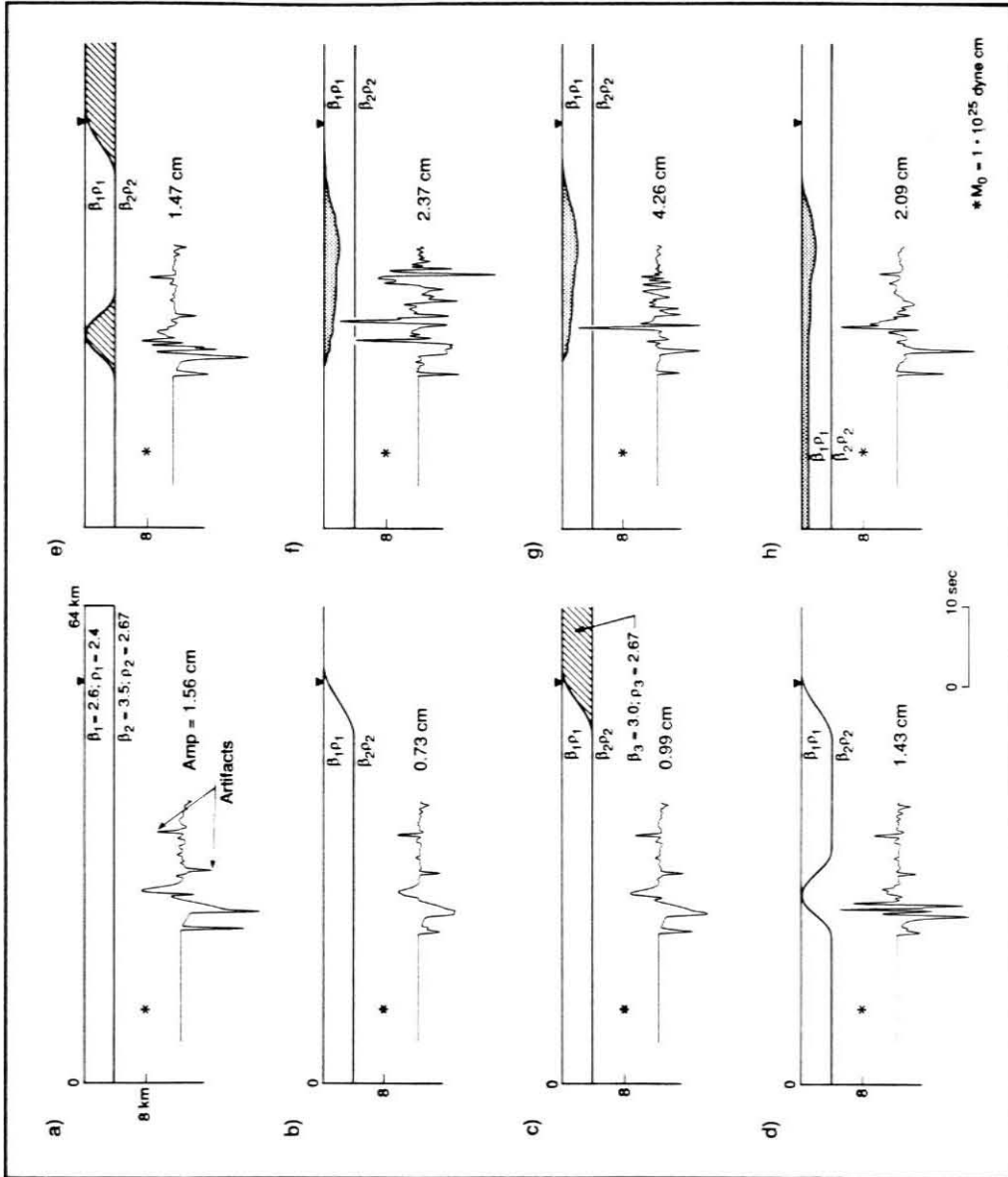
Figures 3.12bc show the effect of a ridge structure introduced beneath the PAS station. The effect is basically a low-pass filter. When an intermediate velocity is introduced into the ridge (Figure 3.12c) many of the characteristics of the layer over a half-space model synthetics are retained, although there is a reduction of the higher frequency energy. The WASP instrument synthetics would be affected by this structure. Since the ridge structure attenuates the upward propagating higher frequency energy, initial downward propagating energy, reflected back to the receiver would be expected to be more important in the WASP synthetics. This figure demonstrates that a ridge structure beneath PAS does not have a large effect at lower frequencies, but may be significant at higher frequencies.

Figures 3.12de show the effect of the addition of a ridge between the source and

the receiver. The character of the waveform is completely changed, especially the Love waves. Vidale and Helmberger [1988] found that shear body waves convert to surface waves at the edge of the basin closest to the source, and propagate across the basin. Vidale and Helmberger [1988] also saw evidence of surface waves crossing ridge structures as body waves. In our models the secondary surface waves are typically richer in higher frequencies than those for models with no ridge between the source and receiver (compare Figures 3.12abc to Figures 3.12de). These higher frequency phases are probably critically reflected arrivals generated at the ridge. In fact, the character of the waveform resembles that of the shallow source in model LOHS1 (see Figure 3.8). The synthetics for these ridge structures do not fit the Upland data. Figures 3.12fgh explore the possibility of a shallow basin within the surface layer. Figure 3.12f has a basin with a 1.8 km/s shear wave velocity and a 2.0 g/cm density. Figures 3.12gh differ in that the velocity within the basin is a linear gradient where $\beta = 1.8 + 0.4Z$. The geometry of the shallow basin for Figures 3.12fg was interpolated from the depth to basement results of Yerkes et al., [1965]. In these calculations, the layer at 4 km depth was retained because of its importance in producing the S_1 and S_2 multiple phases as well as the Love wave as discussed earlier.

For Figures 3.12fgh the synthetics are amplified by factors of 1.3 to 2.7 compared to Figure 3.12a. The synthetic seismograms also have extended durations compared to Figures 3.12abcde. Both of these effects are the result of the trapping and the reverberation of energy in the basin which subsequently escapes at the shallow basin boundary. The escaping energy encounters the deeper layer responsible for S_1 and S_2 at near critical angle, and is reflected back up to the receiver. Similarly, the high frequency energy transmits at the ridge structure beneath the receiver, while the longer-period energy is unaffected. The differences in the synthetic waveforms for Figures 3.12fg are the result of the effect of the gradient on the development of a local Love wave within the basin. The basin model lacking a velocity gradient has

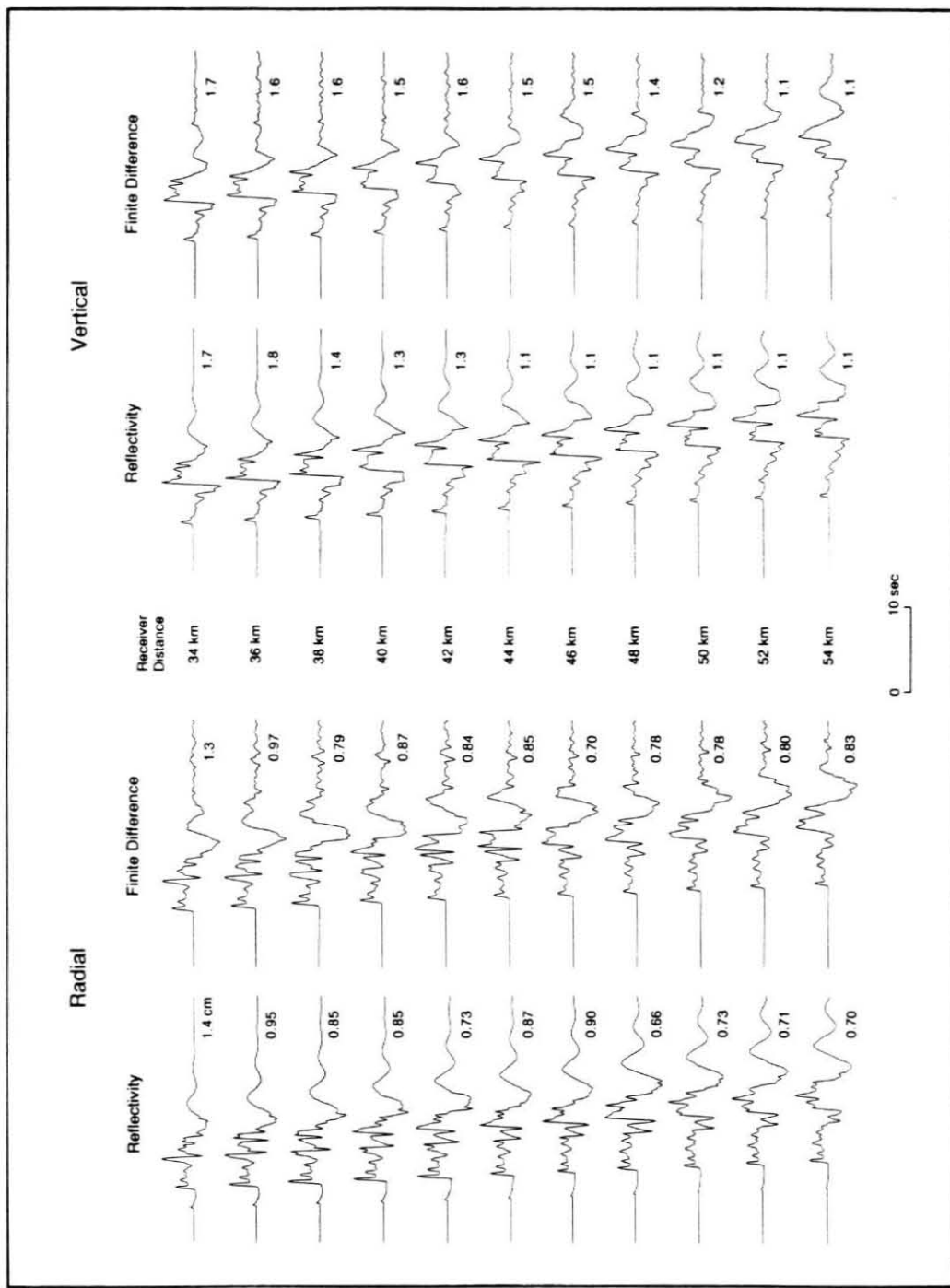
Figure 3.12: SH finite-difference calculations using ridge structures and realistic basins after Yerkes [1965]. Dotted region in (f) represents $\rho = 2.0gcm^{-3}$ and $\beta = 1.8kms^{-1}$. For (g) and (h) the dotted region represents a linear gradient in velocity with the form $\beta = 1.8 + 0.4Z$. The moment used is 10^{25} dyne-cm. Each seismogram is scaled to the maximum amplitude of (a), with the exception of (f), (g) and (h). For each synthetic the maximum amplitude is given. A source depth of 9 km was used.



a slower velocity which serves to extend the duration of the synthetic waveforms. Figure 3.12g shows that much of the amplification observed in Figure 3.12f is due to the energy being trapped by the dipping basin wall closest to the source. Shallower sources are more effective at generating surface waves and are probably also effective at generating stronger coda via this type of scattering.

Figure 3.13 shows the radial and vertical component finite-difference synthetics using the model of Figure 3.12c. These synthetics are compared with the reflectivity calculations for the layer over a half-space. The synthetic waveforms do not change dramatically for this two-dimensional structure. The Rayleigh wave seems to be the most affected phase, with a slight phase shift. Array measurements would be required to examine possible timing relationships of higher frequency scattered ridge phases in the data. The results of both the SH and P-SV two-dimensional studies indicate that the effects of these structures are frequency dependent.

Figure 3.13: Radial and vertical component synthetics showing the difference between a flat layer over a half-space (reflectivity synthetics) and the model (c) in Figure 3.12 (finite-difference synthetics). A moment of 10^{25} dyne-cm is used. Each seismogram is scaled to its maximum amplitude. A source depth of 9 km was used.



3.1.6 Discussion and Conclusions

We envision the usefulness of these Green's functions in several ways. First, they can be used to study less well recorded historic events where the only seismological waveform data available are a pair of long period horizontal torsion recordings (WALP), as is the case at PAS. This is especially valuable in extending available data sets for a given source to receiver path. Second, they can be used in the simulation of large events from small ones and can compliment empirical Green's functions in such studies. Mori and Hartzell [1990] use an empirical Green's function approach to determine the plane of faulting of the main event. Although our objective was to develop Green's functions for the path from Upland to PAS, and to demonstrate the methodology of studying broadband seismograms to find the Green's functions, it is interesting to compare our estimates of seismic moment and stress drop with theirs.

The fundamental assumption in the empirical Green's function approach is that the waveform distortions caused by the path and site conditions are shared by the mainshock and the aftershock. If the mechanisms are identical, one can use the aftershock waveforms to generate the main event waveforms by considering finite rupture on the two possible focal planes ($\phi = 125^\circ$, $\delta = 85^\circ$, $\lambda = 130^\circ$, or $\phi = 221^\circ$, $\delta = 40^\circ$, $\lambda = 8^\circ$). Mori and Hartzell [1990] did this for the 1988 Upland mainshock and found that the southwest trending plane gave the best results indicating left-lateral motion which is consistent with the overall motion in the Transverse Ranges frontal fault zone. They obtained a seismic moment of 4.2×10^{22} dyne-cm for the main event from the P-wave amplitude. Their inversion gave a source area of 1 km^2 and a stress drop of 38 bars assuming a rectangular rupture.

We obtained a larger moment, $(6 \pm 2) \times 10^{22}$ dyne-cm by modeling the amplitudes of the three-component displacement data convolved with a Press-Ewing instrument response. A considerably larger stress drop, based on the far-field time duration, τ ,

was estimated, by assuming that:

$$\tau = \frac{a}{\beta} \left[\frac{16}{7\pi} + \left(\frac{1}{0.8} + \sin\delta \right) \right]$$

where a is the fault dimension (circular fault), β is the shear velocity and δ is the angle between the normal to the fault plane and the ray path [Cohn et al., 1982]. The duration of a trapezoidal far-field time function is defined as $\tau = 0.5\delta T_1 + \delta T_2 + 0.5\delta T_3$ [Helmberger and Malone, 1975] For a τ of 0.3 seconds, this expression yields an estimate of fault dimension a , of 0.4 km. Assuming, $\Delta\sigma = 7M_o/16a^3$ [Kanamori and Anderson, 1975], where $\Delta\sigma$ is stress drop and M_o is moment, and a as defined above, a stress drop of 410 bars is obtained. This estimate of stress drop is considerably larger than Mori and Hartzell's [1990] estimate. However, different models of fault rupture were used.

We found that both the mainshock and aftershock could be modeled with the same source time function. The width of the S_0 phases are well modeled with the source time function that was used. The aftershock was about 6 times smaller in seismic moment indicating that it was a lower stress drop event. The aftershock appears to be slightly richer in higher frequencies than the mainshock on the radial and vertical components, however. If it is assumed that both events had the same stress drops then $\tau = 0.16$ is obtained for the aftershock which is too short. Therefore, while there are slight differences in the sources of the two events, they are probably not sufficient to account for all of the differential between the calculated stress drops. Mori and Hartzell [1990] report that rupture on the southwest trending fault plane (their preferred fault plane) propagated upward and to the southwest toward PAS. Unilateral rupture toward PAS would tend to reduce our estimate of the actual fault dimension and would result in an over estimate of stress drop. Another process that would affect the calculation of stress drop is the effect of attenuation. The generalized ray synthetics (Figure 3.5) have no Q in the calculation, while the reflectivity synthetics used throughout this study were computed with $Q_\alpha = 600$ and $Q_\beta = 300$.

The differences in the synthetics are negligible. If the value of Q that we have used is too large then the source dimension is over estimated and the seismic moment under estimated; both of which give rise to an under estimate of stress drop. In any case, clearly a combination of numerical and empirical approaches would be the most powerful, in which the longer-period properties, namely moment, effective time history and orientation, are modeled numerically, and shorter-period effects, namely rupture properties, are modeled empirically.

In conclusion, it is possible to interpret local broadband records with relatively simple models. The broadband records facilitate the identification of different arrivals, particularly phases with different frequency content (i.e., near-field, post-critical, and surface-wave phases). The results of the forward modeling indicate that the waveforms of the two Upland, California earthquakes are controlled by the relatively slow material at the surface for which a single-layer structure is an adequate approximation. The forward modeling approach used here is also useful in studying source complexities. This is facilitated by studying two or more earthquakes in a given area. The differences in the waveforms can be understood in terms of differing focal mechanism, location, source-time function, or in dislocation complexities. In the case of the $M_L=4.6$ Upland, California earthquake it was found that the waveforms were better modeled with synthetics computed with a source depth of 6 km, roughly 3 km shallower than the array location. This is not surprising in that a strong trade-off in depth vs. origin time exists in earthquake location solutions. Thus, one of the first contributions of local broadband waveform data will be on source depth control.

The sensitivity analyses indicate that the upper layer must be between 3 to 5 km thick, but that the contact can be smoothed with a 1 to 2 km wide velocity gradient. The deeper crustal structures that were examined produce a greater number of short-period arrivals that are not resolvable with the available data. Two-dimensional near

receiver ridge structures can affect the waveforms in a manner similar to attenuation. Random scatters can also produce an effect similar to attenuation [Frankel and Clayton, 1984]. Therefore, care must be exercised when differentiating intrinsic Q from the effects of receiver structures and heterogeneous media. Neither of the closed basin models, nor the shallow basin models satisfied the data. However, the extended duration produced by shallow basins may account for the observed extended duration of S waveforms for other earthquakes which occur south of Upland (Figure 3.1 and Figure 3.2), and in Los Angeles basin [Saikia, et al., 1992]. Fortunately, the relative insensitivity of the synthetics to details of boundary sharpness, layer thickness, and to some degree two-dimensional near receiver structure, shows that useful Green's functions can be found without knowing the fine structural details.

3.2 Broadband Modeling of the 1990 Upland Sequence

3.2.1 Introduction

The occurrence of the Upland, California $M_L=5.2$ earthquake on February 28, 1990, approximately 43 km east of the IRIS/TERRAScope broadband, high dynamic range station at Pasadena, California (PAS) provided an opportunity to compare waveforms of different sized events from the same source region. In particular, the waveforms of the 1990 mainshock are compared with those of two smaller events which occurred on June 26 and July 6, 1988. Such comparisons prove to be very fruitful in studying source complexities of larger earthquakes. The high dynamic range of the PAS station allows one to study the smaller, more frequent events as well as the larger events. Using the waveforms of smaller earthquakes with relatively simple sources, the effects of the propagation path on the waveforms can be identified. The broadband character of the seismograms allows many different phases with different frequency content to be studied together in a whole waveform modeling exercise.

Records of the June 26, 1988 ($M_L=4.6$) Upland event, and its largest aftershock ($M_L=3.7$ on July 6, 1988) were used in an earlier study [Dreger and Helmberger, 1990] to examine the effects of various crustal structure models on wave propagation. In that study one-dimensional and two-dimensional velocity models were tested for the path from Upland to PAS. Gradient structures, deep crustal-velocity structure, and near-receiver two-dimensional structures were evaluated in terms of the effect on the synthetic waveforms. The results of that study indicate that a one-dimensional layer over a half-space model works very well in producing synthetic seismograms which accurately model the data. The preferred plane layered model was LOHS1 (Table 3.1). The source depths of the 1988 $M_L=4.6$ and $M_L=3.7$ events were determined to be 6 km and 9 km, respectively.

Figure 2.1 shows the location of PAS, together with the locations of the two

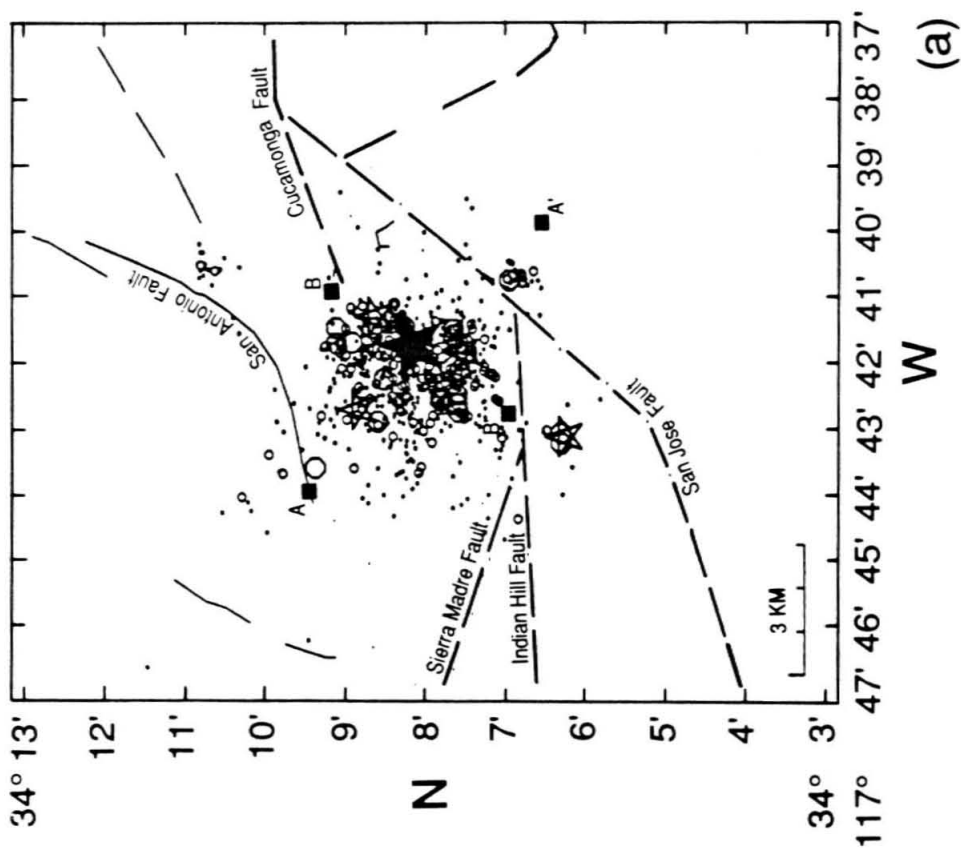
1988 Upland events and the 1990 mainshock as calculated by the Caltech-USGS, Southern California Seismic Network (SCSN). These events occurred in nearly the same location and share similar propagation paths. PAS is located at a distance of about 43 km at an azimuth of 272° from the 1990 mainshock epicenter. The four focal mechanisms shown on Figure 3.1 were determined from SCSN first motion polarities. Mechanisms M1 and M2 were determined for the June 26 and July 6, 1988 Upland events, respectively. Mechanisms M3 and M4 were computed for the 1990 mainshock. The focal mechanism parameters and references are listed in Table 3.2. The effects of the focal mechanisms M1 and M2 on synthetics computed using model LOHS1 are discussed in Dreger and Helmberger [1990]. The focal mechanism M3 was determined by Hauksson and Jones [1991] for the 1990 mainshock using a regional one-dimensional velocity model (SoCal, Table 3.1). They used a different velocity model with slower near surface velocities for stations located in Los Angeles basin. Focal mechanism M4 was calculated for the 1990 mainshock using a 3-dimensional velocity model (H. Magistrale, personal communication, 1990). All of these focal mechanisms are very similar. Of the two possible fault planes the southwest trending plane is favored for the 1988 mainshock based on observed directivity [Mori and Hartzell, 1990]. The locations of the 1990 aftershocks (Figure 3.14a) show that these events also occurred on a southwest trending fault plane where the depths of the aftershocks (Figure 3.14b) range from about 3 to 13 km on a northwest dipping plane [Hauksson and Jones, 1991]. The southwest trending fault plane has a left lateral sense of motion which is consistent with the inferred motion of the Cucamonga fault in this area [Cramer and Harrington, 1987]. Fault plane solutions for the 1988 aftershock and the 1990 mainshock (Table 3.2) have steep dips for the southwest trending plane that are consistent with the observed aftershock distribution for the 1990 sequence.

The aim of this study is to utilize the Green's functions developed in the ear-

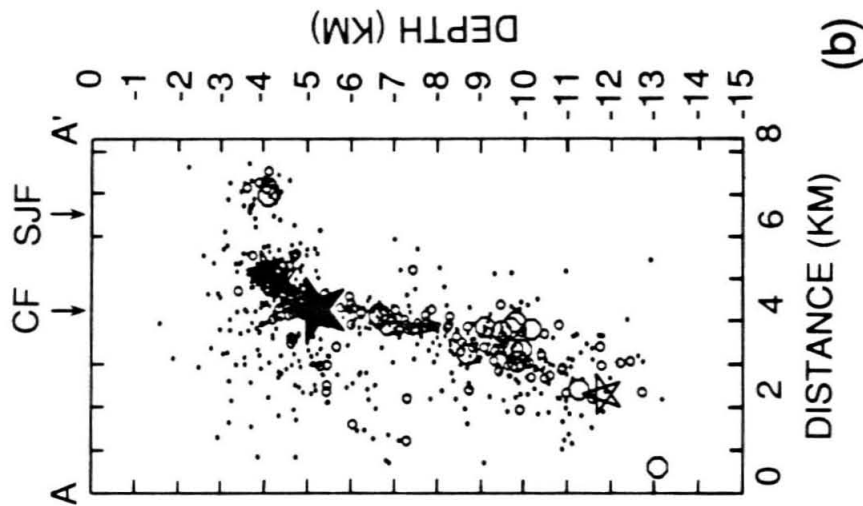
Figure 3.14: (a) Map view and (b) depth section locations of the February 28, 1990 Upland Sequence (modified from Hauksson and Jones, 1991). The mainshock is denoted by the solid star. AA' shows the location of the depth section. BB' shows the location of the top (depth of 6 km) of the fault we used in the distributed fault calculations shown in Figure 3.19.

Upland Earthquake Sequence

February 28 - April 17, 1990



(a)



(b)

ID	Strike	Rake	Dip	Reference
M1	221	8	40	L. Jones (personal comm.)
M2	212	-6	60	L. Jones (personal comm.)
M3	220	0	70	Hauksson and Jones [1991]
M4	215	-20	70	H. Magistrale (personal comm.)

Table 3.2: First Motion Polarity Fault Plane Solutions

lier work to determine the source characteristics of the February 28, 1990 Upland, California mainshock, using the broadband data recored at PAS. We use a frequency-wavenumber (F-K) approach [Saikia, 1992] to compute synthetic seismograms. This approach computes the complete solutions for a layered stack, including near-field terms. All of the synthetics in this paper were computed using the LOHS1 velocity model (Table 3.1). We use these synthetics to invert for long-period source parameters (orientation, moment, depth, time function) and to model the data using point-source and finite distributed source models.

3.2.2 Data Comparisons and Analysis

As stated above, the 1990 sequence occurred in about the same location and had a focal mechanism similar to the two largest events of the 1988 sequence. Since location and orientation are nearly the same there should be similarities in the waveforms of these three events. Figure 3.15 displays the displacement data and simulated short-period Wood-Anderson (WASP) seismograms for the 1990 mainshock, 1988 mainshock, and 1988 aftershock. To the first order, similarities in the waveforms are readily apparent. On the tangential component the direct S (S_0), multiple S (S_1), and Love waves are all observed. Beginning at the P-wave travel-time there is a

ramp shaped phase which continues to the phase S_0 . This phase was identified as a near-field arrival [Dreger and Helmberger, 1990]. The three events are also similar in that the tangential components have the largest displacement amplitudes followed by the radial and then the vertical components. The displacement records for the 1990 mainshock and the 1988 mainshock are the most similar. Both events have approximately the same S_0 to S_1 ratio, and the amplitude ratios of the Love wave to S_0 and S_1 are also nearly the same. In addition, the long-period coda is also well correlated. The largest difference between these two events is that the 1990 mainshock has a larger long-period to short-period energy ratio compared to the 1988 mainshock due to a relatively larger fault area. A curious observation for the 1990 mainshock though, is that while the displacement waveforms generally appear longer period than the 1988 data the phase S_0 does not. The 1988 mainshock was best modeled using a source depth of 6 km [Dreger and Helmberger, 1990]. Thus, the similarity in the waveforms suggests that these two events occurred at nearly the same depth, with similar focal mechanisms. The focal depth of the 1990 mainshock determined from SCSN first motions was 5.2 km [Hauksson and Jones, 1991], which is in agreement with the first order depth estimate obtained above by simply comparing the waveforms.

Next we compare the tangential WASP records. The 1990 mainshock most closely resembles the WASP record of the 1988 aftershock (depth = 9 km), not that of the 1988 mainshock (depth = 6 km). This is in contrast to the displacement records just discussed, suggesting that the short-period energy originated closer to the location of the 1988 aftershock. Considering the effect of source depth on the phases S_0 and S_1 discussed in Dreger and Helmberger [1990] it appears that the short-period energy originated at a greater depth than the longer period energy, suggesting the existence of an asperity at depth.

If one examines the direct P-waves on the radial and vertical component WASP

Comparison of 1990 Upland Mainshock and 1988 Events

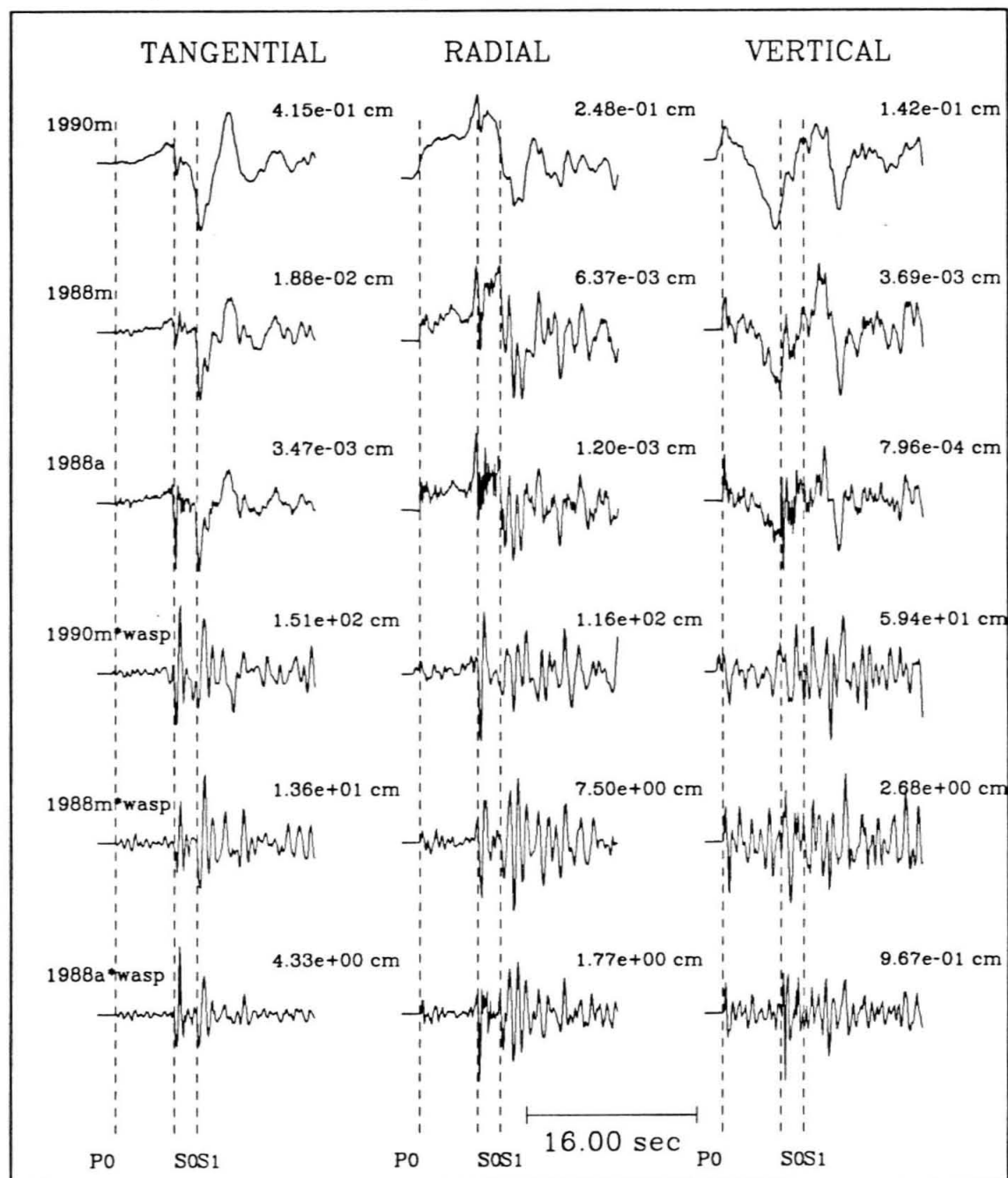


Figure 3.15: Three-component displacement data for the February 28, 1990 (1990m), June 26, 1988 (1988m) and July 6, 1988 (1988a) Upland earthquakes. "*wasp" refers to the respective displacements convolved with the short-period Wood-Anderson instrument response. The labels P_0 , S_0 and S_1 mark the arrival times of direct P, direct S and multiple S. The amplitudes are in centimeters.

records there is clearly a double pulse for the 1990 mainshock compared to the single pulse observed for both the 1988 mainshock and aftershock. This indicates that the 1990 mainshock is indeed more complicated than a simple point-source with a simple time function. In order to align the tangential data along S_0 and S_1 arrival times it was necessary to advance the 1990 mainshock 0.4 seconds. The line showing P_0 is aligned on the first arrival P-waves of the 1988 data. The P_0 line aligns with the second pulse of the P-wave for the 1990 mainshock. This suggests that a second source follows the first arrival by about 0.4 seconds. On the tangential component there is also a relatively large phase before the line S_0 compared to the 1988 data which may be due to a complicated source. To address this apparent complexity, we examine double point-source models and distributed fault models.

3.2.3 Point Source Models

As discussed earlier the two fault plane solutions determined from first motion polarities and the depth distribution of aftershocks for the 1990 mainshock indicate that this event occurred on a steeply dipping plane. To provide further constraints and to obtain an estimate of the long-period source time function and seismic moment we invert the three-component displacement data convolved with a Press-Ewing instrument response. The method we employ is that of Liu and Helmberger [1985] in which the fault plane parameters (strike(θ), dip(δ) and rake(λ)) are iteratively solved for in a least squares sense using an amplitude sensitive error function defined as

$$e_i = \int_0^T [f_i(t) - g_i(t)]^2 dt \quad (3.1)$$

where $f_i(t)$ and $g_i(t)$ are the data and synthetic for the i^{th} component and T is the length of the record being inverted. Seismic moment and time function are determined by mapping the error space and determining the combination of parameters that minimizes the error defined by equation 3.1. The whole waveform is used in the

inversion. A more detailed description of the method and resolution capabilities is given in chapter 2.

Source depths of 4.5, 6, 7, and 8 km were tested and a source depth of 6 km gave the lowest errors. Using this source depth a best-fitting long-period point-source solution of $\theta = 216^\circ$, $\lambda = 5^\circ$, $\delta = 77^\circ$, $M_o = 2.5 \times 10^{24}$ dyne-cm, and a source duration (τ) of 1.2 seconds was obtained. Helmberger and Malone [1975] define τ as $(0.5\delta T_1 + \delta T_2 + 0.5\delta T_3)$, where the δT 's represent the length of the positive, zero and negative slopes of a trapezoidal time function. For simplicity we limited the trapezoidal time function to the case where the δT 's are all the same value.

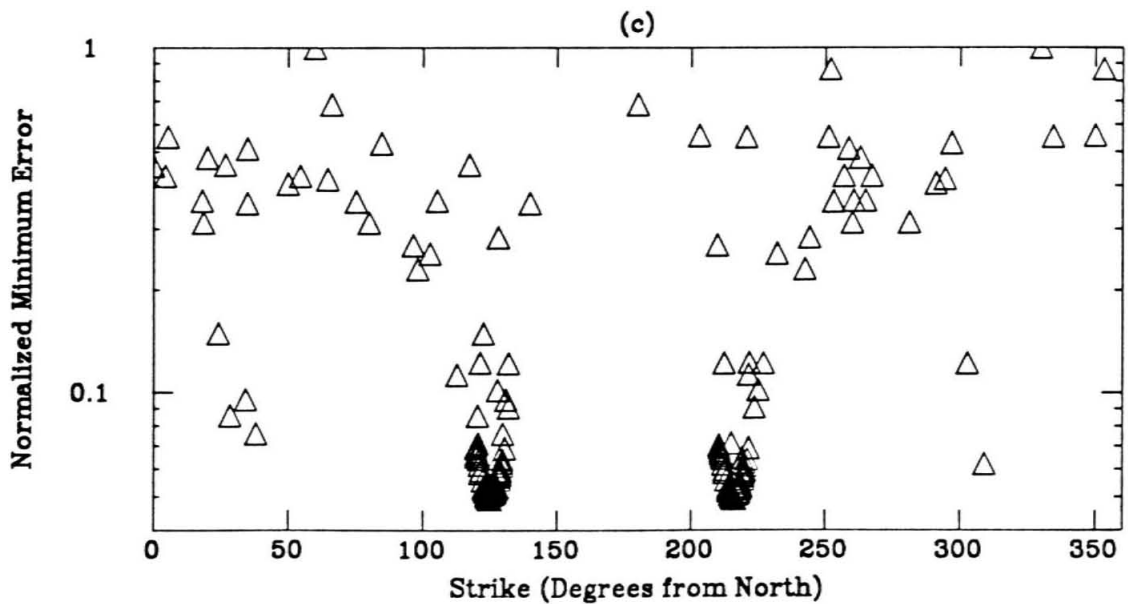
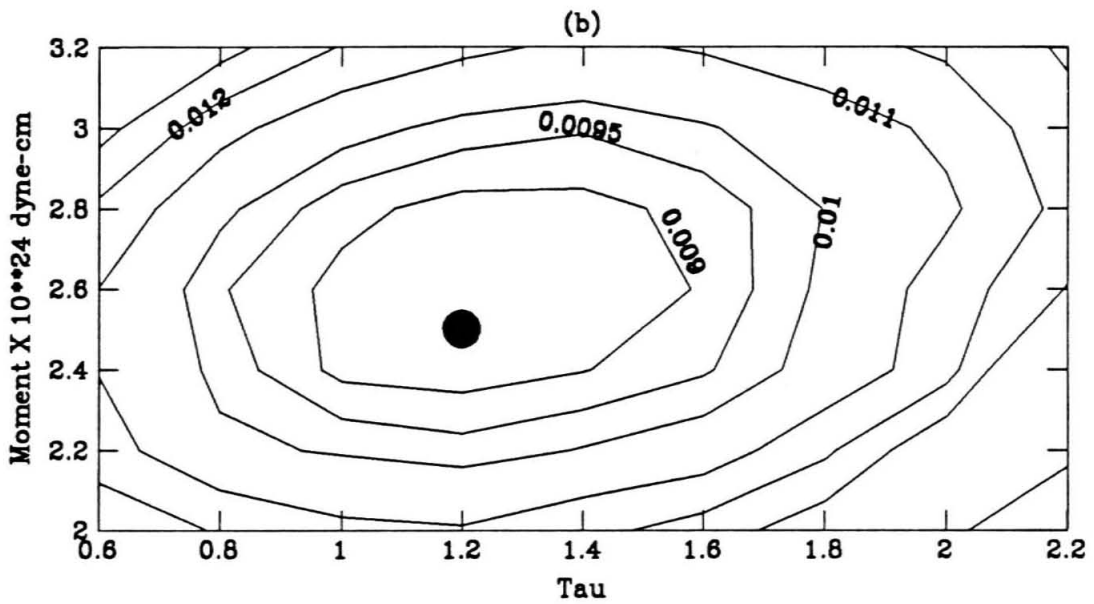
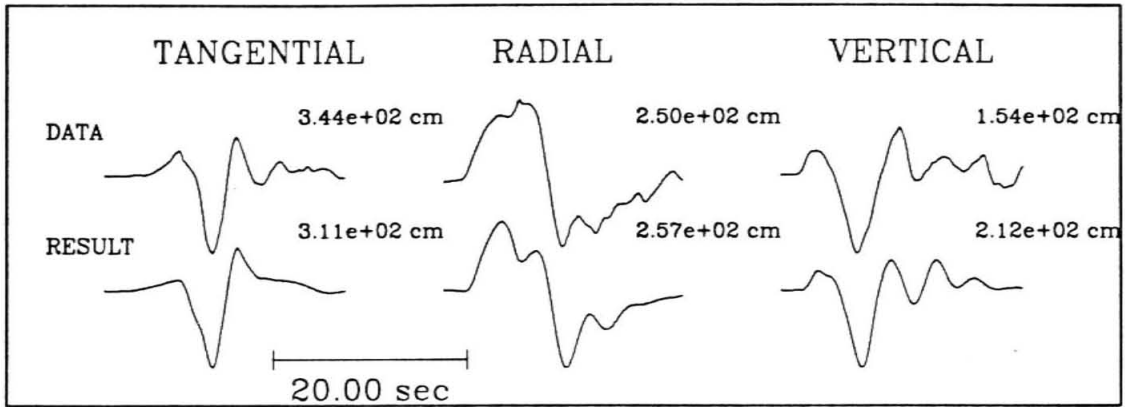
Figure 3.16a compares the data to synthetic waveforms determined by the inversion. The waveforms are in good agreement in both wave-shape and amplitude. Figure 3.16b is a plot showing the error as a function of both moment and τ . The lowest error occurs for a moment of 2.5×10^{24} dyne-cm and a $\tau = 1.2$ seconds. The region of lowest error indicates that τ can range from 1.0 to about 1.5 seconds and seismic moment can range from 2.4×10^{24} to 2.8×10^{24} dyne-cm. An alternative definition of duration (τ) for a circular fault after Brune [1970], is

$$\tau = \frac{2.62a}{\beta} \quad (3.2)$$

where a is the radius of a circular fault and β is the shear velocity in the vicinity of the source [Cohn et al., 1982]. The range in τ gives values of 6 to 13 km^2 for the area of a circular fault. This is much less than suggested by the aftershock distribution (Figures 3.14ab) for which an area of 40 km^2 is obtained. Figure 3.16c shows the behavior of the fitting error to the model parameter θ . Similar plots for δ and λ show that the solution is also unique for these parameters.

As discussed in the last section there is some evidence that the mainshock was a relatively complicated event. To address this possibility several single and double point-source models were considered as shown in Figure 3.17. The synthetics were computed using the fault plane solution and seismic moment obtained above. The

Figure 3.16: Long-period inversion results. (a) compares simulated Press-Ewing data with synthetics determined by a three-component waveform inversion. The amplitudes are in centimeters. (b) Misfit error defined by equation 3.1 as a function of seismic moment and source duration (τ). The filled circle marks where the lowest misfit error occurs. (c) Normalized minimum error as a function of strike (θ) for the moment and τ indicated by the circle in (b). Each triangle represents the error of a single iteration, where both the auxiliary fault plane and the fault plane determined by the inversion are plotted. Four starting fault plane solutions were used in these calculations. The inversion results are: $\theta = 216^\circ$, $\lambda = 5^\circ$, $\delta = 77^\circ$, and $M_o = 2.5 \times 10^{24}$ dyne-cm.

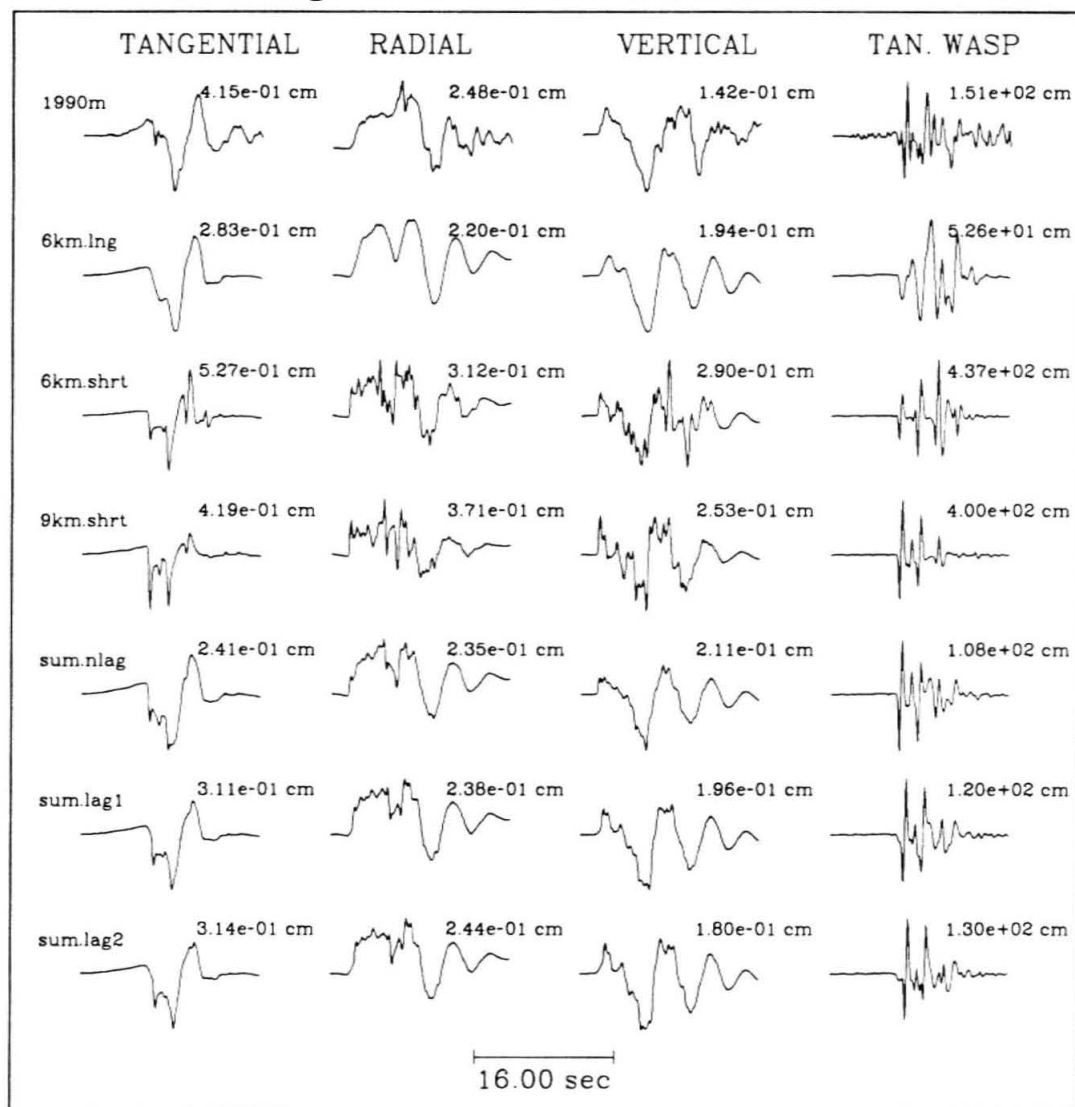


top trace shows the 1990 three-component displacement and the tangential WASP data. The first synthetic shown (6km.lng) is for a source depth of 6 km and a long-period trapezoidal time function with $\tau=1.2$ seconds. These synthetics explain the observed durations of S_1 and the Love wave well, but are enriched in long-period energy as compared to the data. Both the phase S_0 in the tangential displacement data, and the tangential WASP waveform are poorly modeled by the long-period source time function. Next we compare synthetics with a source depth of 6 km and a shorter time function (6km.shrt) with the data. For this model a trapezoidal time function with $\tau=0.3$ seconds is used. Here the phase S_0 on the tangential component is fairly well modeled, but the rest of the synthetic displacement waveforms are generally too short-period. The frequency content of the WASP record seems to be correct, although the synthetic waveform is in poor agreement with the data. Next synthetics computed using a source depth of 9 km (9km.shrt) and the short-period time function used above in model 6km.shrt are compared with the data. The displacement synthetics clearly do not fit the displacement data, however the tangential WASP record is well modeled by the 9 km source depth, and the period of the WASP synthetic matches that of the WASP data.

Summarizing, the inversion of the three-component long-period waveforms results in a fault plane solution that is compatible with that obtained by Hauksson and Jones [1991]. The minimum in the waveform fitting error for τ between 1.0 and 1.5 seconds shows that an upper bound for the fault area is about 13 km^2 , which is much less than is suggested by the aftershock distribution (Figure 3.14ab), indicating that perhaps the mainshock did not rupture the entire area of the aftershock zone. For reference, a circular fault with a τ of 2.0 seconds yields from equation 3.2, an area of 22 km^2 which is still only 56 % of the area defined by the aftershock zone. Comparison of the displacement data to displacement synthetics computed with the source parameters obtained by the inversion of long-period waves shows that the displacement records,

Figure 3.17: Three-component displacement and tangential component WASP data for the February 28, 1990 mainshock, and single (6km.lng, 6km.shrt, and 9km.shrt) and double (sum.nlag, sum.lag1, and sum.lag2) point source synthetics. The synthetics were computed using an F-K integration method, and the focal mechanism and seismic moment determined by inverting the long-period waves (Figure 3.16). See the text for details of the source time functions and lag times used. The amplitudes are in centimeters.

Single and Double Point Source Models



with the exception of the phase S_0 , are better modeled by a point-source with a source depth of 6 km and a relatively long-period time function ($\tau=1.2$ seconds). The tangential WASP data however, is better modeled using a point-source at 9 km depth and a shorter period time function ($\tau=0.3$ seconds).

To examine the possibility of a double source we simply added the 6km.lng and 9km.shrt synthetics together with various time lags and amplitude weightings following a trial-and-error procedure. It was found that the deeper source (9km.shrt) with about 30 percent of the total seismic moment release worked reasonably well. The amplitude ratio of the tangential WASP to the tangential displacement, for which the data has a value of about 360 was used as a constraint. The long-period point-source model under estimates this value by a factor of about two, while the short-period point-source synthetics over estimate it by more than a factor of two. For reference the 1988 mainshock and aftershock have values averaged over the three-components equal to 880 and 1310, respectively. In the following double point-source models we use the 30 % weighting value and demonstrate the effects of shifting the sources in time. The long-period moment estimate obtained earlier is the total moment used in the double point-source models.

The first model (sum.nlag) has no time lag between the two point-sources. This model exhibits a reasonable fit to the data. The long duration of S_1 and the Love wave is maintained while S_0 is shorter period. The tangential WASP is also well modeled and the WASP to displacement ratio is about 440. The second model (sum.lag1) considers the case where the 9 km deep source is lagged in time by 0.5 seconds. This synthetic fits better than the case with no time lag because of improvements to the shape of direct P (P_0), in which there is a break in slope on the displacement P waveforms as observed in the data. The timing between S_0 and S_1 is also good. In addition, the two distinct S_0 phases observed in the data are beginning to separate in the synthetics and the phase S_0 is distinctly sharper than the phase S_1 and the Love

wave. The WASP to displacement ratio is about 370. The third model (sum.lag2) is a summation in which the deeper source is lagged by 0.75 seconds. The shape of direct P (P_0) on the radial and vertical components is well modeled as are the three-component displacement records. In addition, the tangential WASP is very well modeled. Two S_0 phases are produced, and the WASP to displacement ratio is about 400. With increasing lag time between the sources however, the separation of S_0 and S_1 becomes too small. This is due to interference of the S_1 phases for the long and short-period sources. Since the S_0 phase for the long-period source is rather subdued, the addition of the short-period source does not produce the same kind of interference for S_0 . The waveforms in Figure 3.17 demonstrate that simple, single point-source models do not adequately model the data and that a double point-source model better explains both the long and short-period waveform data. This is similar to the result of Kanamori et al. [1990] in which they found that to explain both the long-period and short-period phases recorded for the December 3, 1988 Pasadena earthquake recorded at PAS, two time functions were needed. In particular a long-period time function was needed to explain the near-field displacements but it failed to model the far-field pulses which required a shorter period time function.

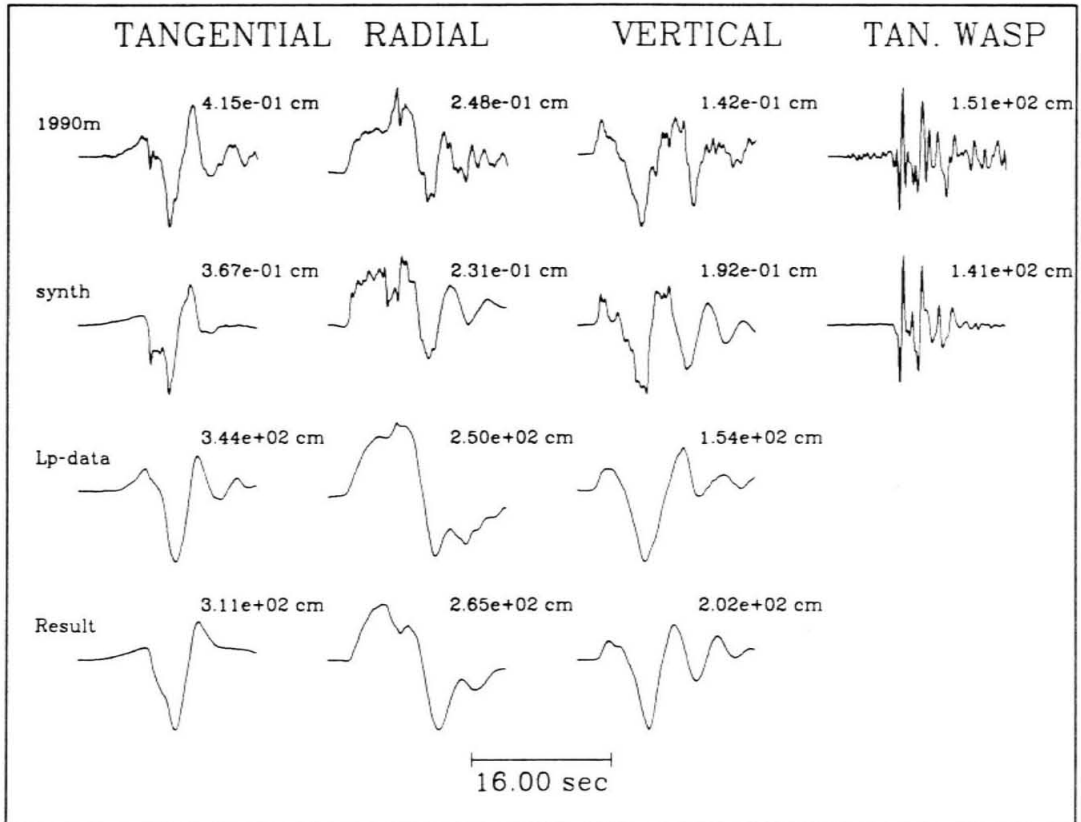
Judging from models sum.nlag and sum.lag1 the time lag of the second, deeper source could be between 0.0 and 0.5 seconds, although the 0.5 second value is close to the time shift used to align the 1990 data in Figure 3.15. The case where there is no lag time could mean that the deeper, short-period event is not directly related to a propagating rupture front but a subevent more closely akin to an aftershock. The case where there is a lag time could be as above but may also be due to an asperity triggered by a propagating rupture front. The next section examines the second case in more detail.

Before moving on to the distributed fault models it is interesting to use the double point-source model sum.lag1, in the long-period waveform inversion to see

the effect on the orientation and moment estimate. It is assumed that both the long-period and short-period sources have the same orientation. Figure 3.18 shows the results of this inversion. Visually the fit to the long-period data is as good as in Figure 3.16a, however there is a slightly larger waveform fitting error. The wave-shapes and amplitudes show little change at long-periods and the inversion results in only a slightly different solution where $\theta = 215^\circ$, $\lambda = 6^\circ$, $\delta = 74^\circ$ and $M_o = 2.5 \times 10^{24}$ dyne-cm. The differences are only a 1° change in strike (θ) and rake (λ), and a 3° change in dip (δ). Comparing the displacements and tangential WASP data to synthetics computed with this solution, however, produces better agreement in maximum amplitudes. Thus, the addition of a second, short-period source doesn't appreciably affect the fault plane solution obtained by inverting the long-period waves, but results in better agreement with the displacement and WASP data.

Figure 3.18: Long-period inversion using the sum.lag1 Green's functions. 1990m is the 1990 mainshock displacement and tangential WASP data. "synth" are the predicted displacements and tangential WASP computed with a mechanism determined by inverting the long-period data using the sum.lag1 Green's functions. "Lp-data" is the simulated Press-Ewing data and "Result" is the Press-Ewing synthetic determined by the inversion. The inversion results are: $\theta = 215^\circ$, $\lambda = 6^\circ$, $\delta = 74^\circ$, and $M_o = 2.5 \times 10^{24}$ dyne-cm. The amplitudes are in centimeters.

Inversion Results for Double Source



3.2.4 Distributed Fault Models

The point-source models just discussed are useful in that they accurately model the three-component displacement and tangential WAMP waveforms. The best double point-source model uses a time lag of 0.50 seconds between the shallow and deep sources. Next we would like to determine if such a lag time between the shallow and deep sources is physically possible given the orientation of the fault and a reasonable rupture velocity. We investigate the dimensions of the distributed fault and attempt to constrain the size of the deep asperity using the distributed finite fault summation technique after Hartzell [1978] and Heaton and Helmberger [1979]. This method operates on the premise that distributed fault slip can be approximated by a summation of small sub-fault slips (point-sources convolved with the rise time of a subfault). Using equation 3.2 and assuming that each subfault source fills the interstitial spaces in the grid yet minimizing overlap we assume $a = w/\sqrt{2}$ where w is the length of a subfault side. We use a grid spacing of 0.25 km and a triangular time function with a duration (τ) of 0.14 seconds is convolved with the subfault Green's functions. Because the distance between the fault and PAS is large compared to the length of the fault it is assumed that the changes in the azimuth from each element on the fault to the station are small. All of the distributed fault models shown here use the orientation of the fault plane solution and the moment obtained from the inversion of the long-period waves in which the double point-source Green's functions were used. A rupture velocity of 3.0 km/s (85 % of the shear wave velocity in model LOHS1) is assumed. We use the locations of aftershocks (Figures 3.14ab) to obtain the initial dimension of the distributed fault and the location of the hypocenter. Figure 3.14 shows that the hypocenter is centered laterally and is near the top of aftershock distribution. Based on these observations we use a laterally centered hypocenter located at a depth of 6 km. The top of the fault is also located at 6 km depth. Slip complexity on the fault is accomplished by differentially weighting

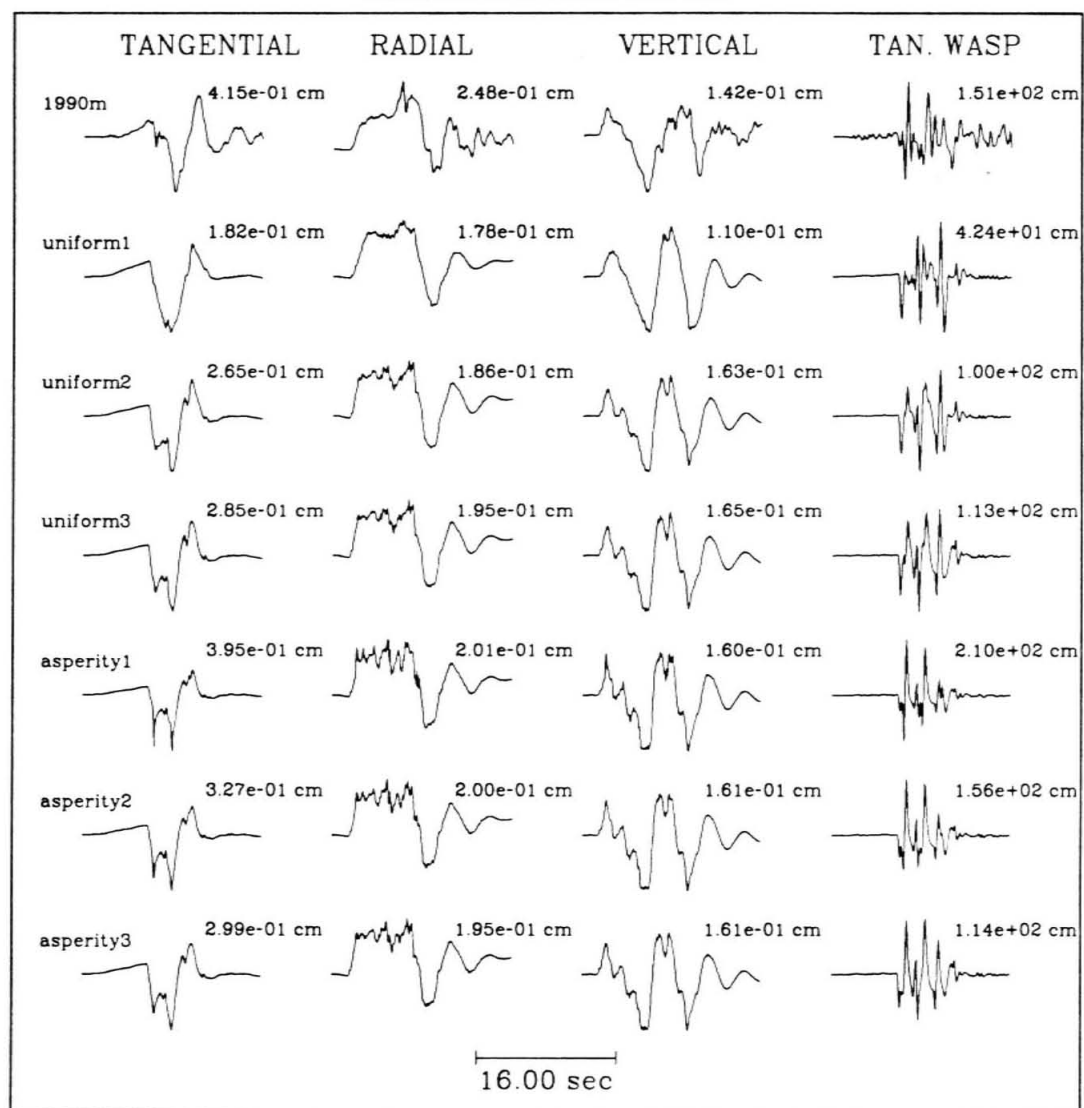
each of the sub-faults. These subfault weights are determined in a forward modeling sense.

Figure 3.19 shows the results of the distributed fault modeling. The top row displays the three-component displacement and tangential WASP data as in Figure 3.17. The first model (uniform1) was computed using a 5 by 7 km (length by width) fault. The moment and fault plane solution obtained in the last section was used and all of the subfault weights are equal to describe uniform slip. This model does a poor job in fitting the displacement and WASP data. Furthermore the moment of 2.5×10^{24} dyne-cm is not large enough to produce the amplitudes observed in the data. The next model (uniform2) is also a uniform rupture model with a dimension of 5 by 3.5 km and does a much better job in modeling the displacement data. The maximum amplitudes are still too small but there is good agreement in the displacement waveforms. The tangential WASP synthetics fail to fit the data. To increase the amplitudes and to use an area similar to that suggested by the long-period waves (less than 13 km^2) a 3.5 by 3.5 km fault (uniform3) was tried. This fault increases the amplitudes slightly and the displacement waveforms are fairly well modeled, however the phase S_0 is too long-period and the tangential WASP is still not satisfactorily modeled. Other uniform fault models with smaller areas were tested and they resulted in larger amplitudes but they show little improvement in explaining both the long-period and short-period data simultaneously. The progression though, from a 5 by 7 km fault to a 3.5 by 3.5 km fault shows that a distributed fault model with a smaller area agrees with the earlier result obtained from the long-period waveform inversion.

One of the purposes of using the distributed fault models was to examine whether or not the time lag of 0.5 seconds found earlier is physically possible using a reasonable rupture velocity. Much of the area southwest of the hypocenter (the area between the epicenter and B' on Figure 3.14) has lag times less than 0.6 seconds

Figure 3.19: Three-component displacement and tangential component WASP data for the February 28, 1990 mainshock, and distributed finite fault synthetics. The moment and fault plane solution determined by using sum.lag1 Green's functions (Figure 3.18) was used. Profile BB' (Figure 2.14a) shows the orientation of the finite fault relative to the aftershock zone. The hypocenter is centered laterally and located at the top of the fault, at a depth of 6 km. 1990m is the displacement and tangential WASP data. "uniform1" is a uniform slip model with fault dimensions of 5 by 7 km (length by width). "uniform2" is a uniform slip model with fault dimensions of 5 by 3.5 km. "uniform3" is a uniform slip model with fault dimensions of 3.5 by 3.5 km. "asperity1" is a distributed slip model with a 0.25 km^2 asperity releasing 30 % of the total moment. The center of the asperity is located at 0.875 km southwest of the hypocenter at a depth of 8.5 km. "asperity2" is a distributed slip model with a 1.0 km^2 asperity releasing 30 % of the total moment. "asperity3" is a distributed slip model with a 2.25 km^2 asperity releasing 30 % of the total moment. Both "asperity2" and "asperity3" are centered at the same location as "asperity1". The amplitudes are in centimeters.

Distributed Fault Models



when a rupture velocity of 3 km/s is used. The following three models use the fault area of model uniform3 and asperities containing 30 % of the total moment are centered 0.875 km southwest of the hypocenter at a depth of 8.5 km. The first model asperity1, uses an asperity with an area of 0.25 km^2 . This model produces arrivals that are too short-period, but the synthetic WASP waveform is in good agreement with the data. The model asperity2, uses an asperity with an area of 1.0 km^2 . This model produces a reasonably good fit to both the displacement and WASP data. The shape of direct P on the radial and vertical components compares well with the data in that the seismogram begins with a gentle slope and later steepens. The tangential WASP synthetic and data are in good agreement but there is a problem with the ratio of WASP to displacement maximum amplitudes where the synthetic value is too large. Reducing the moment of the asperity would correct this ratio. The next model (asperity3) uses an asperity with an area of 2.25 km^2 . This model produces good waveform fits to both the displacement and WASP data however the tangential and radial amplitudes are lower than in the data. There is some broadening of S_0 in both the displacement and WASP synthetics and this model probably represents an upper bound for the size of the asperity.

The relatively low amplitudes in the distributed fault models could be due to directivity that we did not consider. All of our calculations assume bilateral rupture horizontally. To better understand lateral directivity it would be necessary to use multiple stations with good azimuthal coverage, and of course Green's functions for the paths to these stations that accurately model the source depth dependence in the data. In addition, the amplitudes would increase if the mainshock ruptured an area smaller than used in model uniform3 with an asperity located on the periphery or beyond the region of the mainshock slip. Furthermore small changes in fault orientation could affect the amplitudes and waveforms of the short-periods while having little affect on the long-periods. Additional complexities we did not consider

and would not be able to resolve with single station data are multiple slips, variable rupture velocity, complicated subfault time functions and any combination of these. The number of parameters in the simplified distributed finite fault model we use, and the levels of complexity neglected make this problem tremendously non-unique. While these distributed fault models do not produce synthetics that fit better than the double point-source models they do lend support for the small faulting area suggested by the long-period data and the timing of the second point-source in model sum.lag1.

3.2.5 Discussion and Conclusions

The availability of Green's functions for the path from Upland to Pasadena, California, provided an opportunity to invert the long-period, three-component waveform data recorded at PAS for source information. The long-period source of the 1990 Upland mainshock had a strike (θ) of 216° , rake (λ) of 5° , dip (δ) of 77° , moment of 2.5×10^{24} dyne-cm, and a duration (τ) of 1.2 seconds. The depth was relatively shallow at about 6 km. The above fault plane solution and source depth are in good agreement with the results of Hauksson and Jones [1991]. This result is important in that it demonstrates the power of using three-component, broadband, high-dynamic range data in source studies of large historic and future earthquakes where smaller, simpler events are available to determine crustal Green's functions to calibrate various paths.

The epicenters of the three events discussed in this paper plot close to the inferred trace of the Cucamonga fault. In this area the Cucamonga fault bends to the south with a strike of about 225° from north, which is consistent with the four focal mechanisms in Table 3.2 and the mechanism determined in this paper. The dip of surface exposures located east of the Upland source region on the Cucamonga fault are about 35° to the north [Cramer and Harrington, 1987]. The primary prob-

lems with the Cucamonga fault being the causative structure is that the observed dip of the aftershocks (Figure 3.14) and the dips of the fault plane solutions are much steeper. Furthermore, Hauksson and Jones [1991] point out that the aftershock zone lies southeast of the inferred trace of the Cucamonga fault and projects to the location of the San Jose fault. It must be noted however, that the location of the Cucamonga fault in this area is inferred, and concealed by alluvial deposits. It is possible the pronounced change in strike mentioned above is accompanied by a steepening of dip.

The San Jose fault to the east of the epicentral location (Figure 3.14a) is a likely candidate as the causative structure. The southern extension of the San Jose fault, within the San Jose Hills shows left-lateral offset [Cramer and Harrington, 1987]. The location of the northern portion of the San Jose fault is inferred from basement topography in which the southeast side is faulted down relative to the northwest side [Jennings, C. W., 1975; Yerkes et al., 1967], and from ground water barriers [California Dept. Water Res., 1970]. Our fault plane solution is consistent with the vertical sense of motion on the fault in that it shows a slight thrust component in which the northwest side is up relative to the southeast side. The thrust component is small however and the motion is predominantly left-lateral strike-slip. The Upland earthquakes occurred in a complicated region in which there are several inferred faults in close proximity and unfortunately there are no surface exposures of the event to confirm the sense of slip on the fault. It is possible that the apparent vertical offset across the San Jose fault could be due to strike-slip faulting of an irregular surface.

Both the point-source and distributed fault models require a complicated rupture which includes an asperity at 8-9 km depth. The ratio of tangential displacement amplitude to tangential WASP amplitude help to constrain the size of the asperity to be about 30 % of the total moment. Assuming a circular fault for the asperity stress drop is defined as $\Delta\sigma = 7M^o/16a^3$ [Kanamori and Anderson, 1975], where $\Delta\sigma$ is

the stress drop in dyne-cm^{-2} , M_0 is the seismic moment and a is the fault radius as defined in equation 3.2. The models *sum.lag1*, *asperity1* and *asperity2* have greater than 1 kbar stress drops for the asperity. The stress drop obtained from the seismic moment and area determined by the inversion of long-period waves is 265 bars. The distributed fault models with uniform slip indicate that the fault area was smaller than the aftershock zone. Using a rupture velocity of 3.0 km/s and the long-period fault orientation it is possible to have a lag of 0.5 seconds for an asperity located at 8 to 9 km depth as suggested by the double point-source modeling. Similar results were also obtained using a rupture velocity of 2.8 km/s.

It is interesting to compare the depth distribution of aftershocks (Figure 3.14b) with the location of the asperity and the source area determined by inverting the long-period waves. Figure 3.14b shows that at 9 km depth there is a change in the dip of the fault. Below 9 km depth there are two trends. One continuing with a steep dip and the other with a shallower dip. The shallow dip lies north of the line AA' and the steeper dip lies to the south of AA' [Hauksson and Jones, 1991]. The changes in dip of the fault at this depth could be a source of stress accumulation as evidenced by the large stress drop of the asperity. Additional evidence is a clustering of the larger aftershocks at this depth. Hauksson and Jones, [1991] report that there is not an obvious gap in aftershocks along strike when aftershocks of all sizes are considered. They point out however, that for events larger than magnitude 3.8 there appears to be a gap extending from 5 to 11 km depth. When considering all of the events (their figure 6) it appears that there is a relatively small gap (1 km^2) at 10 km depth slightly southwest of the epicenter. Mendoza and Hartzell, [1988] report that gaps in aftershock distributions correlate well with areas that experience the greatest slip during mainshock rupture. Furthermore, the best fitting long-period point-source solution gives a source duration of 1.2 seconds which according to equation 3.2 corresponds to an 8 km^2 fault. This is a factor of 5 smaller than the area of the

aftershock zone. The distributed fault models with uniform slip also indicate that the fault area was smaller than the aftershock zone. Thus our modeling results argue that the mainshock did not rupture deeper than 9 km depth. It is possible that the observed fault complexity at this depth inhibited the propagation of the mainshock rupture front.

There is also a rather abrupt termination of aftershocks above 4 km depth. The velocity model LOHS1 from which we calculated our synthetics has an interface at this depth in which there is about a 25 % reduction in S-wave velocity. In comparison, the more regional velocity model SoCal (Table 3.1), used to locate the events and to determine fault plane solutions has its shallowest interface at 5.5 km. Artifacts introduced into the locations of the hypocenters would occur at the depth of this interface and not shallower as observed [Hauksson and Jones, 1991]. Thus, the abrupt termination of aftershocks at about 4 km depth could represent a change in material properties, perhaps caused by a lack of strength.

In conclusion, the use of broadband waveform data compliments first motion studies by providing additional constraints to focal depth and focal mechanism determinations as demonstrated in this study. With the continued installation of broadband stations, effort needs to be directed at developing Green's functions from potential source regions to these stations. Such a calibrated network will have the potential for quick assessment of strong earthquakes, as well as providing the detailed information needed to better understand source physics.

Chapter 4

The 1991 Sierra Madre Earthquake

4.1 Inversion of Long-Period Body Waves

4.1.1 Introduction and Data Analysis

On June 28, 1991 at 14:43:54 (GMT) a $M_L=5.8$ earthquake occurred approximately 21 km northeast of Pasadena, California. The event was located at 34.261° north latitude and 117.996° west longitude at a depth of 12 km (E. Hauksson, personal communication). This is the first sizable earthquake to be recorded by six stations of the broadband, high dynamic range TERRAScope array. Figure 4.1 shows the location of the the event and the TERRAScope stations. Table 4.1 lists the distances and azimuths from the event to each station.

Remarkably, four of the stations (GSC, ISA, PFO and SBC) were located at 159.2 ± 0.7 km from the event. Observations from three of the stations namely GSC, ISA and PFO display strong similarities in waveform and are also quite similar to synthetics computed using standard southern California velocity models.

It is interesting to compare the broadband displacement data recorded at GSC, ISA and PFO with displacement synthetics (Figure 4.2) to demonstrate the use-

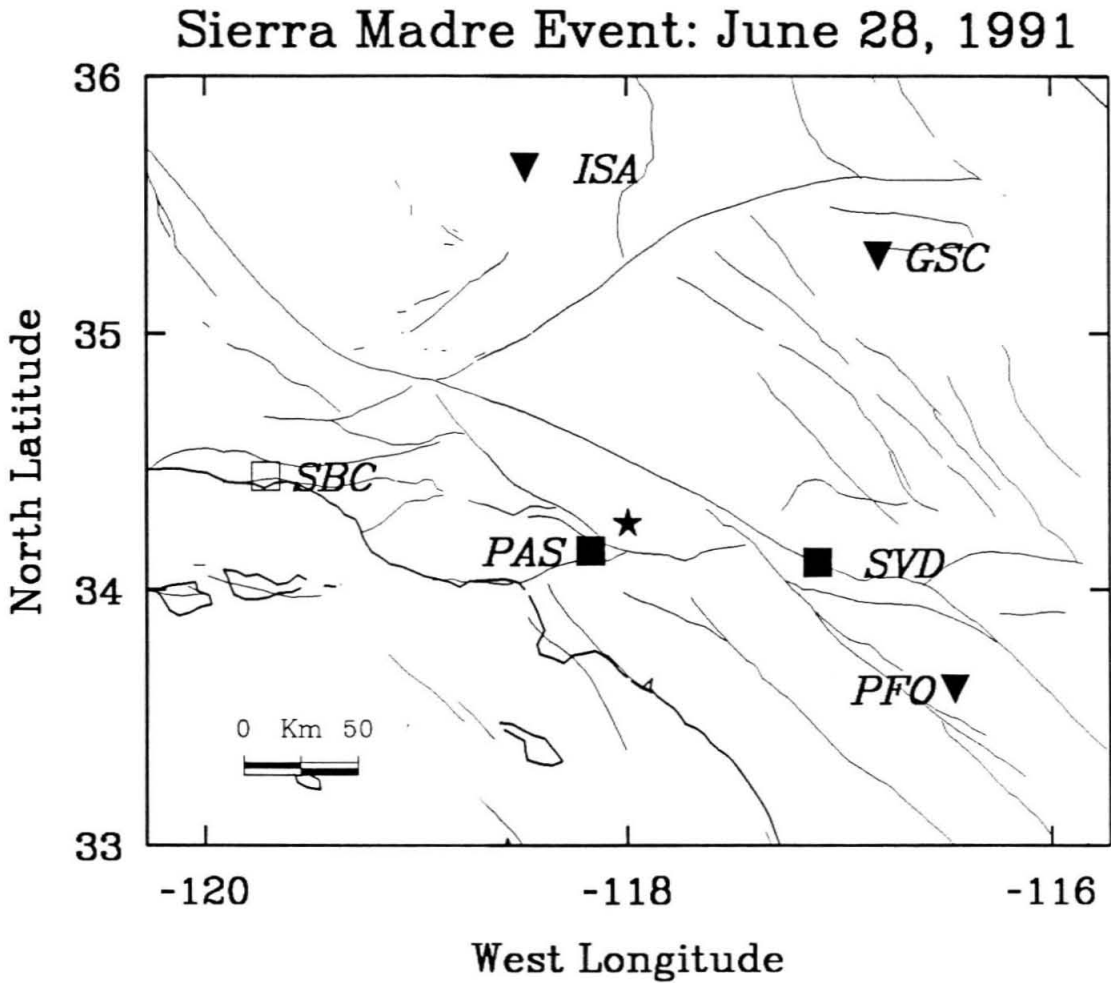


Figure 4.1: Generalized map of southern California showing the location of the Sierra Madre earthquake (star) and the stations used in this study. Stations represented by solid inverted triangles and solid squares were used in the inversion. SBC (open square) was not used.

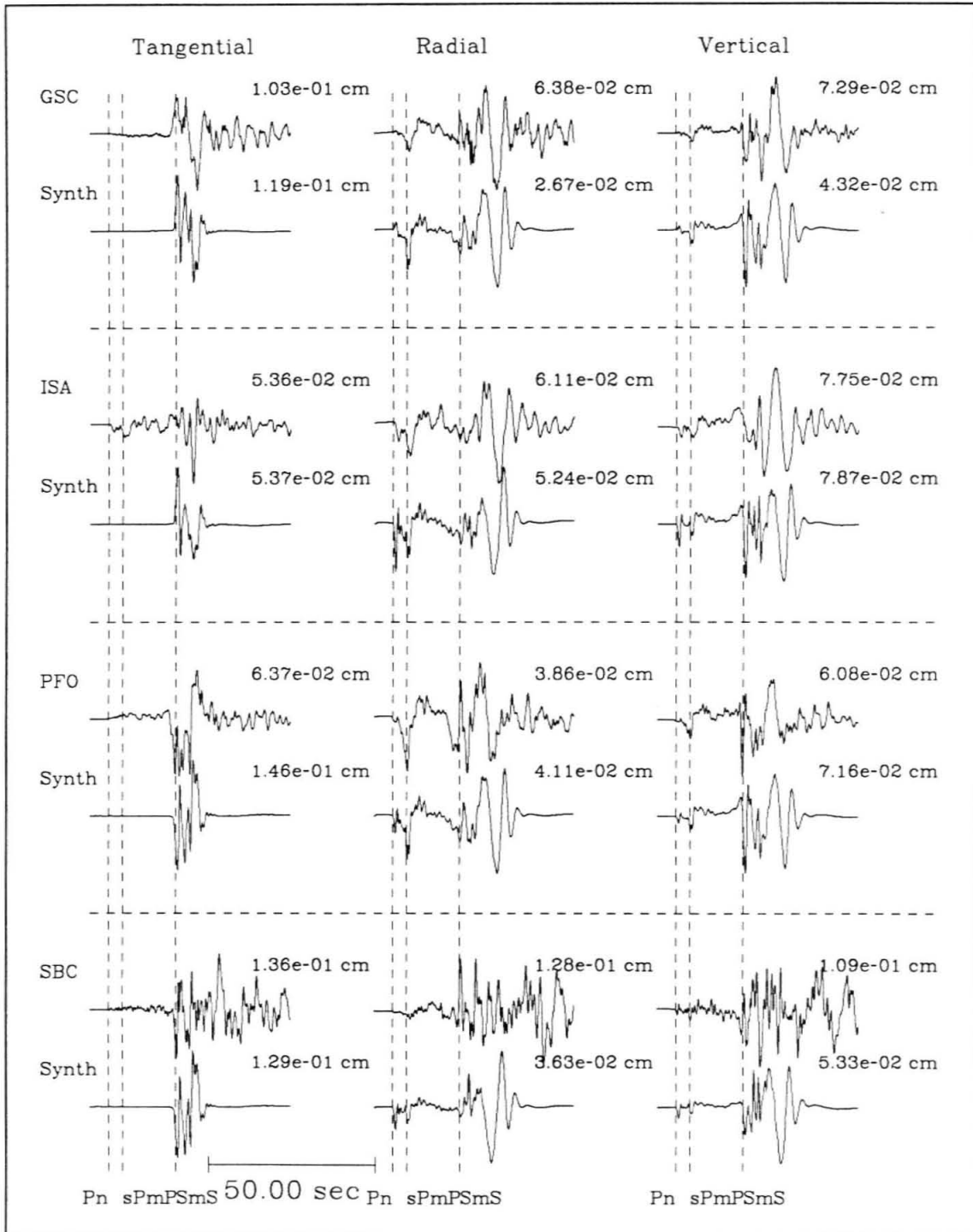
Station	Lat. (N)	Lon. (W)	Dist. (Km)	<i>Azi.</i> ¹
GSC	35.300	116.810	158.2	44
ISA	35.643	118.480	159.6	344
PAS	34.148	118.172	20.6	232
PFO	33.609	116.455	159.6	117
SBC	34.442	119.713	159.4	277
SVD	34.104	117.098	84.4	102

Table 4.1: Station Locations. (1) Azimuth to the station in degrees.

fulness of a one-dimensional velocity model in explaining the data. The synthetics were computed using an F-K integration method, the SC velocity model (Table 4.2), and the source parameters obtained in this study as discussed in the next section. The synthetics have been delayed 0.35 seconds in order to align them with the first arrival. The variation in P_n travel-time is less than 2 % of the average travel-time of 26.2 seconds. For S_n the variation is less than 3 % of the average travel-time of 44.6 seconds. The short-period phase sP_mP is well modeled for all of the stations, and S_mS is a strong arrival in both the GSC and PFO data. S_mS in the synthetics has the correct relative travel-time for station GSC, but arrives a little too late at PFO, indicating small differences in travel path. The surface waves are relatively well modeled at stations GSC and PFO but they show the largest variation in arrival time. The surface waves at SBC are delayed by approximately 10 seconds compared to GSC, ISA and PFO which is most likely due to the multipathing of energy through the San Fernando and Ventura basins. The best fits are for the longer period waves arriving between P_n and S_mS . These waves are composed of an interference of P to S

Figure 4.2: Comparison of broadband displacement and synthetic seismograms computed with the fault plane solutions obtained in this study. Amplitudes are ground displacement in centimeters.

Comparison of Broadband Data and Synthetics



LOHS1			SC				
V_P	$V_S\rho$	Z	V_P	V_S	ρ	Z	
4.5	2.6	2.4	0.0	5.5	3.18	2.4	0.0
5.9	3.5	2.67	4.0	6.3	3.64	2.67	5.5
6.6	3.8	2.8	16.0	6.7	3.87	2.8	16.0
8.0	4.1	3.1	26.0	7.8	4.5	3.0	35.0
8.2	4.2	3.3	30.0				

Table 4.2: One-Dimensional Velocity Models.

and S to P converted head waves that propagate along the interface of the shallowest layer and those that propagate along the top of the mantle. The latter type, commonly referred to as PL waves, are relatively insensitive to short wavelength crustal heterogeneity [Helmberger and Engen, 1980 ; Wallace et al., 1981], and are therefore useful in determining the source parameters of earthquakes. Generally the synthetics agree well with the data in terms of amplitudes and waveforms. For station GSC however the radial and vertical component synthetics under-predict the amplitudes, which could be due to a slightly different crustal model or site effect. We filtered the data with a Press-Ewing instrument response and inverted only the long-period crustal body waves from P_n to just after the S_mS arrival to minimize errors due to misalignment of the short-period body waves and the surface waves. For station PAS however, the entire displacement records were used.

4.1.2 Inversion Results

Since the stations GSC, ISA and PFO displayed such similarity in waveform we performed two inversions. The first used only stations GSC, ISA and PFO. The

second included stations PAS and SVD. Station SBC was not used in the inversion because of additional complexity observed in the data due to propagation and site effects. We use the inversion method described in detail by Liu and Helmberger [1985], and modified to invert local and regional body waves recorded by sparse networks [Dreger and Helmberger, 1992]. Generally, the method can be described as a least squares inversion, parameterized using an L2 norm (see section 2.3). This parameterization allows the inversion to be sensitive to both the amplitudes and the waveforms. The method is non-linear and requires iteration on a starting model. Uniqueness of the solution is determined by using a number of starting models and by graphically examining the model parameter space. For stations GSC, ISA, PFO and SVD we used model SC (Table 4.2) to compute the Green's functions. For PAS we used model LOHS1 (Table 4.2) determined by modeling local earthquakes occurring to the east of Pasadena. A number of different source depths were tried (9 to 13 km) with the best results obtained using a source depth of 11 km. We used a triangular source time function with a duration of 1 second, that was determined by measuring the width of the tangential component direct S-wave recorded at PAS. Since PAS was only 21 km from the epicenter, attenuation is negligible and the width of the direct S-wave is a good approximation to the source time function.

The results of both inversions give a strike of 235° , rake of 74° , dip of 50° and a seismic moment of 2.5×10^{24} dyne-cm. Figure 4.3 compares the data to synthetics calculated using these parameters. There is good agreement in amplitude and in waveform for all of the stations. Figure 4.4 shows the seismic moment as a function of error. There is a pronounced minima and the lowest errors were obtained with the seismic moment reported above. We tested the uniqueness of our solution by using a number of starting models to see if there is common convergence. The iterative process of the inversion serves to map out the error space and allows one to determine if the minima are global. Figure 4.5 shows the error space for the orientation model

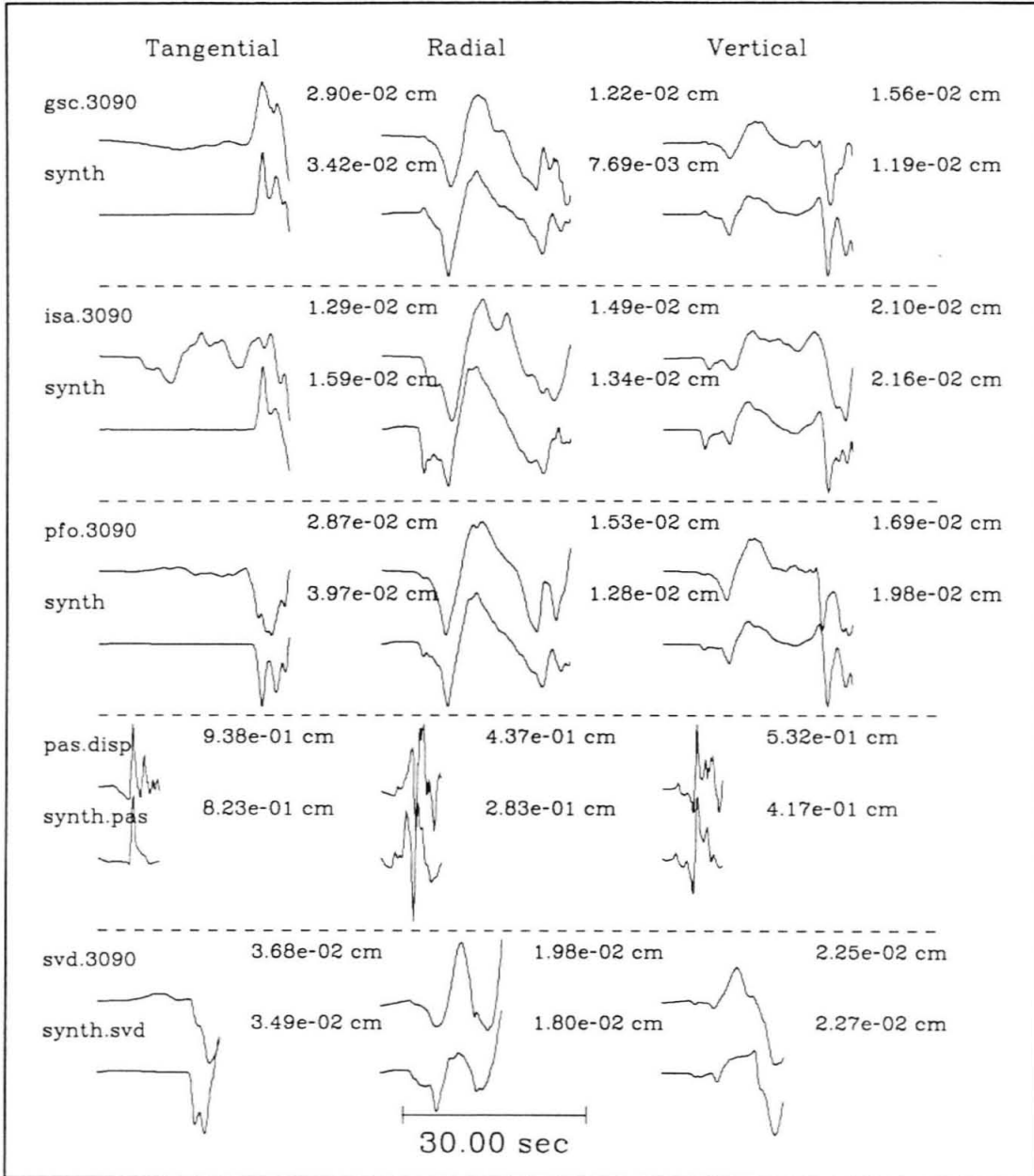


Figure 4.3: Results of the three-component waveform inversion. Only the length of record used in the inversion is plotted. The data from stations GSC, ISA, PFO and SVD has been filtered with the response of a Press-Ewing instrument (unit gain). The PAS data is ground displacement within the frequency band 0.05 to 7.0 Hz.

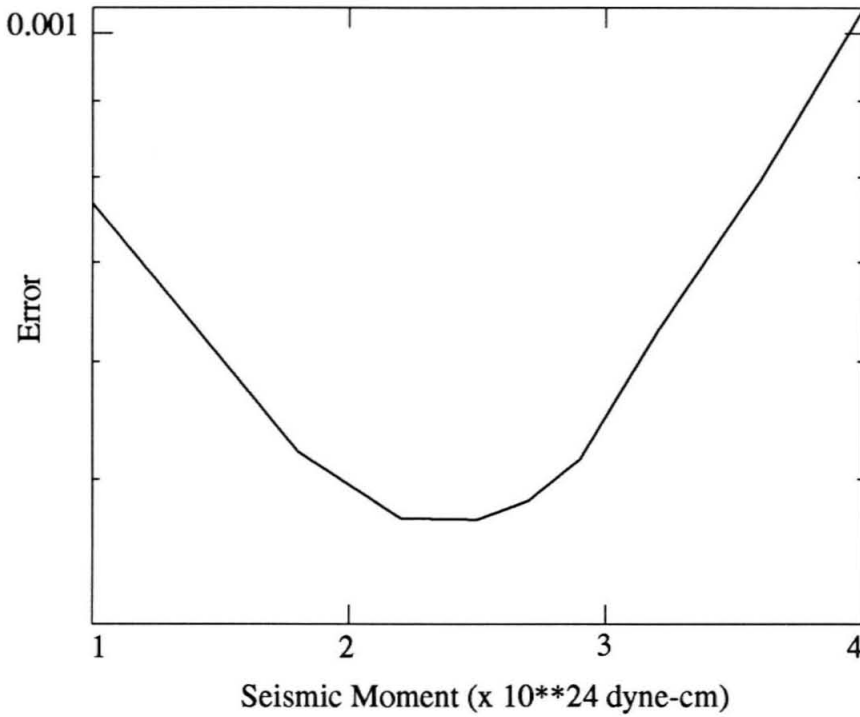


Figure 4.4: Fitting error plotted against seismic moment.

parameters using only stations GSC, ISA and PFO. Each iteration is represented by two points one for the solution obtained by that iteration and the other, the conjugate fault to the solution. For each starting model we computed 50 iterations, although convergence was usually obtained within 10. The error space has well defined minima describing a unique double couple solution. This is expected because the waveform similarities and the low variance in travel-time for these stations indicates that a single velocity model should perform well. This calculation was also made for the five station inversion and as stated above the same results were obtained. There was however a greater scatter in the points. Analysis of the points representing iterations with greater than 0.9 error reduction revealed that the scatter was 3° for the three station inversion and 12° for the 5 station inversion.

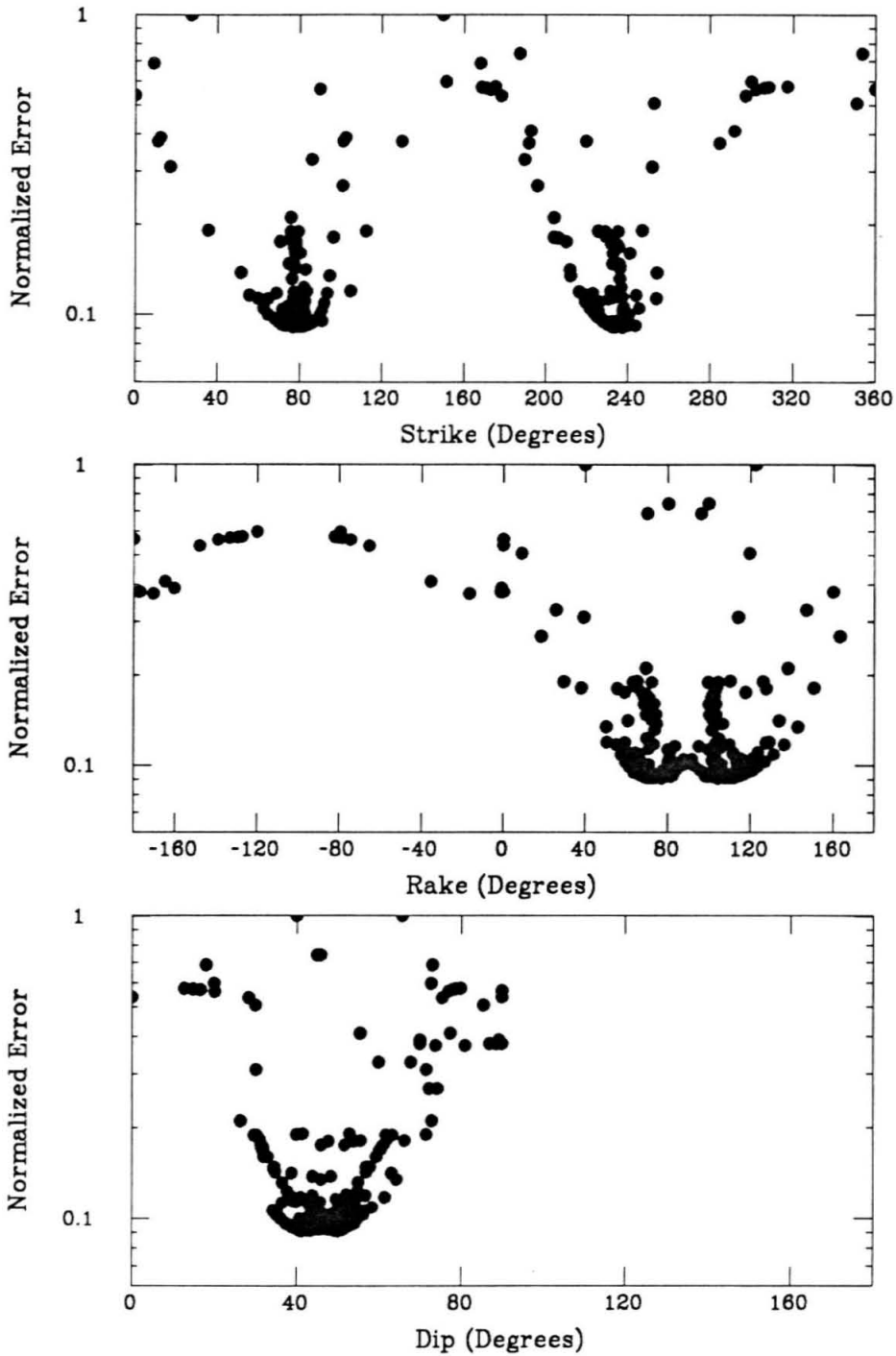


Figure 4.5: Fitting error plotted against orientation model parameters.

4.1.3 Conclusion and Implications

In conclusion, we inverted the lowpass filtered, three-component data recorded by the broadband, high dynamic range TERRAScope array to determine the source parameters of the June 28, 1991 Sierra Madre earthquake. We found a strike(θ) of 235° , a rake(λ) of 74° , a dip(δ) of 50° and a seismic moment (M_o) of 2.5×10^{24} dyne-cm. This result compares well with that obtained from first motion polarities ($\theta=242^\circ$, $\lambda=82^\circ$ and $\delta=50^\circ$) [Hauksson, 1992]. For rupture on a circular fault the source duration is proportional to the radius divided by the shear wave velocity [Brune, 1970]. The source duration can be written as $\tau = 2.62a/\beta$, and the stress drop for a circular fault can be written as $\Delta\sigma=7M_o/16a^3$, where τ is the source duration in seconds, a is the radius in km, M_o is the seismic moment, and β is the shear velocity in the vicinity of the source [Cohn et al., 1982]. Using the parameters obtained in this study an area of 5.6 km^2 and a stress drop of 460 bars are obtained.

The observation that variations in absolute travel-times were less than 2 % of the total travel-time for P_n and 3 % for S_n indicates that a relatively uniform lower crust can explain this data. Furthermore, the PL type waves propagating in the upper crust appear to be important in the local data and relatively insensitive to lateral heterogeneity. The upper crust is relatively more complicated however, since the surface waves show variation in dispersion relationships for the different stations (H. K. Thio, personal communication).

The results of this study imply that since the lower crust is fairly uniform it should be possible to routinely invert the long-period body waveforms to obtain earthquake source parameters. The fact that one-dimensional models are able to explain a great deal of the waveform data in a broadband sense suggests that an on-line catalog of several standard velocity models should prove useful in obtaining preliminary results in waveform modeling studies. Fine tuning for specific source-receiver pairs, and regionalizing the velocity models will provide important information about variations

in the lower crust and should improve future source and wave propagation studies.

4.2 Broadband Analysis of the Mainshock Source

4.2.1 Introduction

The goal of this section is to understand the motions recorded for the Sierra Madre earthquake in a broadband sense. By first studying longer period motions one can learn something about the average earthquake source and propagation effects. By including the shorter period information a greater amount of detail is incorporated into the models and the problem becomes significantly more complicated. Returning to Figure 4.2 we find that the standard southern California velocity model together with a point source model with a 1 second triangular source time function provides a good level of fit with the data. As pointed out previously many of the shorter period phases are evident in the data but have minor travel-time mismatches. There are also some mismatches in the relative amplitudes of some of the body wave phases compared to the surface waves. For example the relative amplitudes of S_mS and later arriving phases (sS_mS) are not correct on the tangential synthetics at GSC and PFO. The relative amplitudes of these phases are strongly dependent upon source depth and will be addressed in following sections.

Several studies have been performed to date to determine the source parameters of the mainshock. These studies have used data that covers the broadband spectrum of the source from 10-30 second regional surface waves to the onset of rupture with first motion polarities. These studies provide a glimpse of the source mechanism in different frequency bands. Figure 4.6 shows the results of these studies and Table 4.3 lists the solutions and the references. The short-period studies include first motion polarities [Hauksson, 1992] and P-SV, P-SH amplitude ratios of nearby stations (K. F. Ma, personal communication). In the intermediate range, Wald [1992] inverted teleseismic P and SH waveforms. Wald [1992] also investigated rupture complexity using local strong motion recordings. The results of this study

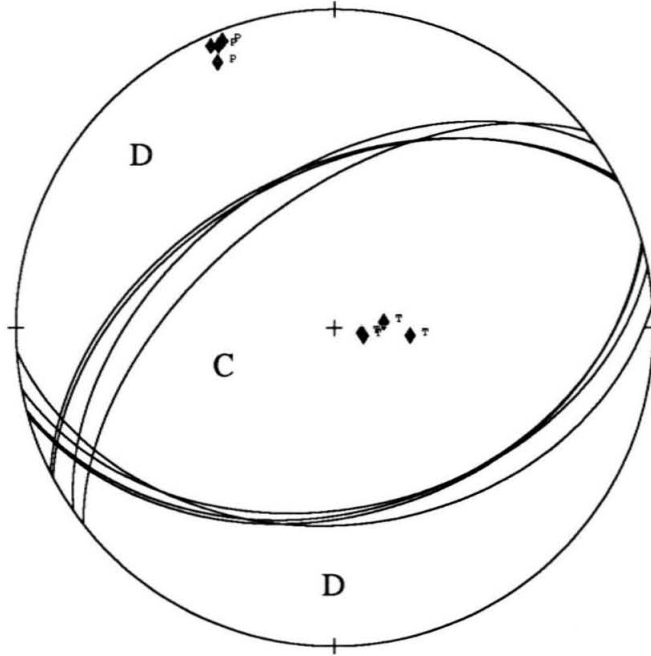


Figure 4.6: Fault plane solutions determined from various data sets and methodologies

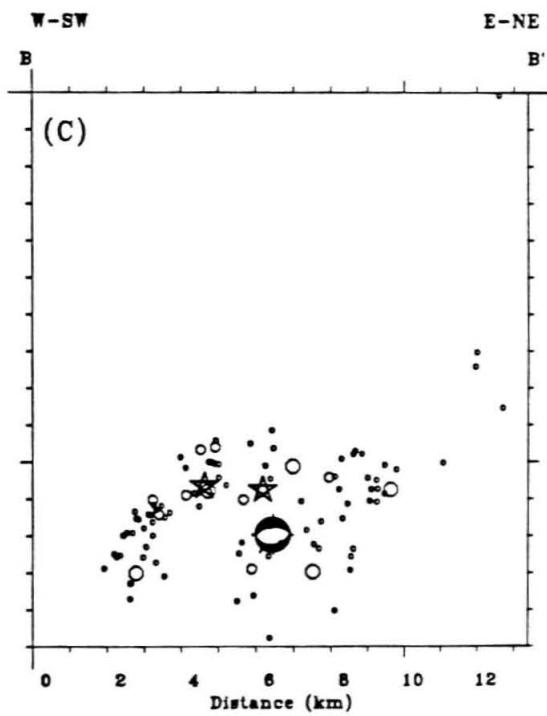
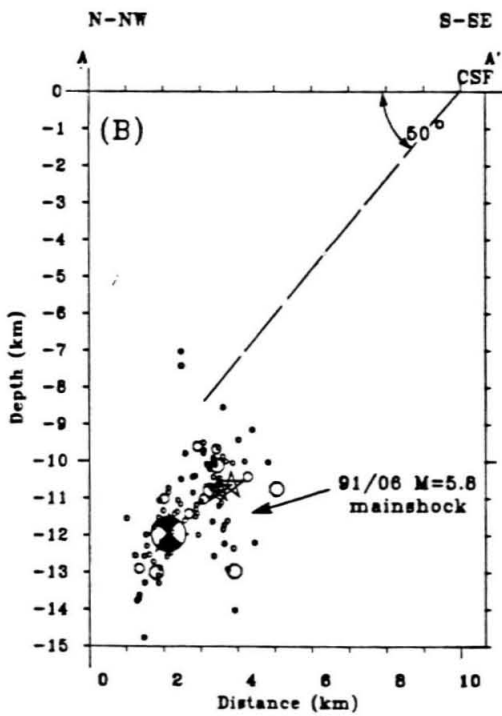
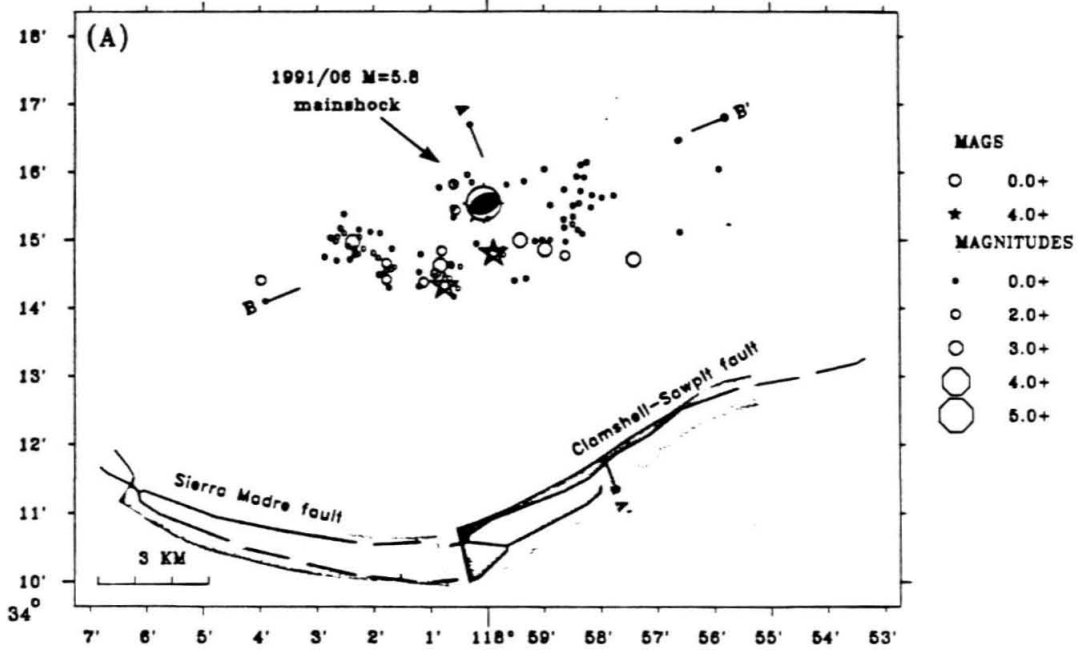
θ	λ	δ	M_o .	Reference
235	74	50	2.5	Dreger and Helmberger, 1991
232	70	57	2.7	Ma and Kanamori, 1991
242	82	50		Hauksson, 1992
243	82	49	2.8	Wald, 1992
243	82	49	2.7	Thio, 1992
240 ± 6	78 ± 6	50 ± 4	2.7 ± 0.1	

Table 4.3: Fault plane solutions. M_o is in units of 10^{24} dyne-cm.

are useful as a comparison and to help constrain the results presented later in this section. The long-period determinations include inversions of regional body waves [Dreger and Helmberger, 1991b] and regional surface waves (H. K. Thio, personal communication). All of these studies arrive at similar results, where the average focal mechanism and seismic moment are, $\theta = 240 \pm 6^\circ$, $\lambda = 78 \pm 6^\circ$, $\delta = 50 \pm 4^\circ$, and $M_o = (2.7 \pm 0.1) \times 10^{24}$ dyne-cm. The small differences in the mechanisms indicates that the orientation did not change significantly during the rupture. The aftershock distribution (Figure 4.7) shows two distinct trends however [Hauksson, 1992]. One trends to the northeast, consistent with the focal mechanism studies and another trends west-northwest. In cross-section, profile A-A' confirms the dip determined by the various focal mechanism studies. Profile B-B' along strike shows a curious lack of aftershock seismicity to the west-southwest of the hypocenter. It has been noted for other events that there is a strong correlation between the lack of aftershocks and regions of high slip [Mendoza and Hartzell, 1988]. Thus it is possible that this lack of aftershocks represents the region in which the largest mainshock slip took place.

Figure 4.7: Aftershock locations in (a) map view, (b) cross-section perpendicular to strike and (c) cross-section along strike, from Hauksson, [1992].

Sierra Madre 28 June - 15 August 1991



4.2.2 Amplitude Constraints on Directivity

As a first order investigation into whether faulting directivity influenced the data recorded by TERRAscope, we compare mainshock-aftershock amplitude ratios in two bandwidths. The low-frequency bandwidth is chosen to be below the corner frequency. In this case the data is filtered with the long-period Wood-Anderson (WALP) and the short-period Wood-Anderson (WASP) instrument responses. The following ratio is then computed:

$$\frac{\left[\frac{\Sigma WASP}{\Sigma WALP}\right]_{main}}{\left[\frac{\Sigma WASP}{\Sigma WALP}\right]_{after}} \quad (4.1)$$

Table 4.4 lists the amplitude ratios obtained for each of the events. By taking the average of the three components the effect of differing radiation pattern is reduced, and the ratio of the mainshock to the aftershocks corrects for propagation effects. Note that for stations where both aftershocks were recorded the amplitude ratios are nearly the same, with the exception of PAS where there is a rather significant difference in the ratios. Where possible, the ratios of the smaller aftershock (aftershock2) were used since it most likely had a smaller source area and most closely resembles a point source. Figure 4.8 shows the results of this calculation. We find that generally the amplitude ratio is smaller for stations to the north and to the east than to the west, indicating that records of the mainshock are depleted in higher frequencies relative to lower frequencies at eastward azimuths. The point source solution in the WASP bandwidth over predicts the amplitudes. The velocity data requires only 35 % of the total seismic moment to explain the amplitudes [Helmberger et al., 1992c]. The effect of directivity is the broadening of source functions with a corresponding decrease in amplitude in directions opposite from the rupture direction. The reverse is true in the direction of the rupture. Thus the amplitude ratios suggest that rupture progressed toward the southwest. The isoseismal pattern [Stover and Reagor, 1991] and the strong motion data also suggest a southwest rupture [Wald, 1992].

Mainshock				
Station	Tangential	Radial	Vertical	Average
GSC	0.26	0.36	0.33	0.32
ISA	0.16	0.11	0.16	0.14
PAS	0.35	0.60	0.34	0.43
PFO	0.32	0.21	0.30	0.28
SBC	0.37	0.32	0.33	0.34
SVD	0.40	0.31	0.16	0.29

Aftershock1: June 28, 1991; 1700 UT				
Station	Tangential	Radial	Vertical	Average
GSC	0.91	1.16	0.64	0.90
ISA	0.42	0.67	0.45	0.51
PAS	0.47	0.73	0.50	0.57
PFO	0.55	0.65	0.94	0.71
SBC	-	-	-	-
SVD	1.05	0.63	0.74	0.81

Aftershock2: July 6, 1991; 2254 UT				
Station	Tangential	Radial	Vertical	Average
GSC	-	-	-	-
ISA	0.44	0.59	0.50	0.51
PAS	0.92	0.90	0.74	0.85
PFO	0.76	0.62	0.80	0.73
SBC	0.61	0.63	0.59	0.61
SVD	0.67	1.01	1.00	0.87

Table 4.4: WASP/WALP Amplitude Ratios for mainshock and aftershocks

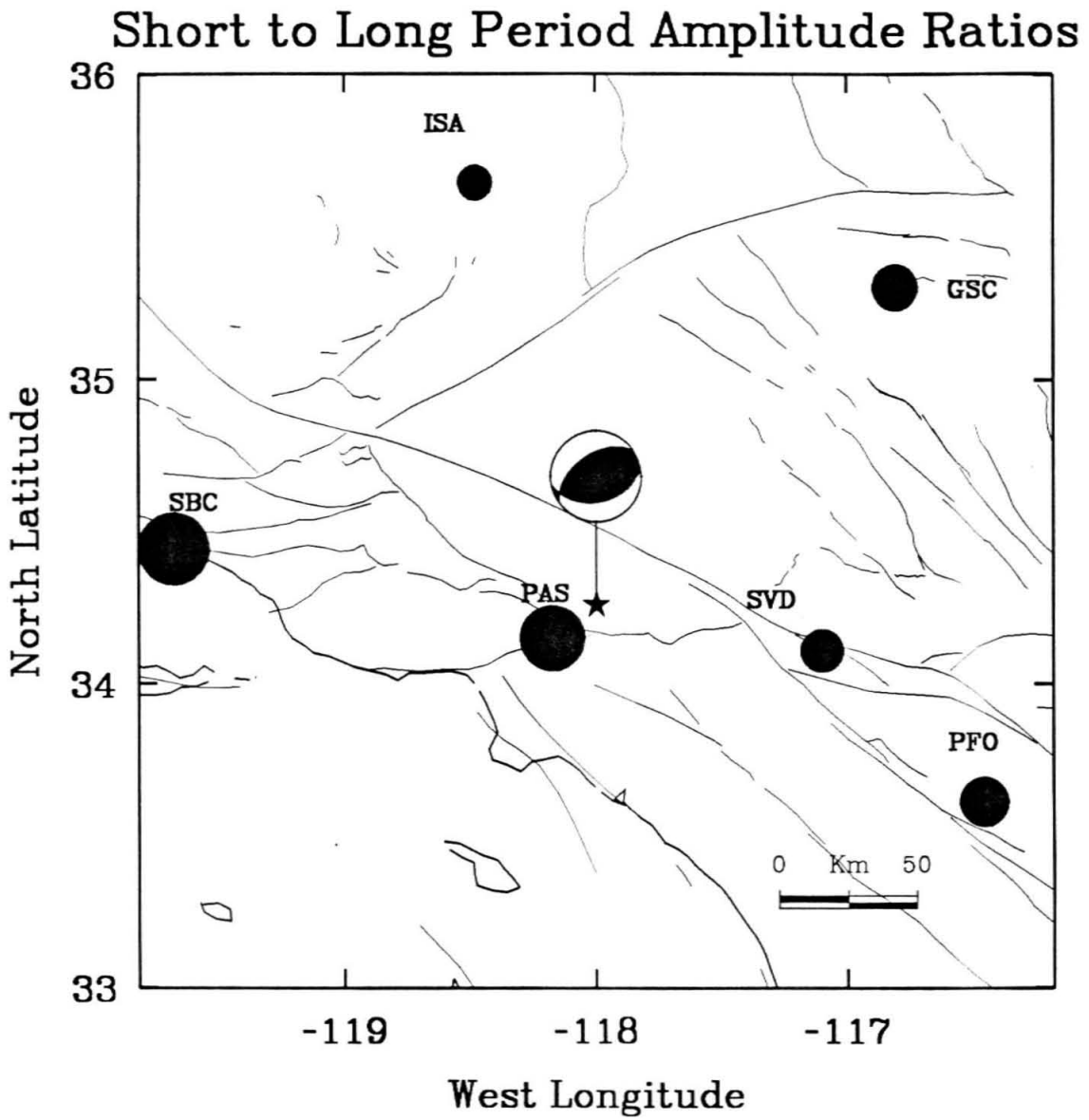


Figure 4.8: Map showing the WASP/WALP peak amplitude ratios formed according to equation 4.1

4.2.3 Waveform Constraints on Directivity

The first order analysis of short to long-period amplitude ratios was useful in determining if the source displayed complexity in terms of rupture directivity. It tells nothing of the vertical directivity and slip distribution however. Commonly the slip distribution is determined by inverting local strong motion records using either theoretical or empirical Green's functions. Usually the former requires that close in stations are used so that simple velocity models can explain much of the propagation. The latter while taking propagation into account, requires that the mechanisms of the events used as empirical Green's functions be very similar to the mainshock mechanism. Another drawback of the empirical approach is that the Green's functions need to be distributed along the entire rupture surface. As mentioned earlier there is evidence that areas that experience the greatest slip during the mainshock usually are deficient in aftershocks.

In areas that do not have dense local networks both methods are difficult. The purpose of this section is to demonstrate that regional waveforms despite their additional complexity may be used to learn about the source processes of earthquakes. Studies of this type will prove to be important in regions that do not have dense local strong motion instrumentation and for events that are too small to be recorded teleseismically.

Methodology

The methodology is the same as described in section 3.2.4 for the 1990 Upland earthquake. In the following calculations we used a grid spacing of 0.5 km, and a point source time function consisting of a 0.30 second triangle. The moment and orientation determined by inverting the long-period body waves (section 4.1) was used in all of the calculations. The area of the fault was determined from the region deficient in aftershocks (Figure 4.7). We used a 3 by 4 km (length by depth) fault.

The top of which was located at 10 km. For stations ISA, GSC and PFO we used synthetics computed using a model developed by Helmberger et al. [1992c] to better model the absolute travel-times and the tangential waveforms at the stations. Since the length of the fault is small compared to the distance to the stations only one distance was used to compute the synthetics. The PAS station was much closer to the fault so several distances were used. The change in radiation pattern due to variations in back azimuth has been neglected.

The effect of source depth is very important on the relative amplitudes of various phases in the synthetics. This is most readily seen when the wavefield is decomposed using rays. For example, Figure 4.9 shows the decomposition of the wavefield into Love wave, up-going, and down-going ray sets. At this particular distance all of the ray sets are equally important in terms of amplitude, at least for the vertical strike-slip fault. The level of importance varies with distance as described in Helmberger et al. [1992c], source depth and with focal mechanism. Figure 4.10 shows the effect of different source depths on the synthetic waveforms computed with a reflectivity method. Generally, with increasing source depth the down-going energy is amplified relative to the up-going and surface wave energy. Because of the large influence of source depth on the waveforms we used several source depths in the range from 10 km to 13 km in the distributed fault modeling.

Ray Decomposition

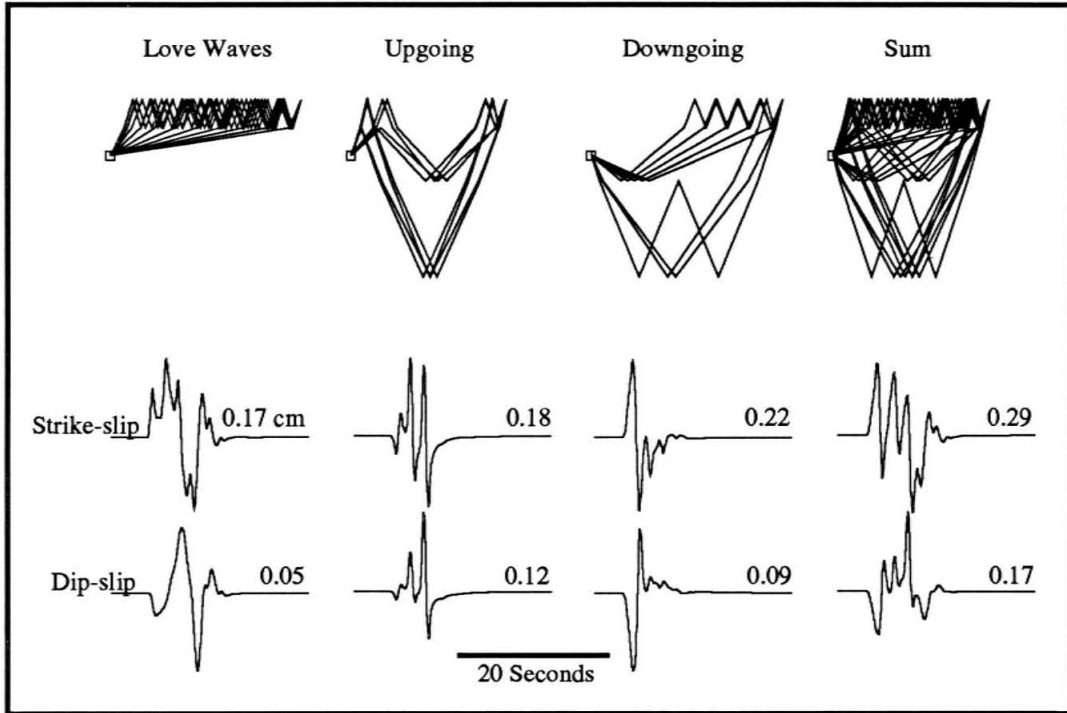


Figure 4.9: Ray decomposition. Vertical strike-slip and dip-slip mechanism synthetics with a seismic moment of 2.5×10^{24} dyne-cm and a triangular source time function with a duration of 1 second are plotted with respect to ray set.

Variation of Synthetics with Source Depth

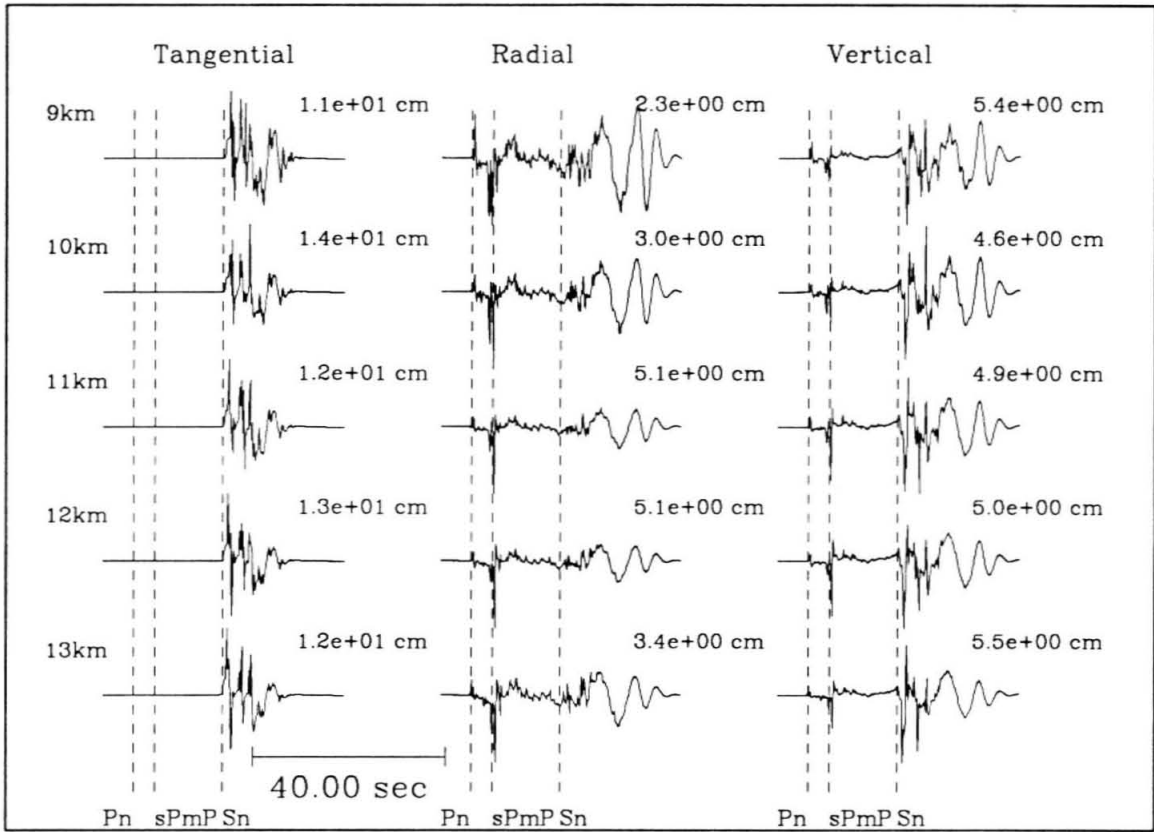


Figure 4.10: Source depth sensitivity of reflectivity synthetics with an orientation appropriate for GSC. A seismic moment of 2.5×10^{24} dyne-cm was used. The more important arrivals in the synthetics are marked with dashed lines.

Uniform Slip Models

Several rupture models were tested with the orientation and seismic moment parameters prescribed as above. These models have uniform slip in that each of the point sources have equal seismic moment. The rupture velocity was held fixed at 2.7 km/s (75 % of the shear wave velocity). Figure 4.11 shows the location of the hypocenters tested on the fault plane. A circular rupture front was allowed to propagate away from each of the hypocentral locations at the rupture velocity. When the rupture front passes a particular point the subfault “fires” and the response is summed. The integral of the point sources on the fault plane comprise the mainshock motion.

Figure 4.12 shows the results for station PAS. Only model NE.12.7 provides a good fit to the data. This model has a hypocenter in the lower NE corner of the fault (Figure 4.11) with the rupture proceeding updip toward the southwest, in the direction of station PAS. The fits to the waveforms are good for all three components, but the amplitudes are over predicted for the radial and vertical components. Closer examination of the tangential waveform reveals that there is a multiple S phase similar to that observed for the Upland earthquakes (section 3.1). Flat layered models are not sufficient to produce this arrival since the PAS station was located only 21 km from the event. Two-dimensional models have promise, but further discussion is beyond the scope of this section. In any case the simple plane layered model that we used adequately predicts the SH pulse and the near-field phase which dominate the waveforms. Two point source models are also shown on this figure for comparison. “Point1” has a source depth of 11 km and a 0.5,0.5,0.5 second trapezoidal source time function. This is clearly too long-period to model the data. The second, “Point2” has the same source depth as “Point1” but used a 1 second triangular source time function. This model performs better but also seems to be lacking some short-period energy evident in the data.

Next, the different rupture scenarios are compared with data recorded by stations

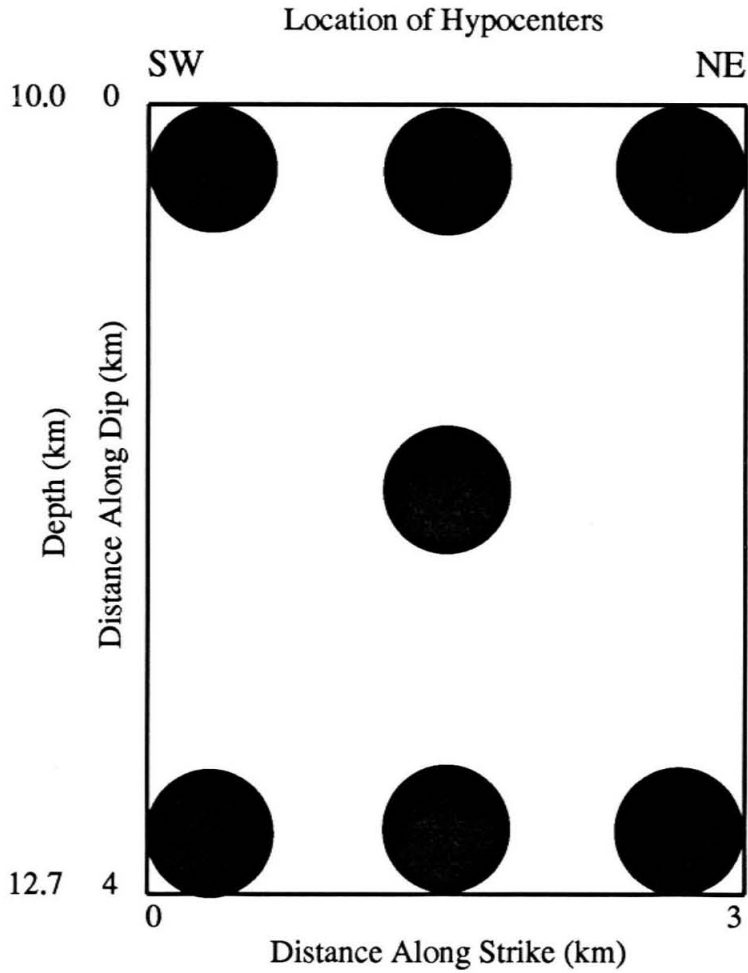
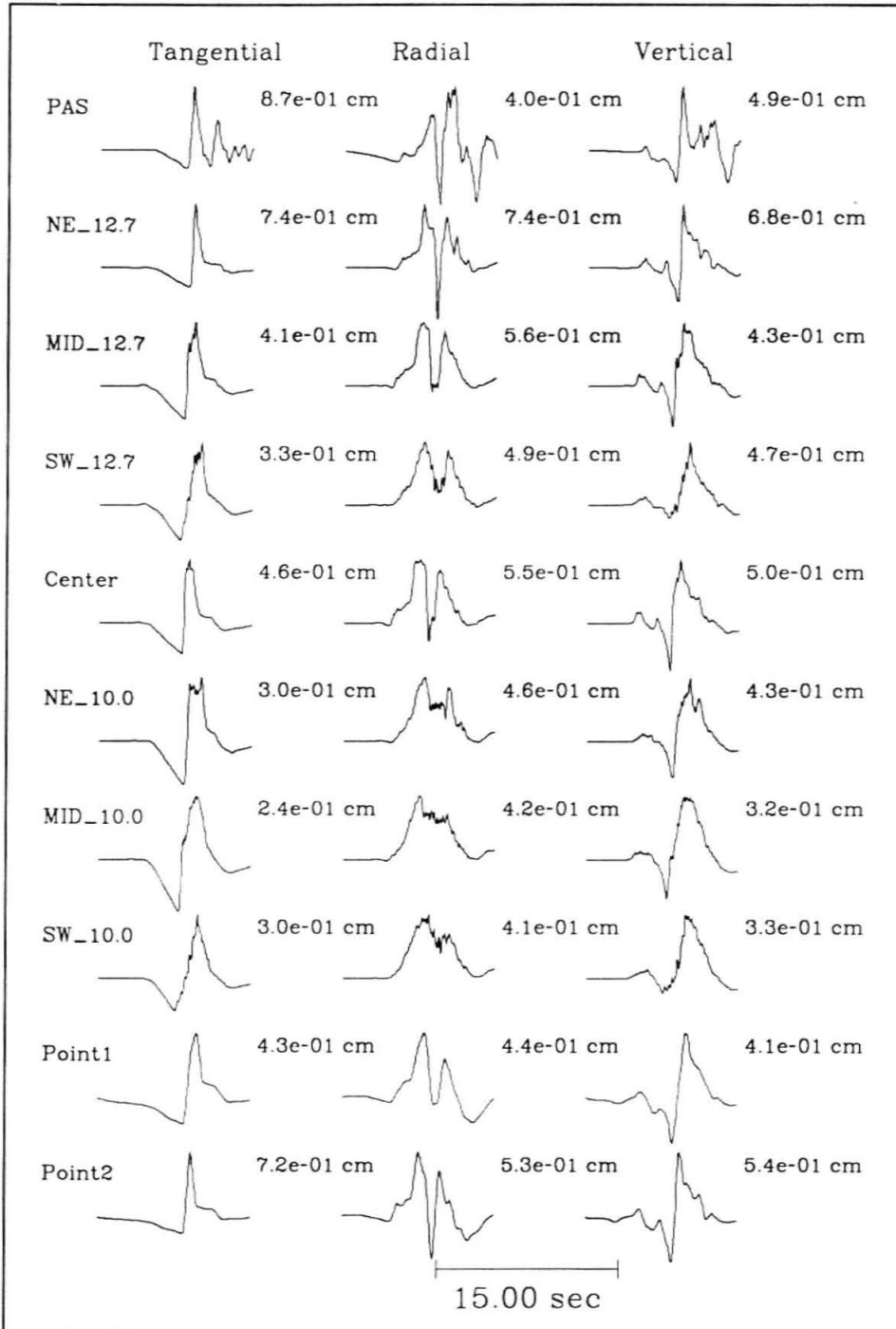


Figure 4.11: Locations of assumed hypocenters on the fault plane for the various rupture scenarios. E. g. NE_12.7 refers to a rupture model in which slip initiates at the lower left corner and propagates out radially.

Figure 4.12: Directivity analysis for PAS. The displacement data (PAS) are compared with upward rupturing models (NE_12.7, MID_12.7 and SW_12.7) and downward rupturing models (NE_10.0, MID_10.0 and SW_10.0). “Center” is a circular rupture model. “Point1” is a point source model where a depth of 11 km and a trapezoidal source time function with a duration of 1.5 seconds were used. “Point2” is a similar point source model in which a triangular source time function with a duration of 1.0 second was used.

Directivity Analysis at PAS (uniform slip)

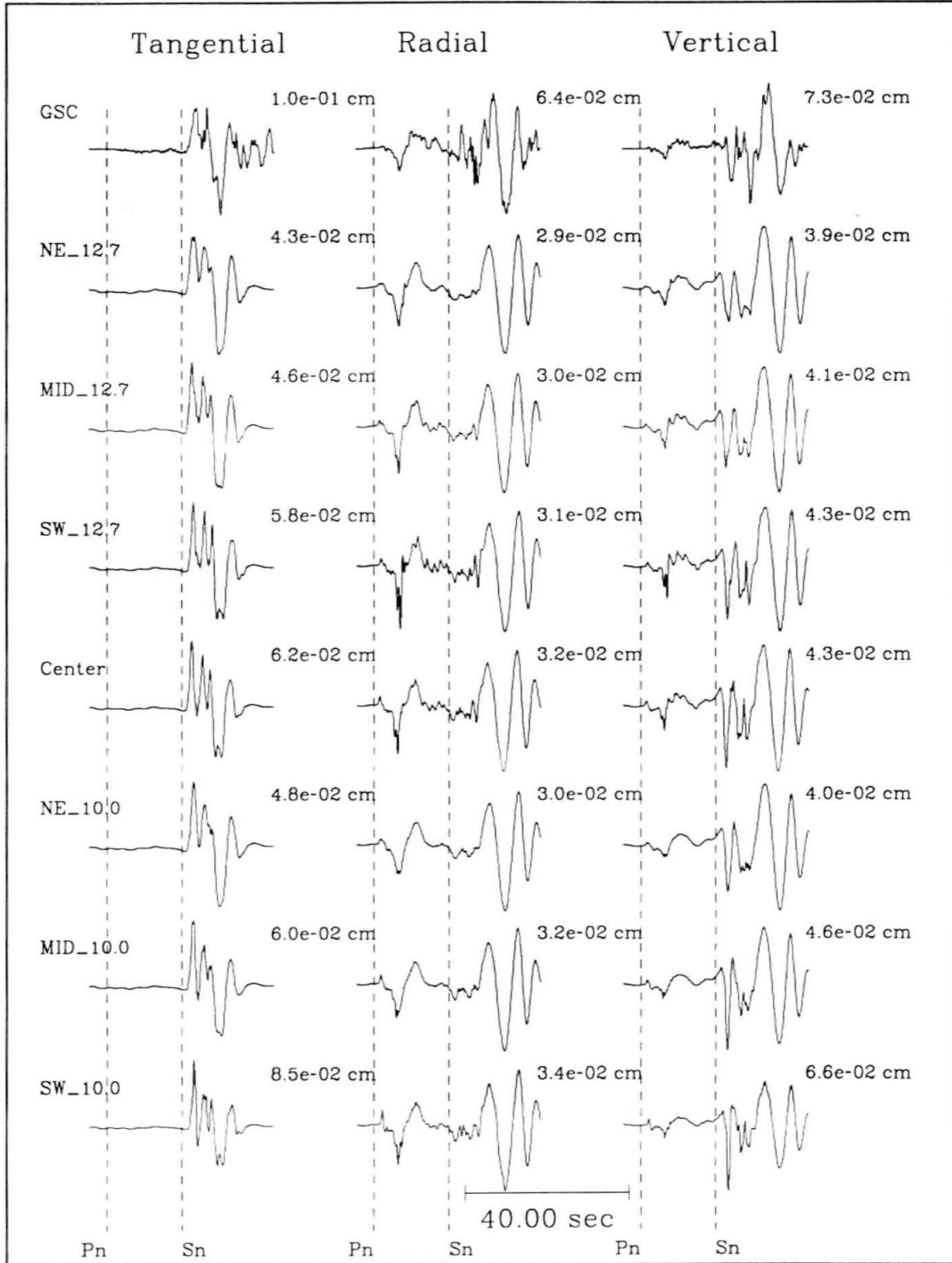


GSC, ISA and PFO (Figure 4.13). First comparing the upward rupturing models, NE_12.7, MID_12.7, and SW_12.7 with the downward rupturing models NE_10.0, MID_10.0, and SW_10.0 we find that the tangential waveforms at GSC and PFO are significantly better modeled with the upward rupturing model. This is especially apparent in the relative amplitude of the sS_mS phase. Comparing the P waveforms on the radial and vertical components we note that relative amplitudes are slightly better modeled with the upward rupturing models. Stations GSC and ISA exhibit a smaller S_mS arrival compared to PFO and the point source synthetics (Figure 4.2). The upward propagating models tend to produce this effect for these stations while the strength of S_mS remains nearly the same at PFO. In comparing the upward rupturing models the model with rupture propagating toward the southwest better matches the frequency content of the data.

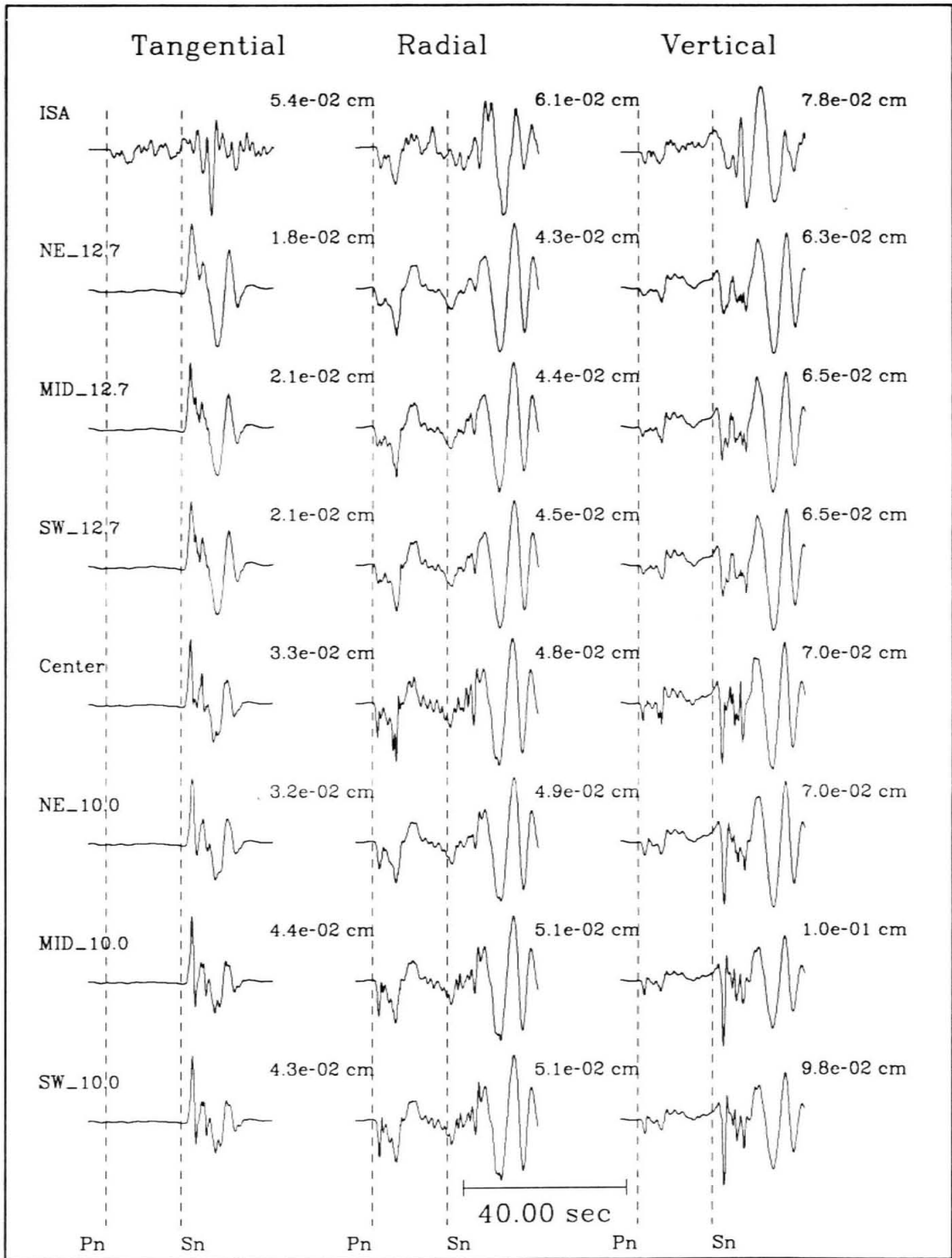
One of the conclusions that can be drawn from this analysis is that the effective source time function at PAS (1 second) is shorter than at the other stations. Examination of the delay times for the other stations revealed that overall durations for azimuths appropriate for ISA, GSC and PFO are 1.8 to 1.5 seconds. Stations GSC, ISA and PFO were located 160 km from the event compared to the 21 km for PAS, and therefore one must consider the possibility that the apparent broadening of the source time function is the systematic effect of Q and a longer travel path. Figure 4.14 compares the SH displacement amplitude spectra for the mainshock and two of the largest aftershocks. The data was rotated to the tangential component, and a 30 second window around the SH wave-train was fast Fourier transformed (FFT). The amplitude spectra was computed from the FFT and were normalized to the peak spectral amplitude corresponding to a seismic moment of 10^{20} dyne-cm. The aftershock spectra were compared to several Q models (Appendix A) and it was found that the uniform Q model ($Q_\alpha = 600$ and $Q_\beta = 300$) compares well with the data. The shapes of the aftershock spectra for a particular station are consis-

Figure 4.13: Directivity analysis for (a) GSC, (b) ISA and (c) PFO. See Figures 4.11 and 4.12 for a description of the various rupture scenarios.

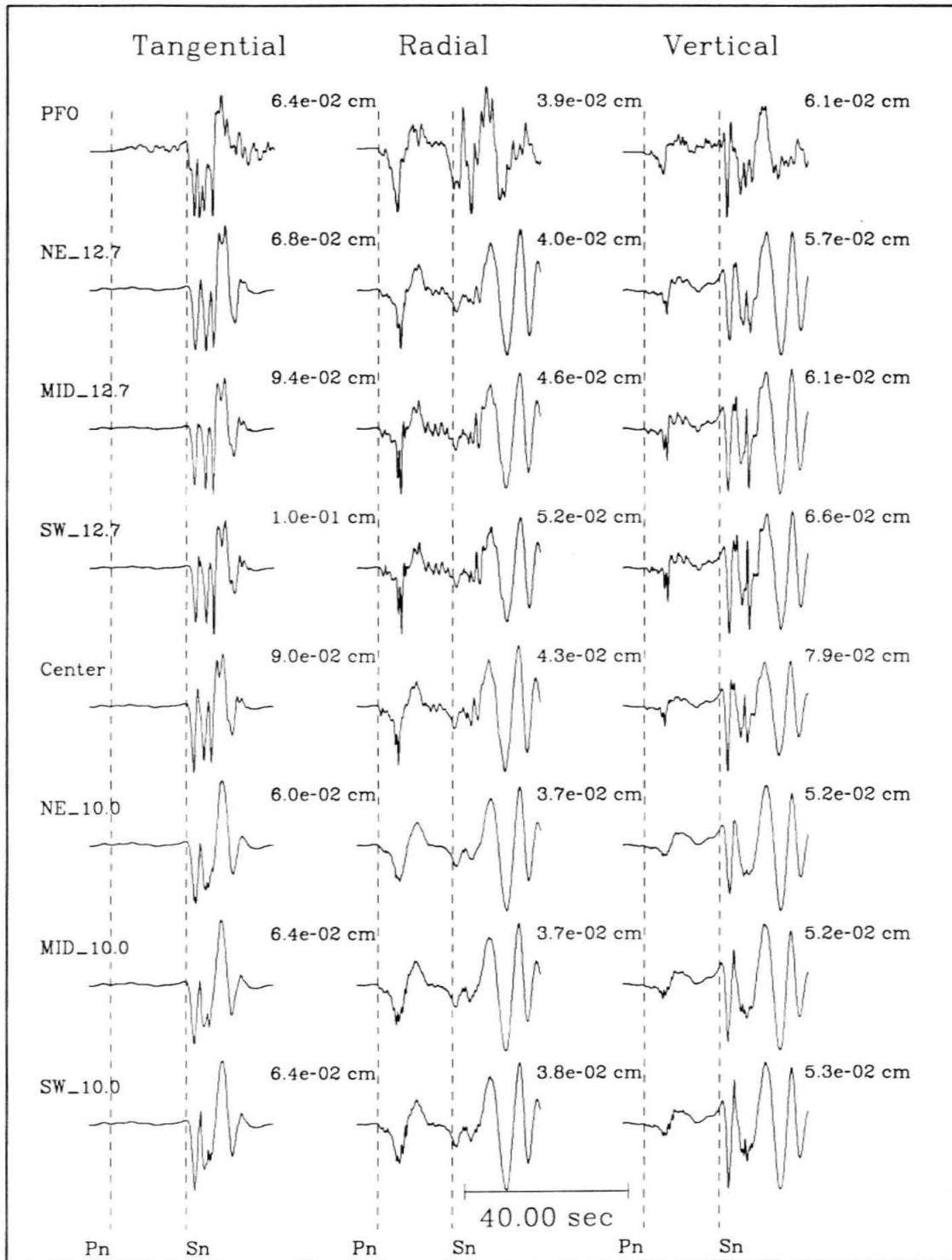
Directivity Analysis at GSC (uniform slip)



Directivity Analysis at ISA (uniform slip)



Directivity Analysis at PFO (uniform slip)



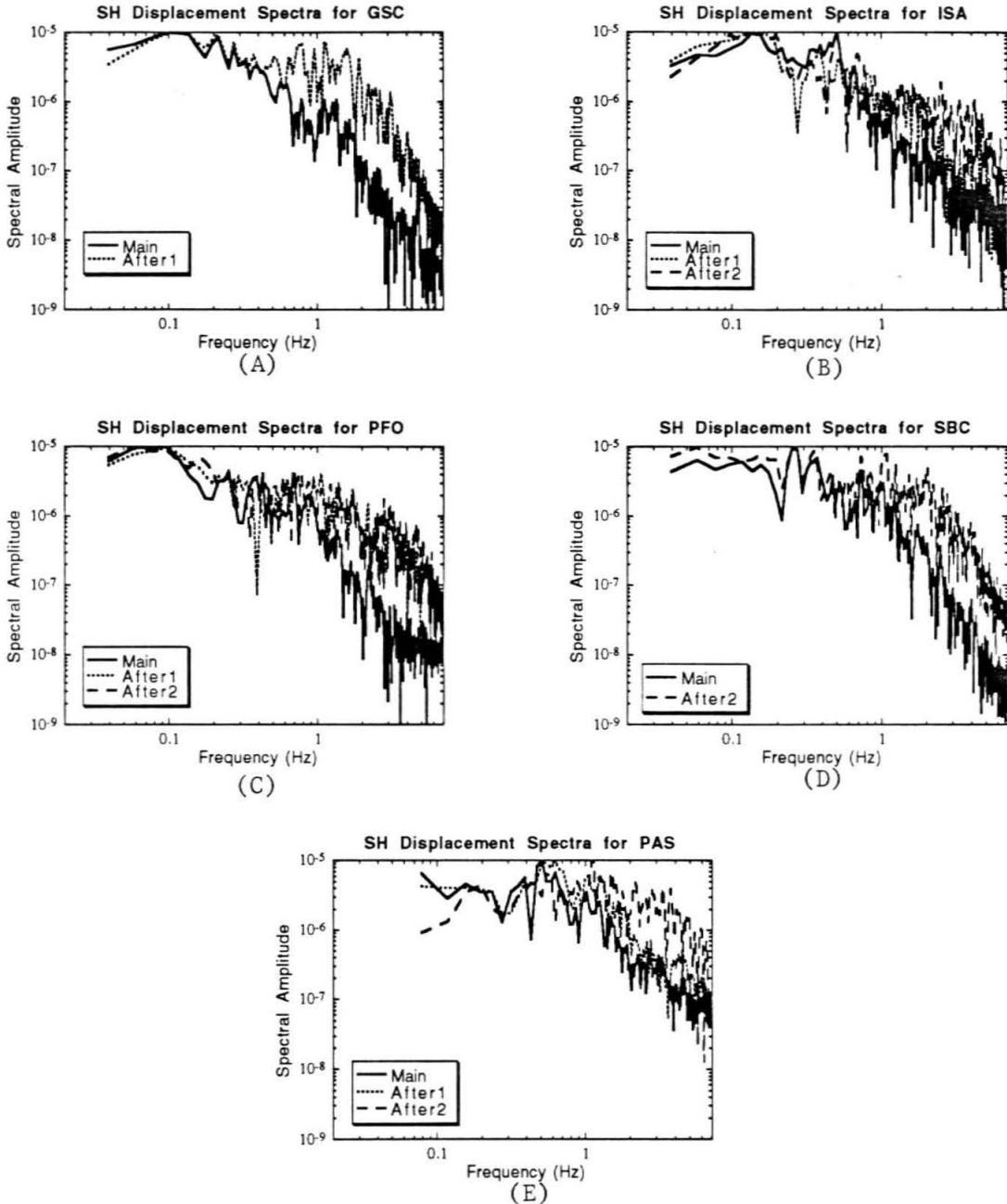


Figure 4.14: SH displacement amplitude spectra at (a) GSC, (b) ISA, (c) PFO, (d) SBC, and (e) PAS. The amplitude spectra were computed from 30 sec windows around the SH wave-train, except at PAS where a window around the direct S pulse was used. After1 refers to the June 28, 1991 1700 UT event and After2 refers to the July 6, 1991 2254 UT event.

tently very similar and display a significantly higher corner frequency and different spectral falloff than the mainshock, with the exception of aftershock1 recorded at PAS. For this event the spectral shape is very similar to the mainshock, indicating that perhaps this aftershock also had some component of directivity. While at 1 Hz the spectral amplitude at all of the stations are similar, at higher frequencies the spectral amplitudes of GSC, ISA and PFO are as much as an order of magnitude lower than at PAS. The aftershock spectral amplitudes show substantially higher values that are comparable with the PAS mainshock values precluding attenuation as an explanation for the apparently longer source durations observed at stations GSC, ISA and PFO. The similarity of the spectral shape for the aftershocks at the more distant stations reinforces the observation that amplitude ratios of the two aftershocks discussed earlier (Table 4.4) are the same, and the variations in the mainshock-aftershock amplitude ratios (Figure 4.8) are due to a source effect.

Figures 4.15abc compare the NE_{12.7} uniform rupture model in the broadband, WALP and WASP bandwidths for stations GSC, ISA and PFO. There is good agreement with the displacement and WALP data, but the WASP amplitudes are under predicted by approximately a factor of two.

Directivity Analysis GSC (uniform slip)

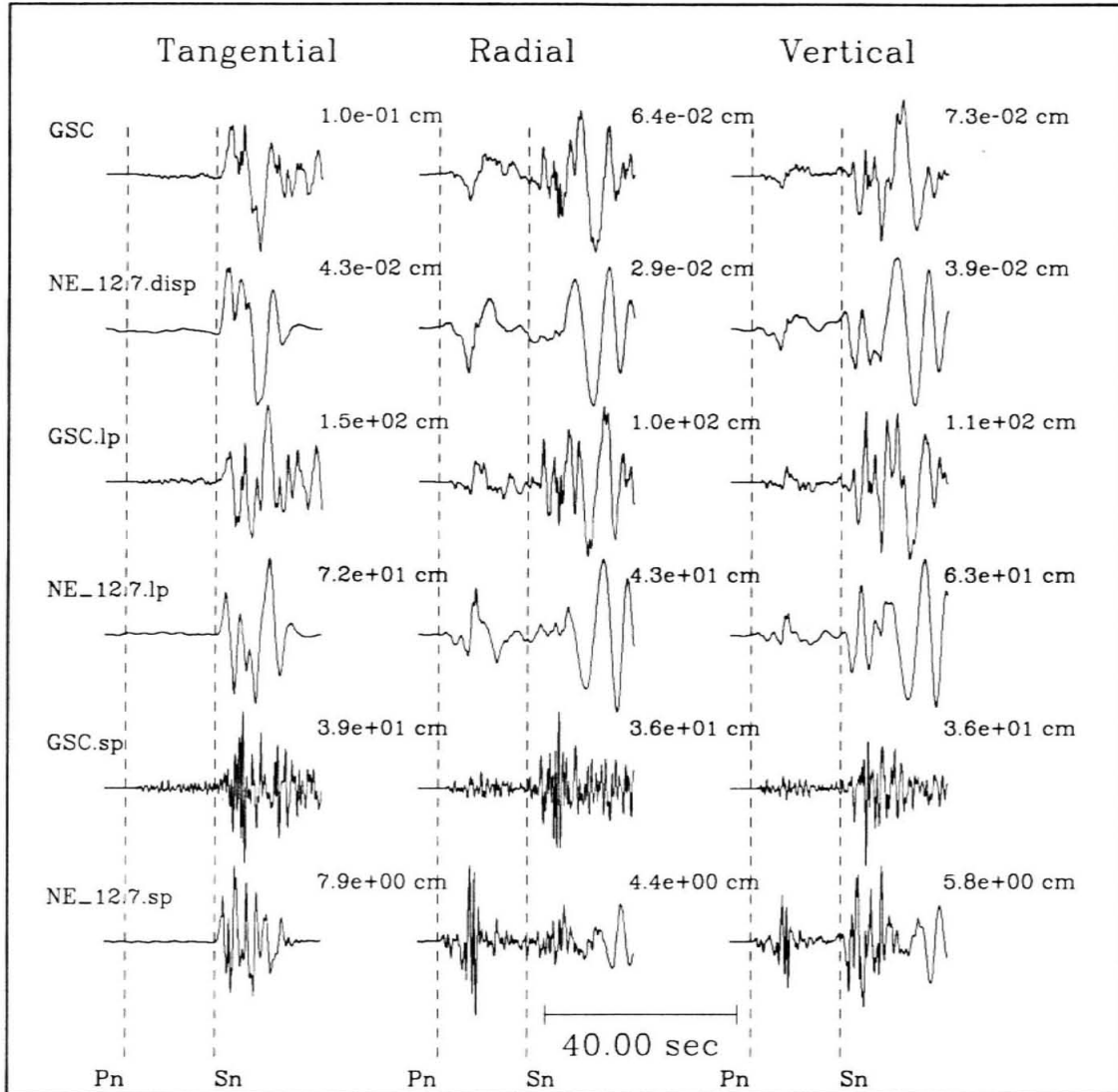
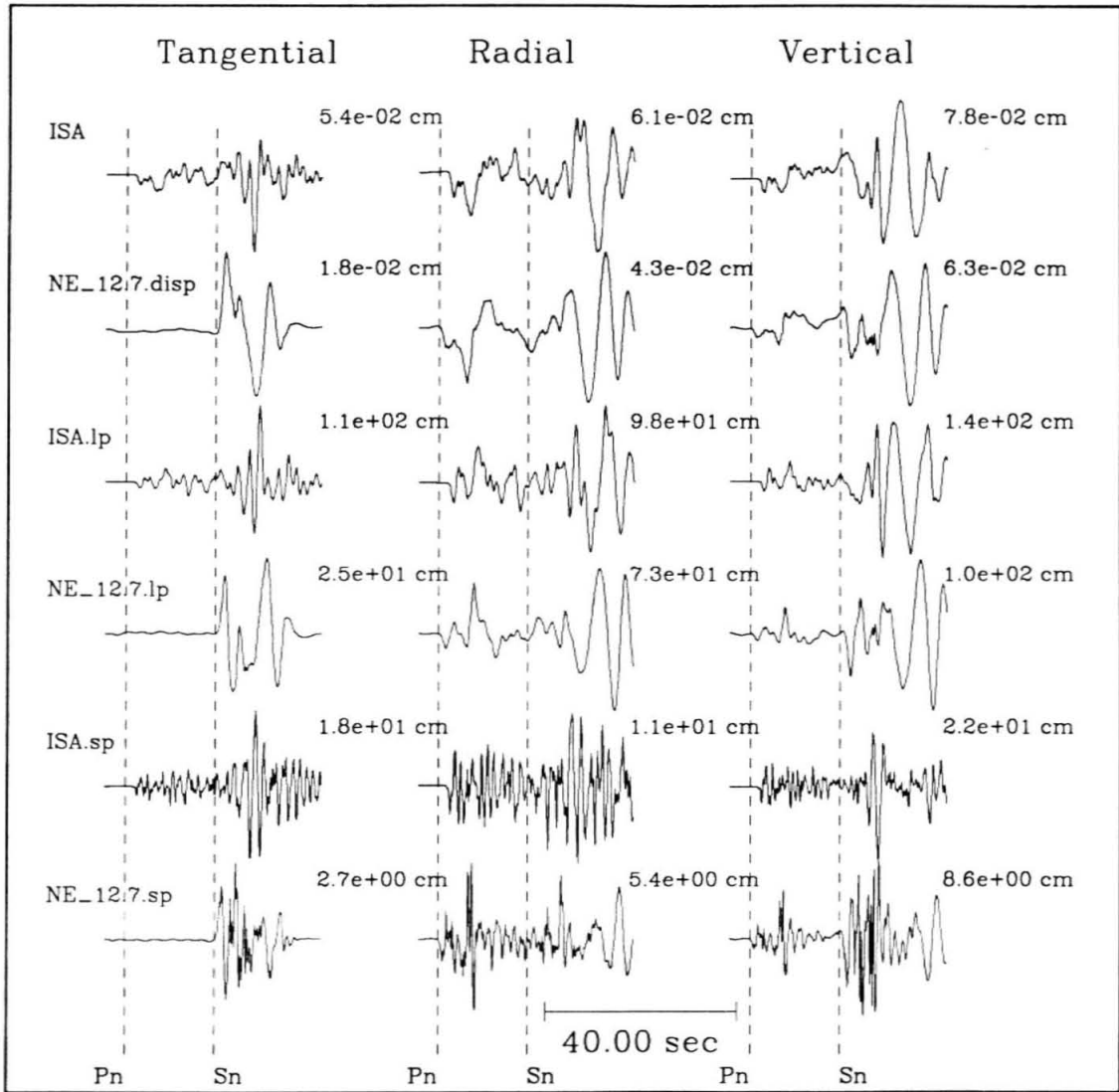
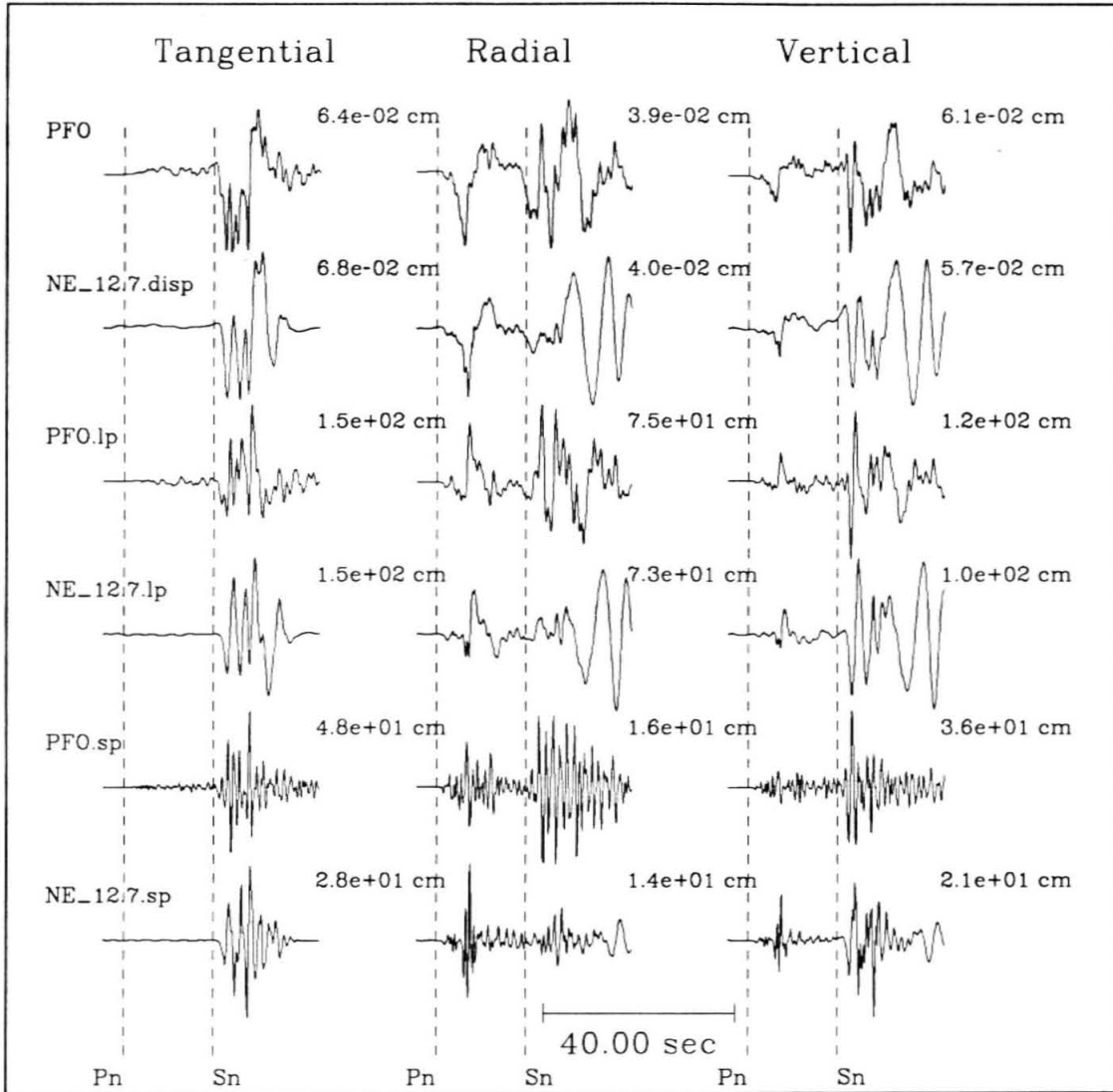


Figure 4.15: Comparison of displacement, WALP, and WASP data and synthetics for the preferred slip model NE_12.7 at (a) GSC, (b) ISA and (c) PFO.

Directivity Analysis ISA (uniform slip)



Directivity Analysis PFO (uniform slip)



Non-Uniform Slip Models

Several non-uniform slip models were tested. Since the number of parameters far out number the data this analysis is non-unique. It is interesting however, to see if it would be possible to improve on the fits, especially in terms of being able to fit the low and high frequencies together. Figure 4.16 shows the distribution of slip for one of the models that was tested. Figure 4.17abc compare the data and the synthetics. This model clearly does not affect the lower frequency motions very much but does improve the fit to the peak amplitudes in the WASP bandwidth. It appears that the shorter periods are controlled by the regions of greatest slip (asperities) and not the overall rupture. The asperity in this model released 35 % of the total seismic moment which is consistent with the lower seismic moment required by the velocity data, as reported by Helmberger et al. [1992c]. The area of this asperity is 4 km^2 which is in agreement with the results of Wald [1992] in which the greatest slip was concentrated in a relatively small area. There is also clearly an increase in the level of complexity in the data with increasing frequency. While our synthetics do explain much of the three component data at the longer periods (displacement and WALP) there are problems at higher frequencies. The most apparent is the lack of any significant SV energy on the radial component in the WASP bandwidth. This problem is probably in part due to incorrect receiver functions [Helmberger et al., 1992c]. Scattering, and undulations in the crustal interfaces also play a role in generating high frequency SV on the radial components.

Figure 4.18 compares the uniform and non-uniform models at PAS. The non-uniform slip model produces a higher frequency S pulse than the uniform model and the amplitude is larger. The disagreement can be due to a number of factors such as unaccounted for source complexity, incorrect Q , and unaccounted for propagation complexity in the synthetics. A $Q_\beta = 300$ was used in the synthetics for PAS. It is possible that this value is too high and should be more like 80 (K. Ma, personal

communication). As discussed earlier there are some propagation arrivals that are not accounted for. Most notably the large secondary arrival following direct S by approximately 1.7 seconds. This is probably a near receiver multiple phase as discussed earlier. Another phase that is evident at higher frequencies in the aftershocks follows direct S by approximately 0.2 seconds, and is evident in the mainshock at 0.3 seconds (Figure 4.19). This arrival is clearly not evident in the displacement waveforms, but contributes to the observed durations of the displacement pulse. For example, if the velocity records for After2, After3 and After4 are compared, the initial S wave durations are nearly the same. After2 has a substantially simpler waveform, and compares with the synthetic seismogram computed with model LOHS1 (Table 4.2). After3 and After4 have more complicated velocity waveforms that contribute to the duration of the displacement pulse. Thus, it may be possible to improve on the fits at PAS by incorporating these additional complexities. In any case as Figure 4.12 shows, the shape of the mainshock S-wave recorded at PAS is probably dominated by the directivity and not the slip distribution.

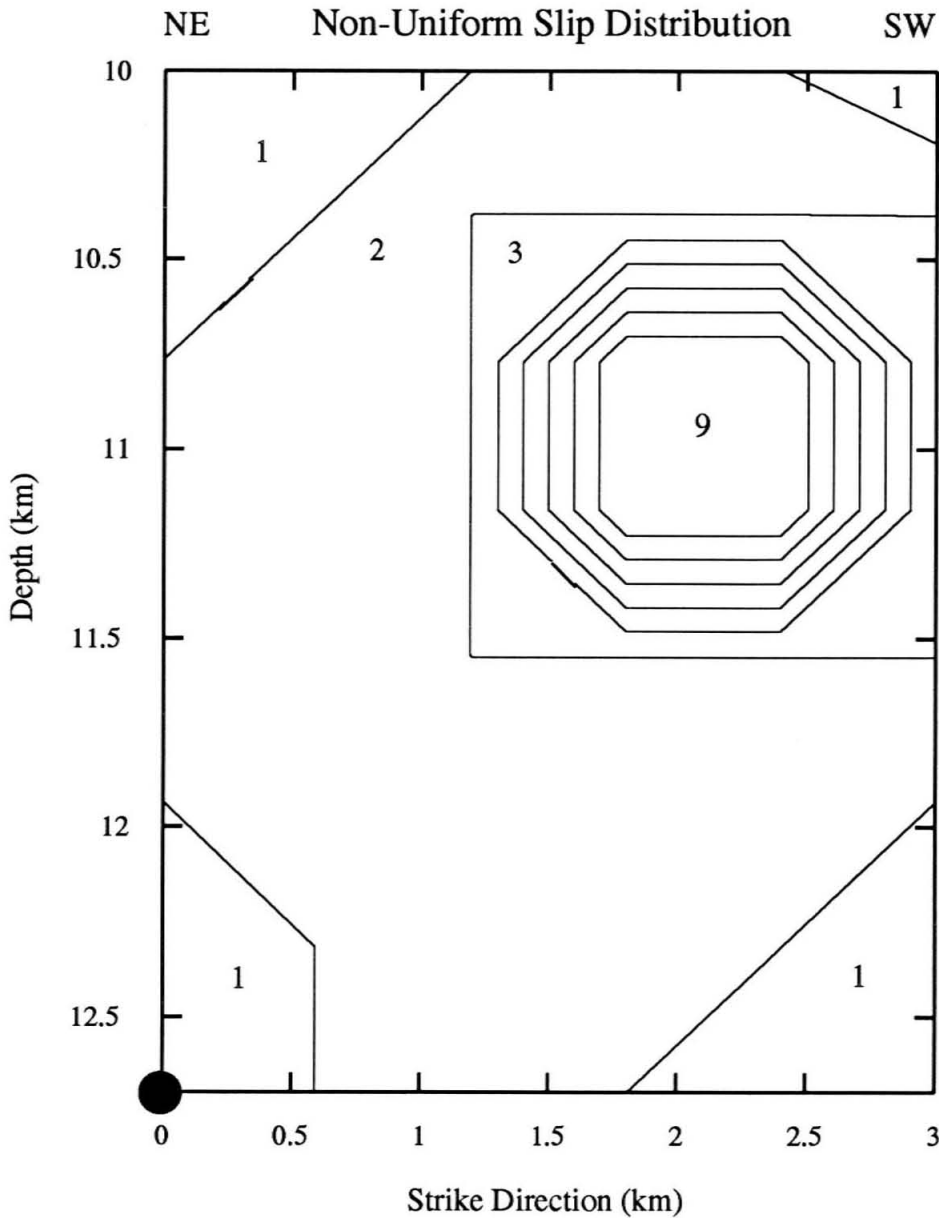


Figure 4.16: Non-uniform slip model. The circle shows where rupture begins. The numbers show the relative weighting in seismic moment. The region weighted 9 represents 15 % of the total seismic moment, and the region weighted 3 and larger represents 35 %.

Directivity Analysis GSC (non-uniform slip)

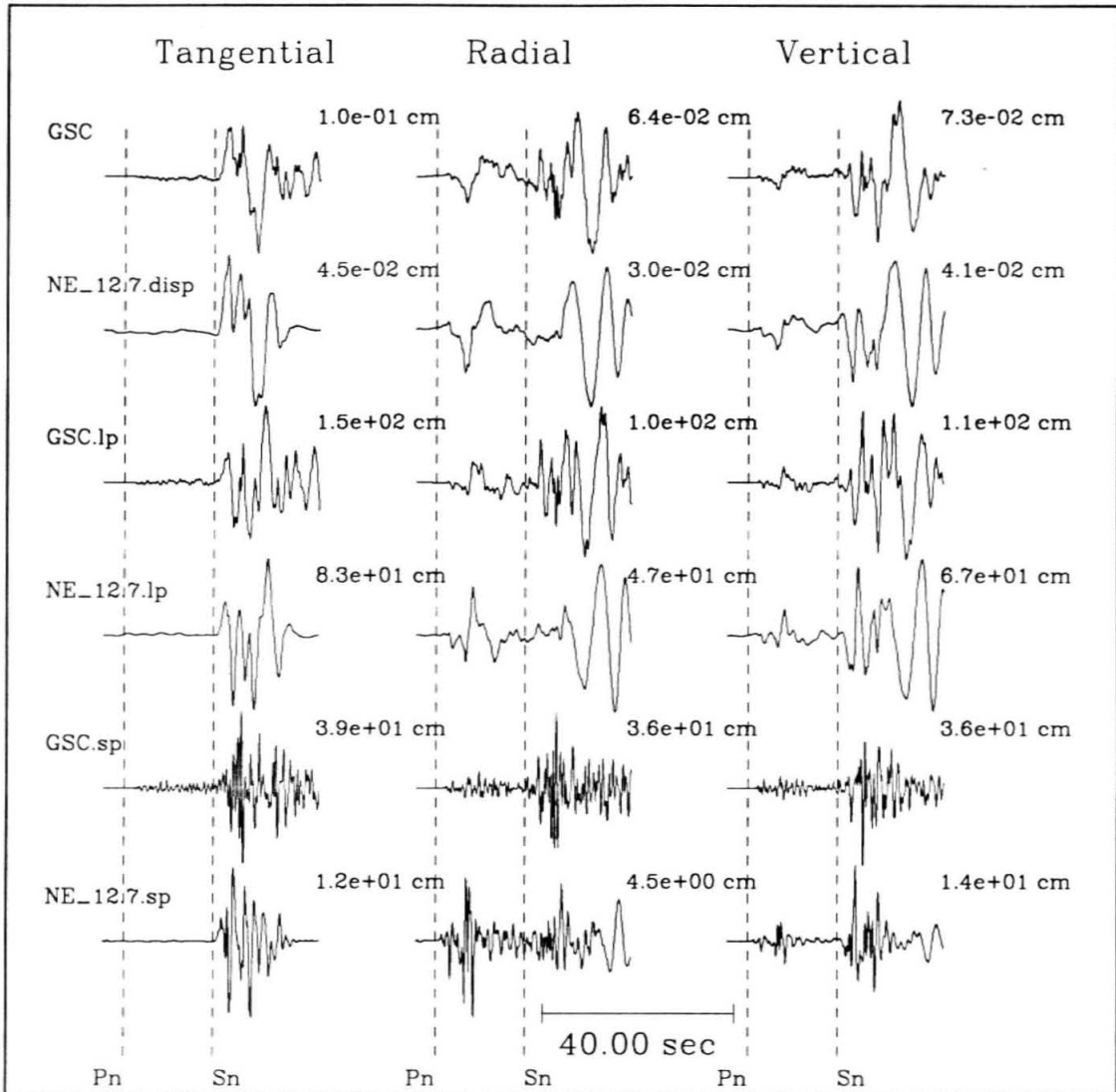
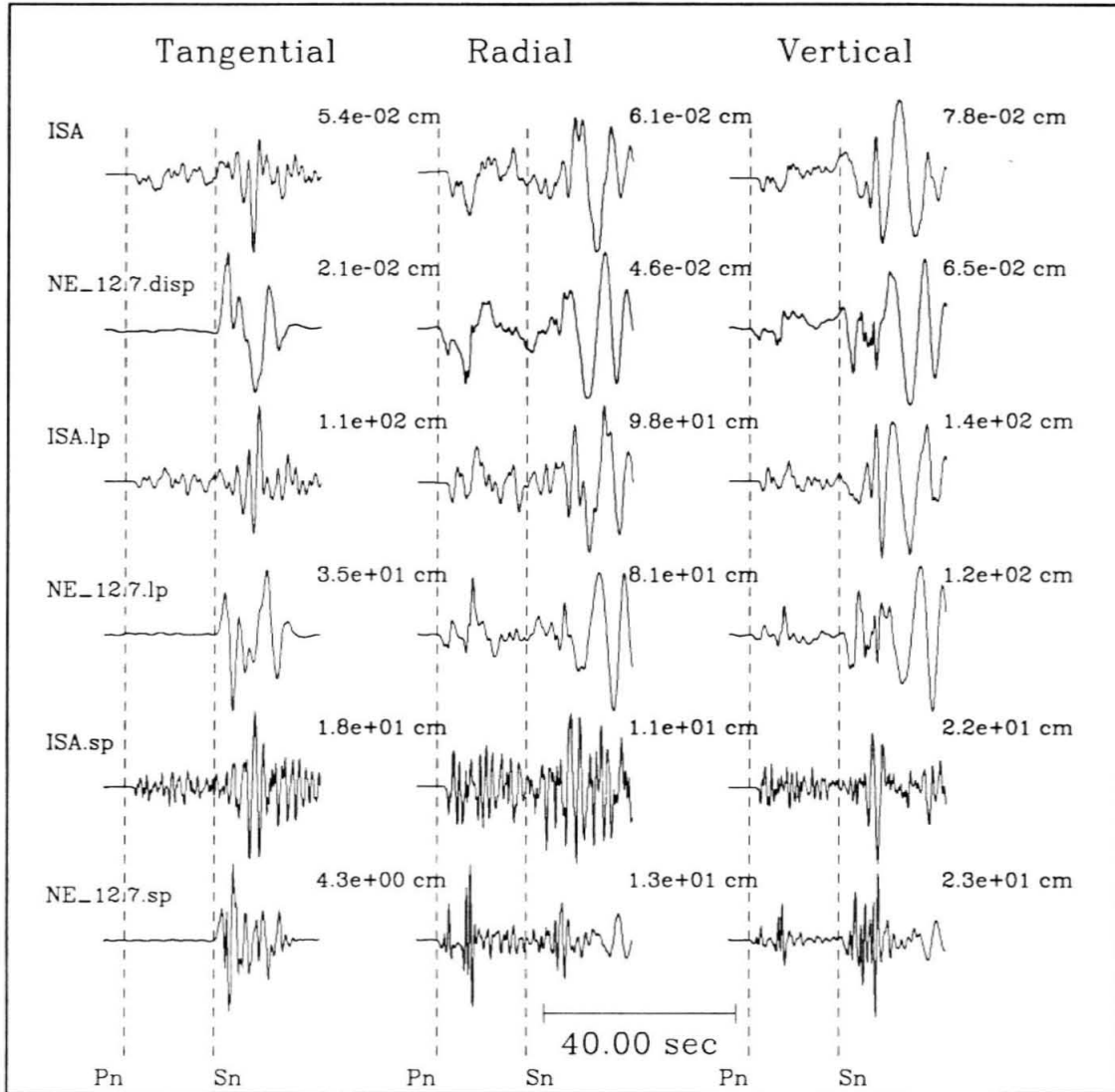
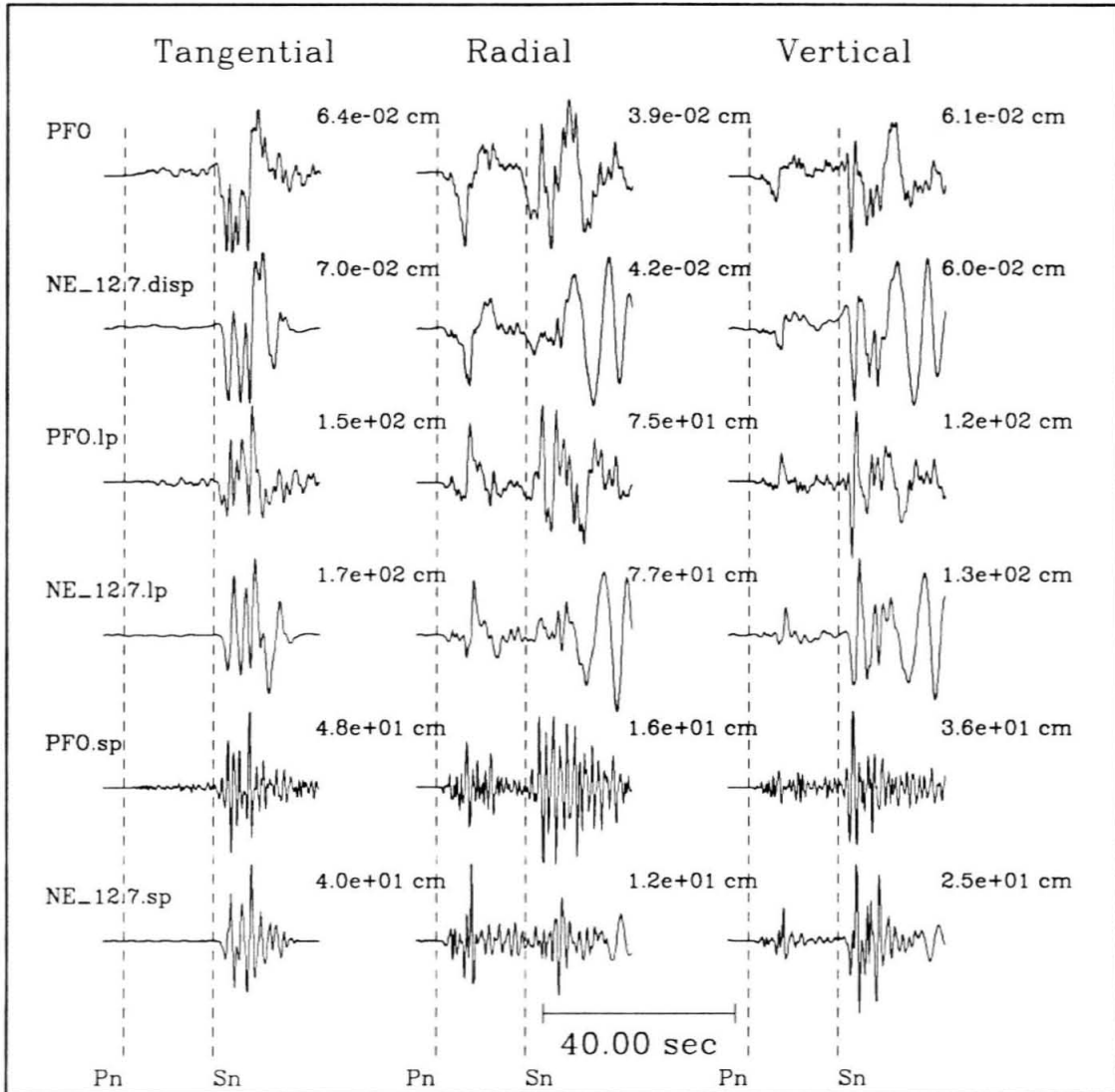


Figure 4.17: Comparison of displacement, WALP, and WASP data and synthetics for a non-uniform slip model at (a) GSC, (b) ISA and (c) PFO.

Directivity Analysis ISA (non-uniform slip)



Directivity Analysis PFO (non-uniform slip)



Comparison of Uniform and Non-uniform slip at PAS

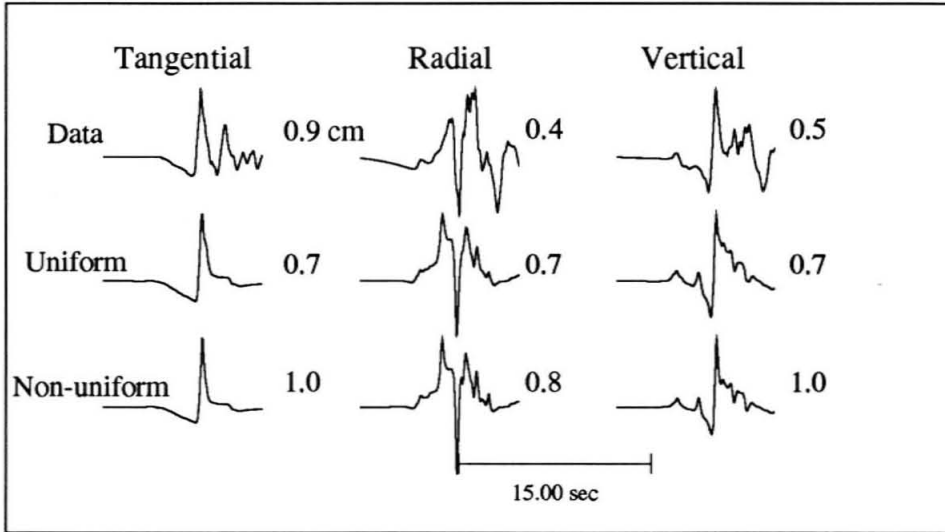


Figure 4.18: Comparison of the PAS displacements with synthetics computed with the uniform and non-uniform slip models

4.2.4 Discussion and Conclusions

The use of regional broadband data to determine information about higher order source processes such as directivity and slip distribution is important for the study of earthquakes that occur outside dense local strong motion arrays, and are too small to be studied teleseismically. At these distances the propagation effects are complicated and care is needed in developing Green's functions that describe the propagation. The contributions from the upper crust as well as the lower crust need to be included. The interaction of initially up-going versus down-going waves is especially important in studies of this type. Energy reflected from the deep crust appears to be less affected by scattering than the direct arrivals which have a longer travel path in heterogeneous near surface material and therefore directivity may be more apparent [Helmberger et al., 1992c].

The results of this study show that source directivity can be identified in the

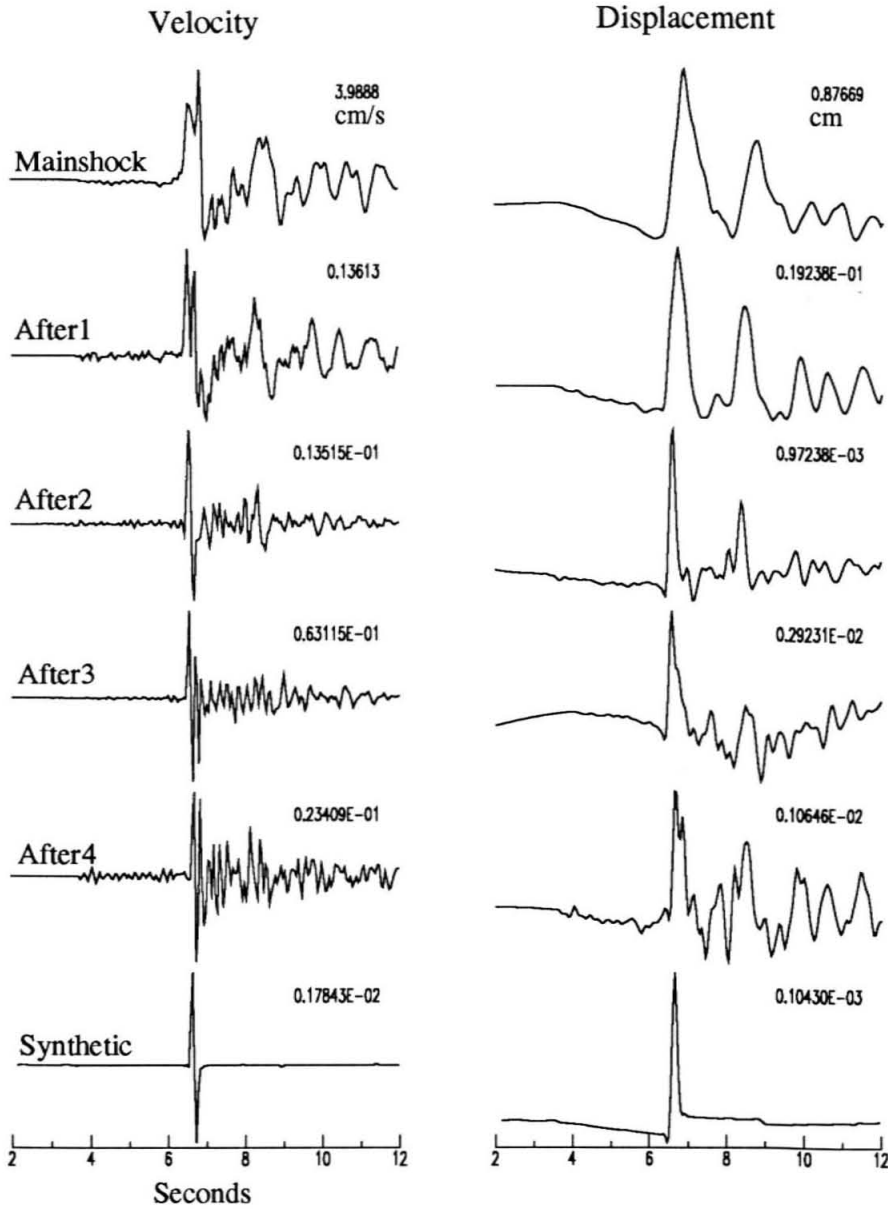


Figure 4.19: Comparison of tangential component velocity and displacement waveforms for the Sierra Madre mainshock and several aftershocks. The synthetic seismogram was computed with a $Q_{\beta} = 300$, distance of 21 km, the mainshock mechanism and a seismic moment of 10^{20} dyne-cm.

near-regional distance data. The directivity is manifest in the data by azimuthally dependent short to long period amplitude ratios, which are also evident in the SH displacement spectra. The waveform modeling indicates that good fits are obtained in the broadband and WALP bandwidths with a uniform slip model that ruptures updip toward the southwest. This model under predicts the amplitudes in the WASP bandwidth however. A non-uniform slip model which has a relatively small (4 km^2) asperity releasing 35 % of the total seismic moment improves the fit in the WASP bandwidth. Wald's [1992] dislocation model shows that a large fraction of slip occurred on a relatively small patch of fault compared to the whole faulting surface. These results agree with Helmberger et al.'s [1992c] observation that the velocity records require less seismic moment to explain the amplitudes than required by the long-period data. A comparable observation was made for the 1990 Upland earthquake, where a relatively small patch of large slip controlled the shape and amplitude of the shorter-period waveforms recorded at PAS. Similarly, Kanamori et al. [1990] found that the seismic moment required by the two far field source pulses of the December 3, 1988 ($M_L = 4.9$) Pasadena earthquake was one-half of the seismic moment required by the near field motions. Furthermore, the rise times of each of the far field pulses were significantly less than required to explain the near field motions. Their conclusion was that the two far field pulses were produced by high stress drop asperities with source dimensions considerably less than the overall rupture dimension, and that the region surrounding the asperities slipped during the event but at a slower rate. In addition, observed differences in teleseismic short-period and long-period seismic moment estimates by as much as a factor of 6 have been reported by Bent and Helmberger [1991b] for events that have occurred along the south coast of California. Imprecise knowledge of Q along the paths places doubt on individual measurements, but since all of the events in that study have similar travel paths the differences among the events is probably meaningful. Thus it appears that shorter-

period energy often is radiated from asperities within the fault that comprise only a fraction of the total fault surface that undergoes slip during an earthquake.

Bibliography

- Beck, S. L., and H. J. Patton. Inversion of Regional Surface-wave Spectra for Source Parameters of Aftershocks from the Loma Prieta Earthquake. *Bull. Seism. Soc. Am.*, **81**, 1726-1736, 1991.
- Bent, A. L., and D. V. Helmberger. A Re-examination of Historic Earthquakes in the San Jacinto Fault Zone, California. *Bull. Seism. Soc. Am.*, **81**, 2289-2309, 1991a.
- Bent, A. L., and D. V. Helmberger. Seismic Characteristics of Earthquakes Along the Offshore Extension of the Western Transverse Ranges. *Bull. Seism. Soc. Am.*, **81**, 339-422, 1991b.
- Brune, J. N. Tectonic Stress and the Spectra of Seismic Shear Waves from Earthquakes. *J. Geophys. Res.* **75**, n. B6, 4997 - 5009, 1970.
- California Dept. Water Res. Meeting Water Demands in the Chino-Riverside Area: Appendix A - Water Supply. *Calif. Dept. Water Res. Bull.*, **104-3**, pp 108, 1970.
- Clark, M. M., D. P. Hill, K. R. Lajoie, A. R. Lindy, D. H. Openheimer, and J. C. Yount. Mono Basin Earthquake of October 23, 1990. *U.S. Geologic Survey Internal Report*, 1991.
- Cohn, S. N., T. Hong, and D. V. Helmberger. The Oroville Earthquakes: A Study of Source Characteristics and Site Effects. *J. Geophys. Res.* **87**, **87**, n. B6, 4585 - 4594, 1982.
- Cramer, C. H. and J. M. Harrington. Seismicity and Tectonics of the Cucamonga Fault and the Eastern San Gabriel Mountains, San Bernardino County. *USGS Professional Paper*, **1339**, p 7 - 26, 1987.
- Depolo, D. M. and S. P. Horton. A Magnitude 5.0 Earthquake near Mono Lake, California. *Seismological Research Letters* **62**, No. 1, p 52, 1991.

- Dreger, D. S. and D. V. Helmberger. Broad-band Modeling Local Earthquakes. *Bull. Seism. Soc. Am.* **80**, 1162 - 1179, 1990.
- Dreger, D. S. and D. V. Helmberger. Complex Faulting Deduced from Broadband Modeling of the February 28, 1990 Upland Earthquake ($M_L=5.2$). *Bull Seism Soc. Am.* **81**, 1129-1144, 1991a.
- Dreger, D. S. and D. V. Helmberger. Source Parameters of the Sierra Madre Earthquake from Regional and Local Body Waves. *Geophys. Res. Let.* **18**, No. 11, 2015-2018, 1991b.
- Dreger, D. S. and D. V. Helmberger. Determination of Source Parameters at Regional Distances with Three-Component Sparse Network Data. *Submitted to Journ. Geophys. Res.*, 1992.
- Fan, G. and T. C. Wallace. The Determination of Source Parameters for Small Earthquakes from a Single Very Broadband Seismic Station. *Geophys. Res. Let.* **18**, No. 8, 1385-1388, 1991.
- Frankel, A. and R. W. Clayton. A Finite Difference Simulation of Wave Propagation in Two-dimensional Random Media. *Bull. Seism. Soc. Am.* **74**, 2167-2186, 1984.
- Hadley, D. and H. Kanamori. Seismic Structure of the Transverse Ranges, California. *Bull. Seism. Soc. Am.*, **88**, 1469-1478, 1977.
- Hadley, D. and H. Kanamori. Regional S-wave Structure for Southern California from the Analysis of Teleseismic Rayleigh Waves. *Geophys. J. R. Intern.*, **58**, 655-666, 1979.
- Hartzell, S. Earthquake Aftershocks as Green's Functions. *Geophys. Res. Let.* **5**, p 1 - 5, 1978.
- Hauksson E. and L. M. Jones. The 1988 and 1990 Upland Earthquakes: Left-Lateral Faulting Adjacent to the Central Transverse. *J. Geophys. Res.* **96**, No. B5, p 8143 - 8165, 1991.
- Hauksson E. The 1991 Sierra Madre Earthquake Sequence in Southern California: Seismological and Tectonic Analysis. *submitted to J. Geophys. Res.*, 1992.
- Heaton, T. H. and D. V. Helmberger. Generalized Ray Models of the San Fernando Earthquake. *Bull. Seism. Soc. Am.* **69**, 1311 - 1341, 1979.
- Helmberger, D. V. Generalized Ray Theory for Shear Dislocations, *Bull. Seism. Soc. Am.* **64**, No. 1, 45 - 64, 1974.

- Helmberger, D. V., and S. D. Malone. Modeling Local Earthquakes as Shear Dislocations in a Layered Half Space. *J. Geophys. Res.* **80**, No. 35, 4881 - 4888, 1975.
- Helmberger, D. V. and G. R. Engen. Modeling the Long-Period Body Waves from Shallow Earthquakes at Regional Distances. *Bull. Seism. Soc. Am.* **70**, 1699-1714, 1980.
- Helmberger, D. V. Theory and Application of Synthetic Seismograms. *Earthquakes: Observation Theory and Interpretation* Soc. Italiana di Fisica, Bologna, Italy, p 174 - 222, 1983.
- Helmberger, D. V., and J. E. Vidale. Modeling Strong Motions Produced by Earthquakes with Two-Dimensional Numerical Codes. *Bull. Seism. Soc. Am.* **78**, No. 1, 109 - 121, 1988.
- Helmberger, D. V., R. Stead, P. Ho-Liu, and D. S. Dreger. Broadband Modeling of Regional Seismograms; Imperial Valley to Pasadena. *Geophys. J. Intern.*, **In press**, 1992a.
- Helmberger, D. V., L. S. Zhao, D. S. Dreger, and V. LeFevre. Exploration of the Lower Lithosphere; Northeastern United States. *Phys. Earth Planet. Inter.*, **70**, Nos 1 - 2, 22-38, 1992b.
- Helmberger, D., D. Dreger, R. Stead, and H. Kanamori. Impact of Broadband Seismology on Strong Motion Attenuation. *In Preparation*, 1992c.
- Ho-Liu, P. I. Attenuation Tomography II. Modeling Regional Love Waves: Imperial Valley to Pasadena. *Ph. D. Thesis*, California Institute of Technology, Pasadena, California, 1988.
- Ho-Liu P., and D. V. Helmberger. Modeling Regional Love Waves: Imperial Valley to Pasadena. *Bull. Seism. Soc. Am.* **79**, 1194-1209, 1989.
- Jennings, C. W. Fault Map of California with Locations of Volcanoes, Thermal Springs and Thermal Wells. California Division of Mines and Geology, No. 1, 1975.
- Jones, L. M., and R. S. Dollar. Evidence of Basin-and-Range Extensional Tectonics in the Sierra Nevada: The Durwood Meadows Swarm, Tulare County, California (1983-1984). *Bull. Seism. Soc. Am.* **76**, 439-461, 1986.
- Kanamori, H. and D. L. Anderson. Theoretical Basis of some Empirical Relations in Seismology. *Bull. Seism. Soc. Am.* **65**, 1073 - 1095, 1975.

- Kanamori, H., J. Mori, and T. H. Heaton. The 3 December 1988, Pasadena Earthquake ($M_L=4.9$) Recorded With the Very Broadband System in Pasadena. *Bull. Seism. Soc. Am.* **80**, 483 - 487, 1990).
- Langston, C. Scattering Under Pasadena, California. *J. Geophys. Res.* **94**, 1935 - 1952, 1989.
- Liu, H., and D. V. Helmberger. The 23:19 Aftershock of the 15 October 1979 Imperial Valley Earthquake: More Evidence for an Asperity. *Bull. Seism. Soc. Am.* **75**, 689 -708, 1985.
- Ma, K. F., and H. Kanamori. Aftershock Sequence of the 3 December 1988 Pasadena Earthquake. *Bull. Seism. Soc. Am.*, **81**, 2310-2319, 1991.
- Mendoza, C., and S. H. Hartzell. Aftershock Patterns and Mainshock Faulting. *Bull. Seism. Soc. Am.* **78**, 1438-1449, 1988.
- Mori, J. and S. Hartzell. Source Inversion of the 1988 Upland Earthquake: Determination of a Fault Plane for a Small Event. *Bull. Seism. Soc. Am.* **80**, 507 -518, 1990.
- Patton H. J., and D. I. Doser. Inversion of Regional P_{nl} and Surface-wave data for the Source Parameters of the Borah Peak Aftershock. *Geophys. Res. Lett.*, **15**, 459-462, 1988.
- Saikia, C. Synthetics of Seismograms at Buried Receivers in a Multi-layered Medium using Frequency-Wavenumber Integration. *In preparation*, 1992.
- Saikia, C., D. Dreger, and D. Helmberger. Modeling of Energy Amplification Recorded within Greater Los Angeles Using Irregular Structure. *Submitted to Bull. Seism. Soc. Am.*, 1992.
- Scrivner, C. W., and D. V. Helmberger. Constraints on the Seismic Structure in and beneath the Los Angeles Basin. *Seismo. Res. Let.* **63**, 1992.
- Shor, G. G., and E. Roberts. San Miguel, Baja California Norte, Earthquakes of February, 1956. *Bull. Seism. Soc. Am.*, **48**, 101-116, 1958.
- Stead, R.J. Finite Differences and a Coupled Analytic Technique with Applications to Explosions and Earthquakes. *Ph. D. Thesis*, California Institute of Technology, Pasadena, California, 1989.
- Stover, C. W., and B. G. Reagor. Preliminary Iseismal Map for the Sierra Madre, California, earthquake of June 28, 1991. *U.S. Geological Survey Open-File Report*, **91-388**, 1-16, 1991.

- Thio, H. K. and H. Kanamori. A Surface-wave Study on the Structure of the Crust and Mantle Under Southern California. *EOS Trans. AGU*, **72**, p. 324, 1991.
- Tull, J. E. SAC (Seismic Analysis Code) Computer Program. Regents of the University of California, 1987.
- Vidale, J. E., and D. V. Helmberger. Elastic Finite-Difference Modeling of the 1971 San Fernando, California Earthquake. *Bull. Seism. Soc. Am.* **78**, No. 1, 122 - 141, 1988.
- Wald, D. J. Strong Motion and Broadband Teleseismic Analysis of the 1991 Sierra Madre, California, Earthquake. *submitted to Journ. Geophys. Res.*, 1992.
- Wallace, T. C., D. V. Helmberger, and G. R. Mellman A Technique for the Inversion of Regional Data in Source Parameter Studies. *J. Geophys. Res.* **86**, 1679-1685, 1981.
- Yerkes, R. F., T. H. McCulloh, J. E. Schoellhamer, and J. G. Vedder. Geology of the Los Angeles Basin California - an Introduction. *U.S.G.S. Prof. Paper*, **420-A**, 57 pp, 1965.
- Zhao, L. S., Helmberger, D. V. Broadband Modelling along a regional shield Path, Harvard recording of the Saguenay earthquake. *Geophys. J. Int.* **105**, 301-312 (1991).

Appendix A

Comparison of Several Q Models

Figure A.1 compares several Q models with the averaged SH amplitude spectra recorded at stations GSC, ISA, PFO and SBC for the two largest aftershocks of the 1991 Sierra Madre earthquake. The individual amplitude spectra (Figure 4.14) were normalized to a seismic moment of 10^{20} dyne-cm prior to being averaged. The velocity model SC (Table 2.1) was used to compute the synthetic spectra. Model Q_Mod1 has a uniform $Q_\alpha = 6000$ and $Q_\beta = 3000$. Model Q_Mod2 has a uniform $Q_\alpha = 600$ and $Q_\beta = 300$. Table A.1 compares the other Q models. Q_Mod1

Depth (km)	Q_Mod3		Q_Mod4		Q_Mod5	
	Q_α	Q_β	Q_α	Q_β	Q_α	Q_β
0.0	200	100	100	50	100	50
5.5	600	300	600	300	100	50
16.0	600	300	600	300	600	300

Table A.1: Comparison of Several Q models. Below 16 km the Q values remain unchanged.

clearly has too little attenuation and Q_Mod5 has too much. Q_Mod4 also seems to attenuate a little too much. The best agreement is obtained with models Q_Mod2 and Q_Mod3. The differences in the spectra for these two models are not very large.

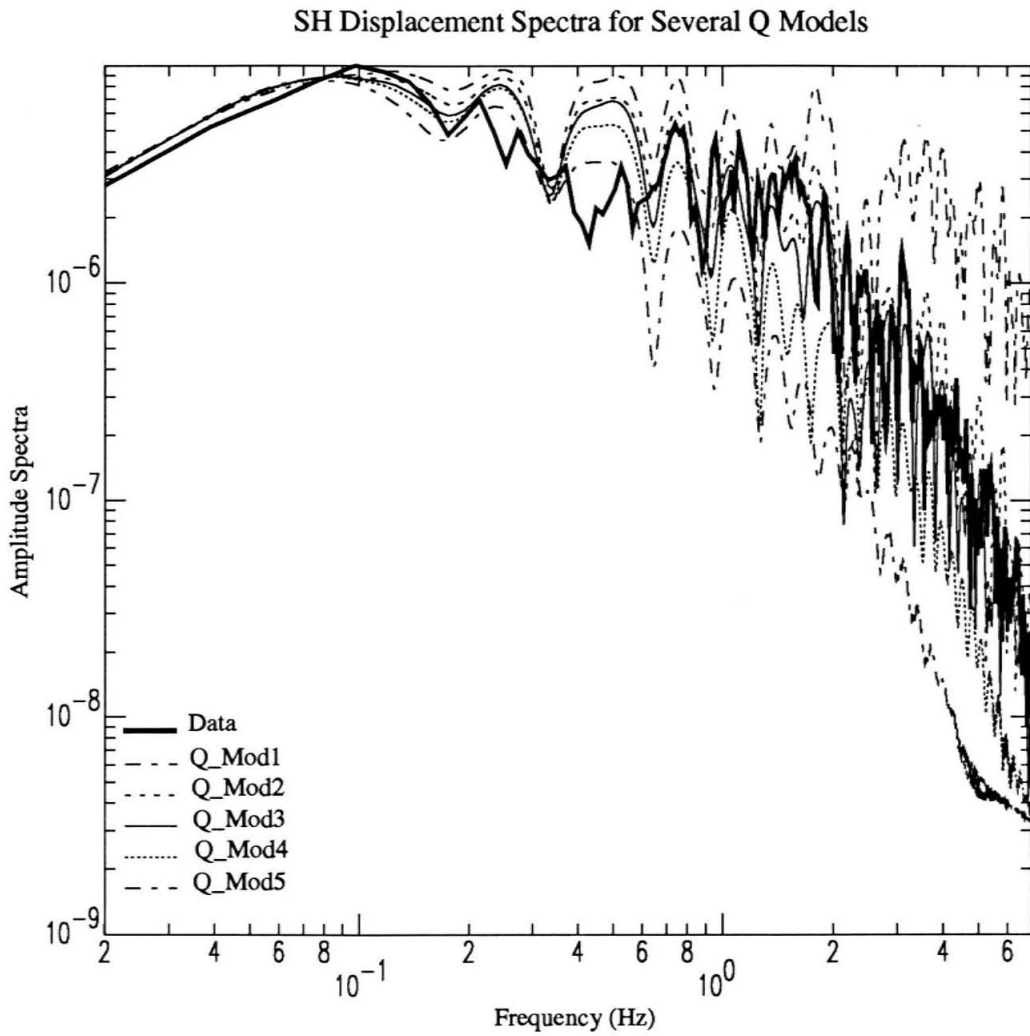


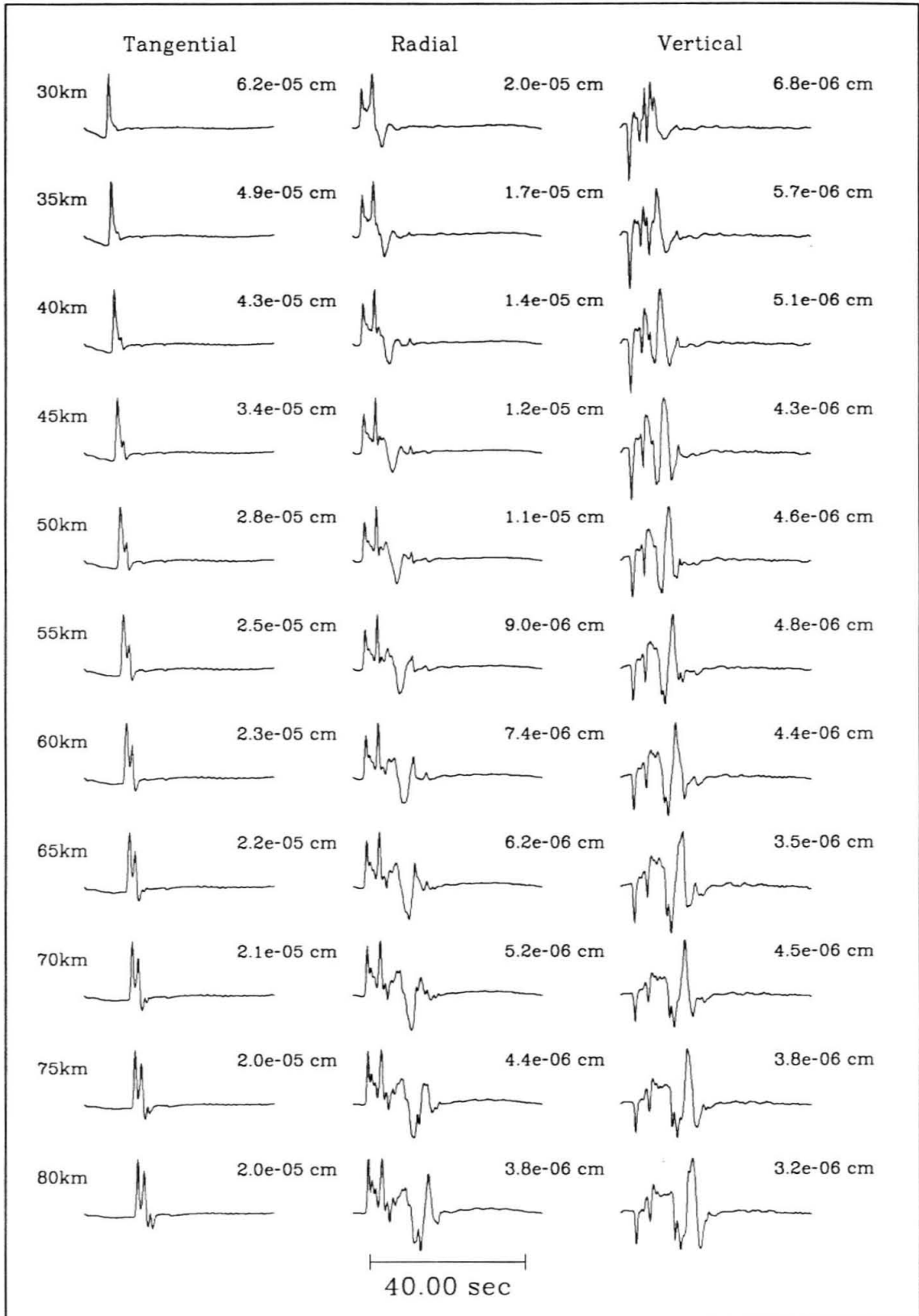
Figure A.1: Comparison of several Q models. See text and Table A.1 for details.

Appendix B

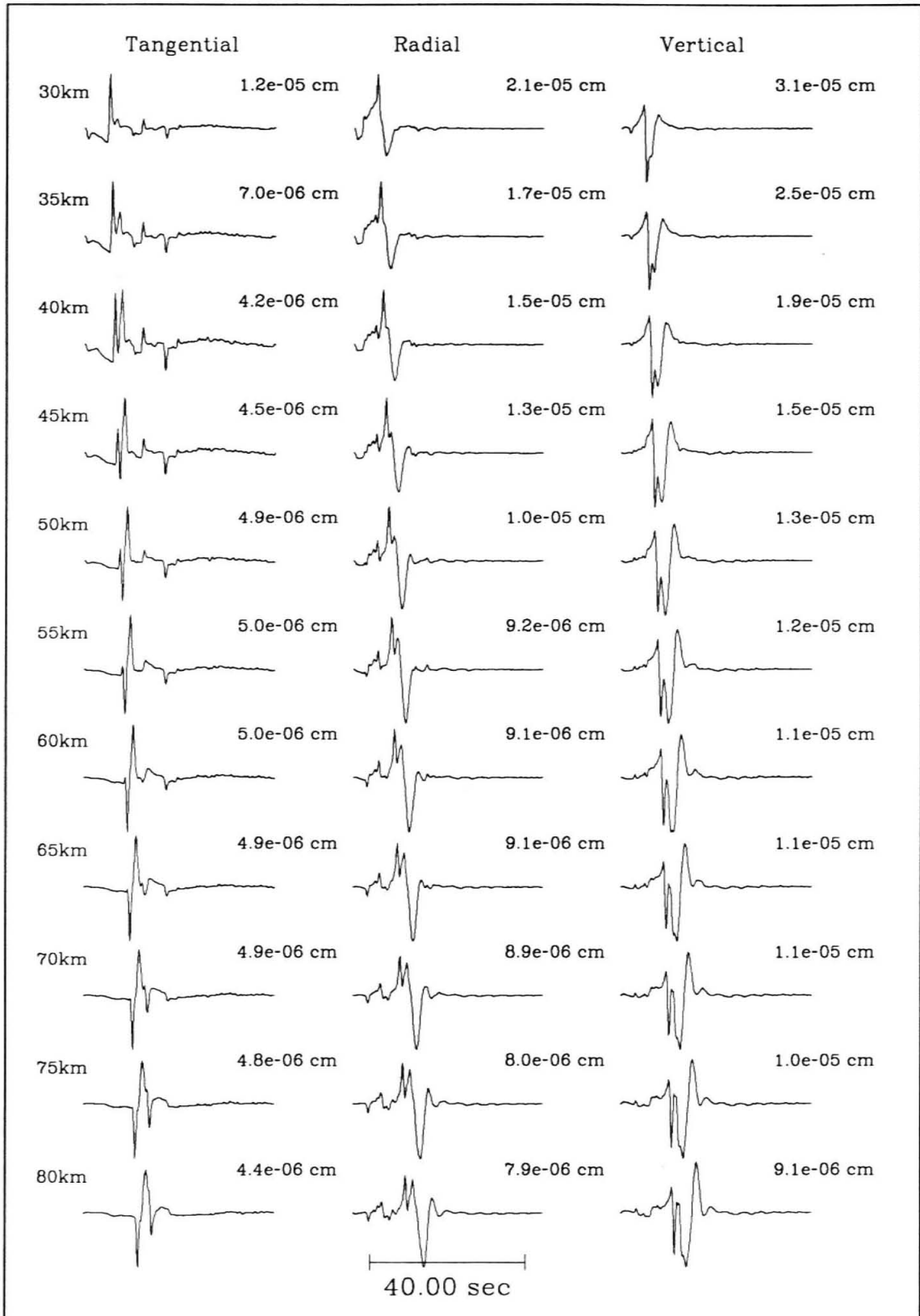
Standard Southern California Model Synthetics

This appendix serves as a catalog of synthetic seismograms for southern California. They have been calculated using model SC (Table 2.1). A seismic moment of 10^{20} dyne-cm was used and the Green's functions were convolved with a 1 second triangular source time function. The synthetics are computed every 5 km in the range from 30 km to 395 km for a source depth of 11 km.

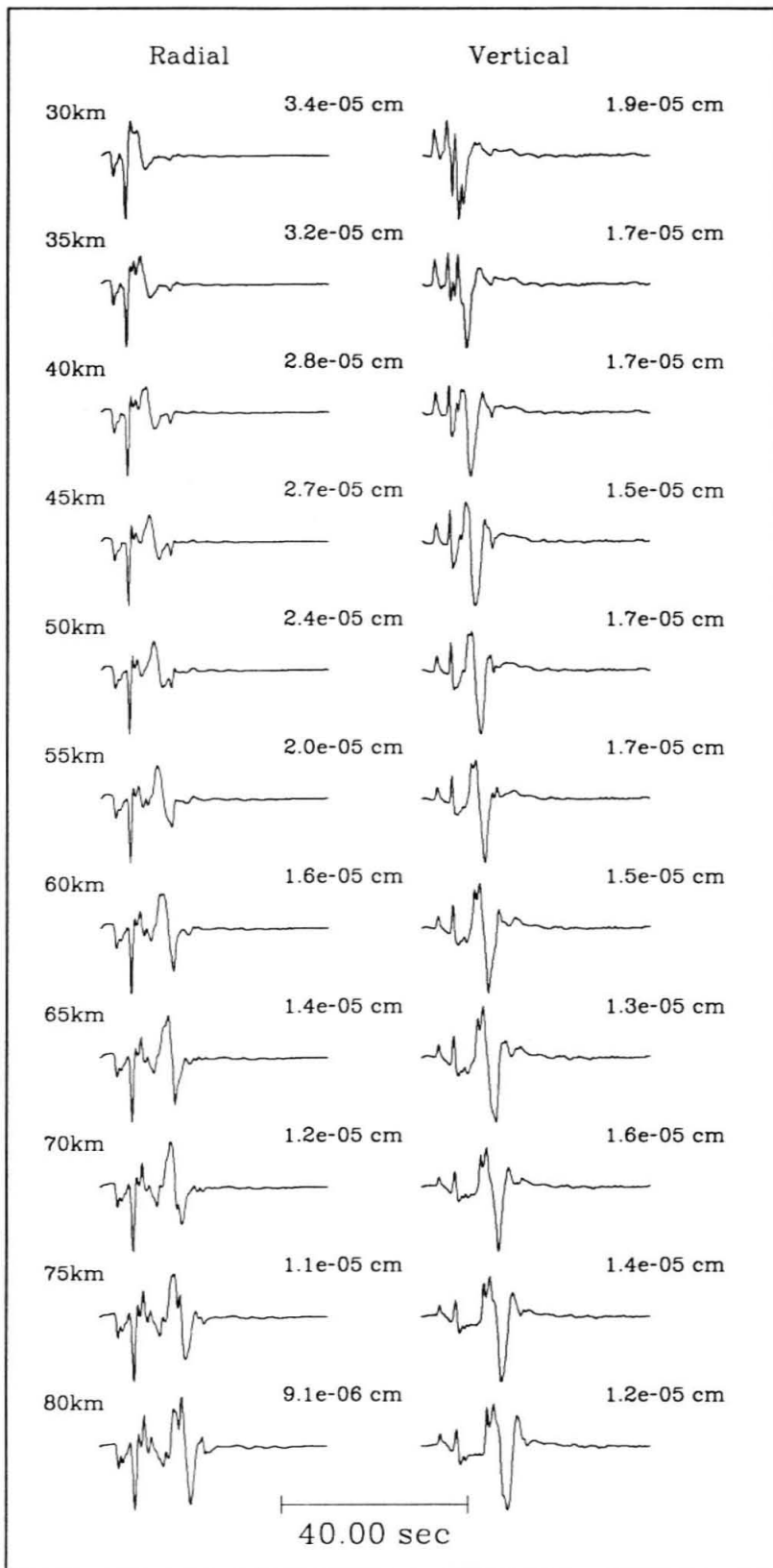
Mechanism: Vertical Strike-slip Depth: 11km



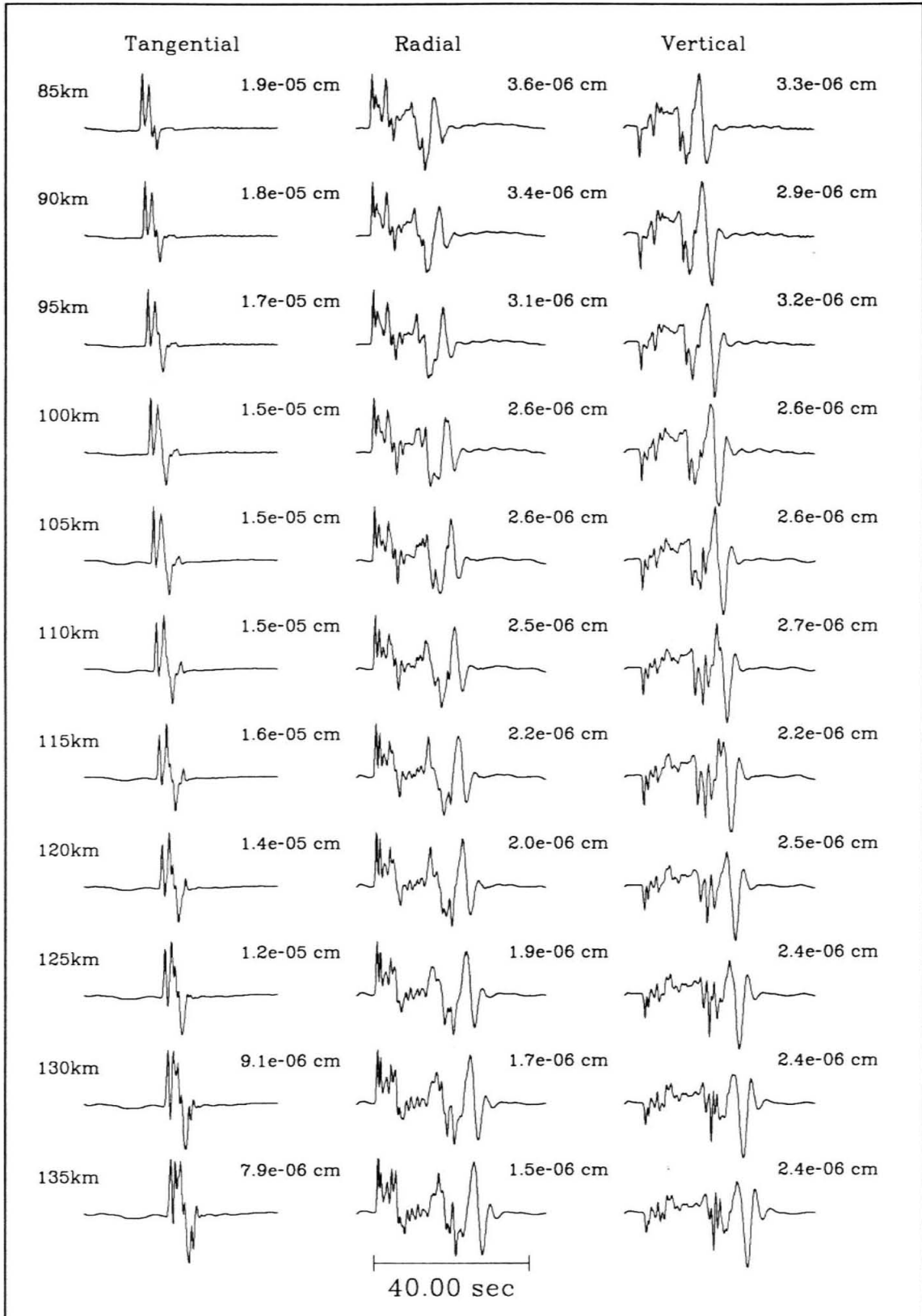
Mechanism: Vertical Dip-slip Depth: 11km



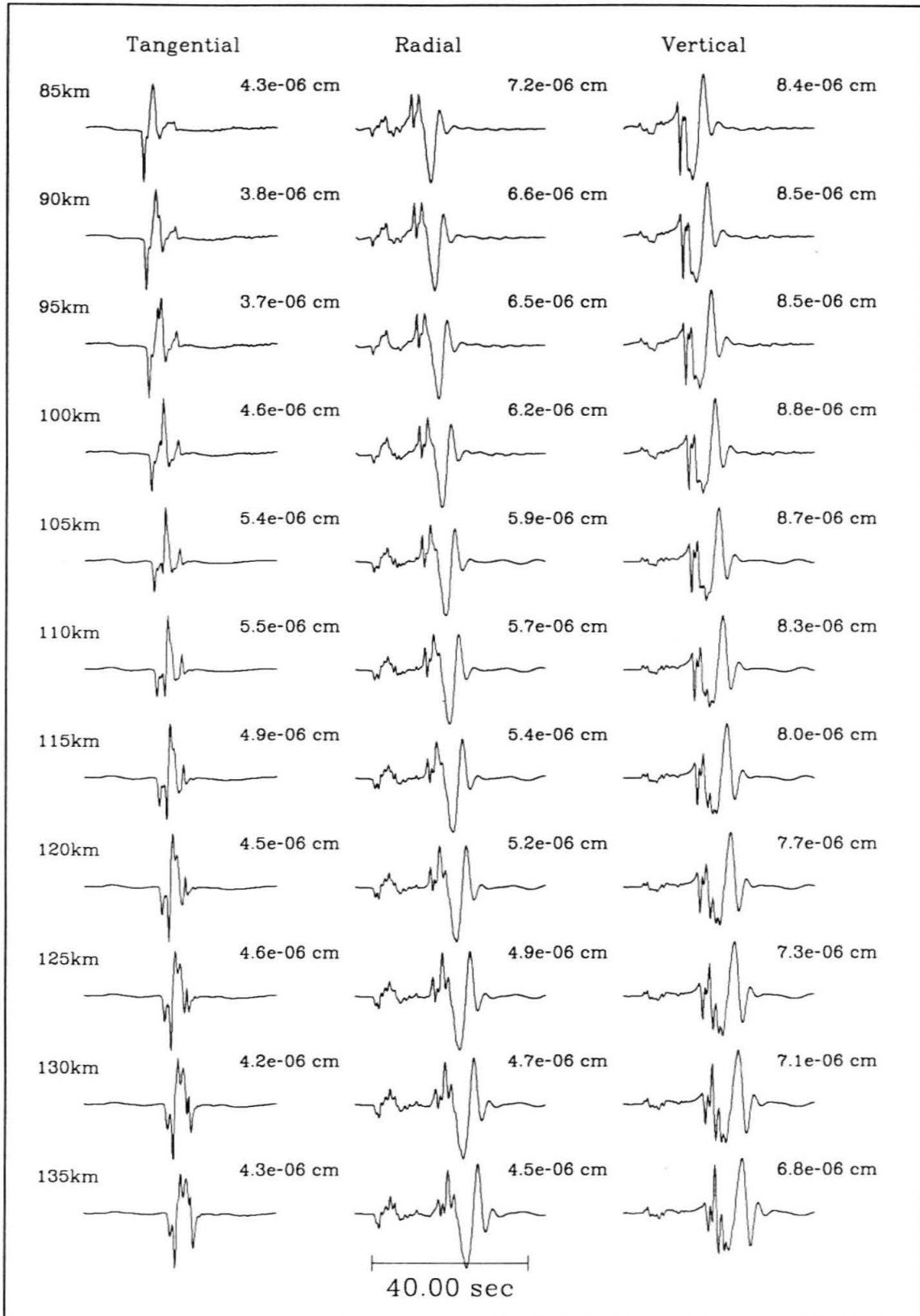
Mechanism: 45 degree Dip-slip Depth: 11km



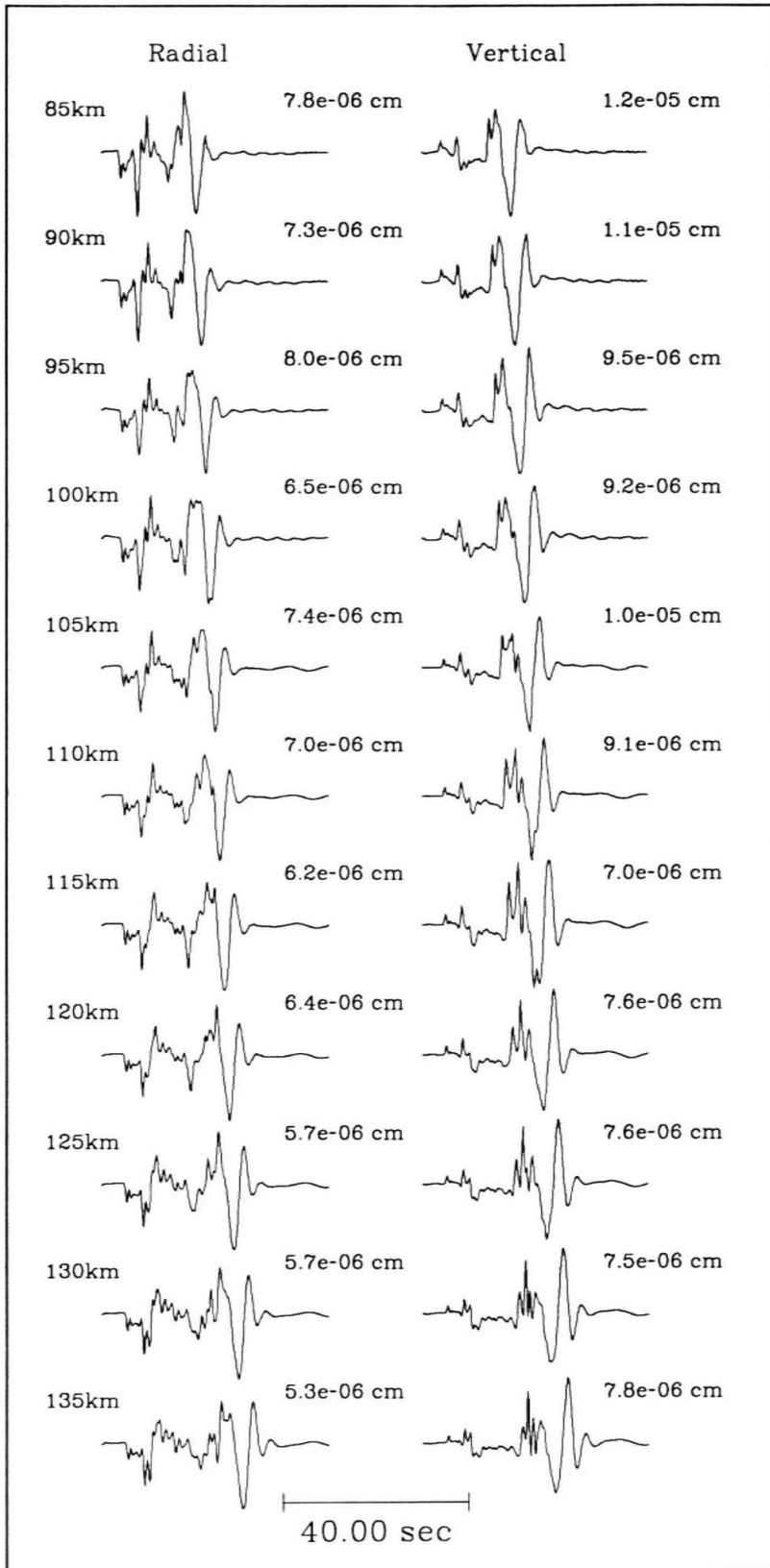
Mechanism: Vertical Strike-slip Depth: 11km

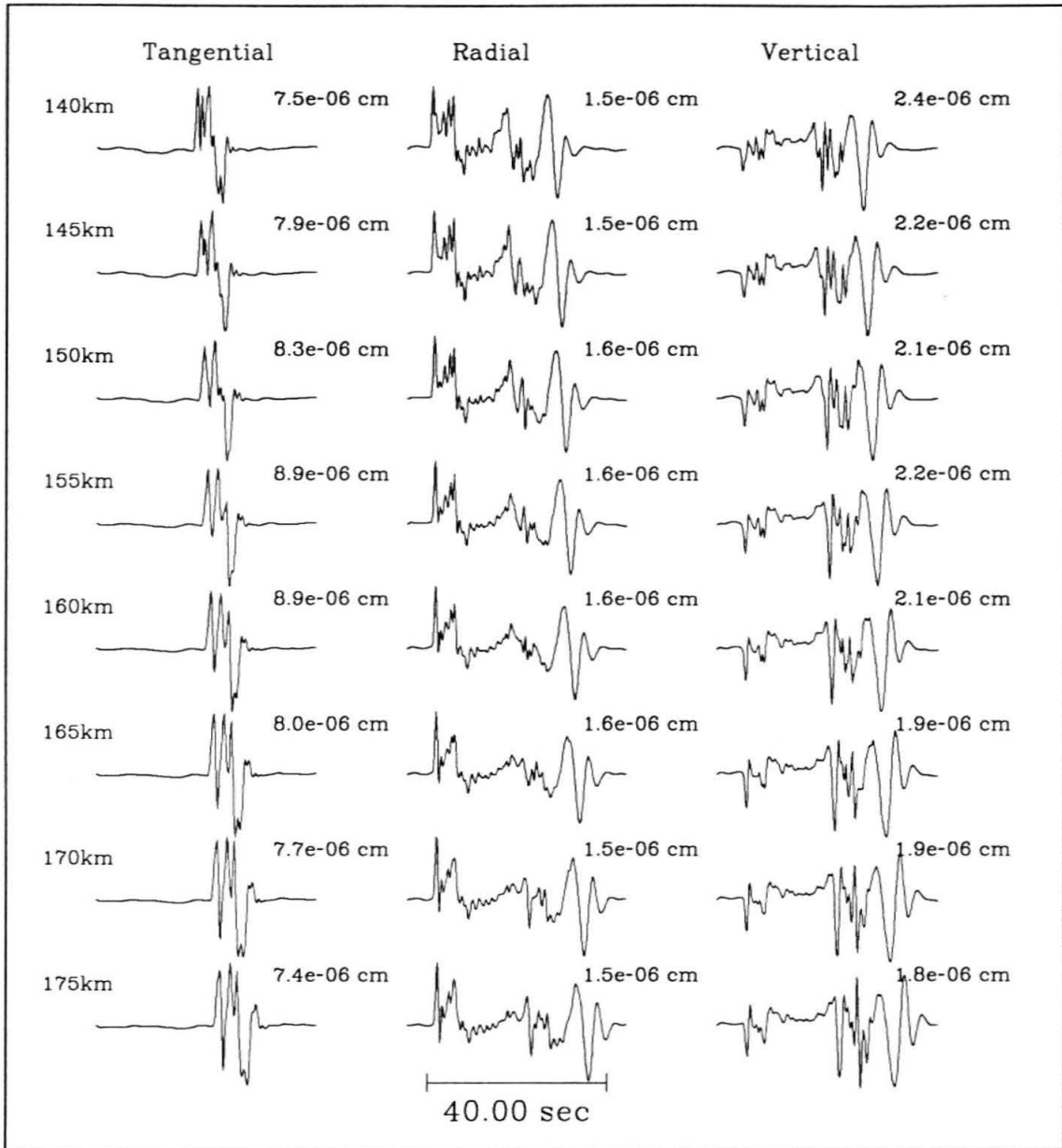


Mechanism: Vertical Dip-slip Depth: 11km

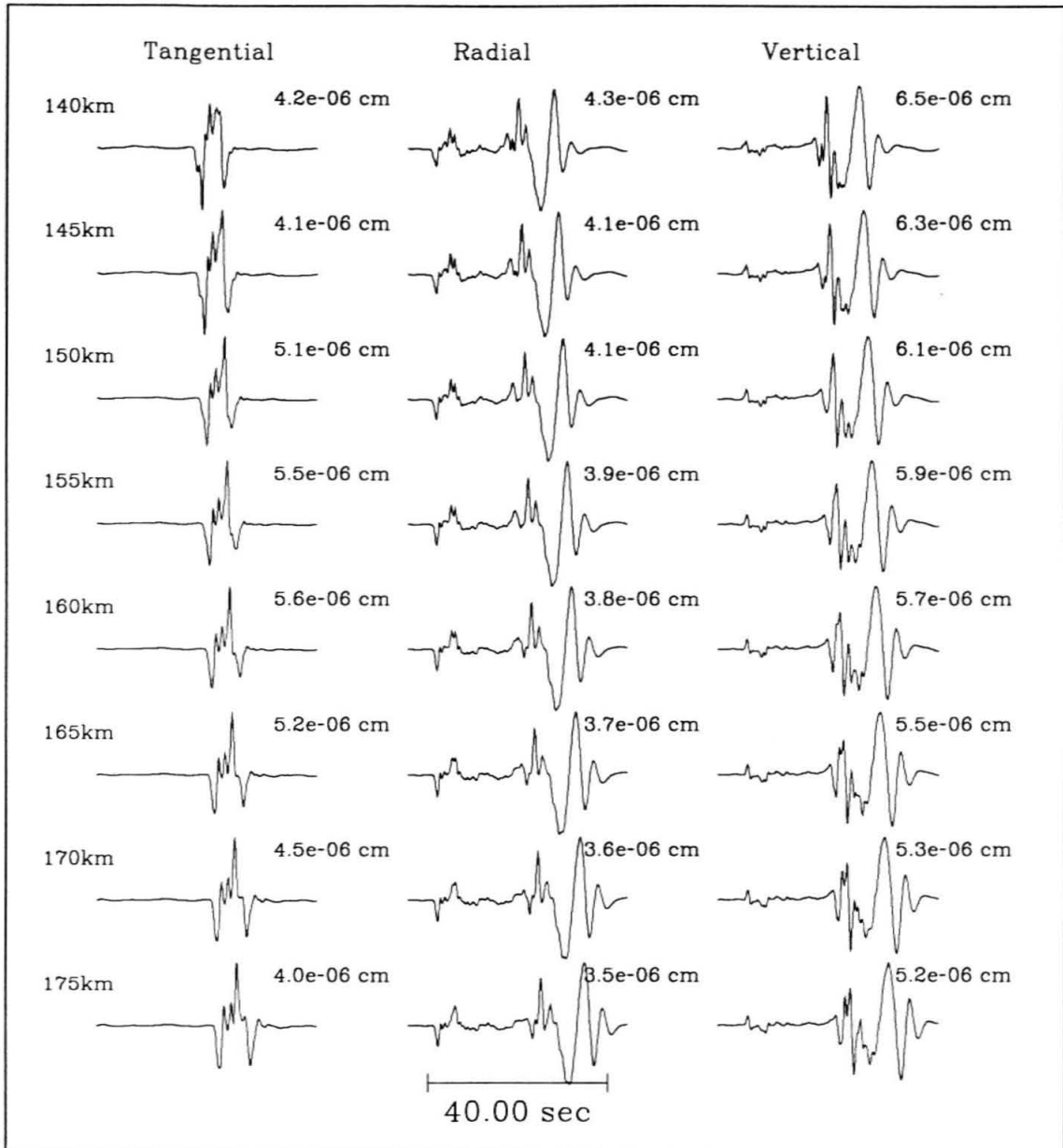


Mechanism: 45 degree Dip-slip Depth: 11km

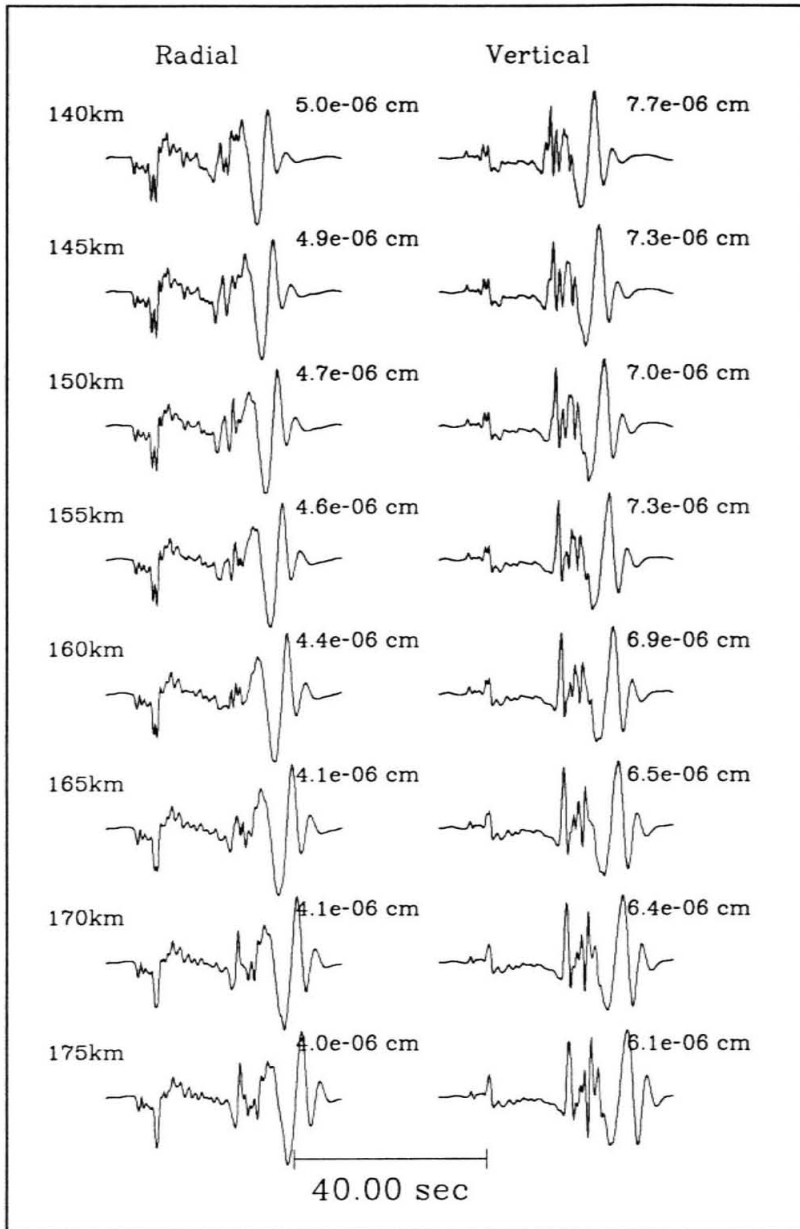


Mechanism: Vertical Strike-slip Depth: 11km

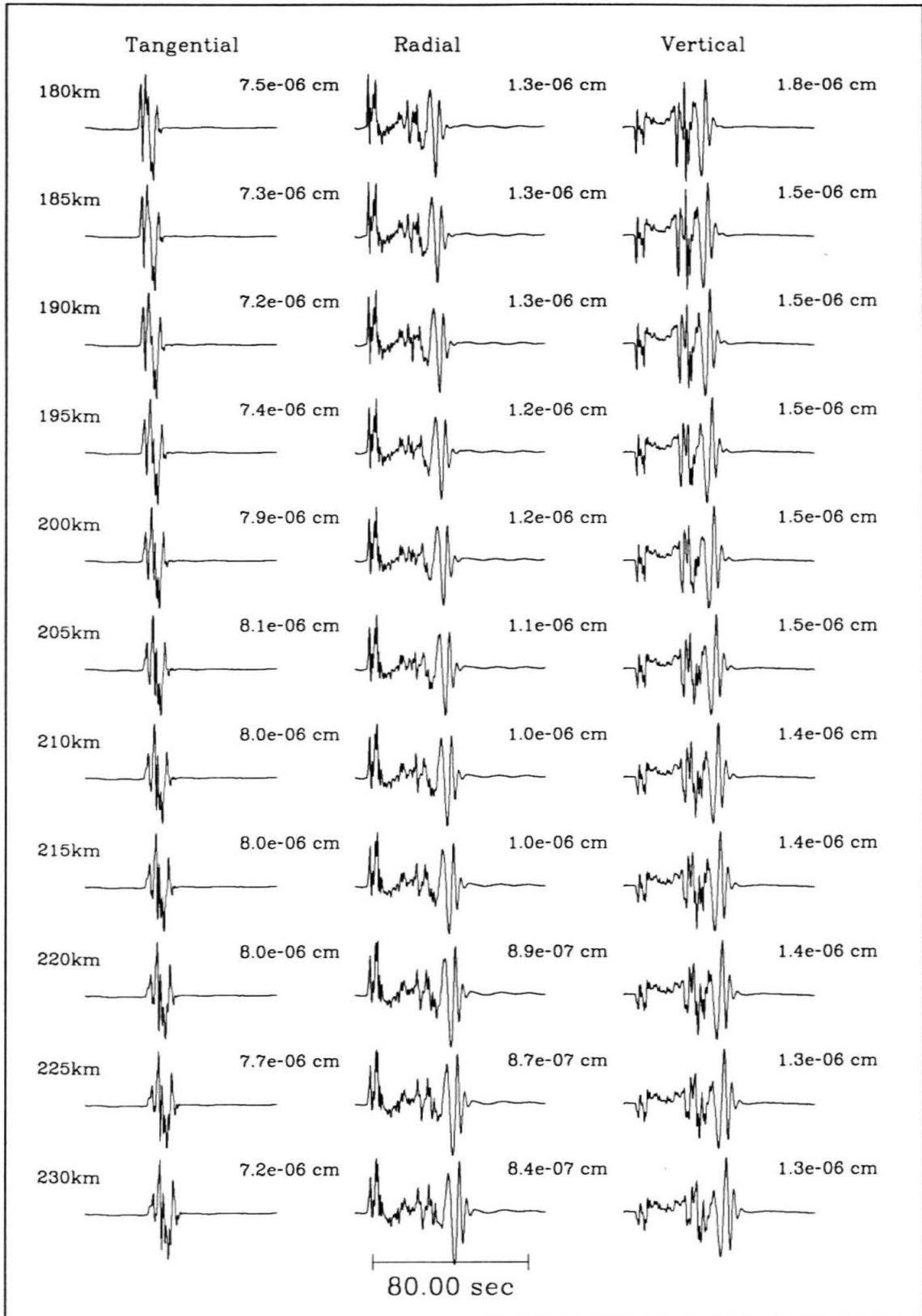
Mechanism: Vertical Dip-slip Depth: 11km



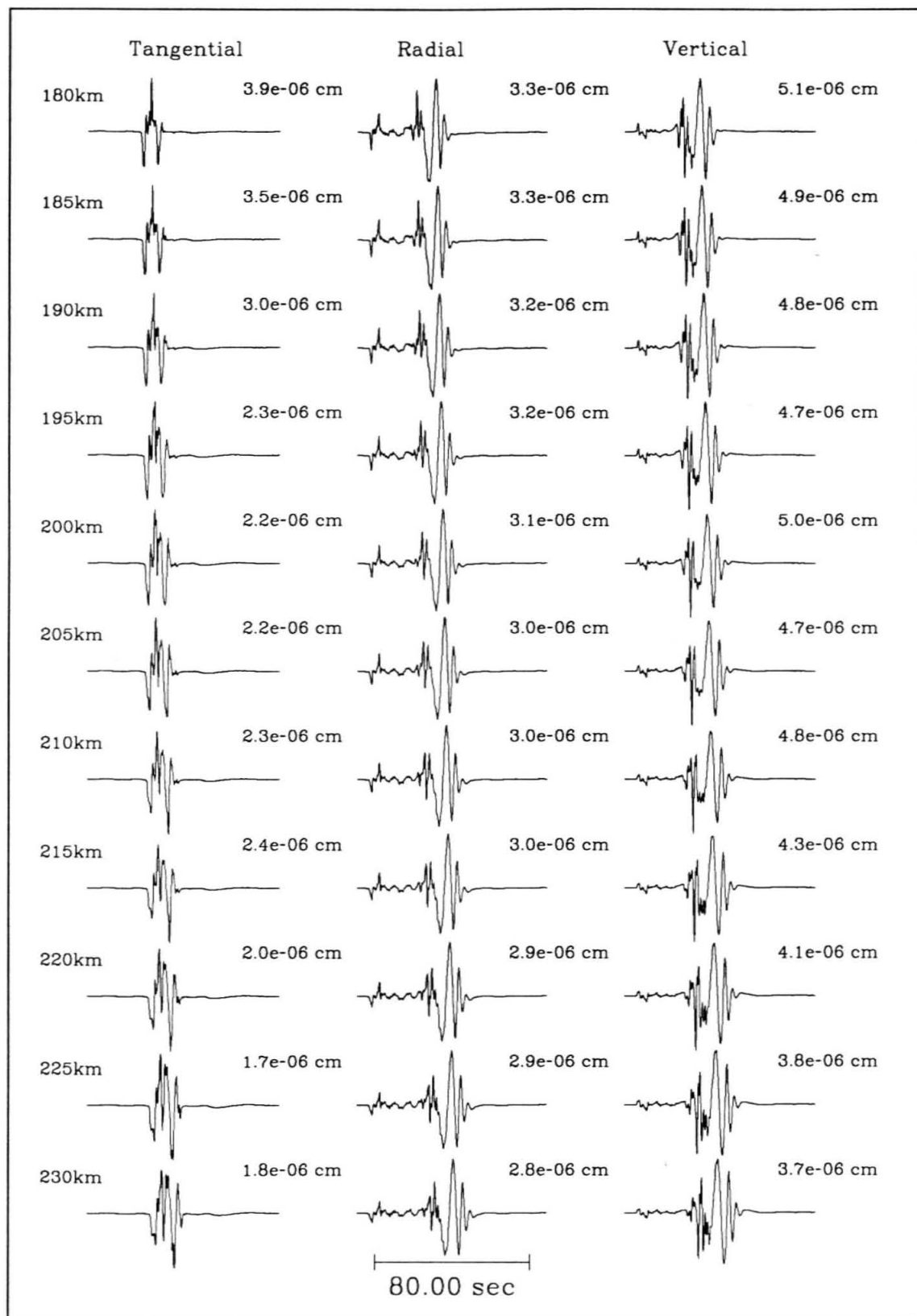
Mechanism: 45 degree Dip-slip Depth: 11km



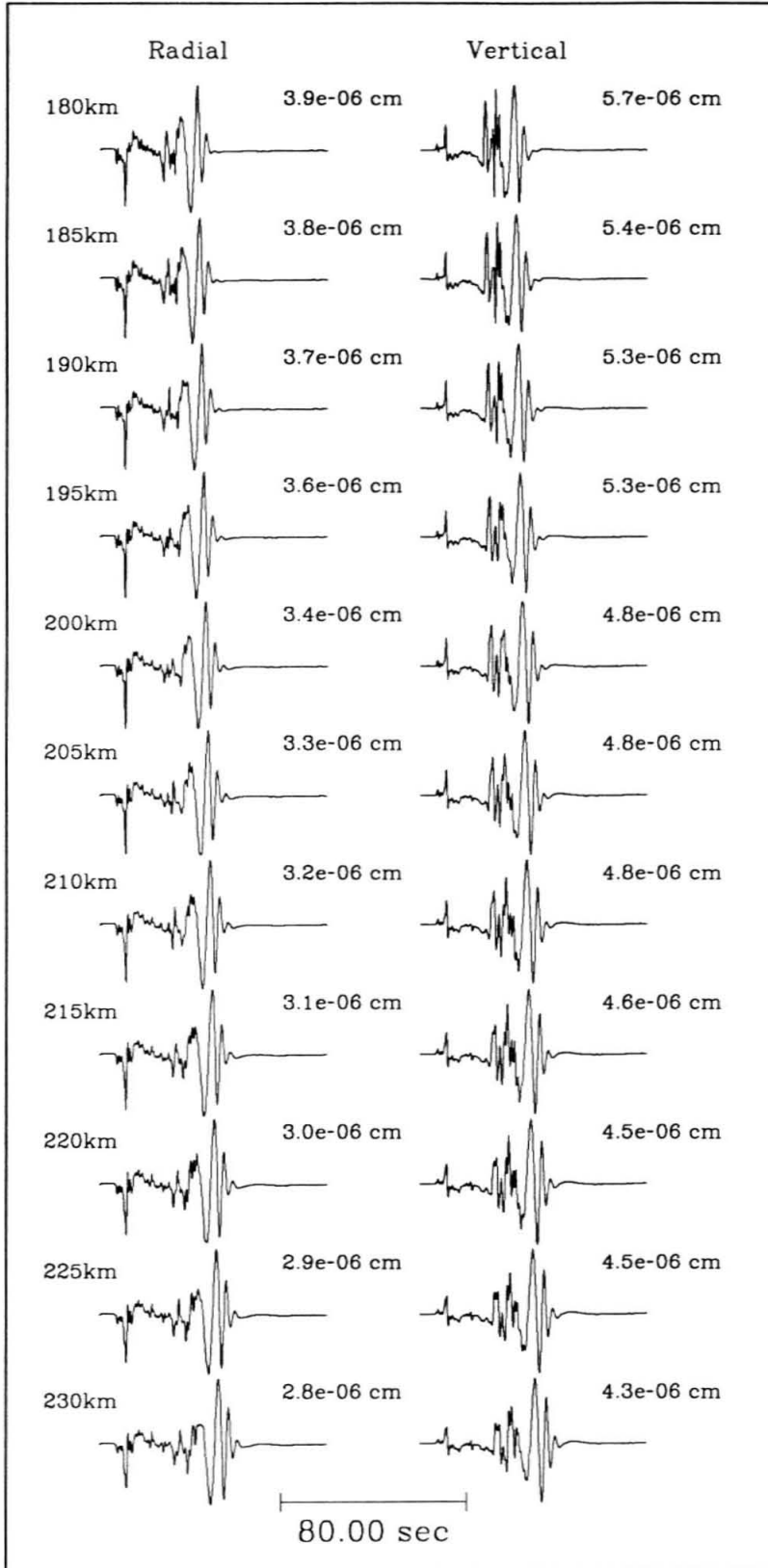
Mechanism: Vertical Strike-slip Depth: 11km



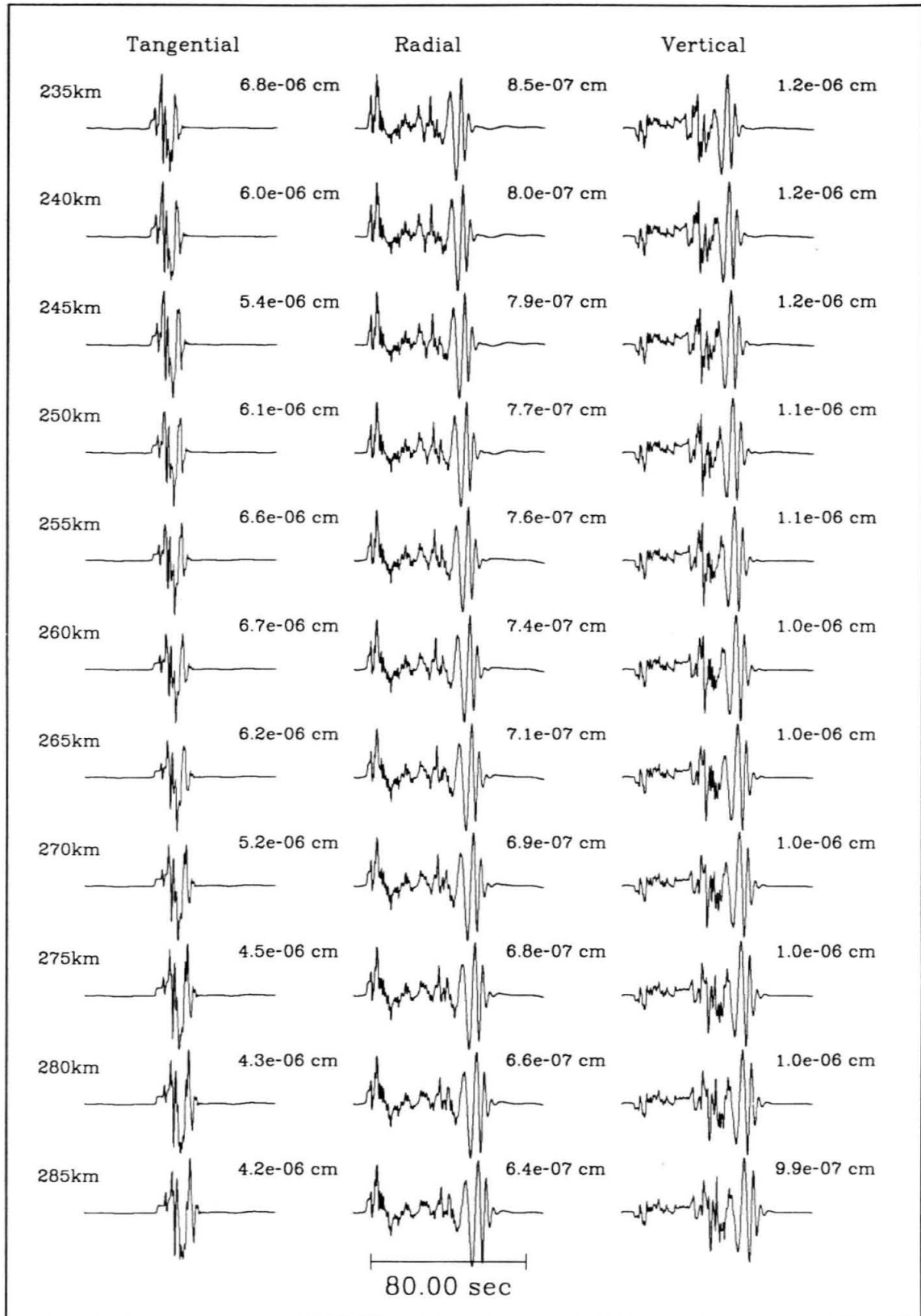
Mechanism: Vertical Dip-slip Depth: 11km



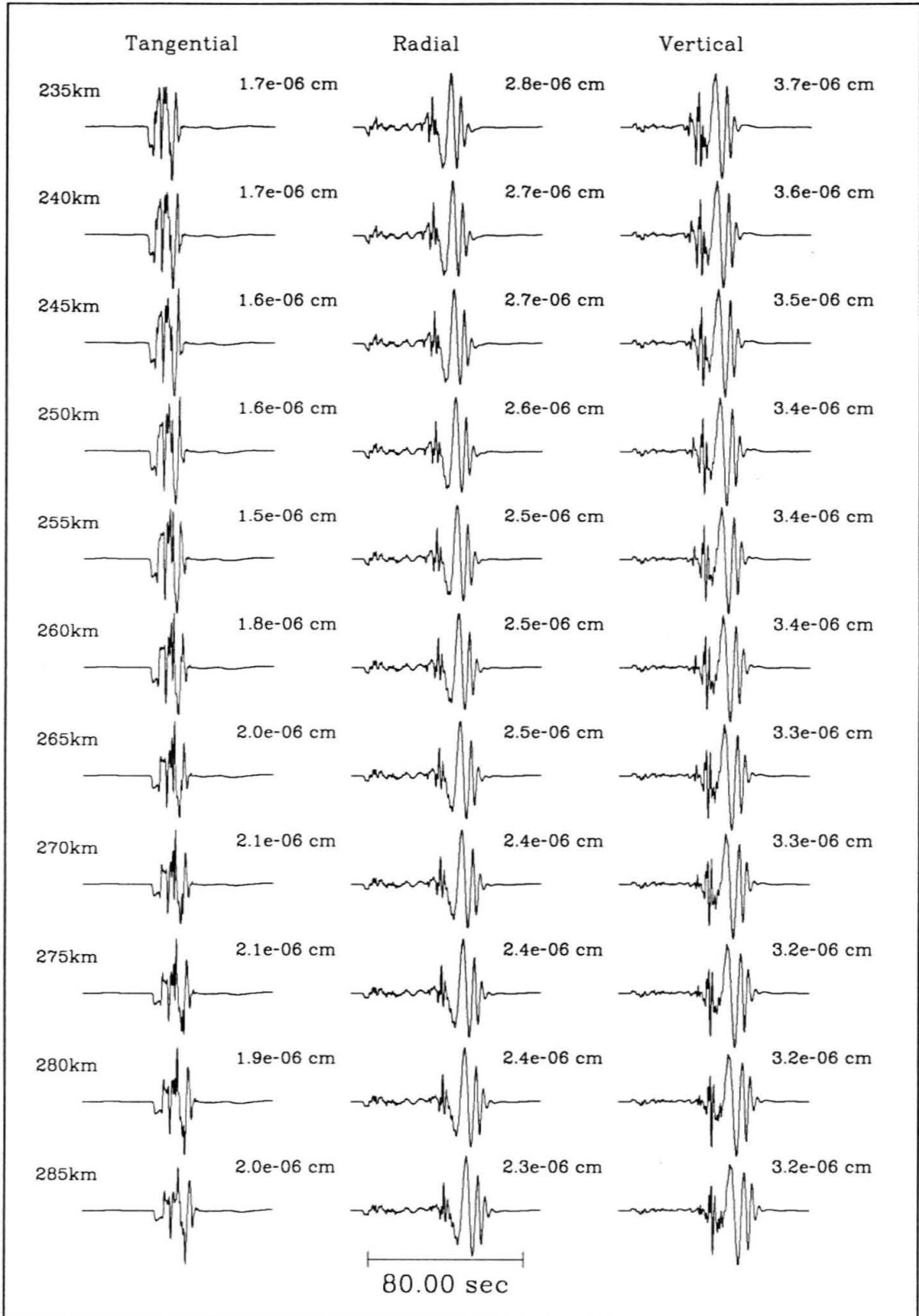
Mechanism: 45 degree Dip-slip Depth: 11km



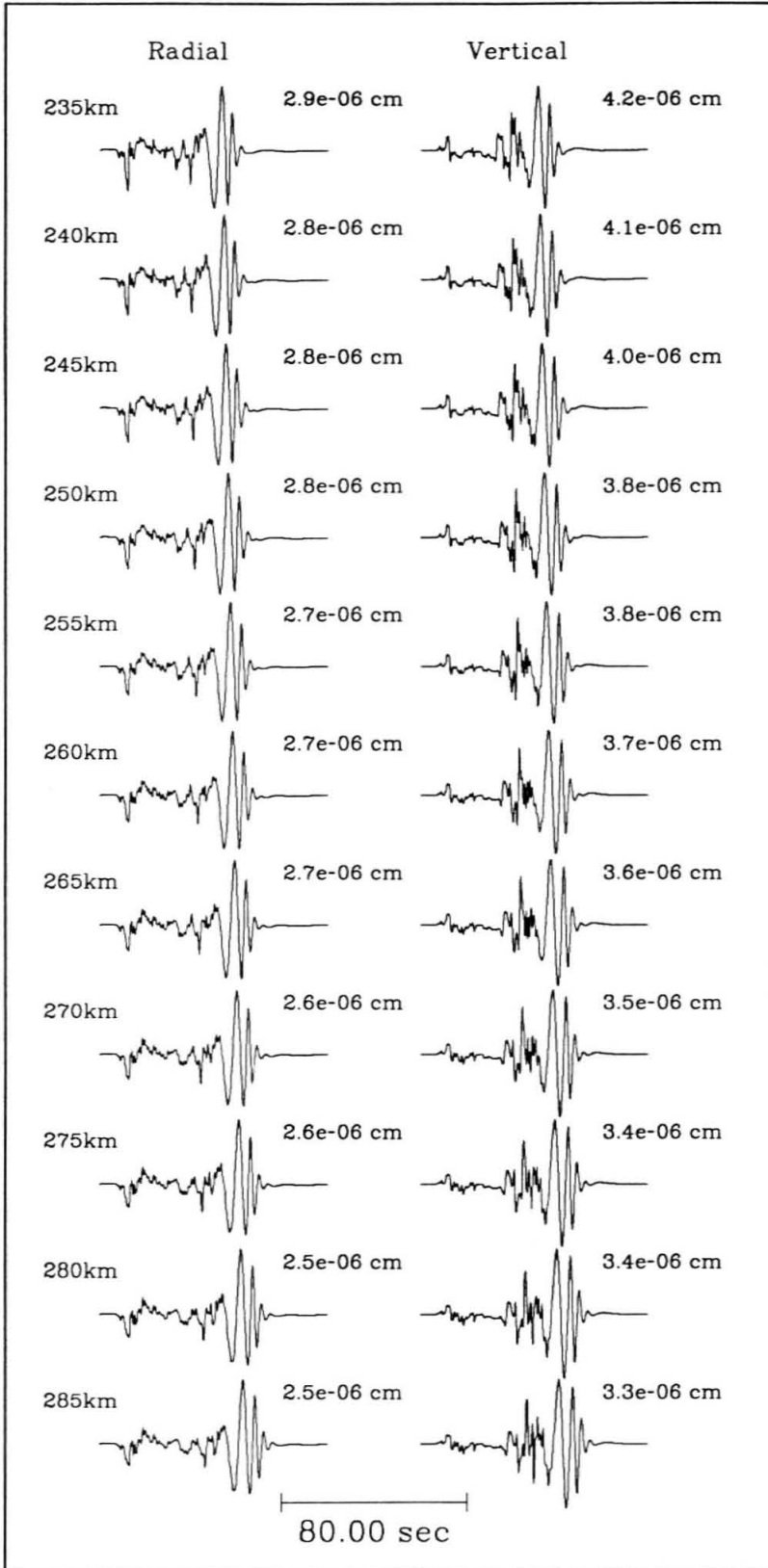
Mechanism: Vertical Strike-slip Depth: 11km



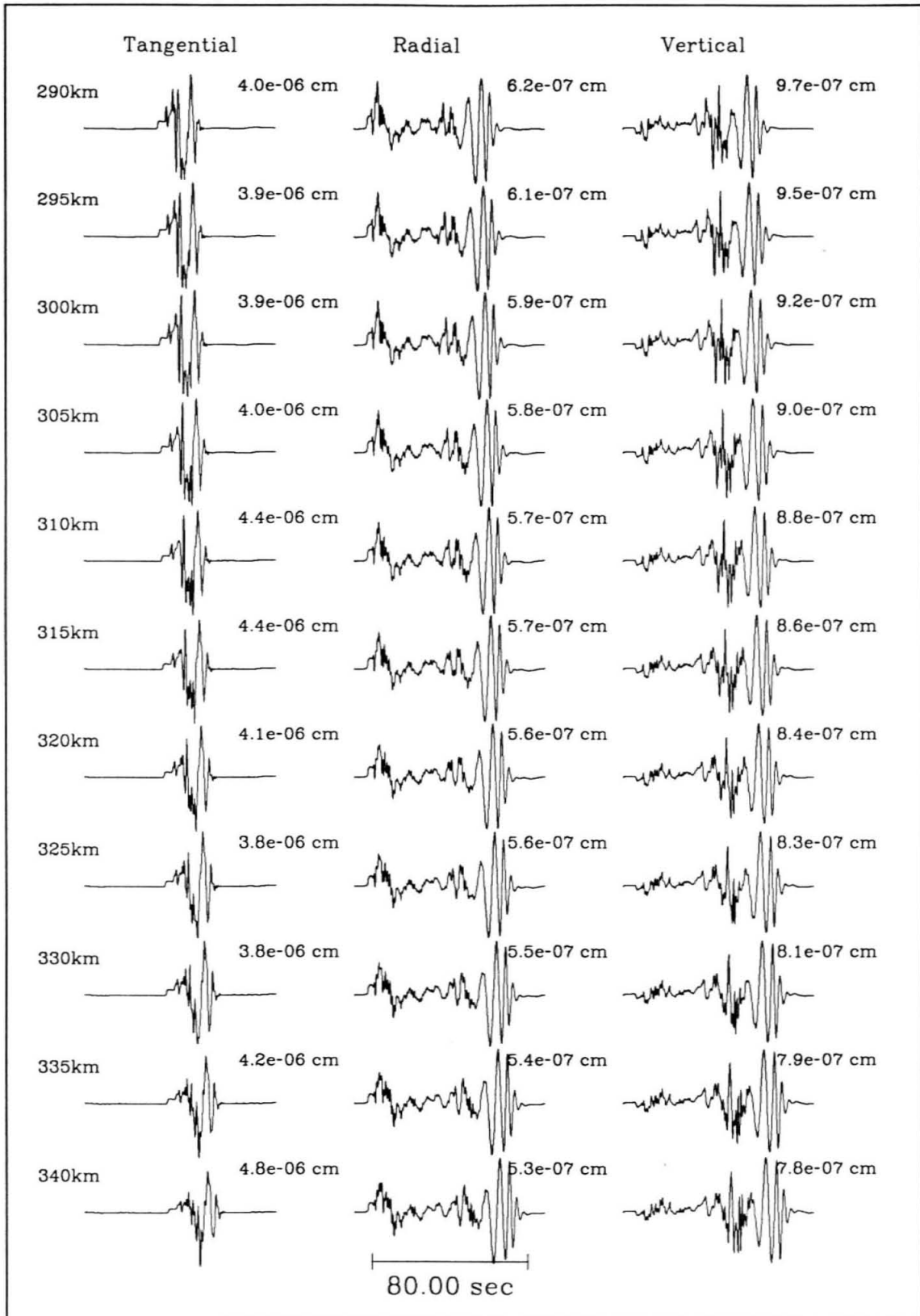
Mechanism: Vertical Dip-slip Depth: 11km



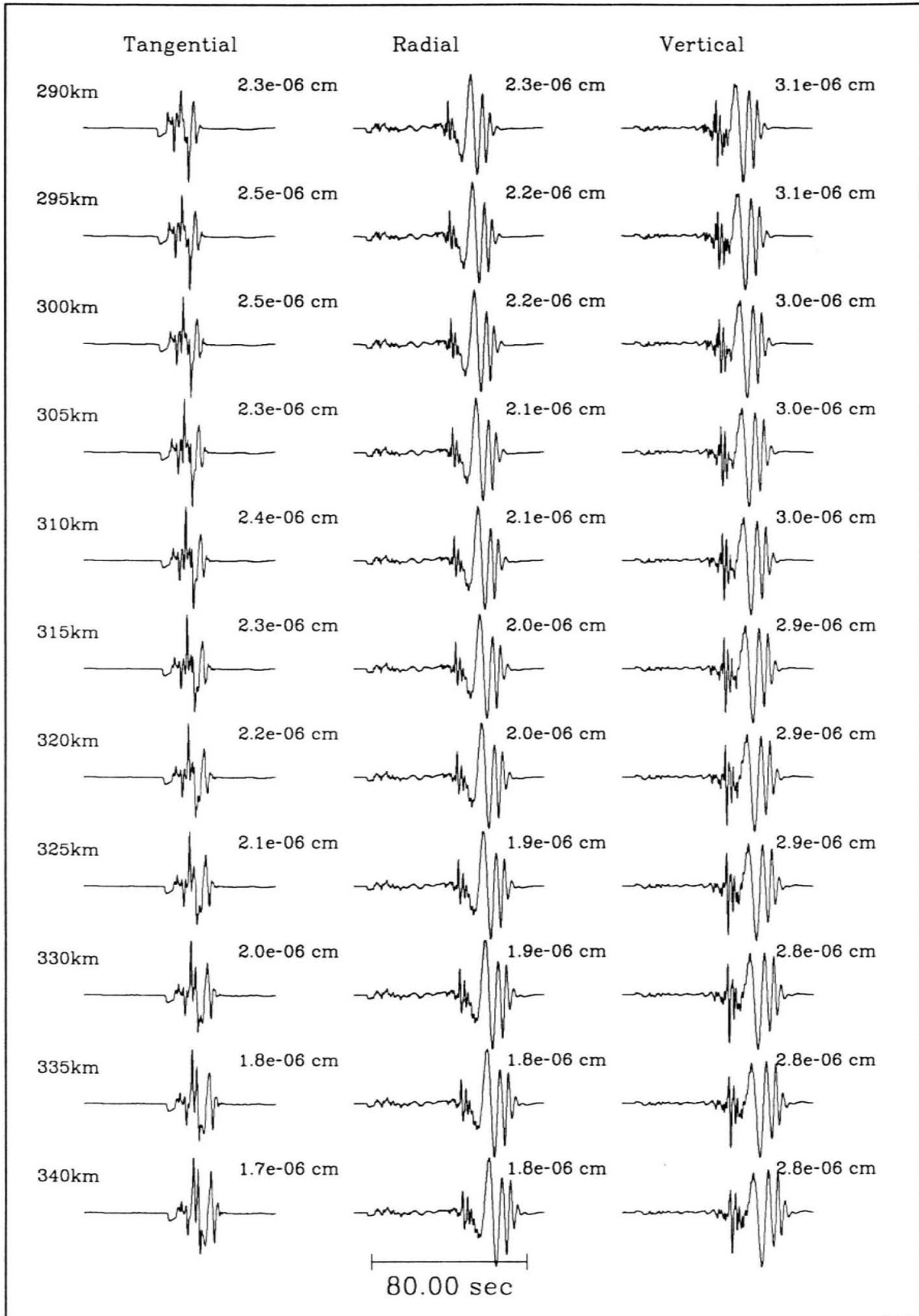
Mechanism: 45 degree Dip-slip Depth: 11km



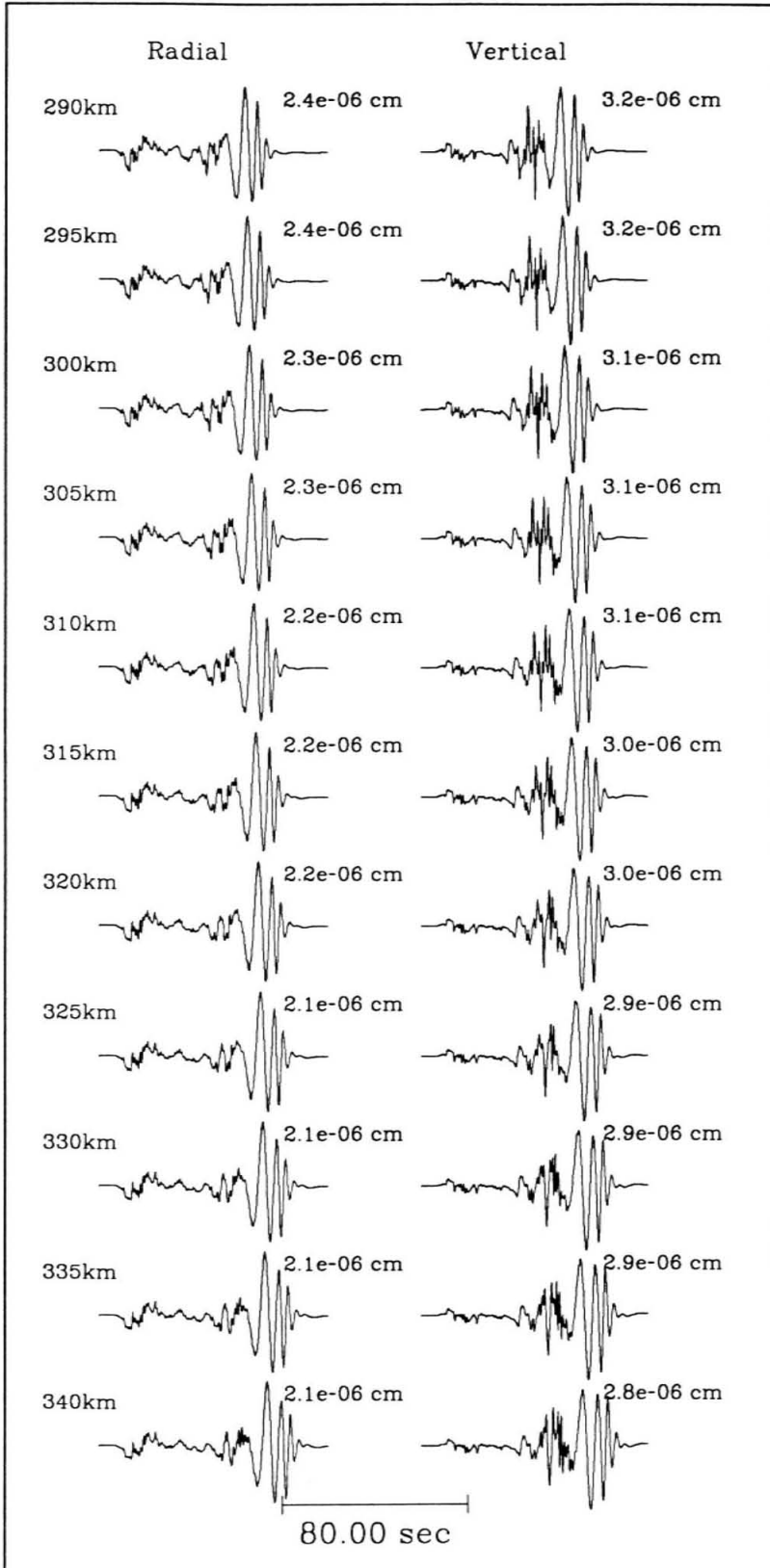
Mechanism: Vertical Strike-slip Depth: 11km



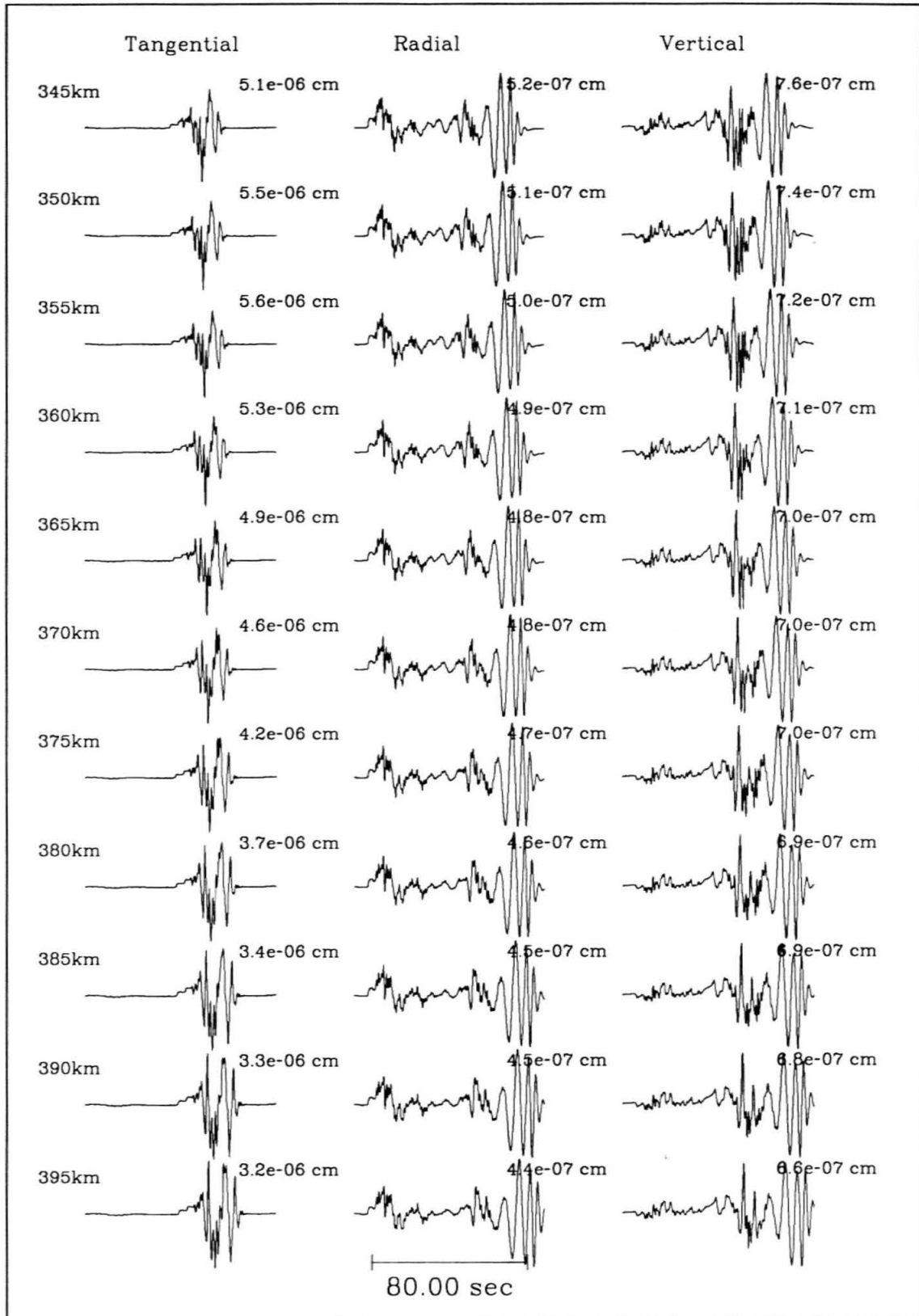
Mechanism: Vertical Dip-slip Depth: 11km



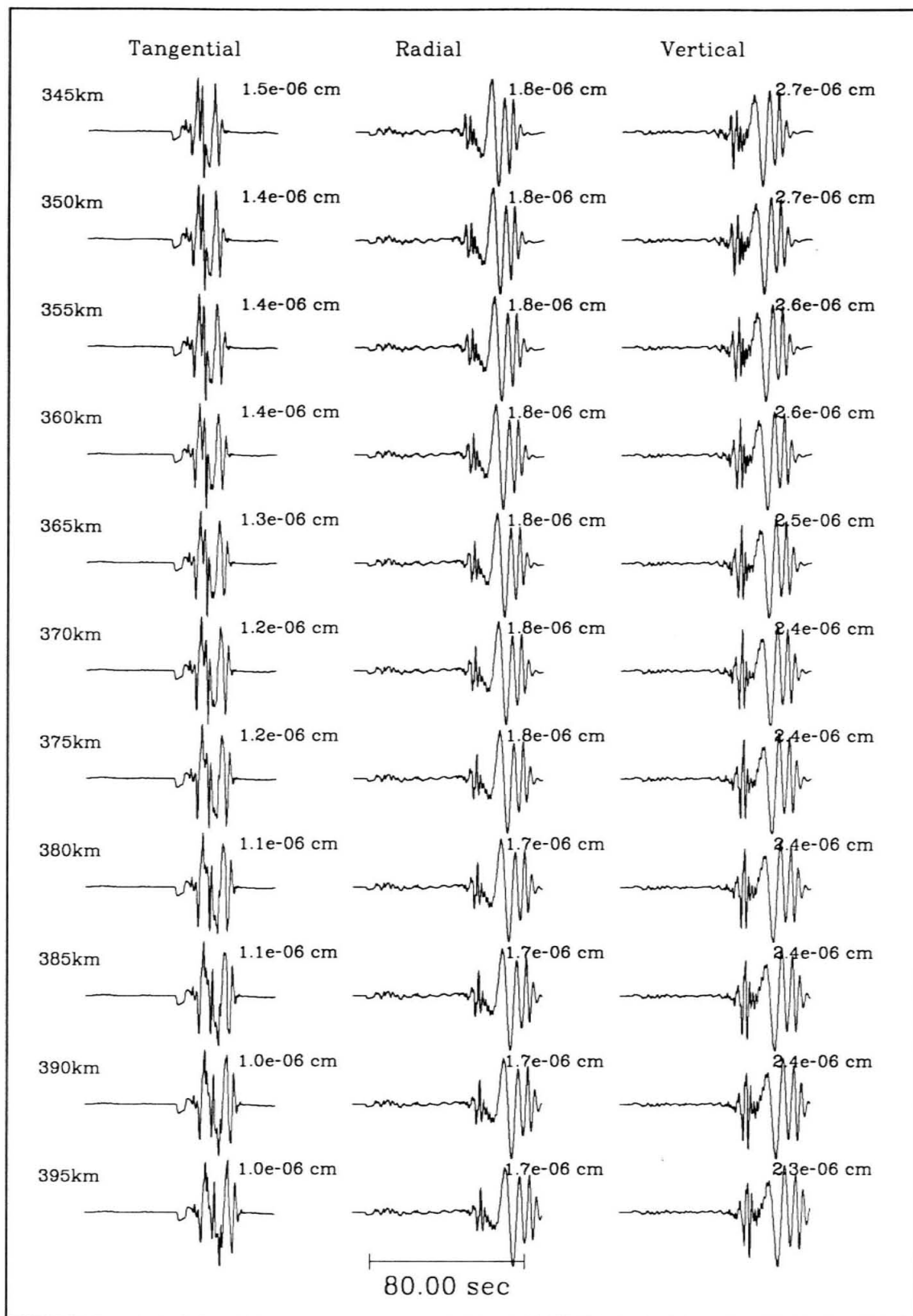
Mechanism: 45 degree Dip-slip Depth: 11km



Mechanism: Vertical Strike-slip Depth: 11km



Mechanism: Vertical Dip-slip Depth: 11km



Mechanism: 45 degree Dip-slip Depth: 11km

